Human movement is based on the healthy function of α-motoneurons, a type of nerve cell found in the spinal cord that triggers muscle contraction. Neuromuscular feedback mechanisms like stretch reflexes modulate α-motoneuron and, therefore, muscle activity. Eliciting the stretch reflex is a way of influencing the activity of α-motoneurons and simultaneously recording their reaction. Human α-motoneuron activity can only be recorded indirectly. This thesis aims to overcome this limitation by using an *in-silico* approach, i. e., computational modelling and simulations, to investigate mechanisms underlying α-motoneuron activity during stretch reflexes that can not be accessed *in vivo*. Motoneurons are simulated using an equivalent electric circuit model. Driven by open questions from experimental research, two aspects of the stretch reflex are addressed. First, the *in-silico* study reveals a non-linear multi-variable influence of experimental and physiological parameters on *in-vivo* estimates of excitation reflex amplitudes. Second, the simulation results suggest that a specific ion channel can facilitate postinhibitory excitation, an unexplained phenomenon repeatedly observed in α-motoneurons. In addition, a concept for extending the computational model to include sensory organ models is presented. The *in-silico* approach provides guidance for the design and interpretation of experimental studies, and the findings on the design of model interfaces can open up new application areas for stretch reflex and neuromuscular system models.

Laura Schmid

ISBN 978-3-946412-15-1

L. Schmid

In-silico analysis of α-motoneurons during stretch reflexes

CBM-15 (2024)

Insights into human alpha-motoneuron discharge properties during stretch reflexes – an in-silico approach

Laura Schmid

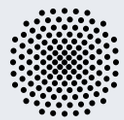

vorgelegt an der
Universität Stuttgart

Insights into human alpha-motoneuron discharge properties during stretch reflexes – an in-silico approach

Von der Fakultät Bau- und Umweltingenieurwissenschaften
der Universität Stuttgart zur Erlangung der Würde
einer Doktor-Ingenieurin (Dr.-Ing.)
genehmigte Abhandlung

Vorgelegt von

Laura Schmid, M.Sc.

aus
Reutlingen

Hauptberichter:	Prof. Oliver Röhrle, PhD
1. Mitberichter:	Prof. Randall Powers
2. Mitberichter:	Utku Ş. Yavuz, PhD

Tag der mündlichen Prüfung: 25. April 2024

Institut für Modellierung und Simulation Biomechanischer Systeme
der Universität Stuttgart
2024

Report No.: CBM-15 (2024)
Institute for Modelling and Simulation of Biomechanical Systems
Chair of Continuum Biomechanics and Mechanobiology
University of Stuttgart, Germany, 2024

Editor:
Prof. O. Röhrle, PhD

Institute for Modelling and Simulation of Biomechanical Systems
Chair of Continuum Biomechanics and Mechanobiology
University of Stuttgart
Pfaffenwaldring 5a
70569 Stuttgart, Germany

ISBN 978-3-946412-15-1
(D 93 – Dissertation, Universität Stuttgart)

Acknowledgements

This work was carried out between 2018 and 2023 during my time at the University of Stuttgart at the Chair for Continuum Biomechanics and Mechanobiology, first as part of the Institute of Applied Mechanics and later, after its founding, at the Institute for Modelling and Simulation of Biomechanical Systems. I am deeply grateful for the great people who have accompanied me on my research journey and contributed to the success of this work.

First of all, I would like to thank Professor Oliver Röhrle for giving me the opportunity to follow this exciting line of research. Thank you for your support on a professional and personal level, your trust in me and for letting me realise my ideas and utilise the exciting possibilities that arose during my journey. Through this environment, you have enabled me to develop myself and my research and to ultimately complete this work.

Dr. Utku Yavuz was no less important for this work's success. Thank you for the professional guidance, uncounted hours in video calls, for providing insights into your experimental work, for sharing your knowledge and data with me, for encouraging me when necessary and, of course, for being the co-examiner of this thesis.

I would also like to thank my second co-examiner, Professor Randall Powers. Your extensive knowledge of the field was invaluable, and your questions always led me to explore topics more deeply.

Many thanks to Thomas Klotz. Thank you for mentoring me, pulling me along with your enthusiasm, sharpening my eye for the essentials and for your commitment to discussing things over and over again.

I also thank my current and former office mates Andreas Hessenthaler, Pouyan Asgharzadeh, and Annika Sahrmann for sharing all the highs and lows. Thanks to Christian Bleiler, Mylena Mordhorst, David Rosin, Leonardo Gizzi and all former and current colleagues for lively discussions, coffee and chocolate breaks, sports activities and the one or other celebration we had. I am lucky to have always found open doors and ears with you.

I want to thank all the co-authors of my publications for the fruitful collaboration. Here, I would like to mention Professor Francesco Negro in particular. Also, thanks to Dr. Jennifer Ernst for the insights into patient care.

I thank my family, especially my parents, who have always encouraged me to pursue my passion. A big thank you also goes to my husband. Thank you for your love and emotional support and for ensuring I always find a filled fridge in busy times.

Laura Schmid

Stuttgart, June 2024

Contents

Abstract

All everyday movements are based on the healthy function of α-motoneurons. Motoneurons are nerve cells, and a particular type of motoneurons found in the spinal cord are α-motoneurons. What makes α-motoneurons unique is that their axons (nerve fibres via which signals are transmitted) leave the spinal cord to activate muscles. Motoneurons have been the subject of intensive research for decades, and today, we know their relevance in physiological movement control and certain diseases.

The entity of an α-motoneuron and the muscle fibres it innervates is called a motor unit and forms the smallest controllable unit of movement generation. The activity of a motor unit is the result of the interplay between the components of the neuromuscular system. Movements are not carried out strictly according to a pre-prepared plan but are constantly adapted to the circumstances. To this end, a large number of sensory organs, e. g., muscle spindles, permanently record the status of the neuromuscular system. Afferent nerves transfer the sensory information to the α-motoneurons and other parts of the central nervous system. In response, α-motoneurons adjust their activity, ultimately resulting in a change of muscle force. This feedback system allows us to perform complex movements in a changing environment. Reflexes are a central part of this feedback system. A reflex describes the process of a signal from sensory organs being transmitted to the central nervous system and evoking a rapid response. An essential class of reflexes relevant to movement control are stretch reflexes. Stretch reflexes are elicited by muscle spindles, which are sensitive to length changes of the muscle tissue and affect the activity of the stretched muscle and other muscles acting on the same joint.

Eliciting the stretch reflex is a way of influencing the activity of α-motoneurons and simultaneously recording their reaction. Human α-motoneuron activity can be recorded indirectly from the muscles they activate. Skeletal muscles are controlled by electrical signals, i. e., action potentials, generated by the α-motoneurons. The action potentials travel along the muscle fibres, initiating the contraction. The frequencies with which α-motoneurons discharge action potentials are related to the resulting muscle force. The propagation of the action potentials along the muscle fibres generates an electric field, which can be recorded using electromyography. As every action potential in the skeletal muscles is preceded by an action potential of the corresponding α-motoneuron, the recorded signals can be used to conclude the activity of the α-motoneurons.

Although α-motoneuron reflex responses are often stereotypical, many factors influence their strength, and they considerably contribute to movement control. As the activity of motoneurons can only be recorded indirectly, these influences have yet to be quantified. As a result, the function of reflexes in movement control and the role of α-motoneurons in neuromuscular diseases are still insufficiently understood. Computer simulations can be used here to supplement and expand the knowledge gained from experimental studies.

In this work, we use an *in-silico* approach, i. e., computational modelling and simulations, to investigate the physiological mechanisms underlying α-motoneuron activity during stretch reflexes that can otherwise not be accessed. In particular, we investigate how motoneuron properties and the experimental conditions influence the discharge behaviour of α-motoneurons in two stretch reflex pathways: the excitatory monosynaptic and the reciprocal inhibition pathway. We simulate motoneurons using an equivalent electric

circuit model. In the model, the motoneuron's spatial structure is summarised in two compartments representing the soma and dendrite. The time course of the motoneuron membrane potential and the generation of action potentials emerge from the dynamics of selected ion channels using the Hodgkin-Huxley modelling approach.

Motoneuron reflex responses can be recorded using electromyography. In particular, the discharge times of the action potentials (spikes) are recorded. The thereby obtained spike trains are commonly analysed by peristimulus analysis. In detail, the peristimulus timehistogram (PSTH) counts discharges relative to the stimulus time, and the peristimulus frequencygram (PSF) shows their instantaneous discharge frequencies. From the cumulative sums of both the PSTH and the PSF, the reflex amplitude can be obtained as an estimate of the reflex strength. The state-of-the-art method to obtain the reflex amplitude is manual evaluation, which is not feasible for many motoneurons simulated under different conditions. Therefore, we introduce a method for the automated determination of reflex amplitudes at the beginning of this thesis. The developed algorithm enables objective evaluation of large amounts of data, which can be obtained from simulations and future experimental studies.

Driven by open questions from experimental research, two aspects of the stretch reflex are addressed in detail. First, the influence of experimental and physiological parameters on *in-vivo* estimates of excitation reflex amplitudes is analysed. The size of reflex amplitudes obtained from *in-vivo* recordings of motor units is commonly used to address topics of basic research and clinical questions. Previous studies showed that the motoneuron properties and the experimental conditions influence the reflex amplitude. However, these influences and their possible interactions have yet to be quantified or weighted. It is also not known whether the PSTH and PSF are equally affected. The *in-silico* study performed within this work revealed a non-linear multi-variable influence of motoneuron properties and external conditions (motoneuron discharge frequency, random membrane potential fluctuations and stimulus strength) on reflex amplitudes. Thereby, the PSTH and PSF are differently sensitive to these influencing factors. We derive recommendations for designing and interpreting experimental studies from the simulation results.

The second aspect of this thesis addresses an unexplained pattern that repeatedly occurs during the inhibitory part of the stretch reflex. Postinhibitory excitation is a transient overshoot of a motoneuron's baseline firing rate following an inhibitory stimulus and can be observed *in vivo* in human motor units. However, the biophysical origin of this phenomenon is still unknown, and both reflex pathways and motoneuron properties have been proposed. We want to investigate if a specific ion channel, i. e., a hyperpolarisation-activated inward current (h-current) channel, can cause postinhibitory excitation. Therefore, the motoneuron model is extended to consider h-currents. In addition, spike trains of human motor units from the tibialis anterior muscle during reciprocal inhibition are analysed and compared to the simulation results. The simulations revealed that the activation of h-currents by an inhibitory postsynaptic potential can cause a short-term increase in a motoneuron's firing probability. Based on the results, we speculate that α-motoneurons can be excited by an inhibitory stimulus under certain conditions. Hallmarks of h-current activity, as identified from the modelling study, were found in 50 % of the human motor units that showed postinhibitory excitation. This study proposes that h-currents can facilitate postinhibitory excitation and act as a modulatory system

to increase motoneuron excitability after a strong inhibition.

In order to increase the range of research questions that can be addressed using an *in-silico* approach, a concept for extending the computer model to include models of sensory organs, i. e., muscle spindles, is presented. We compare two strategies for coupling the required models. The first approach transforms the continuous spindle frequency into a discrete spike train, and for every spike, a current is injected into the motoneurons. The second approach uses a conversion factor to transform the frequency into a current directly. We also investigate how data from reflex experiments can be used to parametrise the coupling parameters (gains). After determining the gains for both interface approaches, the PSTH and PSF in response to different mechanical stimuli are compared to experimental data. With appropriate gains, both approaches can predict the short-latency response of the monosynaptic stretch reflex. However, the gains determined from one type of stretch experiment fail to quantitatively predict the reflex amplitude in response to other types of stretch. The results emphasise that both the interface approach and the data used for parametrisation must be selected precisely for the respective application.

In summary, this thesis shows how motoneuron properties and the experimental conditions contribute to the discharge behaviour of α-motoneurons during two example stretch reflex pathways. The *in-silico* approach enhances the understanding of the system behaviour, which cannot be obtained *in-vivo*. The findings must now be transferred to experimental studies to profit fully from the interplay between experiment and simulation. Specifically, the gained insights on the PSTH and PSF metrics characteristics should be used to re-investigate or re-evaluate *in-vivo* motoneuron reflex responses using improved study protocols. Further, *in-vitro* studies should quantify the actual contribution of h-currents to postinhibitory excitation. The findings on the design of model interfaces can open up new application areas for stretch reflex and neuromuscular system models.

Zusammenfassung

Alle alltäglichen Bewegungen baiseren auf der gesunden Funktion von α-Motoneuronen. Motoneuronen gehören zu den Nervenzellen. Eine spezielle Art von Motoneuronen sind die α-Motoneuronen, welche sich im Rückenmark finden. Einzigartig an α-Motoneuronen ist, dass ihre Axone (Nervenfasern, über die Signale übertragen werden) das Rückenmark verlassen, um Muskeln zu aktivieren. Motoneuronen sind seit Jahrzehnten Gegenstand intensiver Forschung und heute wissen wir um ihre Bedeutung für die physiologische Bewegungskontrolle und bestimmte Krankheitsbilder.

Die Einheit aus einem α-Motoneuron und den von ihm innervierten Muskelfasern wird als motorische Einheit bezeichnet und bildet die kleinste kontrollierbare Einheit der Bewegungserzeugung. Die Aktivität einer motorischen Einheit ist das Ergebnis des Zusammenspiels der Komponenten des neuromuskulären Systems. Bewegungen werden nicht streng nach einem vorgefassten Plan ausgeführt, sondern ständig an die Gegebenheiten angepasst. Zu diesem Zweck registrieren eine Vielzahl von sensorischen Organen, zum Beispiel Muskelspindeln, permanent den Zustand des neuromuskulären Systems. Afferente Nerven leiten die sensorischen Informationen an die α-Motoneuronen und andere Teile des zentralen Nervensystems weiter. Als Reaktion darauf ändern die α-Motoneuronen ihre Aktivität, was letztendlich zu einer Veränderung der Muskelkraft führt. Dieses Rückkopplungssystem ermöglicht es uns, komplexe Bewegungen in einer sich verändernden Umgebung auszuführen. Reflexe sind ein zentraler Bestandteil dieses Systems. Ein Reflex beschreibt den Vorgang, bei dem ein Signal von sensorischen Organen an das zentrale Nervensystem weitergeleitet wird und eine schnelle Reaktion hervorruft. Eine wesentliche Klasse von für die Bewegungskontrolle relevanten Reflexen sind die Dehnungsreflexe, die in dieser Arbeit betrachtet werden. Dehnungsreflexe werden durch Muskelspindeln ausgelöst, die auf Längenänderungen im Muskelgewebe reagieren. Über verschiedene Signalwege beeinflussen sie sowohl den gedehnten Muskel als auch andere Muskeln, die am selben Gelenk ansetzen.

Das Auslösen eines Dehnungsreflexes ist eine Möglichkeit, die Aktivität von α-Motoneuronen experimentell zu beeinflussen und gleichzeitig ihre Reaktion aufzuzeichnen. Die Aktivität der α-Motoneuronen kann indirekt als elektrisches Signal in der Muskulatur erfasst werden. Die Ansteuerung von Skelettmuskeln erfolgt über elektrische Signale, die sogenannten Aktionspotentiale. Die Aktionspotentiale werden von α-Motoneuronen erzeugt und breiten sich entlang der Muskelfasern aus, wo sie die Muskelkontraktion auslösen. Dabei hängt die Entladungsrate, mit der die Motoneuronen die Aktionspotentiale generieren, mit der erzeugten Muskelkraft zusammen. Wenn sich Aktionspotentiale entlang der Muskelfasern ausbreiten, treten in der Muskulatur bioelektrische Felder auf, die mittels Elektromyografie aufgezeichnet werden können. Da jedem Aktionspotential in der Skelettmuskulatur ein Aktionspotential des entsprechenden α-Motoneurons vorausgeht, können die aufgezeichneten Signale genutzt werden, um Rückschlüsse über die Aktivität der α-Motoneuronen zu ziehen.

Obwohl Reflexe oft stereotypisch ablaufen, wird ihre Stärke von vielen Faktoren beeinflusst und sie tragen erheblich zur Bewegungskontrolle bei. Da die Aktivität der Motoneuronen nur indirekt erfasst werden kann, sind diese Einflüsse bisher kaum quantifiziert. Dadurch sind die Funktionsweise von Reflexen in der Bewegungsansteuerung und

die Rolle der α-Motoneuronen bei verschiedenen neuromuskulären Erkrankungen noch unzureichend verstanden.

Hier können Computersimulationen zum Einsatz kommen und das aus experimentellen Studien gewonnene Wissen ergänzen und erweitern. In dieser Arbeit wird ein *in-silico*-Ansatz verwendet. Das beutetet, dass wir computergestützte Modellierung und Simulationen nutzen, um die physiologischen Mechanismen zu untersuchen, die der Aktivität von α-Motoneuronen während Dehnungsreflexen zugrunde liegen und die sonst nicht zugänglich sind. Insbesondere wird untersucht, wie die Eigenschaften der Motoneuronen und die Versuchsbedingungen die Entladungseigenschaften während der Reflexantworten beeinflussen. Dabei betrachten wir zwei Signalwege des Dehnungsreflexes: den erregenden monosynaptischen Dehnungsreflex und den reziproken Hemmungsreflex. Die α-Motoneuronen werden mit Hilfe eines elektrischen Ersatzschaltbildes modelliert. Die räumliche Struktur des Motoneurons wird dabei in zwei Kompartimenten zusammengefasst, die das Soma und den Dendriten repräsentieren. Der zeitliche Verlauf des Motoneuronen-Membranpotentials und die Generierung von Aktionspotentialen ergibt sich aus der Dynamik ausgewählter Ionenkanäle unter Verwendung des Hodgkin-Huxley-Modellierungsansatzes.

Reflexantworten von α-Motoneuronen können mittels Elektromyographie aufgezeichnet werden. Dabei werden insbesondere die Zeitpunkte der Aktionspotentiale (Entladungen) erfasst. Die so gewonnenen Daten zu den Entladungsraten werden in der Regel mit Hilfe der Peristimulus-Analyse ausgewertet. Dabei zählt das Peristimulus-Zeithistogramm (peristimulus timehistogram, PSTH) die Anzahl der Aktionspotentiale relativ zur Stimuluszeit, und das Peristimulus-Frequenzgramm (peristimulus frequencygram, PSF) zeigt, mit welcher Frequenz die Aktionspotentiale jeweils auftreten. Aus den jeweiligen kumulativen Summen über das PSTH und das PSF lässt sich die Reflexamplitude als Schätzwert für die Reflexstärke ermitteln. Üblicherweise wird die Reflexamplitude manuell bestimmt. Dies ist jedoch für viele Motoneuronen, die unter verschiedenen Bedingungen simuliert werden nicht praktikabel. Daher stellen wir zu Beginn dieser Arbeit eine Methode zur automatisierten Bestimmung der Reflexamplituden vor. Der entwickelte Algorithmus ermöglicht eine objektive Auswertung großer Datenmengen, wie sie aus Simulationen und zukünftigen experimentellen Studien gewonnen werden können.

Angeregt durch offene Fragen der experimentellen Forschung werden zwei Aspekte des Dehnungsreflexes im Detail behandelt. Zunächst wird der Einfluss experimenteller und physiologischer Parameter auf *in-vivo*-Schätzungen der Reflexamplituden eines erregenden Reflexes analysiert. Die Größe von Reflexamplituden wird häufig in der Grundlagenforschung verwendet, aber auch um klinische Fragen zu adressieren. Bisherige Studien haben gezeigt, dass die Eigenschaften der Motoneuronen und die Versuchsbedingungen die Reflexamplitude beeinflussen. Diese Einflüsse und ihre möglichen Wechselwirkungen sind jedoch noch nie quantifiziert oder gewichtet worden. Es ist auch nicht bekannt, ob das PSTH und das PSF gleichermaßen beeinflusst werden. Die im Rahmen dieser Arbeit durchgeführte *in-silico*-Studie zeigt einen nicht-linearen, multivariablen Einfluss der Motoneuronen-Eigenschaften und der aufgebrachten Bedingungen (Entladungsfrequenz, zufällige Membranpotentialschwankungen und Reizstärke) auf die Reflexamplituden. Dabei sind das PSTH und das PSF unterschiedlich empfindlich für diese Einflussfaktoren. Aus den Simulationsergebnissen werden Empfehlungen für die Gestaltung und Interpretation experimenteller Studien abgeleitet.

Der zweite Aspekt, der in dieser Arbeit untersucht wird, betrifft ein bisher unerklärtes Muster, das wiederholt während des hemmenden Teils des Dehnungsreflexes auftritt. Die postinhibitorische Erregung ist eine vorübergehende überhöhte Aktivität eines Motoneurons nach einem inhibitorischen Reiz und kann in menschlichen motorischen Einheiten *in vivo* beobachtet werden. Der biophysikalische Ursprung dieses Phänomens ist jedoch noch unbekannt. Zur Erklärung wurden sowohl Reflexwege als auch Motoneuronen-Eigenschaften vorgeschlagen. Wir untersuchen, ob ein spezifischer, von hyperpolarisierten Membranpotentialen aktivierter Ionenkanal, der sogenannte h-Kanal, eine postinhibitorische Erregung verursachen kann. Daher wird das Motoneuronen-Modell erweitert, um h-Kanäle zu berücksichtigen. Darüber hinaus werden Daten zu Entladungsraten menschlicher motorischer Einheiten des Tibialis Anterior Muskels während der reziproken Hemmung analysiert und mit den Simulationsergebnissen verglichen. Die Simulationen ergaben, dass die Aktivierung von h-Kanälen durch ein hemmendes postsynaptisches Potential eine kurzfristige Erhöhung der Entladungswahrscheinlichkeit eines Motoneurons bewirken kann. Auf Grundlage der Ergebnisse spekulieren wir, dass α-Motoneuronen unter bestimmten Bedingungen durch einen hemmenden Reiz erregt werden können. In 50 % der experimentell untersuchten motorischen Einheiten, die eine postinhibitorische Erregung aufwiesen, wurden die in der Modellierungsstudie identifizierten Merkmale der h-Kanal-Aktivität gefunden. Die Ergebnisse legen nahe, dass h-Kanäle die postinhibitorische Erregung fördern und nach einer starken Hemmung als modulierendes System zur Erhöhung der Erregbarkeit von Motoneuronen wirken können.

Um die Bandbreite der Forschungsfragen zu erweitern, die mit einem *in-silico*-Ansatz behandelt werden können, wird ein Konzept zur Erweiterung des Computermodells um Modelle von sensorischen Organen vorgestellt. Wir vergleichen zwei Strategien zur Kopplung eines Motoneuronen- mit einem Muskelspindel-Modell. Dabei wird außerdem untersucht, wie Daten aus Reflexexperimenten zur Parametrisierung der Kopplungsparameter verwendet werden können. Der erste Ansatz wandelt die kontinuierliche Spindelfrequenz in eine Abfolge von diskreten Entladungszeitpunkten um, und für jede Entladung wird eine festgelegte Menge elektrischen Stroms in die Motoneuronen injiziert. Der zweite Ansatz verwendet einen Umrechnungsfaktor, um die Frequenz direkt in einen Strom umzuwandeln. Zunächst werden die relevanten Parameter für beide Schnittstellenansätze bestimmt. Anschließend werden das PSTH und das PSF für verschiedene mechanische Reize mit experimentellen Daten verglichen. Mit geeigneten Kopplungsparametern kann das Modell unter Nutzung beider Ansätze die typische Reflexantwort des monosynaptischen Dehnungsreflexes vorhersagen. Die unter Verwendung von einer Art des Dehnungsreizes ermittelten Kopplungsparameter sind jedoch nicht in der Lage, die Reflexamplitude als Reaktion auf andere Arten von Dehnungen quantitativ vorherzusagen. Die Ergebnisse unterstreichen, dass sowohl der Schnittstellenansatz als auch die zur Parametrisierung verwendeten Daten spezifisch für die jeweilige Anwendung gewählt werden müssen.

Zusammenfassend zeigt diese Arbeit, wie Motoneuronen-Eigenschaften und die experimentellen Bedingungen das Entladungsverhalten von α-Motoneuronen während des Dehnungsreflexes beeinflussen. Der *in-silico*-Ansatz verbessert das Verständnis des Systemverhaltens über die Erkenntnisse hinaus, die mit einem *in-vivo*-Ansatz gewonnen werden können. Die neu gewonnenen Erkenntnisse müssen nun auf experimentelle Studien übertragen werden, um das Zusammenspiel von Experiment und Simulation optimal zu nutzen. Insbesondere sollten die Schlussfolgerungen über die charakteristischen Eigenschaften der

PSTH- und PSF-Metriken genutzt werden, um Reflexreaktionen *in vivo* mit verbesserten Studienprotokollen erneut zu untersuchen beziehungsweise neu zu evaluieren. Darüber hinaus sollten *in-vitro*-Studien den tatsächlichen Beitrag der h-Kanäle zur postinhibitorischen Erregung quantifizieren. Die Nutzung der Erkenntnisse zur Gestaltung von Modellschnittstellen kann neue Anwendungsbereiche für Modelle des Dehnungsreflexes und des neuromuskulären Systems erschließen.

Nomenclature

Subscripts and superscripts

Symbol	Description
∞	steady-state
C	coupling
cap	capacitive
d	dendrite compartment
ex	extracellular
H	h-channel/HCN-channel
i	index
in	intracellular
inj	injected
ion	ionic
Kf	fast potassium ion channel
Ks	slow potassium ion channel
L	leakage ion channel
m	membrane
Na	sodium ion channel
s	soma compartment

Symbols

This table is arranged with Greek characters first, followed by Latin and calligraphic letters. Small letters precede capital letters.

Symbol	Unit	Description
α	ms^{-1}	ion channel gate forward rate
β	ms^{-1}	ion channel gate backward rate
λ	cm	length constant
τ	ms	time constant
Φ	mV	potential
a	cm	radius
b	-	a parameter
c_m	$\mu\mathrm{F\,cm}^{-1}$	transverse membrane capacitance
C	µF	capacitance
C_m	$\mu\mathrm{F\,cm}^{-2}$	specific membrane capacitance per unit area

d	cm	diameter
E	mV	equilibrium potential
f_{spindle}	Hz	muscle spindle frequency
F	$\text{C}\,\text{mol}^{-1}$	Faraday's constant
g	mS	conductance
$\overline{g}$	mS	maximum conductance
G	$\text{mS}\,\text{cm}^{-2}$	specific conductance per unit area
$\overline{G}$	$\text{mS}\,\text{cm}^{-2}$	maximum specific conductance per unit area
h	-	sodium channel inactivation gate
I	µA	electric current
J	$\mu\text{A}\,\text{cm}^{-2}$	electric current density
k	-	reference value for the cumulative sum
l	cm	length
L	-	electrotonic length
m	-	sodium channel activation gate
n	-	potassium channel activation gate
N	counts	number
N_{MN}	counts	number of motoneurons
p	-	p-value (statistics)
P	$\text{m}\,\text{s}^{-1}$	permeability
PSC	µA	postsynaptic current
q	-	potassium channel activation gate
r_{i}	$\text{k}\Omega\,\text{cm}^{-1}$	longitudinal resistance of the cytoplasm
R_{i}	$\text{k}\Omega\,\text{cm}$	cytoplasm resistivity
r_{m}	$\text{k}\Omega\,\text{cm}$	transverse membrane resistance
R_{m}	$\text{k}\Omega\,\text{cm}^2$	specific membrane resistance
R_{N}	$\text{k}\Omega\,\text{cm}^2$	input resistance
s	-	h-channel activation gate
S	-	cumulative sum
$\mathbf{S}$	-	cumulative sum vector
t	ms	time
T	K	absolute temperature
V_{half}	mV	ion channel half-maximum activation potential
V_{m}	mV	membrane potential
$V_{\text{overshoot}}$	mV	overshoot potential
V_{rest}	mV	resting potential
V_{slope}	mV	ion channel slope factor potential
V_{step}	mV	step potential
w	-	a general ion channel gate variable

x	cm	distance/position
X	-	an arbitrary ion
y	-	an arbitrary variable
$\bar{y}$	-	an arbitrary mean value
z	counts	number of electrons
$\mathcal{R}$	$\mathrm{J\,mol^{-1}\,K^{-1}}$	universal gas constant

Acronyms

Symbol	Description
AP	Action potential
AHP	Afterhyperpolarisation
AMI	Agonist-antagonist myoneural interface
Ca^{2+}	Calcium ion
Cl^{-}	Chloride ion
CoV	Coefficient of variation
CUSUM	Cumulative sum
e. g.	exempli gratia (for example)
EMG	Electromyogram
EPSP	Excitatory postsynaptic potential
FF-type	Fast fatigable motor unit type
FR-type	Fast fatigue resistant motor unit type
HCN	Hyperpolarization-activated cyclic nucleotide-gated non-selective cation
HDsEMG	High-density surface electromyogram
Ia	primary muscle spindle afferent
Ib	Golgi-tendon organ afferent
i. e.	id est (that is)
II	secondary muscle spindle afferent
IISP	Interspike interval superposition plot
IPSP	Inhibitory postsynaptic potential
ISI	Interspike interval
K^{+}	Potassium ion
LIF	Leaky integrate-and-fire
MN	Motoneuron
MVC	Maximum voluntary contraction
Na^{+}	Sodium ion
ODE	Ordinary differential equation

PIC	Persistent inward current
PSC	Postsynaptic current
PSF	Peristimulus frequencygram
PSP	Postsynaptic potential
PSTH	Peristimulus timehistrogram
S-type	Slow motor unit type

1 Introduction

"The terminal path may, to distinguish it from internuncial common paths, be called the final common path. The motor nerve to a muscle is a collection of such final common paths."

Sir Charles Scott Sherrington[1] (1906)

1.1 Motivation

Running, jumping, dancing, eating a piece of cake – none of it would be possible without motoneurons. Motoneurons are nerve cells responsible for movement generation, and α-motoneurons in particular are a type of motoneuron located in the spinal cord (Burke et al., 1977). What makes α-motoneurons unique is that their axons (nerve fibres via which signals are transmitted) leave the spinal cord to activate muscles, making them the "final common path" of movement generation. Motoneurons have been the subject of intensive research for decades, and we know their relevance today. The pathological loss of α-motoneurons leads to paralysis, severely impairs quality of life and can even be fatal (O'Donovan and Falgairolle, 2022). However, the physiological function of the α-motoneurons enables us to execute the various movements required for an active life.

The entity of an α-motoneuron and the muscle fibres it innervates is called a motor unit and forms the smallest controllable unit of movement generation (Liddell and Sherrington, 1925). The activity of a motor unit is the result of the complex interplay between the components of the neuromuscular system. Movements are not carried out strictly according to a pre-prepared plan but are constantly adapted to the circumstances (Kandel et al., 2013). To this end, sensory organs, e. g., muscle spindles and Golgi-tendon organs, permanently monitor the current state of the neuromuscular system. Afferent nerves transfer the sensory information to the central nervous system. The signals are transmitted to the α-motoneurons in the spinal cord directly or through several other neurons. In response, the α-motoneurons adjust their activity, ultimately resulting in a change of muscle force (Kandel et al., 2013). This feedback system allows us to perform complex movements in a dynamic environment. Reflexes are a central part of this feedback system. A reflex describes the process of a signal from sensory organs being transmitted to the central nervous system and evoking a rapid response (Pierrot-Deseilligny and Burke, 2005).

Different reflex pathways involve α-motoneurons, but the most known might be the knee-jerk reflex. A tap on the patella tendon yields a rapid extension of the knee joint. The muscle contraction that produces the knee extension is a reflex response to the stretch applied to the muscle by the tendon tap. This and other rapid reactions to stretching a muscle are known as stretch reflexes. The sensory organs associated with stretch reflexes are the muscle spindles, which are, in every muscle, located in parallel to the muscle fibres (Macefield and Knellwolf, 2018).

Reflex responses of human α-motoneurons can be recorded indirectly as an electrical

[1] Sir Charles Scott Sherrington (*27 November 1857, †4 March 1952) was rewarded the Nobel Prize in Physiology or Medicine 1932 for his discoveries regarding the functions of neurons.

signal in the muscle. Motoneurons and muscle fibres communicate via electrical signals, the so-called action potentials. Action potentials emerge from the activity of ion channels in the motoneuron's cell membrane. An action potential produced by an α-motoneuron is transferred via the axon to the muscle fibres of the respective motor unit. Then, the action potential propagates along the muscle fibre, initiating the contraction. The frequencies with which α-motoneurons discharge action potentials are related to the resulting muscle force (De Luca and Hostage, 2010). The propagation of the action potentials along the muscle fibres generates an electric field, which can be recorded using electromyography (EMG). Since every action potential of a muscle fibre is preceded by an action potential in the corresponding α-motoneuron, the recorded signals can be used to draw conclusions about the activity of the α-motoneurons.

Eliciting the stretch reflex is one way of influencing the activity of α-motoneurons and simultaneously recording their reactions. The advantage of EMG recordings is that they can be performed *in vivo*, i. e., in the living organism. Thereby, the activity of α-motoneurons can be observed in their physiological environment and under physiological conditions. However, the method is indirect and only records the final result of the reflex mechanism. Insights on the processes within the α-motoneuron can be obtained using the *in-vitro* approach. Here, the activity of single α-motoneurons is recorded, e. g., with microelectrodes outside the organism. This way, input-output relationships can be determined, albeit under conditions that do not necessarily correspond to the physiological situation.

Although reflex responses are often stereotypical, their strength can be modulated by many factors such that they create complex patterns and coordinate movements (Kandel et al., 2013). Due to the limitations of current experimental techniques, these influences have hardly been quantified to date. As a result, the functioning of reflexes in movement control and the pathophysiology of associated neuromuscular diseases are still poorly understood. Over the past decades, computer models have been developed to overcome the limitations of experimental methods. *In-silico* studies describe experiments performed on a computer based on computational modelling and simulation. The *in-silico* approach offers several advantages over *in-vivo* and *in-vitro* studies. The internal system properties are known, and the input parameters can be controlled completely. Further, there are no limitations concerning the signal quality, recording times or available recording technologies. Therefore, *in-silico* studies can provide otherwise unfeasible insights.

In this work, we use computational modelling and simulations to investigate physiological mechanisms underlying α-motoneuron activity during stretch reflexes that can otherwise not be accessed. Thereby, we build on the large basis of modelling approaches that were developed in the last decades. At the same time, we rely on *in-vivo* data with which we compare the model predictions to draw conclusions about physiological processes. As a result, this work contributes to a better understanding of *in-vivo* recordings of α-motoneuron activity during stretch reflexes, which can lead to a better understanding of movement generation in general and, eventually, of pathological disorders concerning the neuromuscular system.

1.2 State of the art

Computational modelling of physiological systems can be divided into two primary categories: phenomenological and biophysical approaches. Phenomenological models focus on describing input-output relationships to fit experimental data without delving into the underlying mechanisms, essentially adopting a "black-box" methodology. In contrast, biophysical models use available knowledge to describe the mechanisms underlying a physiological process. Phenomenological models are valuable for simplifying complex processes and may be necessary when computational resources are limited. However, mechanistic models are crucial for comprehending behaviours in complex systems.

Modelling the behaviour of motoneurons during stretch reflexes requires at least two model components. These are a motoneuron model and a model representing the sensory input. Muscle spindle models can provide an estimate of the sensory input to motoneurons during stretch reflexes. This section describes state-of-the-art (α-)motoneuron models, muscle spindle models, and stretch reflex models and their applications. This section is partly based on Haggie, Schmid et al. (2023).

1.2.1 Computational motoneuron modelling

Computational models representing motoneuron behaviour exist on many levels of abstraction. Two fundamentally different approaches can be distinguished. The first approach is based on a phenomenological description of the input-output behaviour of the motoneurons. Thereby, a quantity representing the input is projected via a mathematical function onto a quantity representing the resulting activity of the motoneurons. For example, a sigmoid transfer function or a weighted sum can be used to describe the input-output behaviour of a population of motoneurons (e. g., Li et al., 2015; Raphael et al., 2010). Due to its fast computation, this approach is especially suited to model large networks of neurons. Input-output functions can also be employed to predict the discharge frequencies of individual motoneurons (e. g., Fuglevand et al., 1993; Heckman and Binder, 1991). For example, these models have been used to investigate muscle fatigue (Potvin and Fuglevand, 2017) or the adaptation of the neuromuscular system in response to exercise (Altan, 2022).

The second modelling approach aims to predict individual motoneuron spiking (discharging) based on the motoneuron membrane's characteristic behaviour. Two main classes of spiking models can be distinguished: threshold-crossing and compartmental models. Threshold-crossing models describe the sub-threshold time course of the membrane potential and how, by integration of inputs, the membrane potential approaches the spike threshold. These models refrain from explicitly describing the time course of the action potential. Instead, when the threshold is reached, the firing time is registered, the membrane potential is reset, and the integration process starts again.

Different possibilities exist to describe the sub-threshold membrane potential trajectory, the most commonly used being probably the so-called leaky integrate-and-fire model. It was first introduced by Lapicque (1907). The behaviour of the motoneuron membrane is described by a capacitor in parallel with a resistor. Consequently, the membrane potential decays without inputs to the resting state (leaky behaviour). Researchers extended the model to consider e. g., more physiological membrane potential time courses, refractory

times or history-dependent effects (e. g., Burkitt, 2006; Herrmann and Gerstner, 2002).

Threshold-crossing models do not consider the activity of individual ion channels and neglect the spatial dimensions of the motoneuron. Compartmental models were developed to overcome these limitations. Two features characterise them: they consider the motoneuron's anatomical structure and spatial dimension and assign specific properties and ion channels to the respective parts of the neuron. Thereby, the signal propagation within the motoneuron is commonly modelled using the cable equation and the equivalent cylinder theory (see Section 3.3 and Rall, 1962a,b). Active firing behaviour can be incorporated by modelling voltage-gated ion channels based on the framework developed by Hodgkin and Huxley (see Section 3.2 and Hodgkin and Huxley, 1952d). The resulting models integrate input signals based on the respective compartment's membrane properties, and action potentials arise from the function of voltage-gated conductances. Compartmental motoneuron models differ in the number of compartments and conductances (e. g., Booth et al., 1997; Cisi and Kohn, 2008; Elias and Kohn, 2013; Negro and Farina, 2011; Powers et al., 2012; Taylor and Enoka, 2004). Many compartmental models inherently account for physiological motoneuron principles like the size principle and the onion skin principle (see Section 2.3.3). They provided insights into the contribution of different ion channels to complex motoneuron discharge patterns (e. g., Booth et al., 1997; Powers et al., 2012; Taylor and Enoka, 2004), or into control strategies of the central nervous system (e. g., Negro and Farina, 2011). They were also successfully incorporated into neuromuscular system models (e. g., Dideriksen et al., 2015; Elias et al., 2014; Kapardi et al., 2022).

1.2.2 Computational muscle spindle modelling

Muscle spindles are sensitive to muscle stretch and stretch velocity (Macefield and Knellwolf, 2018). Various phenomenological models have been developed to describe the relationship between muscle stretch and changes in muscle spindle activity (Prochazka and Gorassini, 1998b and references therein). While these models successfully reproduce experimental muscle spindle firing frequencies across different stretch velocities, they do not consider the modulation of spindle sensitivity by the fusimotor system (see Section 2.4.1).

Maltenfort and Burke (2003) proposed a phenomenological model that calculates muscle spindle firing frequencies in response to muscle stretch and fusimotor activation. Therefore, separate discharge frequencies are computed for passive stretch and the two types of fusimotor input (static and dynamic). These contributions are combined, with the higher rate partially inhibiting the lower rate before being added to the passive contribution. An updated version of the model was published during the research for this work (Schmid et al., 2022).

Mileusnic et al. (2006) and Lin and Crago (2002b) both developed semi-physiological models by explicitly representing the anatomical structure of the spindle, including the three intrafusal fibre types and their effects on the primary and secondary afferent activity, as well as their sensitivity to fusimotor input. In the physiological spindle, the contributions of each intrafusal fibre to the overall firing frequency are non-linearly combined, resulting in the suppression of lower frequencies by higher ones, a phenomenon known as occlusion (Banks, 1994; Schäfer, 1974). Mileusnic et al.'s model appropriately accounts for this, whereas Lin and Crago's model completely suppresses the lower frequency in

favour of the higher one.

Blum et al. (2020) introduced a sophisticated muscle spindle model based on the physiological contraction mechanism of intrafusal fibres and their interaction with the muscle-tendon complex. This model can predict many experimentally observed patterns of muscle spindle activity without explicitly modelling them. It was recently supplemented by a spike generation model, which is currently still under development (Housley et al., 2024).

1.2.3 Computational modelling of the stretch reflex

Existing computational models of the stretch reflex differ in their components and the pathways they consider (see Section 2.4). Some approaches focus on a single pathway of the stretch reflex, e. g., the monosynaptic stretch reflex (e. g., Chaud et al., 2012; Schuurmans et al., 2009). Others consider the interaction of an agonist and an antagonist muscle and include the monosynaptic as well as reciprocal inhibition pathway (e. g., Dideriksen et al., 2015; Sreenivasa et al., 2015). Sensory signals from secondary muscle spindle afferents or Golgi-tendon organs can also be included (e. g., Raphael et al., 2010; Stienen et al., 2007).

As shown in Sections 1.2.1 and 1.2.2, numerous approaches exist to model the behaviour of the two central components of the stretch reflex, i. e., motoneurons and muscle spindles. Commonly, motoneurons are described using a Hodgkin-Huxley type model and muscle spindles using the model of Mileusnic et al. (2006) (e. g., Chaud et al., 2012; Dideriksen et al., 2015; Elias et al., 2014). Both modelling approaches require solving a set of ordinary differential equations. When computational resources are limited, motoneurons can alternatively be described using leaky integrate-and-fire models, and muscle spindle activity can be represented by the model of Prochazka and Gorassini (1998b) (e. g., Moraud et al., 2016; Schuurmans et al., 2009; Sreenivasa et al., 2015; Stienen et al., 2007). Especially when several reflex pathways are considered, the motoneuron models are often replaced by phenomenological descriptions summarising the activity of the entire motoneuron pool (e. g., Li et al., 2015; Pithapuram and Raghavan, 2022; Raphael et al., 2010). Employing a muscle spindle model to obtain the afferent signals is not always necessary. When assuming values for the afferent input derived from experimental studies, only modelling the motoneurons is sufficient (e. g., Herrmann and Gerstner, 2002; Jones and Bawa, 1997; Matthews, 1999, 2002; Piotrkiewicz et al., 2009; York et al., 2022).

The purpose of computational stretch reflex models ranges from delivering explanations for specific experimental observations, e. g., motoneuron behaviour in response to muscle stretch (e. g., Chaud et al., 2012; Schuurmans et al., 2009), to investigating the effect of specific interventions, e. g., electrical epidural stimulation after spinal cord injury (Moraud et al., 2016). Further, computational stretch reflex models are often used to investigate control strategies of the nervous system to perform a particular motor task, e. g., (postural) stability (e. g., Dideriksen et al., 2015; Elias et al., 2014; Stienen et al., 2007).

Existing studies usually used a minimal amount of output variables. Often, they considered summarised output variables, e. g., the activity of the entire motoneuron pool or an estimate of the resulting muscle force, calculated from a Hill-type muscle model (e. g., Chaud et al., 2012; Dideriksen et al., 2015; Elias et al., 2014). Others investigated the activity of a single motoneuron in response to an afferent signal (e. g., Herrmann

and Gerstner, 2002; Jones and Bawa, 1997; Matthews, 1999, 2002; Piotrkiewicz et al., 2009). None of these studies analysed the contribution of individual motoneurons to the motoneuron pools' stretch reflex response. However, experimental recordings from single motoneurons are widely available, and the field can benefit from insights from computational models.

Considering the parametrisation of stretch reflex models, there is no standard procedure. While motoneuron and muscle spindle models can be validated using appropriate experimental data, this data is not readily available for stretch reflex models. In particular, how much afferent feedback contributes to the total input to motoneurons has yet to be discovered. In the literature, this contribution is, for example, arbitrarily defined, physiologically informed by *in-vitro* studies or fitted to obtain a desired mechanical output (e. g., Dideriksen et al., 2015; Elias and Kohn, 2013; Lin and Crago, 2002a; Raphael et al., 2010; Zhang et al., 2009). Nevertheless, the variety of models for motoneurons, muscle spindles and reflex pathways in the literature provides a pool from which to draw. Thus, this thesis mainly builds on existing models and adapts them if necessary.

1.3 Objectives and Outline

This thesis aims to provide novel insights into human α-motoneuron behaviour during stretch reflexes. The behaviour of the α-motoneurons is assessed regarding their discharge properties or spike trains, as these can be recorded *in vivo*. However, the internal parameters and conditions leading to a particular discharge pattern cannot be accessed *in vivo*. Therefore, we want to use computational models to address open questions from experimental research. This work focuses on three key aspects:

- The reflex amplitude of motor units is often used to derive statements about signals delivered to α-motoneurons. However, experimental studies relating the monosynaptic stretch reflex amplitude and the motoneuron size have shown contradictory results (e. g., Awiszus and Feistner, 1993; Binboğa and Türker, 2012; Heckman and Binder, 1988; Mazzocchio et al., 1995; Semmler and Türker, 1994). These studies emphasise that the contributions of influencing factors to the reflex amplitude are not sufficiently understood. Using a motoneuron model, we want to investigate how different experimental conditions and the motoneuron size influence *in-vivo* estimates of excitatory reflex amplitudes. From this, we derive suggestions for the design of experimental studies.

- Postinhibitory excitation is a phenomenon repeatedly observed when exciting the reciprocal inhibition pathway of the stretch reflex *in vivo*. Postinhibitory excitation is characterised by a transient overshoot of the motor unit activity following the inhibition. The biophysical origin of this phenomenon is still unknown, and both reflex pathways and intrinsic motoneuron properties have been proposed. Using a motoneuron model, we aim to investigate whether hyperpolarisation-activated ion channels can cause postinhibitory excitation.

- A biophysical model of stretch reflex pathways can be applied in many basic physiology and clinical research areas. In order to increase the range of research questions that can be addressed, a concept for extending the utilised motoneuron model to include

models of sensory organs, i. e., muscle spindles, is presented. This concept should serve as a basis for future modelling studies.

To achieve these goals, we use current models from the literature where applicable. An appropriate model selection and model parametrisation and a well-founded interpretation of the results are only possible with a sound background knowledge of the relevant physiology. Therefore, this introductory chapter is followed by a chapter presenting the basic physiology of neuromechanics (Chapter 2). Thereby, the focus lies on the bioelectric behaviour of cells, the specific properties of α-motoneurons and the stretch reflex pathways relevant to this work.

Chapter 3 describes the motoneuron model used in this work and its theoretical foundation. The choice of a suitable model depends on several factors. First, the model must consider the structures of interest, e. g., a specific ion channel. Second, the model output variables must be relatable to experimentally observable variables. Third, the required computational resources should be limited to a bearable amount. The experimentally observed quantity considered in this work is the collection of individual motor unit spike trains obtained from reflex experiments. Accordingly, we use a spiking motoneuron model. Further, the contribution of specific ion channels to how motoneurons integrate input signals is relevant to the aspects addressed by this thesis. Consequently, we use a compartmental model with ion channels. To reduce the computational cost and to keep the number of ion channels to a minimum, a two-compartment model with six conductances, from which three are voltage-gated, is employed (Cisi and Kohn, 2008; Negro and Farina, 2011).

Reflex responses are commonly quantified by peristimulus analysis (e. g., Yavuz et al., 2014). Thereby, two different metrics are available, the peristimulus timehistogram (PSTH) and the peristimulus frequencygram (PSF). Those are presented in Chapter 4 together with the basics of the experimental procedures. The gold standard for determining reflex amplitudes from peristimulus analysis is manual evaluation. However, that would be unfeasible for this work's extensive number of motoneurons and experiments. Consequently, an algorithm for automatically determining reflex amplitudes is presented.

Chapter 5 addresses the size of excitatory reflex amplitudes. While different factors influencing the reflex amplitude have been qualitatively determined, their quantitative influence is unknown. Further, potential differences between PSTH and PSF are not known. Using a model of an α-motoneuron pool, we investigate the influence of the experimental conditions and the motoneuron size on *in-vivo* estimates of the monosynaptic stretch reflex amplitude determined from the PSTH and PSF.

Chapter 6 aims to decipher the motoneuron behaviour during the reciprocal inhibition reflex. In particular, we investigate why motor units occasionally show postinhibitory excitation, a phenomenon of unclear origin. A computational motoneuron model is used to clarify if an internal motoneuron property, i. e., hyperpolarisation-activated ion channels, can cause this behaviour.

The above investigations can be performed solely using motoneuron models. However, many research questions require employing a more complete model of the neuromuscular system. Thus, in Chapter 7, a motoneuron pool model is coupled with a muscle spindle model to build a model of the stretch reflex. Two coupling approaches are presented and parametrised. The predictive power of the two approaches concerning different types of applied stretches is tested by comparison to experimental data.

This work closes with a summary of the main findings and an outlook addressing implications and future directions for computational modelling, experimental studies and clinical applications (Chapter 8). The different sets of parameters used for the motoneuron models are summarised in Appendix A.

1.3.1 List of publications

The research leading to the results presented in this thesis has previously been published in the following articles.

Schmid, L., Klotz, T., Siebert, T., and Röhrle, O. (2019a). Characterisation of electromechanical delay based on a biophysical multi-scale skeletal muscle model. *Frontiers in Physiology*, 10:1270.

Schmid, L., Klotz, T., Siebert, T., and Röhrle, O. (2019b). Simulating electromechanical delay across the scales – relating the behavior of single sarcomers on a sub-cellular scale and the muscle-tendon system on the organ scale. *PAMM*, 19(1):e201900312.

Schmid, L., Klotz, T., and Yavuz, U. Ş. (2022). Spindle model responsive to mixed fusimotor inputs: an updated version of the maltenfort and burke (2003) model. *Physiome*.

Haggie, L.*, **Schmid, L.***, Röhrle, O., Besier, T., McMorland, A., and Saini, H. (2023). Linking cortex and contraction – integrating models along the corticomuscular pathway. *Frontiers in Physiology*, 14.

Schmid, L., Klotz, T., Röhrle, O., Powers, R. K., Negro, F., and Yavuz, U. Ş. (2024). Postinhibitory excitation in motoneurons can be facilitated by hyperpolarisation-activated inward currents: A simulation study. *PLOS Computational Biology*, 20(1):1–22.

Homs-Pons, C., Lautenschlager, R., **Schmid, L.**, Ernst, J., Göddeke, D., Röhrle, O., Schulte, M. Coupled simulations and parameter inversion for neural system and electrophysiological muscle models. *GAMM-Mitteilungen*, e202370009.

* Shared first authorship

2 Fundamentals of Neuromechanics

Human movement is generated by the interaction of the neural system with the musculoskeletal system. Therefore, an interdisciplinary approach combining neurophysiology and biomechanics, i. e., neuromechanics, is required to understand the underlying principles. This chapter summarises the fundamentals of neuromechanics that are the basis of the topics discussed in this thesis. Section 2.1 starts with a short overview of the structures and mechanisms involved in movement generation. Section 2.2 describes cell-to-cell communication, including the electrical activity of cells and the central element of information transport, i. e., the so-called action potential (AP). Motoneurons as a central element of motor control are introduced in Section 2.3. Motoneurons and muscle fibres are organised in functional units, so-called motor units. Motor units and their role in feed-forward control of muscle activity are described in Section 2.3.2. Finally, Section 2.4 describes how feedback control of muscle activity is achieved via sensory organs and spinal reflex pathways.

2.1 The generation and control of movement

This section is based on Enoka (2008) and Kandel et al. (2013), which are recommended for further reading on neuromechanics and neurophysiology.

The generation and control of movement rely on the interplay between the structures and organs of the neural and the musculoskeletal system. It involves the interaction between multiple structures, including the motor cortex, spinal cord circuits, skeletal muscles, and sensory organs (Figure 2.1). Intended movements are planned in the motor cortex area of the brain. From there, corresponding signals are transmitted to neurons in the spinal cord. In the spinal cord, the signals might pass several intermediate neurons, so-called interneurons, until they finally reach α-motoneurons. Each α-motoneuron is connected to specific muscle fibres, forming a functional unit called the motor unit. When activated by their respective α-motoneuron, the muscle fibres of a motor unit contract. The muscle fibres are arranged in parallel so that all active motor units contribute to the muscle force acting on a joint via a tendon. Thereby, muscles can only actively contract but not elongate. Thus, at least two muscles are required to move a joint. These opposing muscles are called agonist and antagonist. Muscles that act on the same joint in the same direction are called synergists.

Sensory organs permanently monitor the current status of the musculo-tendinous structures and send feedback to the spinal cord and brain. For example, muscle spindles lie parallel to the muscle fibres and are sensitive to length changes of their parent muscle (Macefield and Knellwolf, 2018). Golgi-tendon organs are located at the musculo-tendinous junction and are sensitive to muscle fibre contraction (Anderson, 1974; Schoultz and Swett, 1972). The sensory signals provide the α-motoneurons with information on joint and limb position, which is then used to adjust the control command.

Two basic directions of information flow are relevant to the control of movements. To describe these, we need to introduce the central and peripheral nervous systems. The central nervous system includes the brain and the spinal cord. The peripheral nervous

system includes all neural structures anatomically located outside the brain and spinal cord. Signals from the central nervous system towards peripheral nervous system structures are called efferent signals, while signals travelling in the opposite direction are called afferent signals. Signal transmission in both directions is based on the ability of neuronal cells to generate and transmit electrical signals (Section 2.2).

Because α-motoneurons integrate control signals from the brain as well as sensory signals from the periphery to provide the final activating signal for muscle fibres, they play a central role in motor control and are discussed in more detail in Section 2.3.

The signalling pathway from a sensory organ via an afferent nerve to the pool of α-motoneurons and via an efferent nerve back to the muscle fibres is called a reflex arc. Reflexes produce stereotypical responses to sensory signals, but they can also be adapted to the intended task and play a central role in movement control. Reflexes are well suited to investigate α-motoneuron behaviour *in vivo* and help us to understand basic principles of motor control. The stretch reflex, which is mediated by muscle spindles, is described in detail in Section 2.4.

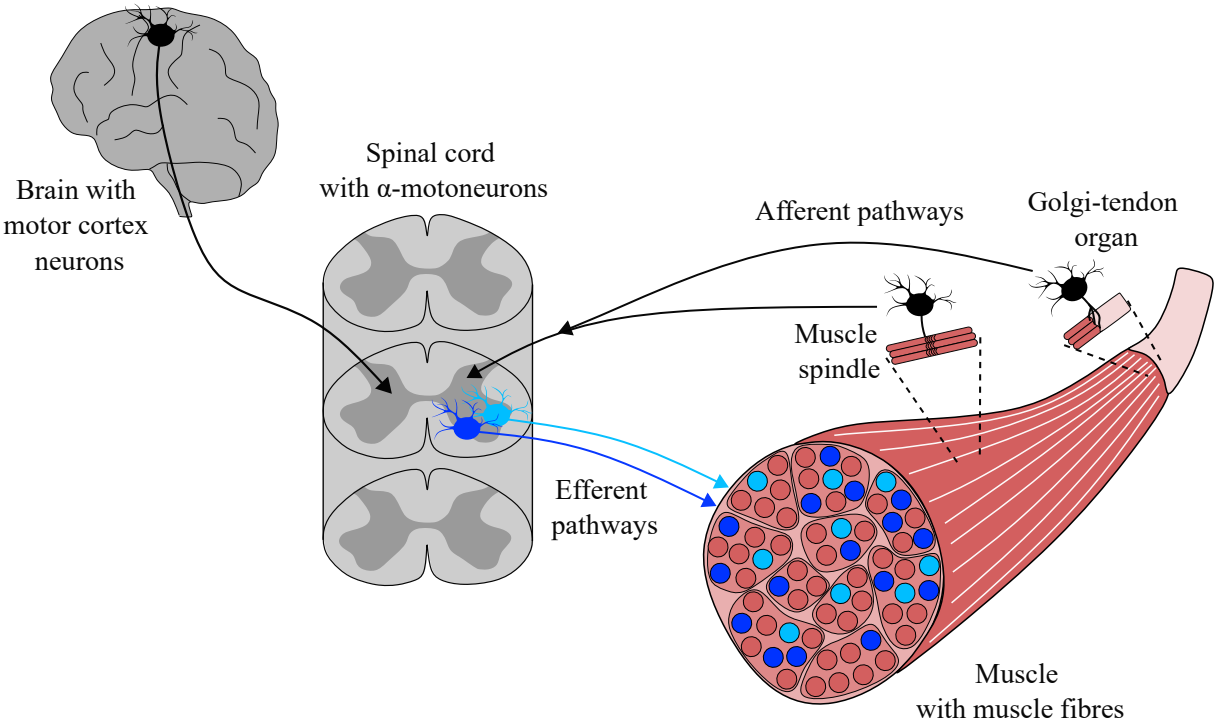

Figure 2.1: Schematic representation of the structures involved in movement generation. Blue colours highlight motor units, i. e., α-motoneurons and associated muscle fibres. Arrows mark the directions of signal transmission.

2.2 Excitable cells

This chapter is based on Aidley (1998), which is also recommended for further reading on the physiology of excitable cells.

Cells build the functional organisational units of life. The coordinated action of organs is only possible through cells communicating with each other. Cells that can exchange

electrical signals rapidly are summarised as excitable cells. They contain nerve, muscle and sensory cells, i. e., the cells involved in producing coordinated movements. Even though they are specialised for different tasks, excitable cells share some essential characteristics, which are described in this section. Excitable cells have a cell membrane that controls the flow and exchange of ions between the inside and outside of the cell. The resulting potential changes are the electrical signals used by excitable cells to transmit information within the cell, to other cells and other parts of the body. This section describes the functioning and structure of the cell membrane and explains how its properties lead to the establishment of a potential difference. Further, two particular states of the membrane potential are described in more detail, i. e., the resting potential and the action potential.

2.2.1 The structure of the cell membrane

Every cell has a membrane that separates the inner of the cell from the outside. The cell membrane of excitable cells controls the location and flow of ions into and out of the cell through its anatomical structure and embedded proteins. The cell membrane consists of a bilayer of phospholipids with a hydrophilic head and a hydrophobic tail. The phospholipids are arranged so that the hydrophobic tails are towards the centre and form a hydrophobic core, while the hydrophilic heads form the inner and outer surfaces of the membrane (Figure 2.2). Ions within and outside the cell are dissolved in water, and the hydrophobic core of the membrane builds a barrier to the diffusion of ions.

Usually, the concentration of ions outside and inside the cell differs (Figure 2.2). Consequently, a potential difference or voltage is established across the membrane. We define the membrane potential or membrane voltage V_m as the difference between the potential at the inside of the cell membrane, i. e., in the intracellular space, Φ_in, and the potential at the outside of the membrane, i. e., in the extracellular space, Φ_ex:

$$V_\mathrm{m} = \Phi_\mathrm{in} - \Phi_\mathrm{ex} \,. \tag{2.1}$$

It is an accepted convention to define the potential of the extracellular space as $\Phi_\mathrm{ex} = 0$.

A notable characteristic of the cell membrane of excitable cells is its capacitive behaviour. That means, when a current step is applied to cross the cell membrane, the change in membrane potential will not follow immediately but with a delay (Figure 2.3). Similarly, when the current is turned off, the membrane potential will not immediately return to its resting value. The delay with which the membrane reacts can be quantified by fitting an exponential function to the time course. The time constant of that exponential is often used to characterise an excitable cell.

While the cell membrane itself is a barrier to ions, the movement of ions across the membrane is enabled by integrated proteins, i. e., ion channels and ion pumps. The relation of the intra- and extracellular concentration of ions is subject to two driving forces: the chemical driving force is a function of the concentration gradient, and the electrical driving force is a function of the potential difference between intra- and extracellular space (Figure 2.2). Ion channels passively transport ions according to their electrochemical gradient, i. e., the process requires no expenditure of metabolic energy (Johnston and Wu, 1995). In contrast, ion pumps transport ions against their electrochemical gradient under consumption of energy (Johnston and Wu, 1995). Ion channels can be in different conformations, determining whether they are in an open or closed state. The transition

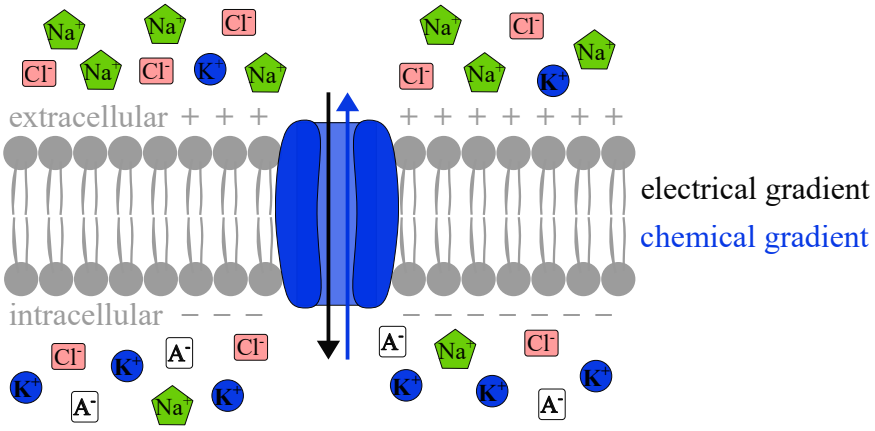

Figure 2.2: The phospholipid bilayer structure of the cell membrane (grey) with one ion channel (blue) embedded. The distribution of K^+ (blue), Na^+ (green) and Cl^- (pink) ions as well as other anions (white) in the intra- and extracellular space is schematically shown. The inside of the membrane is negatively charged, and the outside is positively charged. The ion channel is open and transmissive to K^+ ions. Two opposing forces act on K^+ ions: the electrical gradient (black arrow) and the chemical gradient (blue arrow).

between the states is called gating. The gating can depend on the membrane potential or the presence of other ions, e. g., Ca^{2+}, or on mechanical stimuli. Ion channels are usually selective to one or several specific ions. Numerous ion channels exist, which differ in their electrophysiological properties (Hille, 2001). Further, the occurrence, location and density of channel (sub-)types varies between neuron types (Hille, 2001).

2.2.2 Resting potential

The membrane potential is determined by the concentration of ions on both sides of the cell membrane. At a specific ratio of ions in the intra- and extracellular space, the cell reaches a steady state. In this state, the net ion flux across the membrane is zero. The corresponding membrane potential is called resting potential. The resting potential of neurons is mainly determined by three types of ions: sodium (Na^+), potassium (K^+) and chloride (Cl^-). These ions are present in different concentrations in the intra- and extracellular space (Table 2.1).

The resting membrane potential of a cell evolves due to the equilibrium potentials of the ions and the membrane's conductance to those ions. At the so-called equilibrium potential of a specific ion, the chemical and electrical driving forces are balanced, i. e., there is no net exchange of ions between the inside and outside. The equilibrium potential E of any ion X can be calculated from the Nernst equation:

$$E_{\mathrm{X}} = \frac{\mathcal{R}T}{zF} \ln\left(\frac{[\mathrm{X}]_{\mathrm{in}}}{[\mathrm{X}]_{\mathrm{ex}}}\right) . \tag{2.2}$$

Therein, $\mathcal{R}$ is the universal gas constant ($\mathcal{R} \approx 8.314\,\mathrm{J\,mol^{-1}\,K^{-1}}$), T is the absolute temperature in Kelvin, z is the number of electrons transferred, F is Faraday's constant ($F \approx 9.648 \times 10^4\,\mathrm{C\,mol^{-1}}$) and [X] the concentration of ion X inside and outside the cell. Typical equilibrium potentials for neurons can be found in Table 2.1.

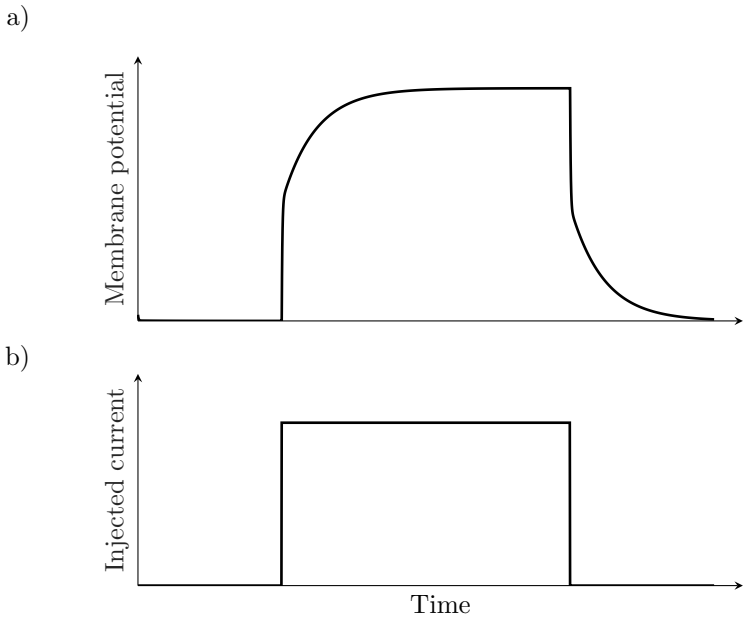

Figure 2.3: The capacitive behaviour of excitable membranes. a) Qualitative time course of the membrane potential in response to a current step shown in b).

The resting potential is additionally defined by the membrane's permeability to the present ion types. The Goldman-Hodgkin-Katz equation considers the permeability P of the membrane for different ions in units of $\mathrm{m\,s^{-1}}$ and their intra- and extracellular concentrations to calculate the resting potential, V_{rest}:

$$V_{\mathrm{rest}} = \frac{\mathcal{R}T}{F}\ln\frac{P_{\mathrm{K}}[\mathrm{K}^+]_{\mathrm{ex}} + P_{\mathrm{Na}}[\mathrm{Na}^+]_{\mathrm{ex}} + P_{\mathrm{Cl}}[\mathrm{Cl}^-]_{\mathrm{in}}}{P_{\mathrm{K}}[\mathrm{K}^+]_{\mathrm{in}} + P_{\mathrm{Na}}[\mathrm{Na}^+]_{\mathrm{in}} + P_{\mathrm{Cl}}[\mathrm{Cl}^-]_{\mathrm{ex}}}\,. \tag{2.3}$$

Since the membrane at rest is most permeable to K^+, the resting potential establishes close to the K^+ equilibrium potential. In nerve cells the resting potential is typically $-60\,\mathrm{mV}$ to $-70\,\mathrm{mV}$ (Aidley, 1998). The resting potential is stabilised and maintained by the Na^+-K^+-pump. This ion pump transports Na^+ and K^+ against their electrochemical gradient by consuming energy (Kandel et al., 2013).

Table 2.1: Typical ionic concentrations and Nernst potentials of different ion types in the squid axon (Aidley, 1998).

Ion	Ionic concentration (mmol)		Nernst potential (mV)
	extracellular	intracellular	
Na^+	440	50	+55
K^+	20	400	-75
Cl^-	560	108	-41

2.2.3 Action potential

The membrane potential at rest changes when ions move across the membrane. Thereby, a shift towards a more positive value is called depolarisation, while a shift towards a more negative value is called hyperpolarisation. Excitable cells use a specific type of massive depolarisation for communication, i. e., the action potential (AP). An AP is triggered whenever the current input into a cell (via synapses, see Section 2.3.1) exceeds a certain threshold. The threshold is typically about 10 mV to 15 mV above the resting potential (Aidley, 1998).

The described mechanism of AP generation is based on Kandel et al. (2013) and visualised in Figure 2.4. If injected currents depolarise the membrane potential to a value that exceeds the excitation threshold, voltage-gated Na^+ channels open and a massive influx of Na^+ depolarises the membrane potential towards the Nernst-potential of Na^+ (+55 mV). This depolarisation triggers two processes: (1) the gradual inactivation of Na^+ channels, reducing the inflow of Na^+ and (2) the opening of voltage-gated K^+ channels, leading to an outflow of K^+. Both processes repolarise the membrane potential towards the resting potential. The K^+ channels remain open a few milliseconds after reaching the resting potential, resulting in a transient hyperpolarisation of the membrane potential. Each AP is followed by a refractory period, during which the cell is not or only hardly excitable. The refractory period can be divided into two parts. The absolute refractory period directly follows the AP and is characterised by Na^+ channels still being inactive. During this period, it is impossible to elicit a new AP. The absolute refractory period is followed by the relative refractory period. During this period, some Na^+ channels are no longer inactivated, but a fraction of potassium channels are still open. During the relative refractory period, an AP can only be elicited by stimuli much higher than usual. The refractory period sets an upper limit to the frequency with which a neuron can produce APs. In α-motoneurons the AP itself typically lasts about 1 ms to 2 ms and the refractory period about 5 ms (Enoka, 2008).

Several characteristics of the AP are of particular importance for motor control. APs show all-or-none behaviour. That means whenever the depolarisation reaches the threshold, an AP is elicited. It does not play a role by how much the threshold was exceeded. Further, the AP always has the same shape, which does not change while transported over long distances (see Section 2.3.1).

A single Na^+ and K^+ channel can explain the generation of APs. These are also the most critical channels for nerve cell function. However, many more channels influence the membrane potential and the specific shape of the AP depending on the nerve cell type. Examples are subtypes of K^+ channels, as utilised in the model described in Section 3.4 and hyperpolarisation activated channels permeable to Na^+ and K^+ (HCN channels) as utilised in Section 6.2.1.

2.3 α-Motoneurons

This section provides an overview of the morphological and electrophysiological properties of α-motoneurons, their functional organisation in motor units and the associated control strategies of the neuromuscular system, i. e., recruitment and rate coding.

That the efferent nerves (axons) of α-motoneurons leave the spinal cord and innervate

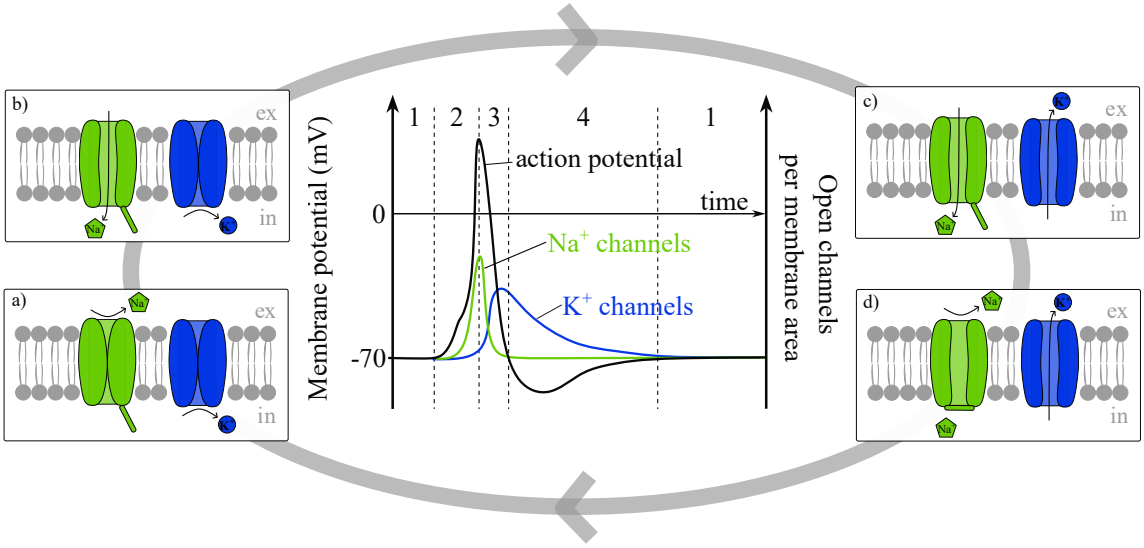

Figure 2.4: Schematic illustration of the generation of action potentials. The membrane potential is shown in black, and the relative opening of sodium (Na^+) and potassium (K^+) ion channels in green and blue, respectively. (1) Resting potential: The Na^+ (green) and K^+ (blue) ion channels are closed (a). (2) Depolarisation: When reaching the excitation threshold, Na^+ channels open and cause a strong influx of Na^+ (b). In turn, voltage-gated K^+ channels open and cause an outflow of K^+ (c). (3) Repolarisation: The Na^+ channels inactivate while the K^+ channels stay open (d). (4) Hyperpolarisation: When the membrane potential returns to resting potential, the Na^+ channel inactivation is removed, and the Na^+ channels close. With a certain delay, the K^+ channels also close (a). in: intracellular space. ex: extracellular space.

muscle tissue makes them unique amongst neurons (Burke, 2022). α-motoneurons are distinguished from two other motoneuron types in the spinal cord: β- and γ-motoneurons. The α-motoneurons exclusively innervate striated muscle fibres, which produce forces that lead to movement. In contrast, γ-motoneurons exclusively innervate specialised, so-called intrafusal muscle fibres, which are located within the muscle spindle sensory organs (Burke, 2022) (see Section 2.4.1). Noteworthy, β-motoneurons innervate both intra- and extrafusal (striated) muscle fibres. However, only little is known about them (Banks, 1994). Other terms denoting α-motoneurons are e. g., spinal motoneurons, lower motoneurons or, less specifically, motoneurons or motor neurons. In this work, the terms α-motoneuron and motoneuron are used equivalently.

Like most neurons, a motoneuron comprises a soma, dendrites and an axon (Figure 2.5). Dendrites branch out in a tree-like fashion and receive incoming signals from other neurons via synapses. Typically, motoneurons have about ten dendrites (Cullheim et al., 1987). The soma is the cell's body and contains the nucleus (which contains the genetic information) and the cell organelles. In the soma, incoming signals are summarised, and action potentials are produced if sufficient input is available. The axon transmits the action potential to the muscle fibres of the respective motor unit (see Section 2.3.2).

The α-motoneurons are located in so-called columns in the ventral horn of the spinal cord (Burke et al., 1977). With soma diameters of 40 µm to 70 µm, they are amongst the largest neurons in the central nervous system (Burke et al., 1977; Cullheim et al., 1987). The resting membrane potential of motoneurons is approximately $-65\,\mathrm{mV}$ to $-75\,\mathrm{mV}$ (Fleshman et al., 1988; Gustafsson and Pinter, 1984; Zengel et al., 1985).

2.3.1 Signal transmission in α-motoneurons

The α-motoneuron structure enables unidirectional signal transmission, i. e., receiving signals on the dendrites and sending signals via the axon. Motoneurons receive many inputs of different signs (excitatory or inhibitory), sizes and also at different locations on the dendrites. Synapses transfer incoming signals to the motoneuron. Thereby, the action potential of the presynaptic cell triggers the release of a messenger agent, the so-called neurotransmitter. The neurotransmitter overcomes the minimal cleft between the pre- and postsynaptic cell and attaches to ion channels on the postsynaptic side (Kandel et al., 2013). Depending on the type of channel, this leads to an increase or decrease of the membrane potential of the postsynaptic cell and thus brings the motoneuron closer to the AP threshold (excitation) or further away from it (inhibition).

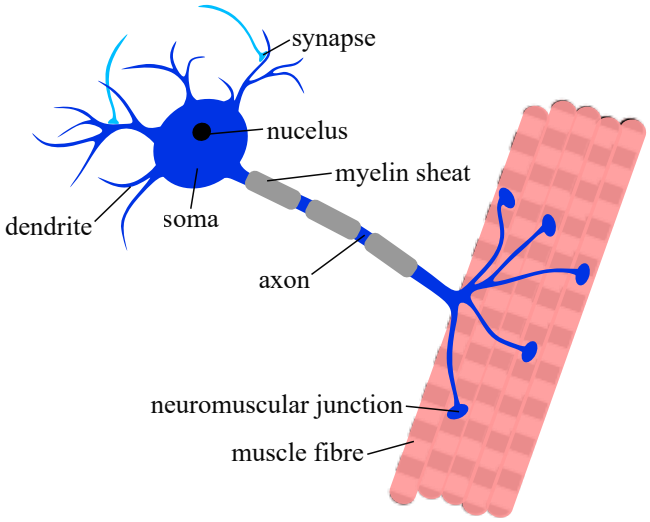

Figure 2.5: Schematic drawing of a motoneuron and its muscle fibres, building the motor unit.

Common to all incoming signals is that they travel towards the soma and are thereby integrated spatially and temporally. The membrane time constant (see Section 2.2.1) determines the amount of temporal summation of inputs arriving at the same sight within a short time. If the signal that arrived first has not entirely decayed, it will be added to the signal that arrives later. The motoneuron's length constant determines how much the amplitude of a postsynaptic potential declines while it travels along the dendritic tree towards the soma (see Section 3.3).

When an AP is generated in the soma, it travels down the axon. The axon's cell membrane is constructed as described in Section 2.2. The AP is the stimulus to elicit a new AP in the neighbouring membrane patch. In this way, the AP is regenerated and travels without loss. Due to the refractory period, the axon can only be excited in one direction, thus preventing the AP from travelling backwards. A motoneuron's axon has a myelin sheath (Figure 2.5) that acts like an insulation and allows an AP to stimulate the membrane several millimetres away (Kernell, 2006). Through this, large AP conduction velocities of $70\,\mathrm{m\,s^{-1}}$ to $120\,\mathrm{m\,s^{-1}}$ can be obtained (Kandel et al., 2013).

The motor axon transmits every motoneuron AP to the muscle fibres of the respective motor unit. The functional contact between a motoneuron's axon and the muscle fibres is called neuromuscular junction (Eccles, 1948). The neuromuscular junction is a particular

type of synapse, which uses acetylcholine as its neurotransmitter (Kandel et al., 2013). Acetylcholine binding to its receptor channels on the muscle fibre membrane causes a rapid depolarisation of the muscle fibres' membrane. In healthy individuals, this always triggers an AP in the muscle fibre, which travels along the fibre to initiate contraction (Kandel et al., 2013).

The fact that every AP of a motoneuron causes an AP in a muscle fibre is fundamental to this work. In short, it allows the conclusion that for every AP observed in a muscle fibre, there must have been an AP in the respective motoneuron. This provides the unique opportunity to measure discharge times of human motoneurons *in vivo* (see Section 4.1).

2.3.2 Functional organisation in motor units

Motor units form the controllable units of movement generation. Liddell and Sherrington defined the term motor unit in 1925. A motor unit comprises a motoneuron and the muscle fibres it innervates. The number of muscle fibres belonging to a motor unit, i. e., the innervation number, can range from less than ten to more than thousand (Heckman and Enoka, 2012). The muscle fibres are also called the muscle unit of the motor unit. The group of motoneurons that controls the muscle fibres of one muscle is called the motor nucleus or motoneuron pool (Burke et al., 1977). The number of motor units and, therefore, the size of a muscle's motoneuron pool ranges from about ten to several hundred (Heckman and Enoka, 2012).

The size of motor units differs considerably within a muscle, as do the intrinsic properties of the corresponding motoneurons and muscle units. Based on the close correlation between the electrical properties of motoneurons and the mechanical properties of the associated muscle fibres, Burke et al. (1973) determined three types of motor units: slow (S), fast fatigue resistant (FR) and fast fatigable (FF) (Burke et al., 1973). The motoneurons of S-type motor units have small cell bodies, a high input resistance and a low recruitment threshold. The corresponding muscle units slowly contract, produce little force and are very fatigue-resistant (Kernell, 2006). On the other end of the spectrum, motoneurons of FF-type motor units have large cell bodies, low input resistance and a high recruitment threshold. The corresponding muscle units are fast contracting, produce high forces and are easily fatigable (Kernell, 2006). The innervation number usually increases from S-type to FF-type motor units.

Note that the contractile properties of motor units can also be classified based on their histochemical fibre type composition. Commonly, three classifications are used, type-I, -IIA, and -IIB, which approximately correspond to the S-, FR-, and FF-type classifications we use in this work.

Even though classified in distinct groups, the motor unit properties build a continuum (Powers and Binder, 2007). The motor unit properties usually distribute exponentially within a muscle, with many S-type and few FF-type motor units (Gustafsson and Pinter, 1984; Heckman and Binder, 1988; Powers and Binder, 1985; Zengel et al., 1985). For further reading on motor units, see Heckman and Enoka (2012).

2.3.3 Recruitment and rate coding

The activation of motor units ultimately leads to the generation of muscle force. Thereby, the central nervous system uses two strategies to modulate the force that is produced by a specific muscle: recruitment and rate coding. Recruitment increases the number of active motor units, and rate coding increases the activity of a specific motor unit. With increasing excitatory synaptic input to a pool of α-motoneurons, motor units are usually recruited in an ordered manner, from smallest (low-threshold, S-type) to largest (high-threshold, FF-type), following Henneman's size principle (Henneman et al., 1965a,b). The size principle is a direct consequence of Ohm's law. Small motoneurons have a higher input resistance and, for the same amount of current applied, experience stronger increases in membrane potential than large motoneurons with low input resistance. At the same time, increasing synaptic input leads to an increasing frequency of action potentials generated by a specific motoneuron. Small motoneurons, recruited earlier, usually fire action potentials at higher rates than large motoneurons. This is known as the onion skin principle (De Luca and Hostage, 2010). Figure 2.6 illustrates the size and onion skin principle. There is evidence that in voluntary contractions and at high forces, small motor units experience a saturation of their firing rate (Monster and Chan, 1977). It is essential to mention that recent evidence suggests that Henneman's size principle might be a simplification and that more complex patterns of motor unit recruitment are possible (Marshall et al., 2022).

The size and onion skin principle describes the rough basic principle of muscle force control. There are different ways to fine-tune motoneuron excitability. One is the amplification of synaptic inputs by persistent inward currents (PICs, Binder et al., 2020; Heckman et al., 2005). PICs are mediated by persistent Ca^{2+} or Na^{+} currents, and the respective channels are widely expressed on the surfaces of motoneurons (Binder et al., 2020). PICs show slow activation and slow or no inactivation (Binder et al., 2020). PICs were recently discovered, but they are found to play a role in more and more aspects of motoneuron physiology. For example, PICs cause hysteresis, which means that motoneurons are de-recruited at lower input levels than recruited (Binder et al., 2020).

2.4 The stretch reflex

According to Kandel et al. (2013) reflexes have traditionally been viewed as "stereotyped responses to specific stimuli that are generated by simple neural circuits in the spinal cord or brain stem". Newer research, however, suggests that reflexes not only provide stereotyped responses but are highly flexible, can be regulated and contribute significantly to motor control (Kandel et al., 2013). What all reflexes have in common is that they cannot be controlled voluntarily. Since the reaction time of the brain is in the range of 150 ms to 200 ms, reflex responses are limited to responses within this period (Kernell, 2006).

The most known reflex might be the knee-jerk reflex. A tendon tap near the patella yields a quick extension of the knee joint. The muscle contraction, which yields the knee extension, is a reflexive reaction to the stretch applied to this muscle by the tendon tap. Stretch reflexes comprise a variety of quick responses to mechanical stimuli. Since muscle stretches are omnipresent during daily movements, stretch reflexes are central to

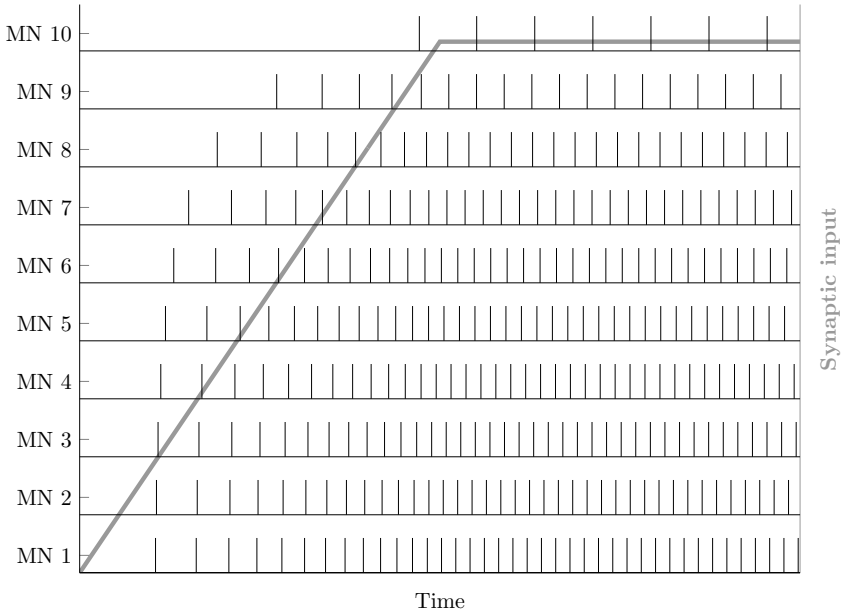

Figure 2.6: Visualisation of orderly recruitment and rate coding. In black, spike trains of ten exemplary α-motoneurons (MN) are shown (left axis). With increasing synaptic input (grey, right axis), successively more α-motoneurons are recruited, and the spike frequency of already recruited α-motoneurons increases. [modified from Haggie, Schmid et al. (2023) under CC BY 4.0]

movement control. In human muscles, stretch is mainly detected by specialised sensory organs, the muscle spindles (Macefield and Knellwolf, 2018).

Responses to mechanical perturbations should be fast and not counterproductive. Therefore, inter-muscle coordination of reflexes is essential. The stretch reflex comprises different reflex pathways, affecting the stretched muscle and its antagonist. Three central components of the stretch reflex are decisive for this work and are described in more detail. This is, the muscles spindles (cf. Section 2.4.1), the monosynaptic stretch reflex pathway (Section 2.4.2) and the reciprocal inhibition pathway (Section 2.4.3).

2.4.1 Muscle spindles

The muscle spindle is a receptor sensing the intrafusal muscle fibre length change, providing stretch feedback to the neuromuscular system (Macefield and Knellwolf, 2018). The number of muscle spindles in human muscles varies between less than ten and more than a thousand (Banks, 2006).

Each muscle spindle consists of a bundle of specialised, so-called intrafusal, muscle fibres lying in parallel with the regular (extrafusal) muscle fibres of the parent muscle (Figure 2.7, Macefield and Knellwolf, 2018). The intrafusal fibres are distinguished as bag1, bag2 and chain fibres (Ovalle and Smith, 1972). They have different viscoelastic properties that make them differently sensitive to muscle length and length changes.

Two types of afferent axons innervate muscle spindles, the so-called primary (Ia) and secondary (II) sensory endings (Figure 2.7). Ia afferents have a larger diameter than II afferents and a faster action potential conduction velocity (Kandel et al., 2013). Ia affer-

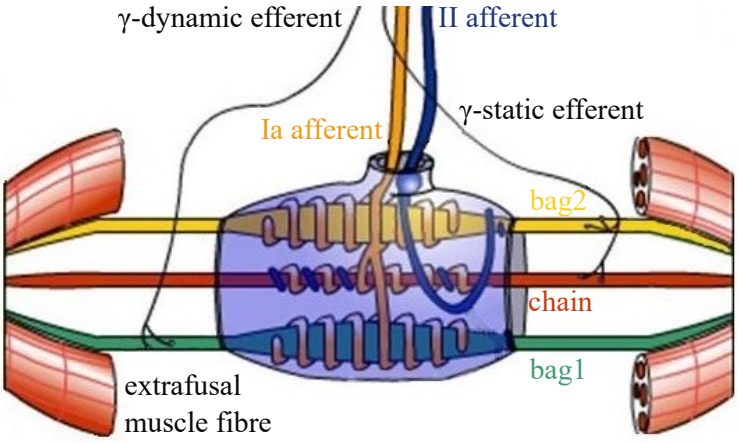

Figure 2.7: Schematic drawing of a muscle spindle. Three types of intrafusal fibres (bag1, bag2, chain) are arranged in parallel to extrafusal muscle fibres. Ia afferents innervate all intrafusal muscle fibres, and II afferents innervate bag2 and chain fibres. Efferent γ-dynamic axons innervate bag1 fibres and γ-static axons innervate bag2 and chain fibres. (Macefield and Knellwolf, 2018; Ovalle and Smith, 1972)

ents reach conduction velocities of $80\,\mathrm{m\,s^{-1}}$ to $100\,\mathrm{m\,s^{-1}}$ (Boyd and Kalu, 1979; Heckman and Binder, 1988). Ia afferents form monosynaptic connections to α-motoneurons of the same (homonymous) muscle, which makes them unique among sensory afferents (Stauffer et al., 1976; Watt et al., 1976). Ia and II afferents connect di- and polysynaptically to the homonymous and other (heteronymous) muscles, i.e., synergists and antagonists (Scott and Mendell, 1976; Watt et al., 1976).

The importance of the muscle spindle is underlined by the fact that it is the only peripheral sensory organ that is controlled by the central nervous system (Ellaway et al., 2015). In detail, the so-called fusimotor system modulates muscle spindle activity. The fusimotor system comprises two types of spinal neurons, static and dynamic γ-motoneurons, which modulate the spindles' sensitivity and, thereby, ensure that spindles remain responsive during muscle contraction (Macefield and Knellwolf, 2018; Matthews, 1962).

Muscle spindles detect length changes of the intrafusal fibres. Thereby, the responses of Ia and II afferents to muscle stretch differ. In relaxed muscles, there is a linear relationship between joint angle and firing rate as well as between joint angle velocity and firing rate (e. g., Day et al., 2017; Grill and Hallett, 1995; Kakuda, 2000). However, this is no longer the case if the stretch exceeds a specific value (Day et al., 2017; Kakuda, 2000) and whilst the muscle is contracting (Hulliger et al., 1985).

2.4.2 The monosynaptic stretch reflex

The stretch reflex involves a monosynaptic pathway that is mediated by muscle spindle Ia afferents. In detail, when a muscle is stretched, the muscle spindles increase their activity and monosynaptically excite the homonymous motoneurons via their Ia afferents (Figure 2.8, Kandel et al., 2013). The monosynaptic stretch reflex can, e. g., be elicited by applying a mechanical perturbation to the muscle, i. e., by tendon jerk, or by direct electrical stimulation of the nerve. The electrically evoked monosynaptic stretch reflex is

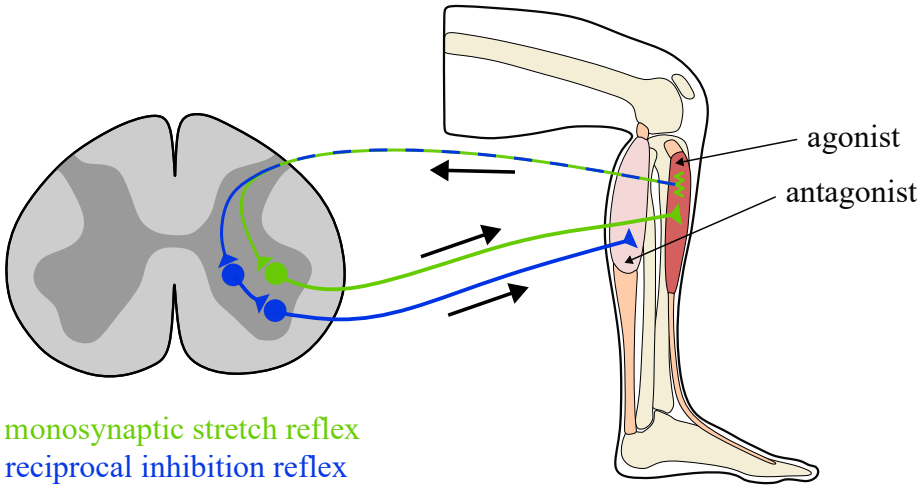

Figure 2.8: Illustration of the stretch reflex pathways. A lengthening of the agonist muscle (red) is registered by muscle spindles (green zick-zack). In response, the muscle spindles activate populations of neurons (circles) in the spinal cord via synapses (triangles). Thereby, the monosynaptic stretch reflex pathway (green) leads to an activation of the agonist muscle. The disynaptic reciprocal inhibition pathway (blue) leads to the inhibition of the antagonist muscle (pink). [modified from Homs-Pons et al. (2024) under CC BY 4.0]

also called Hoffmann-reflex or H-reflex.

The reflex response caused by the monosynaptic pathway is the fastest neuromuscular reflex response that can be observed and is called short-latency or M1 response. The short-latency response is well detectable in experimental recordings. A cat motoneuron has an estimated 1000-2000 Ia afferent synapses (Fyffe, 2001) and the excitatory Ia input to motoneurons contributes to a considerable extent to muscle activation (Gandevia et al., 1990; Hiebert and Pearson, 1999). Therefore, since its discovery, the stretch or H-reflex has been utilised as both a diagnostic and a research tool (Pierrot-Deseilligny and Mazevet, 2000). The monosynaptic stretch reflex is the subject of Chapters 5 and 7.

2.4.3 The reciprocal inhibition reflex

Reciprocal inhibition is, as the monosynaptic pathway, a component of the stretch reflex. In contrast to the monosynaptic stretch reflex, the reciprocal inhibition pathway affects heteronymous muscles that act as antagonists to the muscle the spindles are located in (Kandel et al., 2013). In detail, when muscle spindles are activated, the afferent pathways excite interneurons in the spinal cord, which subsequently inhibit α-motoneurons of the antagonist muscle (Crone et al., 1987; Kudina, 1980). Consequently, the reciprocal inhibition pathway is disynaptic (Figure 2.8).

As part of the stretch reflex, reciprocal inhibition ensures that the antagonist does not counteract the contraction of the agonist. Reciprocal inhibition plays a central role in coordinating voluntary movements since relaxation of the antagonist enhances the movement efficiency (Kandel et al., 2013). The reciprocal inhibition reflex is the subject of Chapter 6.

3 Computational Modelling of Motoneurons

The motoneuron models relevant to this work are derived and described in this chapter. After introducing the sign conventions used in the mathematical models (Section 3.1), the modelling approach used to describe the active spiking behaviour of motoneurons, i. e., the Hodgkin-Huxley model is introduced in Section 3.2. The cable theory, which serves as a basis to include the spatial dimension of motoneurons, is the subject of Section 3.3. Finally, in Section 3.4, the compartmental motoneuron model that serves as the basis for this work is presented in detail.

3.1 Sign conventions for motoneuron models

Sign conventions used to describe membrane voltages and currents usually differ between experimental studies and computational models. The membrane potential is defined as the potential difference between the extracellular and the intracellular space (see Equation 2.1). Since it is a relative measure, two decisions need to be made. First, a reference potential needs to be defined. In physiological measurements, the potential in the extracellular space is usually defined as zero, such that a negative resting potential of approximately $-70\,\mathrm{mV}$ is measured. In contrast, in computational models, the resting potential is usually defined as zero, and all potentials are given with respect to the resting potential. This is also applied within this work. Second, the sign needs to be defined. We treat the potential such that a depolarisation from the resting potential corresponds to a positive sign and a hyperpolarisation to a negative sign. Hodgkin and Huxley introduced the opposite sign convention in their work (Hodgkin and Huxley, 1952d). The equations and parameters have been adjusted in this work to be consistent with the convention described above.

The sign must also be defined for electric currents induced by the movement of ions. An outward movement of positive charge across the membrane corresponds to a positive current for ionic currents. In contrast, for an external current applied to a cell, a current that depolarises the cell, i. e., corresponding to the flow of positive charge into the cell, is defined as positive.

3.2 The Hodgkin-Huxley model of excitable membranes

In a series of papers, Sir Alan L. Hodgkin and Sir Andrew F. Huxley described the electric current flow across the membrane of a nerve fibre, i. e., the giant axon of the squid (Hodgkin and Huxley, 1952a,b,c; Hodgkin et al., 1952).[1] In a final publication,

[1] Together with Sir John C. Eccles they were awarded the Nobel Prize for Physiology or Medicine 1963 “for their discoveries concerning the ionic mechanisms involved in excitation and inhibition in the peripheral and central portions of the nerve cell membrane”.

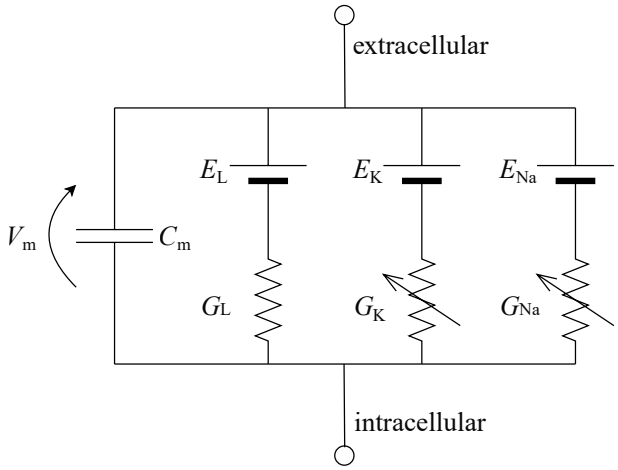

Figure 3.1: The equivalent electric circuit model of an excitable membrane according to Hodgkin and Huxley (1952d). The membrane voltage is denoted by V_m and the membrane capacitance by C_m. The leakage channel is represented by a battery representing the leakage equilibrium potential E_L and a conductance G_L. Accordingly, the potassium (K) and sodium (Na) ion channels are represented by the respective equilibrium potentials, E_K and E_{Na}, and voltage-gated conductances, G_K and G_{Na}, respectively.

they summarised the results of the preceding papers and presented a mathematical model for the electrical behaviour of the cell membrane (Hodgkin and Huxley, 1952d).

From their measurements, Hodgkin and Huxley concluded that the electrical behaviour of the neuron membrane can be described by an equivalent electric circuit composed of a capacitor in parallel to three ionic currents, which are mediated by sodium ions, potassium ions and other ions (Figure 3.1). The flow of ions across the membrane is determined by the membrane's permeability for a specific ion, represented by a conductance, and the driving force, represented by a battery.

The model became known as the Hodgkin-Huxley model and has been widely used and refined since its development. It was successfully employed to describe a variety of excitable cells, e. g., motoneurons (e. g., Cisi and Kohn, 2008; Negro and Farina, 2011; Powers et al., 2012), brain neurons (e. g., Traub et al., 1991) or smooth muscle cells (e. g., Bursztyn et al., 2007). Since it also serves as the theoretical basis for the motoneuron model used within this work, the underlying equations are derived in this chapter. This section is based on Hodgkin and Huxley (1952d) if not stated otherwise.

3.2.1 Mathematical description of the Hodgkin-Huxley model

Hodgkin and Huxley found that the total current density that flows across a patch of the cell membrane J_m is composed of a capacitive component, J_{cap}, and an ionic component, J_{ion}:

$$J_m = J_{cap} + J_{ion} . \tag{3.1}$$

The capacitance C describes the ability to separate charges. It is defined as the ratio between the electric charge and the potential. The capacitive current density is described by the membrane capacitance per unit area C_m and the rate of change of the membrane

voltage:

$$J_{\text{cap}} = C_{\text{m}} \frac{\mathrm{d}V_{\text{m}}}{\mathrm{d}t} . \tag{3.2}$$

The ionic current density is equivalent to the sum of the currents mediated by Na^+, J_{Na}, K^+, J_{K}, and a leakage current, J_{L}:

$$J_{\text{ion}} = J_{\text{Na}} + J_{\text{K}} + J_{\text{L}} . \tag{3.3}$$

The leakage current summarises currents mediated by other ions, mainly chloride. The current mediated by a specific ion X, J_{X}, can be described by Ohm's law, using the conductance per unit area (the inverse of the resistance per unit area) G_{X} and the difference between the membrane potential and the ion's equilibrium potential E_{X}:

$$J_{\text{X}} = G_{\text{X}} (V_{\text{m}} - E_{\text{X}}) . \tag{3.4}$$

The equilibrium potential is the potential at which the electrical and chemical gradients are balanced, and the net ion flow across the membrane is zero. The Nernst Equation (Equation 2.2) describes the equilibrium potential.

In summary, the equation describing the equivalent circuit of the Hodgkin-Huxley model yields:

$$C_{\text{m}} \frac{\mathrm{d}V_{\text{m}}}{\mathrm{d}t} = -G_{\text{Na}} (V_{\text{m}} - E_{\text{Na}}) - G_{\text{K}} (V_{\text{m}} - E_{\text{K}}) - G_{\text{L}} (V_{\text{m}} - E_{\text{L}}) . \tag{3.5}$$

We can consider that so-called gates[2] regulate the conductance of ion channels (Nelson, 2005). A gate can be in permissive or non-permissive state. The fraction of gates in permissive or non-permissive state determines the overall conductance of the channel (Nelson, 2005). We define a specific gating variable w as the fraction of gates in permissive state, such that $w \in [0, 1]$. Thus, at some point in time t, $w(t)$ gates are in permissive state, while $1 - w(t)$ gates are in non-permissive state. The rates at which gates change from permissive to non-permissive and back are called $\alpha_{\text{w}}(V_{\text{m}})$ and $\beta_{\text{w}}(V_{\text{m}})$ and depend on the membrane voltage:

$$1 - w(t) \underset{\beta_{\text{w}}(V_{\text{m}})}{\overset{\alpha_{\text{w}}(V_{\text{m}})}{\rightleftarrows}} w(t) .$$

The unit of the rates α_{w} and β_{w} is ms^{-1} and they are described by first-order kinetics:

$$\frac{\mathrm{d}w}{\mathrm{d}t} = \alpha_{\text{w}}(V_{\text{m}})(1 - w) - \beta_{\text{w}}(V_{\text{m}})w . \tag{3.6}$$

The description of how the rates depend on membrane voltage must be empirically determined for every ion channel type (Section 3.2.2).

One or several gating variables can describe an ion channel depending on the channel type. The overall conductance of a certain channel G_{X} is described by the product of its individual gating variables w_{i}:

$$G_{\text{X}} = \overline{G}_{\text{X}} \prod_i w_{\text{i}} , \quad i \in \mathbb{N} . \tag{3.7}$$

[2]With the knowledge available at that time, Hodgkin and Huxley could not relate the flow of ions across cell membranes to channel proteins. Instead, they hypothesised not closer specified "particles" within the membrane to be responsible for the ion transport (Hodgkin and Huxley, 1952d). Nevertheless, the empirically determined gate model serves as a valid description of voltage-dependent conductances.

Thereby, $\overline{G}_{\mathrm{X}}$ is the maximum conductance when all gates are in the permissive state.

When measuring the time course of the membrane's conductance to K^+ and Na^+, Hodgkin and Huxley (1952d) found that they could describe it best by using four similar gating variables for K^+ (n) and also four gating variables but of two types for Na^+ (m, h):

$$G_{\mathrm{K}} = \overline{G}_{\mathrm{K}} n^4 \,, \tag{3.8}$$

$$G_{\mathrm{Na}} = \overline{G}_{\mathrm{Na}} m^3 h \,. \tag{3.9}$$

Thereby, n and m are so-called activation gates, while h describes an inactivation gate (Nelson, 2005).

In summary, the Hodgkin-Huxley model of the electrical behaviour of the cell membrane is described by a system of four coupled ordinary differential equations (ODEs):

$$C_{\mathrm{m}} \frac{\mathrm{d}V_{\mathrm{m}}}{\mathrm{d}t} = -\overline{G}_{\mathrm{Na}} m^3 h \,(V_{\mathrm{m}} - E_{\mathrm{Na}}) - \overline{G}_{\mathrm{K}} n^4 \,(V_{\mathrm{m}} - E_{\mathrm{K}}) - G_{\mathrm{L}} \,(V_{\mathrm{m}} - E_{\mathrm{L}}) \,, \tag{3.10}$$

$$\frac{\mathrm{d}m}{\mathrm{d}t} = \alpha_{\mathrm{m}}(V_{\mathrm{m}})(1 - m) - \beta_{\mathrm{m}}(V_{\mathrm{m}}) m \,, \tag{3.11}$$

$$\frac{\mathrm{d}h}{\mathrm{d}t} = \alpha_{\mathrm{h}}(V_{\mathrm{m}})(1 - h) - \beta_{\mathrm{h}}(V_{\mathrm{m}}) h \,, \tag{3.12}$$

$$\frac{\mathrm{d}n}{\mathrm{d}t} = \alpha_{\mathrm{n}}(V_{\mathrm{m}})(1 - n) - \beta_{\mathrm{n}}(V_{\mathrm{m}}) n \,. \tag{3.13}$$

3.2.2 Parameters for the Hodgkin-Huxley model

Hodgkin and Huxley determined the parameters for their model from a series of voltage-clamp experiments (Hodgkin and Huxley, 1952a,b,c; Hodgkin et al., 1952). In voltage-clamp experiments, two electrodes are inserted into the cell; one measures the membrane voltage, and the other applies a current. The current that crosses the cell membrane can be estimated by measuring the current required to hold the membrane potential at a specific value.

The parameters of the Hodgkin-Huxley model consist of constant and voltage-dependent parameters. The constant parameters are summarised in Table 3.1 and include the membrane capacitance, the equilibrium potentials and the maximum conductances of the ion channels.

The voltage-dependent rates α_{w} and β_{w}, which determine the opening and closing of the ion channels, are fitted to experimental data. Therefore, Equation (3.6), governing the gates w, is reformulated to rely on values that can be more readily determined from experimental data, i. e., a steady-state value w_∞ and a time constant τ_{w}:

$$\frac{\mathrm{d}w}{\mathrm{d}t} = \frac{w - w_\infty}{\tau_{\mathrm{w}}} \,. \tag{3.14}$$

When the membrane voltage is clamped at a specific value V_{m}, the gate in the permissive state will reach a steady-state value w_∞, which can be expressed in terms of the rates α_{w} and β_{w}:

$$w_\infty = \frac{\alpha_{\mathrm{w}}(V_{\mathrm{m}})}{\alpha_{\mathrm{w}}(V_{\mathrm{m}}) + \beta_{\mathrm{w}}(V_{\mathrm{m}})} \,. \tag{3.15}$$

Table 3.1: Constant parameters for the model by Hodgkin and Huxley (1952d). Potential values are given relative to a resting potential of −75 mV.

Parameter	Symbol	Value
Specific capacitance of the cell membrane ($\mu F\,cm^{-2}$)	C_m	1
Na^+ equilibrium potential (mV)	E_{Na}	115
Na^+ maximum specific conductance ($mS\,cm^{-2}$)	$\overline{G}_{Na}$	120
K^+ equilibrium potential (mV)	E_K	−12
K^+ maximum specific conductance ($mS\,cm^{-2}$)	$\overline{G}_K$	36
Leakage equilibrium potential (mV)	E_L	10.613
Leakage specific conductance ($mS\,cm^{-2}$)	$\overline{G}_L$	0.3

The time course for approaching w_∞ is characterized by a time constant $\tau_w(V_m)$, which can also be related with α_w and β_w:

$$\tau_w(V_m) = \frac{1}{\alpha_w(V_m) + \beta_w(V_m)} . \tag{3.16}$$

By measuring w_∞ and τ_w at different values of the membrane potential and using Equations (3.15) and (3.16), the voltage-dependent rates α_w and β_w can be determined. Exponential functions are fitted to the empirically collected data to obtain continuous voltage-dependent rate formulations. The resulting voltage-dependent functions are:

$$\alpha_n(V_m) = 0.01 \frac{10 - V_m}{\exp\left(\frac{10 - V_m}{10}\right) - 1} , \tag{3.17}$$

$$\beta_n(V_m) = 0.125 \exp\left(\frac{-V_m}{80}\right) , \tag{3.18}$$

$$\alpha_m(V_m) = 0.1 \frac{25 - V_m}{\exp\left(\frac{25 - V_m}{10}\right) - 1} , \tag{3.19}$$

$$\beta_m(V_m) = 4 \exp\left(\frac{-V_m}{18}\right) , \tag{3.20}$$

$$\alpha_h(V_m) = 0.07 \exp\left(\frac{-V_m}{20}\right) , \tag{3.21}$$

$$\beta_h(V_m) = \frac{1}{\exp\left(\frac{30 - V_m}{10}\right) + 1} . \tag{3.22}$$

For the sake of clarity, the units of the parameters are omitted in Equations 3.17 to 3.22. The membrane potential V_m is in units of millivolt, and the rates α and β are in units of ms^{-1}. For more details on the experimental procedure and the fitting method, see Hodgkin and Huxley (1952d).

An action potential and the corresponding time courses of the gating variables in the Hodgkin-Huxley model are shown in Figure 3.2. A CellML-implementation of the

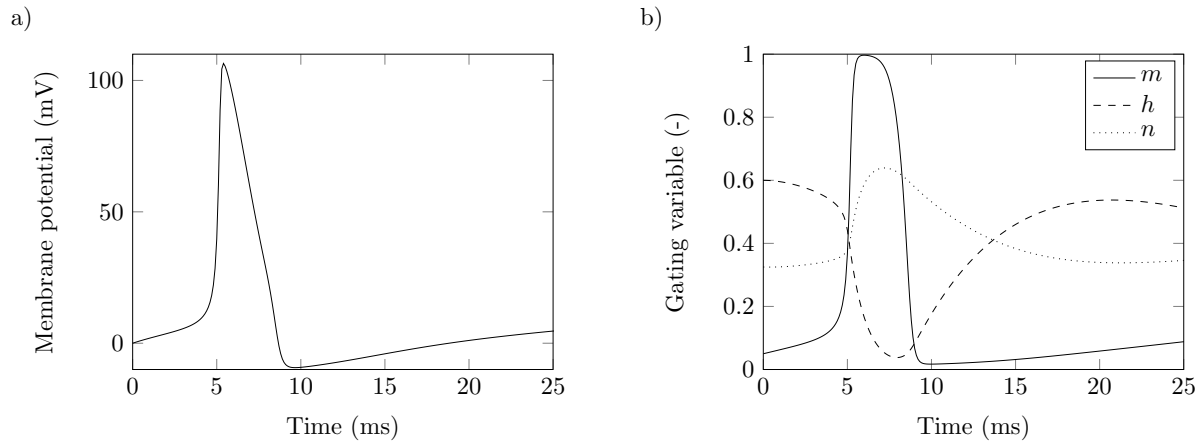

Figure 3.2: An action potential in the Hodgkin-Huxley model. a) Time course of the membrane potential. b) Time course of the gating variables of the sodium (m, h) and potassium (n) ion channels.

Hodgkin-Huxley model, as presented here, can be downloaded from the Physiome model repository website[3].

Today, the current-voltage relation of single ion channels can be recorded using the patch-clamp method (Hamill et al., 1981)[4]. This method considerably increased the amount and predictive quality of ion channel models. While the methods for determining the parameters have progressed, the general approach developed by Hodgkin and Huxley is still used today.

3.3 The equivalent cylinder model of passive electrical membrane properties

The Hodgkin-Huxley model describes the current flow across a patch of the cell membrane. However, neurons have spatial dimensions and broadly branched dendrites. Incoming signals travel from where they arrive at a dendrite to where the action potential is generated in the soma. The passive propagation of electrical signals within the cell and without the influence of the voltage-dependent properties of the membrane is called electrotonic spread. The electrotonic current spread within the cell can be described by equivalent cylinder models based on the cable theory.

In this section, the basic principles of the cable theory are derived. Then, we describe how equivalent cylinders can represent motoneurons and how these principles are applied to a two-compartment motoneuron model.

3.3.1 The cable equation

An equivalent electric circuit, as shown in Figure 3.3, can describe the passive electrotonic properties of a cable-like structure. We assume that the current only flows in x-direction

[3] https://models.physiomeproject.org/exposure/5d116522c3b43ccaeb87a1ed10139016

[4] Erwin Neher and Bert Sakmann were awarded the Nobel Prize in Physiology or Medicine 1991 “for their discoveries concerning the function of single ion channels in cells”.

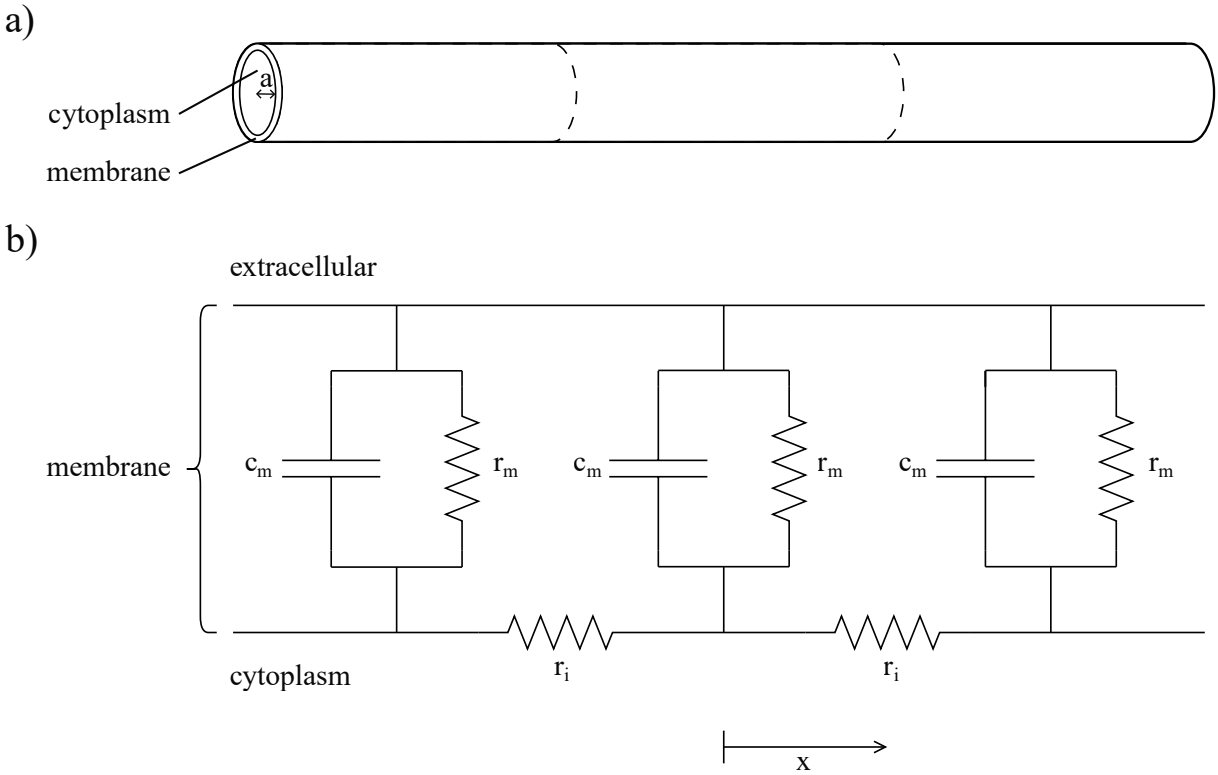

Figure 3.3: Schematic representation of the cable model. a) A neuronal structure can be represented by a cylinder (cable) with radius a. The cable is divided into unit lengths. b) The equivalent electric circuit represents a neuron's passive cable properties. Each unit length of the cable is represented by a capacitance c_m and a resistance r_m. The unit-length circuits are connected by resistances r_i representing the resistance of the cytoplasm. A short circuit represents the extracellular space. The current flows along x.

and that the radial current is zero. The transverse membrane resistance r_m, the transverse membrane capacitance c_m and the longitudinal resistance of the cytoplasm r_i determine the current flow along the cable. These quantities refer to unit length (cm) and do not depend on the membrane potential. Instead of specifying the resistance and capacitance in terms of the unit length, they are often specified in terms of the unit area. The corresponding quantities, $R_\mathrm{m}, C_\mathrm{m}$ and R_i, are obtained using the radius of the cable a:

$$r_\mathrm{m} = \frac{R_\mathrm{m}}{2\pi a} , \tag{3.23}$$

$$c_\mathrm{m} = 2\pi a C_\mathrm{m} , \tag{3.24}$$

$$r_\mathrm{i} = \frac{R_\mathrm{i}}{\pi a^2} . \tag{3.25}$$

The membrane potential in the cable structure is a function of time t and distance x:

$$\frac{1}{r_i}\frac{\partial^2 V_\mathrm{m}}{\partial x^2} = c_\mathrm{m}\frac{\partial V_\mathrm{m}}{\partial t} + \frac{V_\mathrm{m}}{r_\mathrm{m}} . \tag{3.26}$$

Equation (3.26) is called the cable equation.

Here, we introduce two additional variables. The time constant τ describes how fast

the membrane potential changes after current injection:

$$\tau = r_\mathrm{m} c_\mathrm{m} = R_\mathrm{m} C_\mathrm{m} . \tag{3.27}$$

The larger τ, the slower the membrane potential will change in response to a current injection. Note that the time constant is independent of the cable radius. The length constant λ describes how far the injected current will flow:

$$\lambda = \sqrt{\frac{r_\mathrm{m}}{r_\mathrm{i}}} = \sqrt{\frac{a R_\mathrm{m}}{2 R_\mathrm{i}}} . \tag{3.28}$$

The larger λ, the further the current will spread. Using Equations (3.27) and (3.28), Equation (3.26) can be rearranged to:

$$\lambda^2 \frac{\partial^2 V_\mathrm{m}}{\partial x^2} = \tau \frac{\partial V_\mathrm{m}}{\partial t} + V_\mathrm{m} . \tag{3.29}$$

For a more detailed derivation of the cable equation, see e. g., Johnston and Wu (1995).

3.3.2 The equivalent cylinder model

A description of the electrotonic properties of a motoneuron using the cable equation requires approximating the cell's morphology by cylindrical segments of uniform diameter and solving the cable equation for each segment. Considering the complexity of the dendritic structure and the need for boundary conditions for each segment or branch, this is not an efficient method. To overcome this issue, Wilfrid Rall derived a method to collapse the complex dendritic structure into a single equivalent finite cylinder (Rall, 1962a,b). He showed that the entire dendritic tree can be collapsed into one single compartment when R_m and R_i are uniform across all dendritic branches, all terminal branches end at the same electrotonic length from the soma, and the diameters obey the "3/2 power rule" (see Equation 3.31).

The electrotonic length L of a cylindrical branch corresponds to its physical length l divided by its length constant λ:

$$L = \frac{l}{\lambda} . \tag{3.30}$$

The length constant λ is defined in Equation (3.28). The "3/2 power rule" requires that the diameter of a parent branch d_parent is related to the diameters of the daughter branches d_daughter according to:

$$d_\mathrm{parent}^{3/2} = \sum d_\mathrm{daughter}^{3/2} . \tag{3.31}$$

For a detailed derivation of the equivalent cylinder model, see Rall (1962b) and Rall (1962a).

3.3.3 Equivalent cylinder model for a two-compartment motoneuron

The previous section describes how to represent the branched dendritic tree of a neuron using a single cylinder. Based on this model, Rall et al. (1992) developed a two-compartment

motoneuron model and determined its electrotonic parameters based on experimental data by Fleshman et al. (1988). The model consists of one compartment representing the collapsed dendritic structure and one compartment representing the soma.

For the two-compartment model, several electrotonic parameters are required, namely the specific membrane resistances of the soma and the dendrite, R_m^{s} and R_m^{d}, respectively, the specific capacitance of the membrane, C_m, and the cytoplasm specific resistance, R_i. Additionally, the length and diameter of each compartment need to be defined.

Most studies reported that the specific capacitance of the cell membrane, C_m, is relatively invariant and has a value of $1\,\mu\mathrm{F\,cm^{-2}}$ (Burke et al., 1994; Fleshman et al., 1988). The same applies to the cytoplasm specific resistance R_i, which is reported to be $70\,\Omega\,\mathrm{cm}$ (Barrett and Crill, 1974; Burke et al., 1994; Fleshman et al., 1988). Values for the specific membrane resistances of the dendrite and soma cannot be measured directly but can be obtained following the procedure described by Fleshman et al. (1988) and Rall et al. (1992). In short, the input resistance of a motoneuron, the time constant of the membrane potential decay in response to a short current pulse and the cell morphology are quantified from experiments. For details on the experimental procedure, see e. g., Fleshman et al. (1988). Equivalent cylinder models are created for the dendrite and the soma. Using this model and assuming that $R_{\mathrm{m}}^{\mathrm{s}} < R_{\mathrm{m}}^{\mathrm{d}}$, values for R_m^{s} and R_m^{d} are searched such that the calculated whole-cell input resistance and the time constant match the experimental measurements. Thereby, a step-wise increase of the specific resistance from soma to dendrite is assumed. This so-called step-model is widely applied, e. g., by Cisi and Kohn (2008) and Powers et al. (2012).

3.4 A two-compartment model of a motoneuron pool

Based on the equivalent electric circuit model developed by Hodgkin and Huxley (1952d) (Section 3.2) and the work by Fleshman et al. (1988) and Rall et al. (1992) on equivalent cylinder models (Section 3.3), Cisi and Kohn (2008) developed a two-compartment motoneuron model, which was later adapted by Negro and Farina (2011). The model considers a soma compartment, a lumped dendrite compartment and three voltage-gated conductances. As in the original Hodgkin and Huxley model, the voltage-gated conductances include the Na^+ and K^+ conductance. The model further considers an additional slow K^+ conductance, also called the delayed rectifier, that mainly determines the hyperpolarisation period of the action potential. An entire motoneuron pool is created by selecting the appropriate parameters.

This model forms the foundation for the studies conducted in Chapters 5, 6, and 7, and its detailed description is provided in this section[5].

3.4.1 Mathematical description of the motoneuron pool model

The motoneuron model is described by an equivalent electric circuit with two membrane compartments (soma and lumped dendrite) and six conductances, from which three are voltage-gated (Figure 3.4). Both soma and dendrite compartments have a leakage conductance, and a coupling conductance connects the two compartments. The voltage-gated

[5]The model was published in CellML format (for a single neuron) by Röhrle et al. (2019).

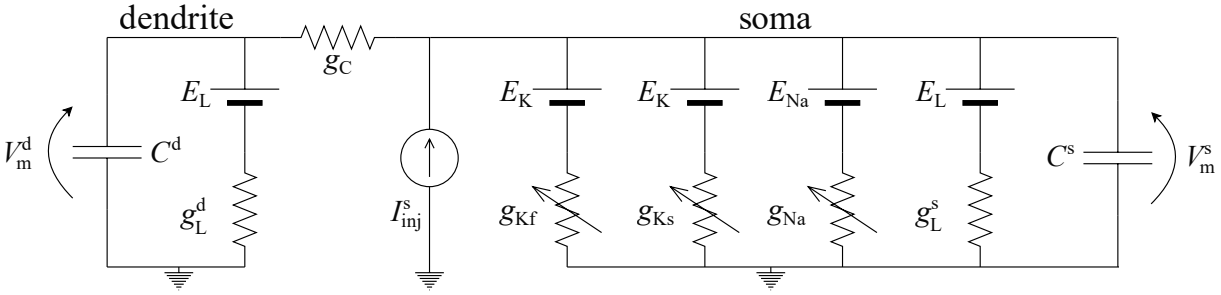

Figure 3.4: The electric circuit of the two-compartment motoneuron model by (Negro and Farina, 2011). Each compartment comprises a capacitance C, and the compartments are coupled via a conductance g_C. Leakage (L), sodium (Na), slow (Ks) and fast (Kf) potassium ion channels are represented by a battery and a (voltage-gated) conductance. The current source I_{inj}^s represents an externally applied current. V_m denotes the membrane potential. Soma and dendrite quantities are denoted by the superscript letters 's' and 'd', respectively.

conductances are exclusively located in the soma and include a Na^+ as well as a fast and a slow K^+ conductance. The membrane potential in each compartment is described by:

$$C^d \frac{dV_m^d(t)}{dt} = -I_L^d - I_C^d \,, \tag{3.32}$$

$$C^s \frac{dV_m^s(t)}{dt} = -I_L^s - I_C^s - I_{ion} + I_{inj}^s \,. \tag{3.33}$$

Therein, V_m denotes the membrane voltage and C the membrane capacitance. The superscript letters 's' and 'd' denote the soma and dendrite compartments, respectively. I_C describes the coupling current between the two compartments, whereby $I_C^d = -I_C^s$ and I_L describes a leakage current. I_{ion} summarises the currents through the voltage-gated ion channels and is defined in Equation (3.43). I_{inj}^s represents an external or injected current.

The membrane capacitance and the coupling and leakage currents are obtained from the electrotonic parameters of the neuron. The compartments are assumed to have a cylindrical shape with sealed ends. The outer surface of the cylindrical compartment, described by length l and radius a, together with the specific conductance of the cell membrane, C_m, determine the total capacitance in each compartment:

$$C^d = 2\pi\, a^d\, l^d\, C_m \,, \tag{3.34}$$

$$C^s = 2\pi\, a^s\, l^s\, C_m \,. \tag{3.35}$$

The leakage current in the dendrite is determined by the membrane potential in the dendrite compartment, V_m^d, the equilibrium potential of the leakage channel, E_L, and the size-dependent leakage conductance, g_L^d:

$$g_L^d = \frac{2\pi\, a^d\, l^d}{R_m^d} \,, \tag{3.36}$$

$$I_L^d = g_L^d \left(V_m^d - E_L\right) \,. \tag{3.37}$$

Therein, R_m^d denotes the specific resistance of the dendrite membrane in units of $k\Omega\,cm^{-2}$.

Accordingly, the leakage current in the soma is given by:

$$g_{\mathrm{L}}^{\mathrm{s}} = \frac{2\pi\, a^{\mathrm{s}}\, l^{\mathrm{s}}}{R_{\mathrm{m}}^{\mathrm{s}}}\,, \tag{3.38}$$

$$I_{\mathrm{L}}^{\mathrm{s}} = g_{\mathrm{L}}^{\mathrm{s}}\,(V_{\mathrm{m}}^{\mathrm{s}} - E_{\mathrm{L}})\ . \tag{3.39}$$

Therein, $R_{\mathrm{m}}^{\mathrm{s}}$ denotes the specific resistance of the soma membrane in units of $\mathrm{k\Omega\,cm^{-2}}$. The coupling current between the two compartments is described by:

$$g_{\mathrm{C}} = \frac{2}{\frac{R_{\mathrm{i}}\, l^{\mathrm{d}}}{\pi\,(a^{\mathrm{d}})^2} + \frac{R_{\mathrm{i}}\, l^{\mathrm{s}}}{\pi\,(a^{\mathrm{s}})^2}}\,, \tag{3.40}$$

$$I_{\mathrm{C}}^{\mathrm{d}} = g_{\mathrm{C}}\left(V_{\mathrm{m}}^{\mathrm{d}} - V_{\mathrm{m}}^{\mathrm{s}}\right)\,, \tag{3.41}$$

$$I_{\mathrm{C}}^{\mathrm{s}} = g_{\mathrm{C}}\left(V_{\mathrm{m}}^{\mathrm{s}} - V_{\mathrm{m}}^{\mathrm{d}}\right)\ . \tag{3.42}$$

Therein, R_{i} is the resistivity of the cytoplasm in units of $\mathrm{k\Omega\,cm}$.

The ionic current is described by three voltage-gated conductances: a $\mathrm{Na^+}$ conductance (Na), a $\mathrm{K^+}$ conductance with fast dynamics (Kf) and a $\mathrm{K^+}$ conductance with slow dynamics (Ks):

$$I_{\mathrm{ion}} = \bar{g}_{\mathrm{Na}} m^3 h\,(V_{\mathrm{m}}^{\mathrm{s}} - E_{\mathrm{Na}}) + \bar{g}_{\mathrm{Kf}} n^4\,(V_{\mathrm{m}}^{\mathrm{s}} - E_{\mathrm{K}}) + \bar{g}_{\mathrm{Ks}} q^2\,(V_{\mathrm{m}}^{\mathrm{s}} - E_{\mathrm{K}})\ . \tag{3.43}$$

As proposed by Hodgkin and Huxley (1952d), the $\mathrm{Na^+}$ conductance is modelled with two different voltage-dependent gating variables, m for activation and h for inactivation. The $\mathrm{K^+}$ conductances are each modelled with one voltage-dependent gating variable, n and q, respectively (both are activation gates). Multiplying the maximum specific conductance $\overline{G}$ with the area of the soma compartment yields the maximum conductance values $\bar{g}$. Note that Equations (3.32) to (3.43) are adopted from (Cisi and Kohn, 2008).

The gating variables m, n, h and q are determined by forward and backward rates α and β as in Equations (3.14) to (3.16). Note that Cisi and Kohn (2008) adopted a simplified mechanism to describe the gating variables based on Destexhe (1997). Thereby, rectangular current pulses approximate the ODEs describing the gating variables. This approach simplifies the original formulation and reduces computational effort. However, this approximation is not suited to describe the sub-threshold contribution of ion channels, which is essential in this work.

Within this thesis, we follow Negro and Farina (2011) who adopted the model proposed by Cisi and Kohn (2008) and replaced the approximation of the gating variables with the formulation based on Traub et al. (1991). Traub et al. (1991) modelled the channel dynamics based on the formalism derived by Hodgkin and Huxley (1952d) as described in Equations (3.14), (3.15) and (3.16). They developed their model to simulate guinea pig hippocampal pyramidal neurons. Thus, Negro and Farina (2011) adapted the parameters to represent typical motoneuron behaviour (see Section 3.4.3).

The Na^+ channel dynamics are governed by Equations (3.44) to (3.47):

$$\alpha_\mathrm{m} = \frac{0.32\ (13 - V_\mathrm{m}^\mathrm{s})}{\exp\left(\frac{13 - V_\mathrm{m}^\mathrm{s}}{5}\right) - 1}\ , \tag{3.44}$$

$$\beta_\mathrm{m} = \frac{0.28\ (V_\mathrm{m}^\mathrm{s} - 40)}{\exp\left(\frac{V_\mathrm{m}^\mathrm{s} - 40}{5}\right) - 1}\ , \tag{3.45}$$

$$\alpha_\mathrm{h} = 0.128 \exp\left(\frac{17 - V_\mathrm{m}^\mathrm{s}}{18}\right)\ , \tag{3.46}$$

$$\beta_\mathrm{h} = \frac{4}{\exp\left(\frac{40 - V_\mathrm{m}^\mathrm{s}}{5}\right) + 1}\ . \tag{3.47}$$

The dynamics of the fast K^+ channel (Kf) are governed by Equations (3.48) and (3.49):

$$\alpha_\mathrm{n} = \frac{0.032\ (15 - V_\mathrm{m}^\mathrm{s})}{\exp\left(\frac{15 - V_\mathrm{m}^\mathrm{s}}{5}\right) - 1}\ , \tag{3.48}$$

$$\beta_\mathrm{n} = 0.5 \exp\left(\frac{10 - V_\mathrm{m}^\mathrm{s}}{40}\right)\ . \tag{3.49}$$

The dynamics of the slow K^+ channel (Ks) are governed by Equations (3.50) and (3.51):

$$\alpha_\mathrm{q} = \frac{3.5}{\exp\left(\frac{55 - V_\mathrm{m}^\mathrm{s}}{4}\right) + 1}\ , \tag{3.50}$$

$$\beta_\mathrm{q} = 0.025\ . \tag{3.51}$$

For the sake of clarity, the units of the parameters are omitted in Equations (3.44) to (3.51). The membrane potential V_m is in units of millivolt, and the rates α and β are in units of ms^{-1}. For each motoneuron, a system of six coupled ODEs has to be solved. For methods to solve ODEs, see e. g., Chapra and Canale (2010).

3.4.2 Parameters for the motoneuron pool model

In this section, we describe how a population of motoneurons is built based on the two-compartment model presented in the previous section. Further, we provide the parameters for a motoneuron pool.

Motoneuron properties are closely related to motoneuron size (see Section 2.3.2). However, some parameters are similar for all motoneurons. Considering the presented model, these are the specific membrane capacitance C_m, the cytoplasm resistivity R_i, the specific conductances and the equilibrium potentials of the ion channels (Table 3.2).

The parameters determining the compartment size, as well as the specific resistance of the cell membrane, vary across the motoneuron pool. Typically, these properties are exponentially distributed between S-type and FF-type motoneurons (Gustafsson and Pinter, 1984; Powers and Binder, 1985). In this work, we order the motoneurons according to

Table 3.2: Constant parameters of the motoneuron pool. Parameters are adopted from Cisi and Kohn (2008) if not indicated otherwise.

Parameter	Symbol	Value
Membrane specific capacitance ($\mu F\,cm^{-2}$)	C_m	1*
Cytoplasm resistivity ($k\Omega\,cm$)	R_i	0.07**
Na^+ equilibrium potential (mV)	E_{Na}	120
K^+ equilibrium potential (mV)	E_K	−10
Leakage equilibrium potential (mV)	E_L	0
Maximum specific Na^+ conductance ($mS\,cm^{-2}$)	$\overline{G}_{Na}$	30
Maximum specific fast K^+ conductance ($mS\,cm^{-2}$)	$\overline{G}_{Kf}$	4
Maximum specific slow K^+ conductance ($mS\,cm^{-2}$)	$\overline{G}_{Ks}$	16

*Burke et al. (1994); Cole (1972); Fleshman et al. (1988) **Barrett and Crill (1974); Burke et al. (1994)

their cell size and assume that the size increases exponentially from S-type to FF-type motoneurons. Consequently, a size-parameter b of a specific motoneuron i is determined by an exponential distribution between the respective parameter of the smallest motoneuron, b_{small}, and the largest motoneuron b_{large} (Enoka and Fuglevand, 2001; Fuglevand et al., 1993; Negro and Farina, 2011):

$$b_i = b_{small} + \frac{b_{large} - b_{small}}{100} \exp\left(\ln(100)\frac{i}{N_{MN}}\right) . \tag{3.52}$$

Therein, N_{MN} is the number of motoneurons in the pool. Values for the model parameters are provided in Table 3.3.

Most parameters of motoneuron models cannot be obtained directly from humans. Thus, Cisi and Kohn (2008) mainly used data from cats to parametrise their model. While some parameters can be directly obtained from experiments, others were chosen such that the overall model behaviour shows good accordance with experimental data, e. g., the current-frequency relation and the shape of the afterhyperpolarisation (AHP), i. e., the hyperpolarisation phase following an action potential. The electrotonic parameters are based on the step model by Rall et al. (1992) (see Section 3.3.3). Note that Cisi and Kohn (2008) used a piece-wise linear interpolation between the smallest and largest motoneuron's parameters. In this work, we follow Negro and Farina (2011) and use the exponential interpolation described by Equation (3.52).

3.4.3 Behaviour of the motoneuron pool model

In this section, we present the fundamental characteristics of the behaviour of the motoneuron model. The time course of the membrane potential and the gating variables, the electrophysiological parameters of the motoneuron pool, and its firing characteristics are addressed.

Table 3.3: Parameters that vary across the motoneuron (MN) pool. Values are given for the smallest and the largest MN of the pool. Parameters are adopted from Cisi and Kohn (2008).

Parameter	Symbol	Value	
		Smallest MN	Largest MN
Soma diameter (cm)	d^{s}	77.5×10^{-4}	113×10^{-4}
Soma length (cm)	l^{s}	77.5×10^{-4}	113×10^{-4}
Soma specific resistance ($\mathrm{k\Omega\,cm^{-2}}$)	$R_{\mathrm{m}}^{\mathrm{s}}$	1.15	0.65
Dendrite diameter (cm)	d^{d}	41.5×10^{-4}	92.5×10^{-4}
Dendrite length (cm)	l^{d}	0.55	1.06
Dendrite specific resistance ($\mathrm{k\Omega\,cm^{-2}}$)	$R_{\mathrm{m}}^{\mathrm{d}}$	14.4	6.05

Simulation

The simulations were performed with MATLAB R2021a (9.10.0.2015706). We chose a motoneuron pool size of 200 motoneurons. To solve the resulting system of 6x200 ODEs, we used MATLAB's ode23 solver (an adaptive, single-step, explicit Runge-Kutta solver, Shampine and Reichelt, 1997) and an absolute and relative error tolerance of 1×10^{-5}. The solver uses optimised time steps within chosen intervals of 0.1 ms.

Membrane potential time course and gating variables

The membrane potential time course of an exemplary motoneuron from the pool is shown in Figure 3.5 for a constant injected current. The exact figure shows the gating variables during two interspike intervals. The Na^+ activation gate, m, closely follows the membrane potential, especially during the action potential. In contrast, the Na^+ inactivation gate, h, quickly declines during the action potential and returns to almost the maximum value closely after the action potential. The K^+ activation gates, n and q, decline after the action potential, but the q-gate declines more slowly than the n-gate.

Electrophysiological parameters

Electrophysiological parameters that can be compared to experimental data include the rheobase, the input resistance, the membrane time constant and the shape of the AHP. The rheobase corresponds to the minimum current, applied for infinite duration, that causes a single action potential. In the simulation, the current pulse was applied for 500 ms. When no action potential could be elicited, the current was increased by 0.1 nA. To obtain the membrane time constant, a constant current of 1 nA was applied for a duration of 100 ms. Then, an exponential of the form $b_1 * [1 - \exp(-t/b_2)] + b_3 * [1 - \exp(-t/b_4)]$ was fitted to the rising phase of the membrane potential using the non-linear least-squares method. The membrane time constant corresponds to the larger value of $[b_2,\ b_4]$. The input resistance R_{N} can be analytically derived from the motoneuron para-

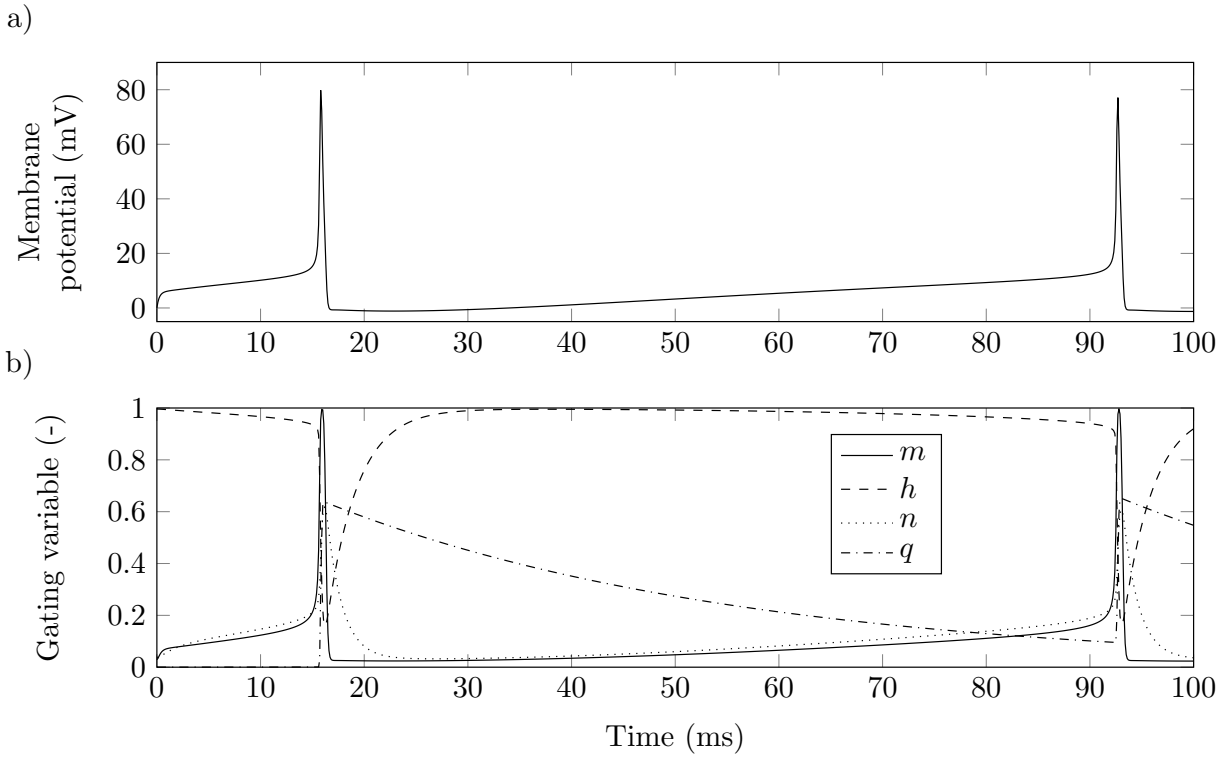

Figure 3.5: Membrane potential and gating variables for one interspike interval of a simulated motoneuron. a) Time course of the membrane potential. b) Gating variables for the sodium (m, h) and the fast (n) and slow (q) potassium ion channels. The data was obtained from the smallest motoneuron in the pool and with a constant injected current of 5 nA.

meters:

$$R_{\mathrm{N}} = \frac{1}{g_{\mathrm{L}}^{\mathrm{s}} + \frac{g_{\mathrm{L}}^{\mathrm{d}}\, g_{\mathrm{C}}}{g_{\mathrm{L}}^{\mathrm{d}} + g_{\mathrm{C}}}} \,. \tag{3.53}$$

The AHP characteristics were determined from the injection of a short (0.5 ms), suprathreshold (50 nA) current pulse. Thereby, the AHP amplitude corresponds to the minimum value of the membrane potential relative to the prestimulus value. The AHP half decay time is the time that elapses from reaching the minimum AHP to reaching half the difference to the resting potential. The AHP duration was set to the time after an action potential when the membrane potential in mV reached the prestimulus value with an accuracy of three digits to the right of the decimal point.

The electrophysiological parameters obtained for the smallest and largest motoneuron of the pool, respectively, are provided in Table 3.4. We also provide corresponding values from experimental studies (Caillet et al., 2022b; Zengel et al., 1985) for comparison. The values for all electrophysiological parameters compare well between the experiment and simulation. Only the AHP duration is considerably shorter in the experimentally recorded FF-type motoneurons.

Firing characteristics

Simulated motoneurons start discharging action potentials when sufficient input current is injected into their soma compartment. When applying a constant drive, smaller mo-

Table 3.4: Electrophysiological parameters of the simulated motoneuron (MN) pool and typical ranges for cat MNs. For the simulated MNs the values for the smallest and largest MN of the pool are provided. Experimental data corresponds to averaged values for S- and FF-type MNs obtained from 19 studies on cat MNs (Caillet et al., 2022b). For afterhyperpolarisation (AHP) amplitude and half-decay time, data is taken from Zengel et al. (1985). Consider there is an inverse relationship between MN size and electrophysiological parameter for all parameters but the rheobase (Caillet et al., 2022b).

Parameter	Simulation		Experiment	
	smallest MN	largest MN	S-type	FF-type
Rheobase (nA)	3.6	19.4	2.3	36.6
Input resistance (MΩ)	2.2	0.5	4.0	0.4
Membrane time constant (ms)	11.6	5.6	10.2	2.9
AHP amplitude (mV)	6.0	4.3	4.9	3.0
AHP half decay time (ms)	36.1	26.4	44.0	18.0
AHP duration (ms)	145.1	128.3	158.7	44.2

toneurons in the pool fire action potentials with a faster frequency than larger motoneurons. This behaviour is exemplarily shown in Figure 3.6. The frequency is defined as the inverse of the time elapsed between consecutive action potentials. Noticeably, the first spike has a faster frequency than the following. This phenomenon is called spike frequency adaptation and is consistently observed in motoneurons (Powers et al., 1999). Several physiological mechanisms seem to contribute to it (Powers et al., 1999). In the model, spike frequency adaptation is mainly caused by AHP summation due to incomplete activation of the K^+ current following the first action potential. Over the following interspike intervals, the slow K^+ conductance sums up and gradually increases the AHP amplitude.

The discharge frequency of a motoneuron increases with increasing input current. The steady-state current-frequency relation for the entire pool of 200 motoneurons is shown in Figure 3.7a. The steady-state frequency corresponds to the mean frequency during constant application of the respective input current for 2000 ms. Here, we can observe two basic physiological principles. First, the more current is injected, the more motoneurons start firing, i. e., are recruited. Second, the firing rate of already recruited motoneurons increases with increasing current. This means the model inherently accounts for Hennemann's size principle and the onion skin principle (De Luca and Hostage, 2010; Henneman et al., 1965a,b).

The current-frequency relation can typically be divided into three sections. At recruitment, cat motoneurons usually discharge with a frequency in the range of 5 Hz to 25 Hz (Kernell, 2006). The following increase in discharge frequency for increasing current is initially very steep. This segment is called the sub-primary range and is characterised by irregular discharges (Jensen et al., 2018; Kudina, 1999; Kudina and Alexeeva, 1992). All simulated motoneurons show a sub-primary range. The sub-primary range is followed by the primary range, which is characterised by a smaller slope and is also shown by all

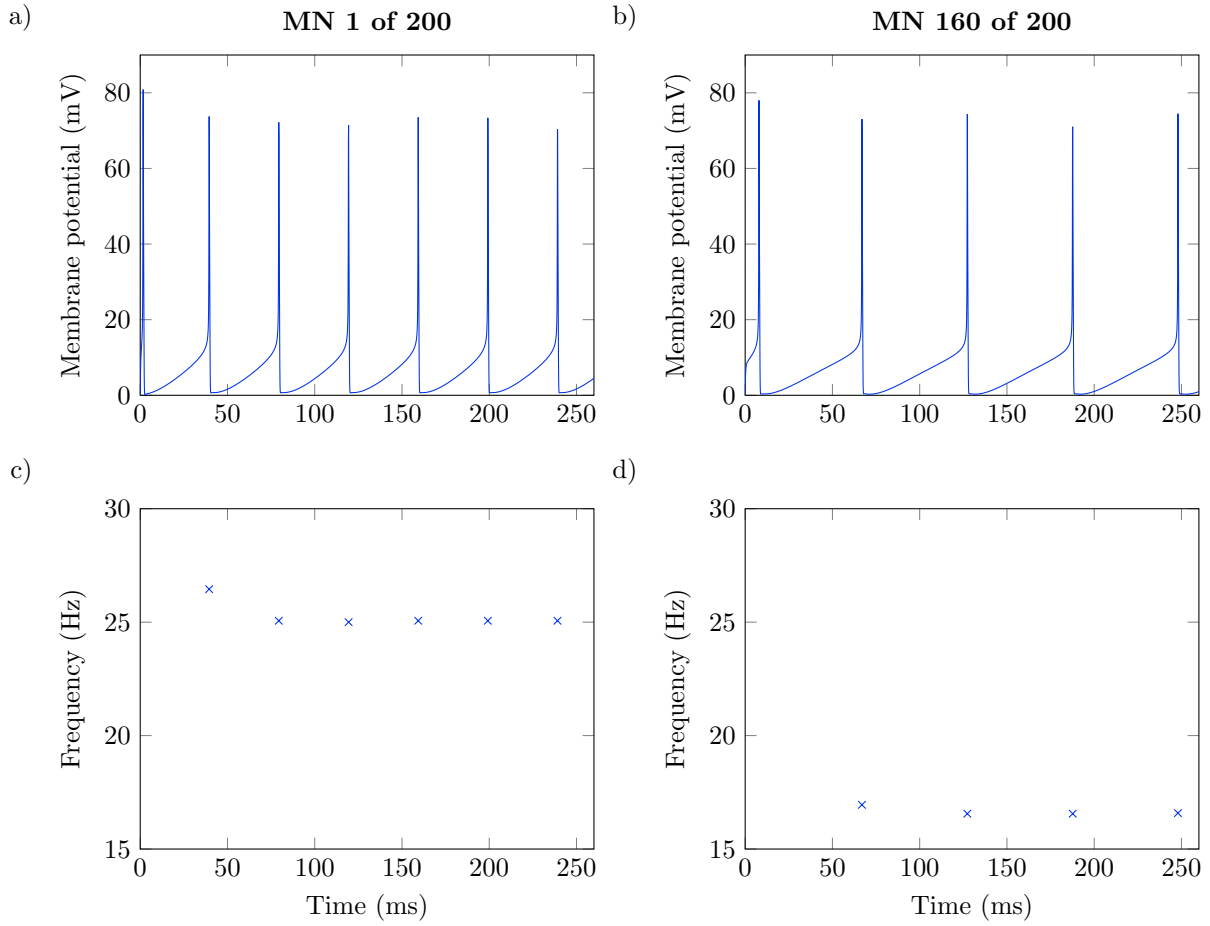

Figure 3.6: Membrane potential time course and instantaneous frequency of the simulated motoneurons. a) Membrane potential time course of the smallest motoneuron (MN) from the pool. b) Membrane potential time course of MN 160 of a pool of 200 MNs. c), d) Instantaneous frequencies of the spikes shown in (a) and (b). Injected drive is 10 nA for both motoneurons.

simulated motoneurons (Kernell, 1965). The slope increases for further increasing input currents, marking the beginning of the secondary range (Kernell, 1965). This transition is usually very sharp in experimental recordings (Kernell, 1965). In Figure 3.7a small motoneurons (blue) reach the secondary range at approximately 25 nA. The larger motoneurons (red) only reach the primary range for the input currents shown. For inputs currents above 32 nA, the smallest motoneurons of the pool show a sudden and vertical increase in firing frequencies, reaching unphysiologically high values of approximately 450 Hz (not shown in the figure).

The corresponding slopes of the current-frequency relations are shown in Figure 3.7b. For frequencies of approximately 10 Hz to 90 Hz the slope is within the range of experimentally recorded values, i. e., $1\,\mathrm{Hz\,nA^{-1}}$ to $4\,\mathrm{Hz\,nA^{-1}}$ in the primary and $3\,\mathrm{Hz\,nA^{-1}}$ to $8\,\mathrm{Hz\,nA^{-1}}$ in the secondary range (Granit et al., 1966; Kernell, 1965). The sub-primary range is characterised by slopes of up to $24\,\mathrm{Hz\,nA^{-1}}$. For frequencies above 100 Hz, the slopes reach unphysiologically high values.

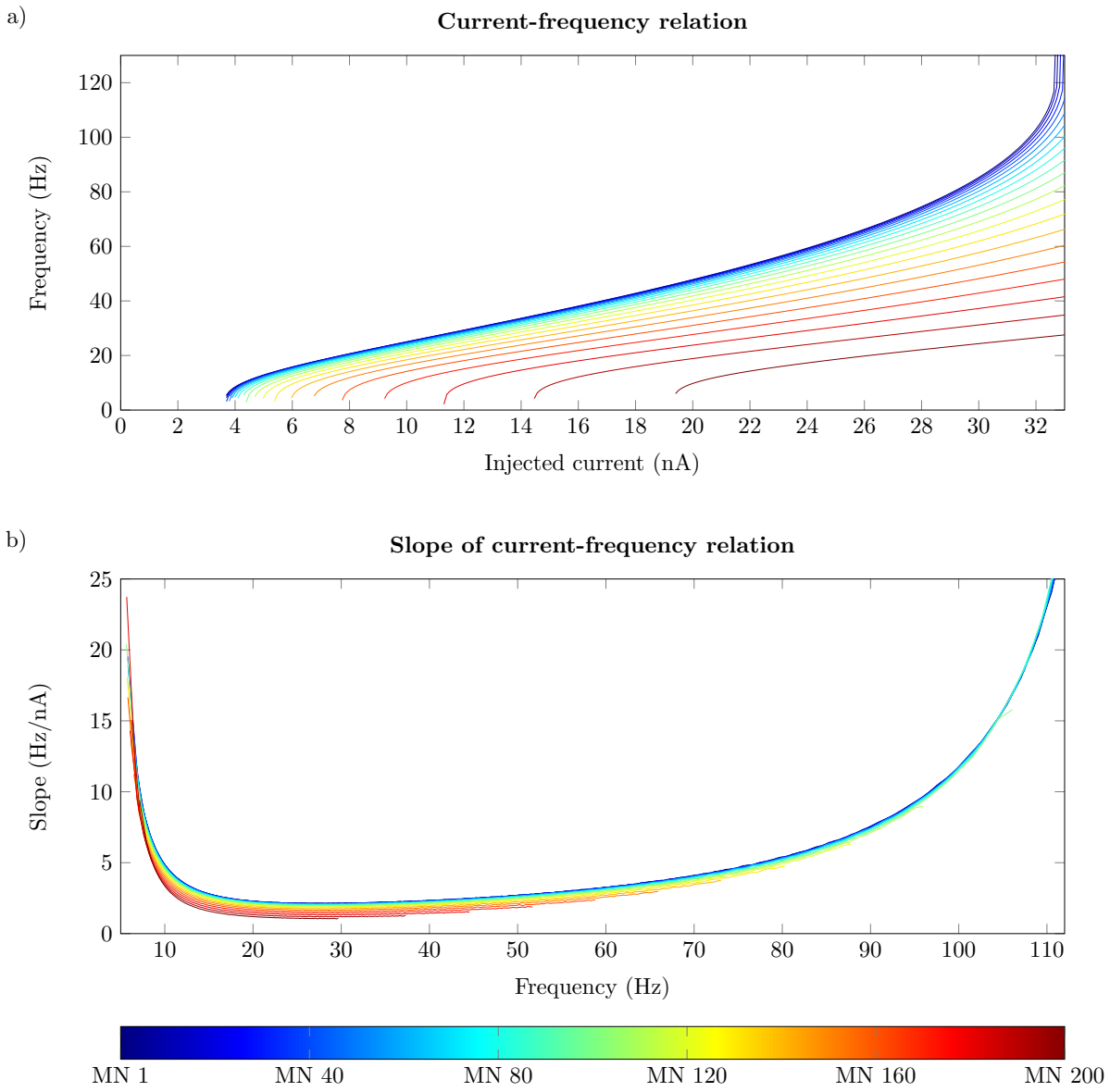

Figure 3.7: a) Current-frequency relation of the simulated motoneuron (MN) pool. b) Slope of the current frequency relation. Small MNs are shown in blue, and large MNs in red. Shown is every tenth MN from a pool of 200 MNs.

3.4.4 Limitations of the motoneuron pool model

As shown in the previous section, the motoneuron pool model qualitatively and quantitatively predicts many aspects of motoneuron behaviour. In this section, we discuss the model's limitations in terms of its comparability to experimental data and how well the model represents the physiological system. The significance of these limitations with regard to the model applications is discussed in the respective chapters.

For all considered properties, the simulated motoneurons show a smaller range of values than reported from experimental studies. However, the experimental data mainly represents a collection of values obtained from motoneurons of different hindlimb muscles. A physiological motoneuron pool is not expected to cover the entire range found across muscles. When comparing the model behaviour to motoneuron recordings from humans, it must be considered that the model was parametrised using cat data. Firing rates of cat motoneurons are reported to be approximately 1.5 times faster than those of human motoneurons (Manuel et al., 2019).

The motoneuron pool shows characteristic behaviour such as spike-frequency adaptation and a partitioned current-frequency relation. However, the simulated motoneurons produce unphysiologically high firing frequencies for very large input currents. Instead of stopping firing or frequency saturation, as observed in experimental studies (Kernell, 2006), the motoneuron membrane potential permanently depolarises. This can be attributed to the model's lack of an absolute refractory period. Consequently, the motoneuron pool model should only be used with inputs leading to maximum firing rates of less than 90 Hz.

The utilised model reduces the morphological complexity of the motoneuron into two lumped compartments and only considers a subset of the ion channels found in motoneurons. While the model can correctly predict many aspects of motoneuron activity, some properties are not considered. Using a single dendrite compartment does not allow for studying the effect of inputs delivered to different parts of the dendritic tree. Further, motoneuron dendrites contain voltage-gated ion channels, i. e., persistent inward currents (PICs). PICs are assumed to be highly active during normal muscle contraction and influence the current-frequency relation and recruitment of motoneurons (Binder et al., 2020). Ca^{2+}-mediated PICs can be included using, e. g., the approach by Elias and Kohn (2013). Further compartments or ion channels can be included following e. g., Powers et al. (2012).

The empirical approach developed by Hodgkin and Huxley enables the description of graded ion channel opening and closing. More complex models consider the underlying chemical reactions, but this is not necessary when studying motoneuron and not channel behaviour. Approaches to model the ion channel behaviour are reviewed by Destexhe and Huguenard (2000).

3.5 Representation of motoneuron input signals

Motoneurons receive many excitatory and inhibitory input signals from different sources, e. g., the motor cortex, sensory afferents or spinal interneurons. With regard to a motoneuron model, this raises the question of where to apply these inputs and how to determine them. The first question is tackled using effective synaptic inputs, described

in Section 3.5.1. The latter question is addressed by dividing the input into different components (Section 3.5.2).

3.5.1 The concept of effective synaptic current

As described in Section 2.3.1 motoneurons receive incoming signals via their dendrites. 98 % to 99 % of a motoneuron's synapses are located on the dendrites (Fyffe, 2001). The resulting postsynaptic potentials travel to the soma, changing their amplitude and summing with other arriving potentials. Based on the observation that only potentials eventually reaching the soma contribute to reaching the threshold for an action potential, Heckman and Binder (1988) introduced the concept of the effective synaptic current. The effective synaptic current corresponds to the current that arrives in the soma. Only this current is relevant for recruitment and rate coding (Heckman and Binder, 1988).

In this work, we will generally inject currents into the soma compartment of the model and assume that those are effective synaptic currents. The soma injected current corresponds to $I_{\mathrm{inj}}^{\mathrm{s}}$ in (3.33).

3.5.2 Common and independent input

Motoneurons receive many inputs from different parts of the nervous system. Some inputs are shared amongst the pool, while others are individual to each motoneuron. Motoneurons of the same pool receive a strong common input that mainly determines the muscle force (Negro et al., 2016b). This common input was shown to contain frequency components of approximately 15 Hz to 35 Hz and makes up the largest proportion of motoneuron inputs (Conway et al., 1995; Halliday et al., 1998; Negro et al., 2016b). Other synaptic inputs, which are unique to each motoneuron, decorrelate the motoneurons within a pool and are, e. g., associated with recurrent or sensory pathways in the spinal cord (Maltenfort et al., 1998). These inputs are also called independent inputs.

In motoneuron modelling studies, the input is commonly modelled as a constant mean, which determines the force level and is common to all neurons of the pool. In addition, common and independent noise components are added. Therefore, filtered zero-mean Gaussian noise can be used. The common noise is usually band-pass filtered (15 Hz to 35 Hz) and the independent noise is low-pass filtered (< 100 Hz). (e. g., Negro and Farina, 2011)

4 Quantification of Reflex Responses Using Peristimulus Analysis

Knowledge of information transmission through neural pathways is the basis for understanding their function in physiology and pathophysiology. Stretch reflexes are a class of neural pathways fundamental to motor control. This chapter summarises the basic principles of recording single motor unit activity in reflex pathways, focusing on non-invasive techniques that can be applied *in vivo*.

A reflex describes the process of an afferent signal from sensory organs being transmitted to the central nervous system and evoking a rapid response (Pierrot-Deseilligny and Burke, 2005). Motor unit reflex activity is used as a tool in many fields. Thereby, the size and duration of the reflex response are used as a biomarker. Basic physiology research utilises reflex recordings to broaden the knowledge on the connectivity of spinal pathways (e. g., Burke, 1999; Yavuz et al., 2018) and to estimate the (relative) size and time course of postsynaptic potentials (PSPs) (for a review, see Powers and Türker, 2010b). Reflex pathways are also used to investigate the physiology and pathophysiology of, e. g., ageing and spasticity (e. g., Aloraini et al., 2015; Biering-Sørensen et al., 2006; Nadler et al., 2002). Further, the size of different reflex responses is used for diagnosis, monitoring, and treatment of different diseases, e. g., stroke, spasticity, spinal cord injuries and other neurological disorders of the brain (e. g., Chen et al., 2003; Cruccu and Deuschl, 2000; Nadler et al., 2004).

Since motor unit reflex responses cannot be directly recorded *in vivo*, researchers developed several indirect measurement techniques based on electromyogram (EMG) recordings. Peristimulus analysis has been established as a mode of representation and analysis of the recorded data. Thereby, motor unit activity in the form of spike trains is analysed with respect to the time of the reflex stimulus.

This chapter overviews peristimulus analysis techniques for quantifying motor unit and motoneuron reflex responses. Section 4.1 provides a brief overview of the recording modalities and Section 4.2 describes the methods of peristimulus analysis. Peristimulus analysis can be applied to both excitatory and inhibitory reflexes and is used in Chapters 5, 6 and 7 of this work. Finally, Section 4.3 presents an algorithm that automatically determines the reflex size and that will be employed in Chapters 5 and 7 of this work.

4.1 Recording of motor unit reflex responses

Different experimental methods are employed to evoke and record stretch reflexes *in vivo* (Figure 4.1). Direct recordings from human motoneurons *in vivo* are impossible. However, every action potential of a motoneuron causes an action potential in the muscle fibres of the respective motor unit. The sum of these single fibre action potentials is called motor unit action potential and can be regarded as an amplified version of the motoneuron activity. This signal can be recorded using EMG. Two methodically different recording modalities are available. For intramuscular EMG, needle or fine-wire electrodes are inserted into the muscle (Figure 4.1C, Merletti and Farina, 2009). This method allows recording motor unit

action potentials from a single or several motor units (Merletti and Farina, 2009; Muceli et al., 2022). During surface EMG, electrodes are placed on the skin above the muscle belly, where they record the summed activity of several motor units (Figure 4.1D, Merletti and Farina, 2016). Sophisticated decomposition algorithms in combination with densely packed grids of electrodes (high-density surface EMG) allow extracting the activity of single motor units from this summed signal (e. g., Del Vecchio et al., 2020; Farina and Holobar, 2016).

Reflexes can be elicited by presenting a supra-threshold stimulus to the appropriate sensory organ. In this work, we focus on the stretch reflex, which is evoked by mechanical stimulation of muscle tissue. Muscle spindles react to the mechanical stimulus by changing their activity, which, in consequence, modulates the afferent input to α-motoneurons and, finally, muscle activity (Macefield and Knellwolf, 2018). Two methods are commonly used to evoke the stretch reflex. A mechanical stimulus can be applied to the muscle-tendon unit, e. g., by enforcing a sudden movement of the joint (Figure 4.1A, e. g., Yavuz et al., 2014). The joint movement mechanically translates into a stretch of the muscle fibres, which the muscle spindles observe. An afferent nerve transmits the sensory signal to the motoneurons, where it causes an excitatory postsynaptic potential (EPSP) (Stauffer et al., 1976; Watt et al., 1976). Alternatively, the reflex can also be evoked by electrical stimulation of the afferent nerve (Figure 4.1B, e. g., Yavuz et al., 2018). Note that the H-reflex is not exactly analogue to the mechanically evoked reflex due to the differences in the stimulation modalities.

In reflex experiments, subjects are usually instructed to maintain a certain level of constant, isometric contraction of the target muscle. EMG sensors permanently record the activity of the target muscle.

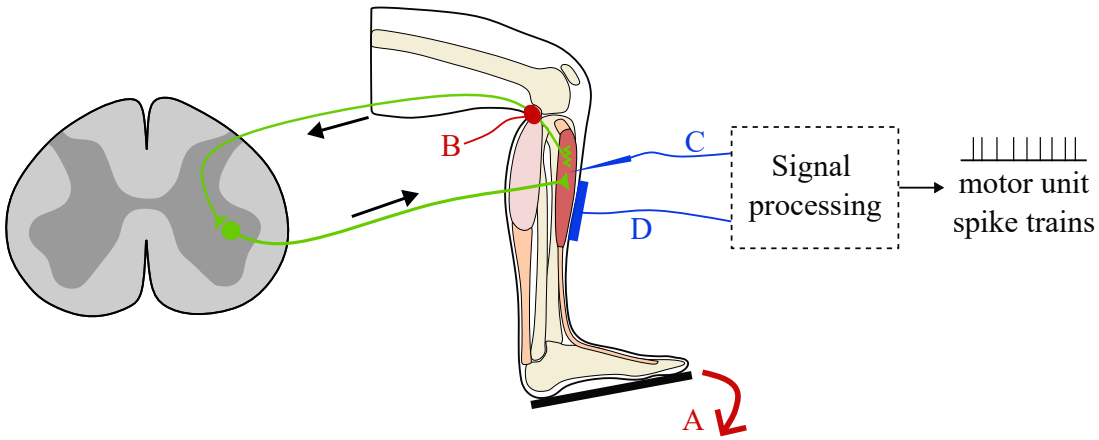

Figure 4.1: Schematic setup of a stretch reflex experiment. The reflex (green pathway) can be elicited by either a mechanical perturbation of the corresponding joint (A) or electrical stimulation of the afferent nerve (B). The intramuscular (C) or surface (D) electromyogram can record motor unit activity. Motor unit spike trains can be obtained from both recording methods by applying appropriate signal processing methods. [modified from Homs-Pons et al. (2024) under CC BY 4.0]

4.2 Peristimulus analysis of reflex responses

In peristimulus analysis, a reflex pathway is considered a stimulus-response circuit. That means when the system is stimulated at one point, an effect can be measured at another point and in temporal relation to the stimulus. For this reason, motor unit/motoneuron activity is evaluated with respect to the stimulus time, which is usually defined as time zero. Typically, a time window of 150 ms to 400 ms before and after the stimulus application is considered. The prestimulus time period provides an estimate for the baseline activity, which is used as a reference. After the stimulation, only the first 200 ms are of interest for reflex studies because later responses can theoretically be influenced by voluntary actions (Kandel et al., 2013).

At the beginning of EMG-based reflex studies, the reflex strength was directly determined from surface EMG recordings. However, the surface EMG amplitude cannot be directly correlated with the activity of single motoneurons (Keenan et al., 2006). Today, we use spike trains of single motor units. The spike trains contain the time points of the occurrence of action potentials and, thus, provide a direct correlate of motoneuron activity. They can be obtained from surface and intramuscular EMG (Yavuz et al., 2015). The spike trains are typically analysed by two means. The peristimulus timehistogram (PSTH) shows the temporal occurrence of spikes with respect to the stimulus time, and the peristimulus frequencygram (PSF) displays the instantaneous discharge frequency of the spikes. Both methods are described in detail in Sections 4.2.1 and 4.2.2, respectively.

4.2.1 The peristimulus timehistogram (PSTH)

The PSTH is based on counting the occurrence of spikes in defined time bins with respect to the stimulus time. Gerstein and Kiang (1960) first used the PSTH to describe the discharge behaviour of neurons. They observed that appropriate stimuli change the temporal distribution of neuron spikes. However, these changes occur with a certain variability and latency and are thus difficult to see in a spike train recorded from a single stimulation experiment. The PSTH is constructed by counting the occurrence of spikes (or events) in time bins of defined width and with respect to stimulus time (Figure 4.2). Thereby, the stimulus time is defined as time zero. This process is repeated for several stimuli (usually several tens or hundreds), and the spike counts are summed for all stimuli.

The PSTH reflects the probability of a neuron to discharge with respect to the time of the stimulus. In Figure 4.2, the PSTH of an example neuron is shown. The peak at time zero indicates an increased firing probability at the time of the stimulus. Considering that an increased or decreased firing probability is not automatically synonymous with motoneuron excitation or inhibition is essential. Instead, synchronisation effects can also lead to peaks or troughs in the PSTH (Türker and Cheng, 1994). The limitations of PSTH are discussed in detail in Section 4.4.1.

4.2.2 The peristimulus frequencygram (PSF)

The PSF is a scatter plot of the instantaneous discharge frequency of spikes with respect to the stimulus time. Bessou et al. (1968) first introduced it to analyse muscle spindle activity. Türker and Cheng (1994) first applied this technique to motor units in reflexes. As in the PSTH, a pattern becomes visible when adding several tens or hundreds of spike

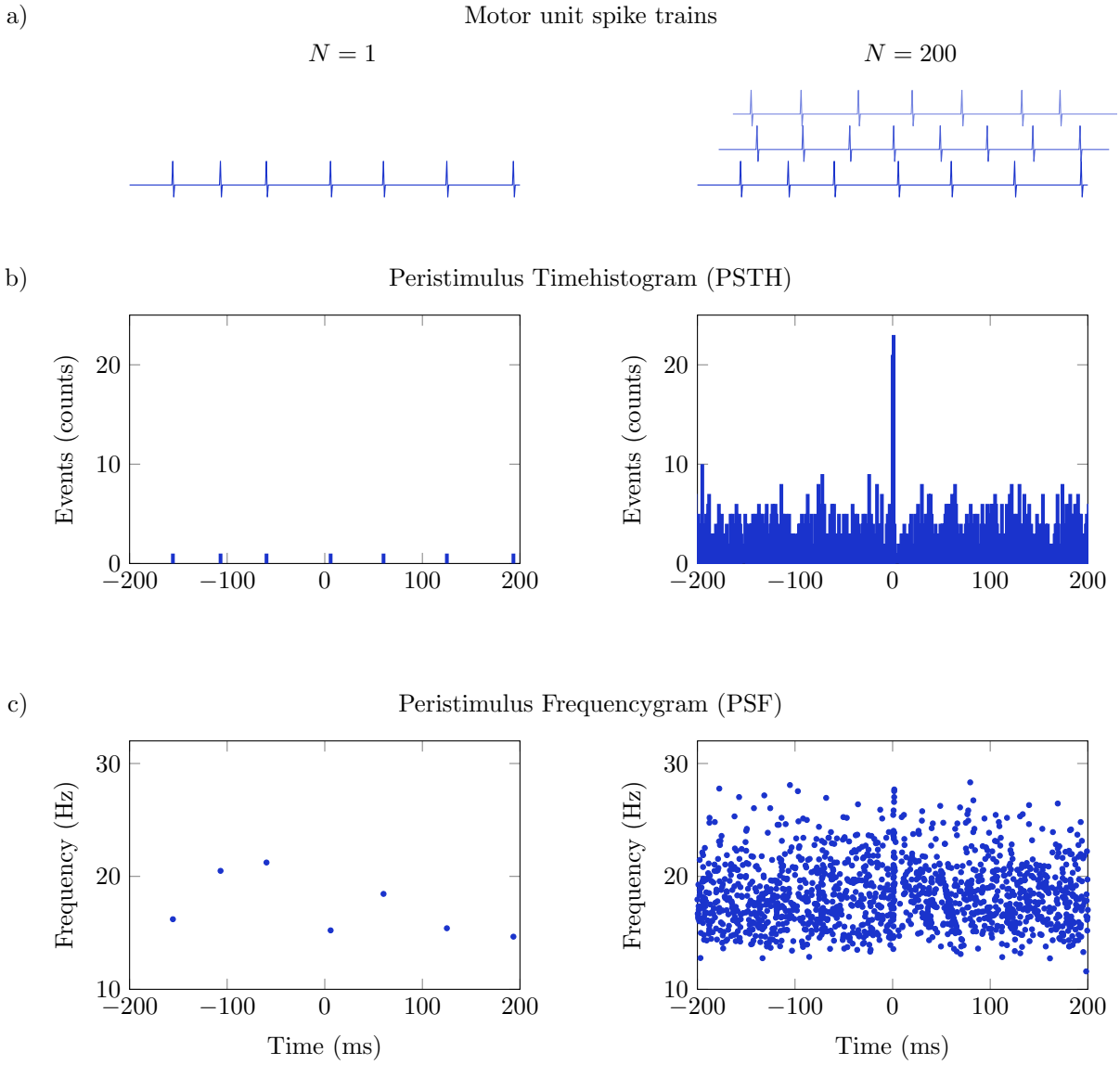

Figure 4.2: Visualisation of peristimulus analysis. a) Single motor unit spike trains from N reflex experiments. b) In the peristimulus timehistogram (PSTH), every motor unit spike is reflected by an event count relative to the stimulus time. c) In the peristimulus frequencygram (PSF), the instantaneous frequency of every spike is plotted with respect to the stimulus time. The stimulus time corresponds to time zero. Counts and frequencies of n spike trains are overlaid in the same plot to recognise an activity pattern.

trains to the scatter plot (Figure 4.2). The PSF assumes a positive relation between a motoneuron's discharge frequency and the net current reaching its soma (Heckman and Binder, 1988; Powers and Binder, 2007; Powers et al., 1992; Schwindt and Calvin, 1973). Under this assumption, any significant change in the PSF reflects the sign and profile of the net input current. Consequently, the PSF can distinguish between a change in motoneuron activity and motoneuron synchronisation (Türker and Cheng, 1994; Yavuz et al., 2014). Thereby, it overcomes the limitations of the PSTH (see Section 4.4.1).

Note that also other frequency-based methods were proposed in the literature, e. g., the interspike interval superposition plot (IISP, e. g., Awiszus et al., 1991). This method

plots the duration of the interspike interval with respect to the stimulus time. Since the duration of the interspike interval is the reciprocal of the frequency, the IISP provides the same information as the PSF, whereby a decrease in the IISP is correlated with an increase in input current.

4.2.3 The cumulative sum (CUSUM)

Quantifiable biomarkers, which can be extracted from reflex responses, are e. g., the reflex amplitude, latency and duration. Obtaining those values requires unified criteria for determining the beginning and end of a reflex response (Lavigne et al., 1983). Today, the respective cumulative sums (CUSUM) of the PSTH and PSF are mainly used for this purpose. The CUSUM method is widespread to visualise small but persistent trends that are not easily visible in the raw data. Ellaway (1978) first applied the CUSUM method in neuroscience.

To obtain the CUSUM of the Nth value a reference value k is subtracted from each value y_i in the histogram and the resulting values are summed consecutively (Ellaway, 1978):

$$S(N) \;=\; \sum_{i=1}^{N} (y_i \;-\; k) \;. \tag{4.1}$$

Usually, the prestimulus mean value is used as the reference value k.

Any deflection of the CUSUM S from zero indicates a difference from the prestimulus mean activity. In detail, values are permanently higher than the prestimulus mean as long as the CUSUM increases. Accordingly, the values are lower than the prestimulus mean as long as the CUSUM decreases. Thereby, the slope of the CUSUM curve corresponds to the difference between the current value and the reference value.

Normalising the CUSUM by the number of delivered stimuli (No. of Stim) gives a metric that can be used to compare experiments. Consequently, the CUSUM is ususally provided in units of counts/No. of Stim for the PSTH and Hz/No. of Stim for the PSF, respectively. Alternative but equivalent units are, e. g., counts/PSP or counts/trigger.

Based on the CUSUM, Türker et al. (1997) defined a significance threshold for reflex responses. The largest absolute prestimulus deflection from zero was used as a symmetrical error box, i. e., as a threshold in the positive and negative direction. Poststimulus deflections of the CUSUM that exceed this error box in either direction are accounted as significant reflex responses.

Building on the error box approach, Brinkworth and Türker (2003) introduced the turning points of the CUSUM as indicators for the onset and the end of a reflex response. In detail, not the crossing of the error box determines the onset of the reflex response, but the point where the CUSUM begins to rise/decrease to exceed the error box (Figure 4.3). Accordingly, the end of the reflex is where the sign of the slope changes again. Although the method introduced by Brinkworth and Türker (2003) was intended for automatic evaluation, manual evaluation is the current gold standard. Reflex onset and end often deviate from the mathematical definition of a turning point when it seems appropriate to the examiner.

The reflex onset and end in the PSTH- and PSF-CUSUM determine the characteristic values of a reflex response. The reflex latency corresponds to the time difference between the stimulus and the reflex onset. Accordingly, the reflex duration corresponds to the

time difference between reflex onset and end. The difference of the CUSUM values at reflex onset and end equals the reflex amplitude (Figure 4.3).

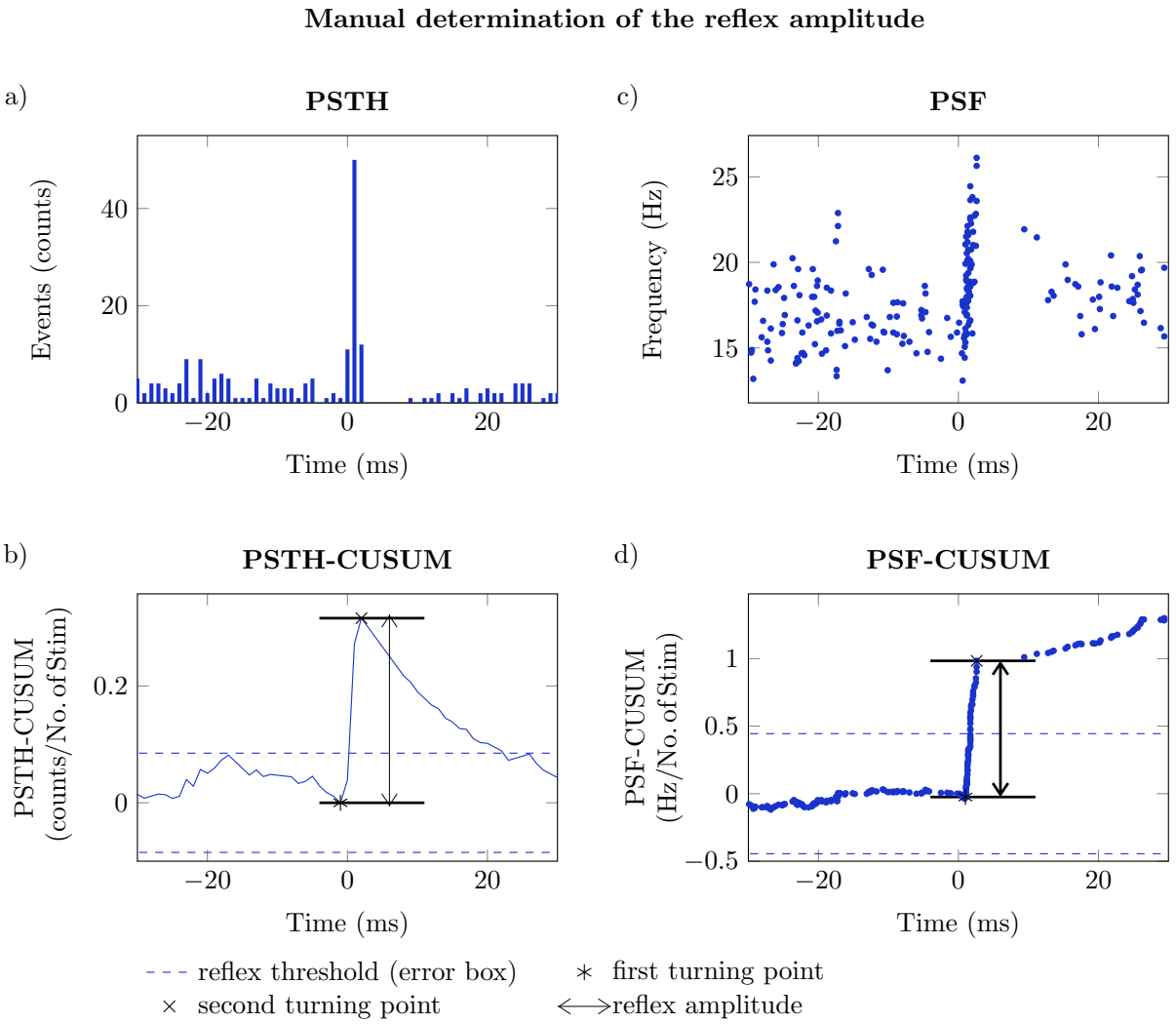

Figure 4.3: Example of how the reflex amplitude is determined manually from the cumulative sum (CUSUM) of the peristimulus timehistogram (PSTH) and the peristimulus frequencygram (PSF). a) PSTH of a reflex response. b) PSTH-CUSUM. c) PSF of a reflex response. d) PSF-CUSUM. The reflex onset is marked with a star (∗), and the reflex end is marked with a cross (×). The reflex amplitude corresponds to the difference in the CUSUM at reflex onset and end (arrow). Time zero corresponds to the time of the stimulus application.

4.3 Automatic evaluation of reflex amplitudes

In experimental studies, the reflex amplitudes are usually determined manually from the PSTH and/or the PSF and the respective CUSUMs. For EMG signals, in contrast, there exist numerous approaches for automatic detection of the reflex onset (e. g., Staude and Wolf, 1999; Vaisman et al., 2010). The turning point method, described in Section 4.2.3, was initially introduced as an automatic method to quantify reflex responses from EMG

signals (Brinkworth and Türker, 2003). Nevertheless, manual determination became the standard when applying the method to peristimulus data. In this work, the reflex amplitudes of several hundred motoneurons are evaluated under numerous experimental conditions. A manual evaluation is not suitable for this purpose.

This section describes and compares two algorithms for determining the reflex amplitude. An expert researcher from the field verified the results. Additionally, a semi-automated validation procedure is introduced, which will be used for the investigations in Chapter 5.

4.3.1 Algorithms for determining the reflex amplitude

We present two algorithms for the determination of the reflex amplitude. Both algorithms are based on peristimulus analysis and can determine reflex amplitudes from both the PSTH- and the PSF-CUSUM. The algorithms take the PSTH, the PSF and the number of delivered stimuli as inputs. Thereby, the bin size of the PSTH and the pre-and post-stimulus periods are determined from the input data. Then, the CUSUM is computed from both the PSTH and the PSF, using Equation (4.1) and the prestimulus mean value as a reference value. The prestimulus mean value $\bar{y}$ is calculated from

$$\bar{y} \;=\; \frac{1}{N}\sum_{i=1}^{N} y_i \;, \tag{4.2}$$

with N values from the prestimulus time period ($t < 0$). To reduce small deflections from the PSF-CUSUM, only the last CUSUM value per 1 ms time bin is considered (Figure 4.4c). The PSTH- and the PSF-CUSUM are normalised by the number of stimuli.

The threshold for a significant reflex (error box) is calculated for the PSTH and the PSF as the maximum absolute deflection of the CUSUM from zero during the prestimulus time (Türker et al., 1997). Both presented algorithms use the slope of the CUSUM to determine the reflex onset and end. Since the CUSUM is a discrete quantity, the slope of the CUSUM $\dot{\mathbf{S}}$ is approximated by the difference between adjective elements of the CUSUM vector $\mathbf{S}$. If the CUSUM is of length N, the approximation of the slope yields

$$\dot{\mathbf{S}} \;\approx\; [\mathbf{S}(2)-\mathbf{S}(1) \;\; \mathbf{S}(3)-\mathbf{S}(2) \;\; \ldots \;\; \mathbf{S}(N)-\mathbf{S}(N-1)] \;. \tag{4.3}$$

The onset and the end of the reflex response can now be obtained from the CUSUM and its approximated slope. Therefore, two different methods are applied. The first approach determines the turning points of the CUSUM to mimic the manual evaluation process closely. The second approach uses the size of the CUSUM slope to indicate a reflex response's beginning and end.

Reflex amplitude determination based on the CUSUM turning points

The so-called turning points often serve as an orientation during the manual evaluation of the reflex amplitude (Brinkworth and Türker, 2003). As shown in Figure 4.3, the point where the CUSUM begins to rise/decrease to exceed the significance threshold marks the beginning of the reflex response. Similarly, the following point where the CUSUM changes its slope marks the end of the reflex response.

In the evaluation algorithm, the CUSUM's first execution of the significance threshold is chosen as a starting point. From there, the previous and the following changes in the CUSUM slope are determined. These are the turning points, and the reflex amplitude is determined as the difference between the CUSUM values of the turning points.

Reflex amplitude determination based on the CUSUM slope

The second method uses the slope of the CUSUM, i. e., the "steepness" of the reflex response, as the indicator for the reflex onset and end. Therefore, a threshold is determined, similar to the CUSUM error box. The largest absolute deflection from zero of the approximated slope of the CUSUM defines the reflex threshold, and any point above the threshold is considered to be part of the reflex response.

Figure 4.4 visualises the procedure. First, the algorithm searches the poststimulus time of the CUSUM slope for values exceeding the threshold. If found, the first such point marks the onset of the reflex response (Figure 4.4, 1.). The next sub-threshold value of the CUSUM slope marks the end of the reflex response (Figure 4.4, 2.). The algorithm verifies that the CUSUM values of the detected reflex response exceed the CUSUM error box and confirms that the response is a significant reflex (Figure 4.4, 3.). If the reflex response is approved, the reflex amplitude is computed as the difference of the CUSUM values at the reflex onset and end (Figure 4.4, 4.). If the reflex response is not approved, the motoneuron is discarded from the analysis.

4.3.2 Assessment of the performance of the algorithms

The reflex amplitudes determined with both algorithms are shown for one exemplary simulation with 200 motoneurons in Figure 4.5. The amplitudes determined by the two algorithms are different in most cases. The reflex amplitudes are generally higher with the turning point algorithm. This trend is more striking for the PSF than the PSTH. The mean reflex amplitudes determined from the PSTH-CUSUM with the slope and turning point algorithms are 0.3 counts/No. of Stim and 0.319 counts/No. of Stim, respectively. The mean reflex amplitudes determined from the PSF-CUSUM with the slope and turning point algorithms are 1.061 Hz/No. of Stim and 1.336 Hz/No. of Stim, respectively.

Figure 4.6 shows the reflex onset and end determined manually and with the different evaluation methods. The reflex onset and end differ according to the two methods. In the PSTH-CUSUM, the reflex onset is determined earlier with the turning point algorithm, while the end is detected earlier with the slope algorithm. Consequently, the reflex amplitude is larger with the turning point algorithm. However, the difference in amplitude is negligible compared to the size of the error box. The manual evaluation coincides with the turning point method.

In the PSF-CUSUM, the slope algorithm also detects a later onset and an earlier end and, thus, a smaller amplitude than in the manual evaluation. For the reflex onset, the turning point algorithm and manual evaluation coincide, while for the end, the time point determined by the turning point algorithm is significantly later and at a higher CUSUM value than with the slope algorithm or according to manual evaluation. Consequently, the reflex amplitude determined with the turning point algorithm is significantly larger than in the manual evaluation.

An expert researcher from the field, who published several studies using the reflex

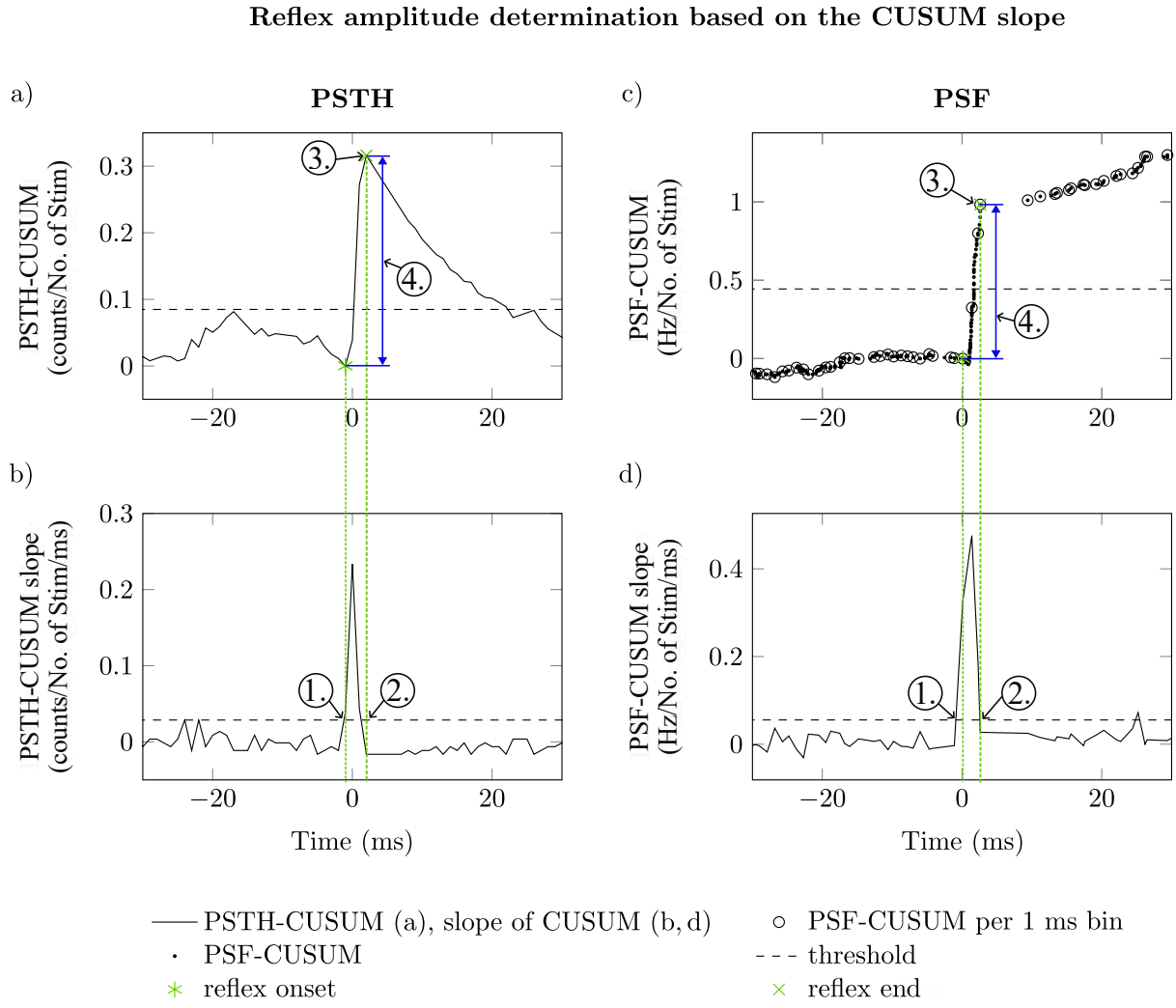

Figure 4.4: Visualisation of the algorithm using the CUSUM slope to determine the reflex amplitude. Shown are the PSTH-CUSUM (a), its slope (b), the PSF-CUSUM (c) and its slope (d), all for an exemplary motoneuron. 1. The reflex onset corresponds to the time when the slope of the CUSUM exceeds the threshold. 2. The reflex end corresponds to the time when the slope of the CUSUM returns to values below the threshold. 3. The CUSUM values must be ensured to exceed the threshold for significant reflexes. 4. The reflex amplitude is determined as the difference between the CUSUM values at the reflex onset and end.

amplitude, favours the slope method over the turning point method for two reasons: (i) it is more robustly applicable to the PSF-CUSUM and (ii) the steep increase in CUSUM is, from a physiological point of view, a better marker for the reflex onset than the onset of a positive slope of any value before exceeding the significance threshold (turning point). If the increase in CUSUM at the beginning of the reflex is small, it cannot be ensured that this increase is related to the reflex stimulus. By defining a slope threshold, random increases in motoneuron activity as they appear during the baseline are not considered reflex responses.

In summary, the slope algorithm was rated superior to the turning point algorithm. Therefore, the slope algorithm is used to evaluate the simulation results.

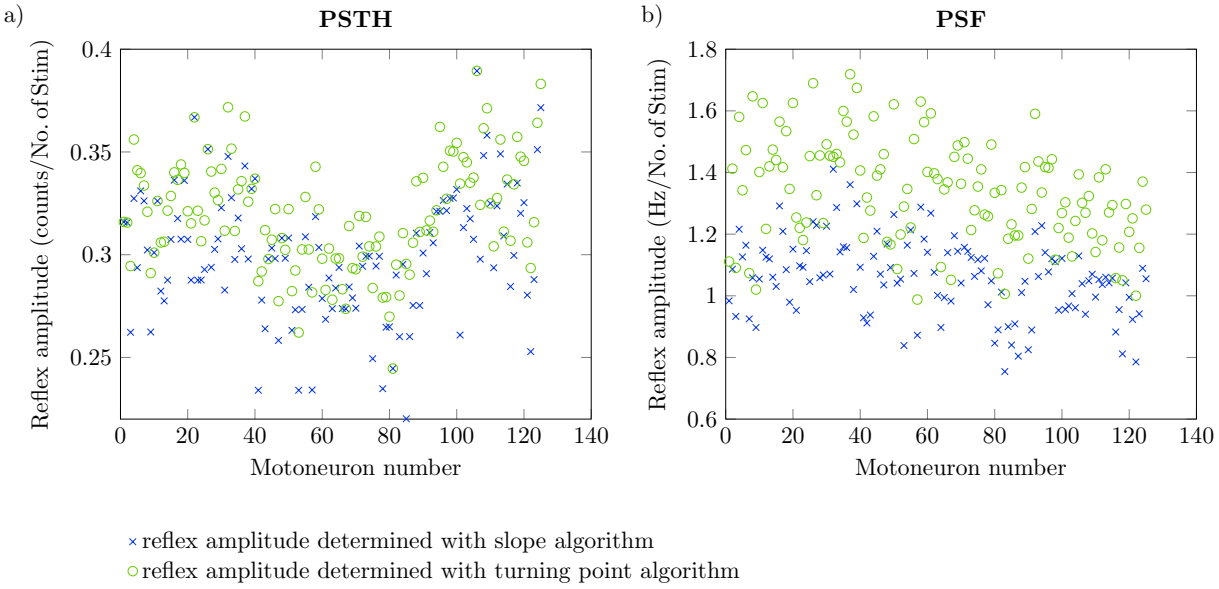

Figure 4.5: Reflex amplitudes determined with turning point (green) and slope (blue) algorithm. Reflex amplitudes determined from PSTH (a) and PSF (b). Results are shown for 200 motoneurons, numbered from smallest to largest. Note that not all 200 motoneurons show a significant reflex amplitude.

4.3.3 A semi-automated validation method for reflex amplitudes

A semi-automated assessment is adopted to exclude wrong assignments of reflex amplitudes. First, an automated exclusion of motoneurons is executed, followed by a visual inspection of the detected reflex responses. Thereby, the plausibility of the reflex responses is rated based on the reflex latency, i. e., the reflex onset time with respect to the stimulus.

In the analysis, only regularly firing motoneurons are included. We ensure this by excluding motoneurons with a mean baseline discharge frequency of less than 7 Hz or a coefficient of variation of the baseline interspike interval of more than 35 %. The coefficient of variation is defined as the ratio of the standard deviation to the mean. Further, reflex responses are automatically excluded when the reflex onset is outside a time window of $[-5\,\text{ms}, 15\,\text{ms}]$ around the stimulus time. Since we do not consider conduction delays, we can be sure that the reflex response must occur in this time period.

The remaining motoneurons are visually inspected. For every simulation, graphs showing the detected reflex responses are examined. In detail, the PSTH- and the PSF-CUSUMs are plotted together with the corresponding reflex onset and end for 20 motoneurons in each graph (Figures 4.7 and 4.8). Motoneurons with a reflex response that is not a short-latency response are manually excluded. In the example of Figure 4.8, motoneurons 110, 114 and 115 should be excluded.

The slope algorithm and the semi-automated inspection of the resulting reflex amplitudes were applied to all simulations performed for Chapter 5. In short, the simulations mimic the monosynaptic stretch reflex by injecting excitatory current kernels into a pool of 200 motoneurons. The motoneurons were simulated using the model described in Negro and Farina (2011) and Section 3.4, respectively. Different baseline activities and different stimulus amplitudes were used. For a more detailed description of the simulations, see

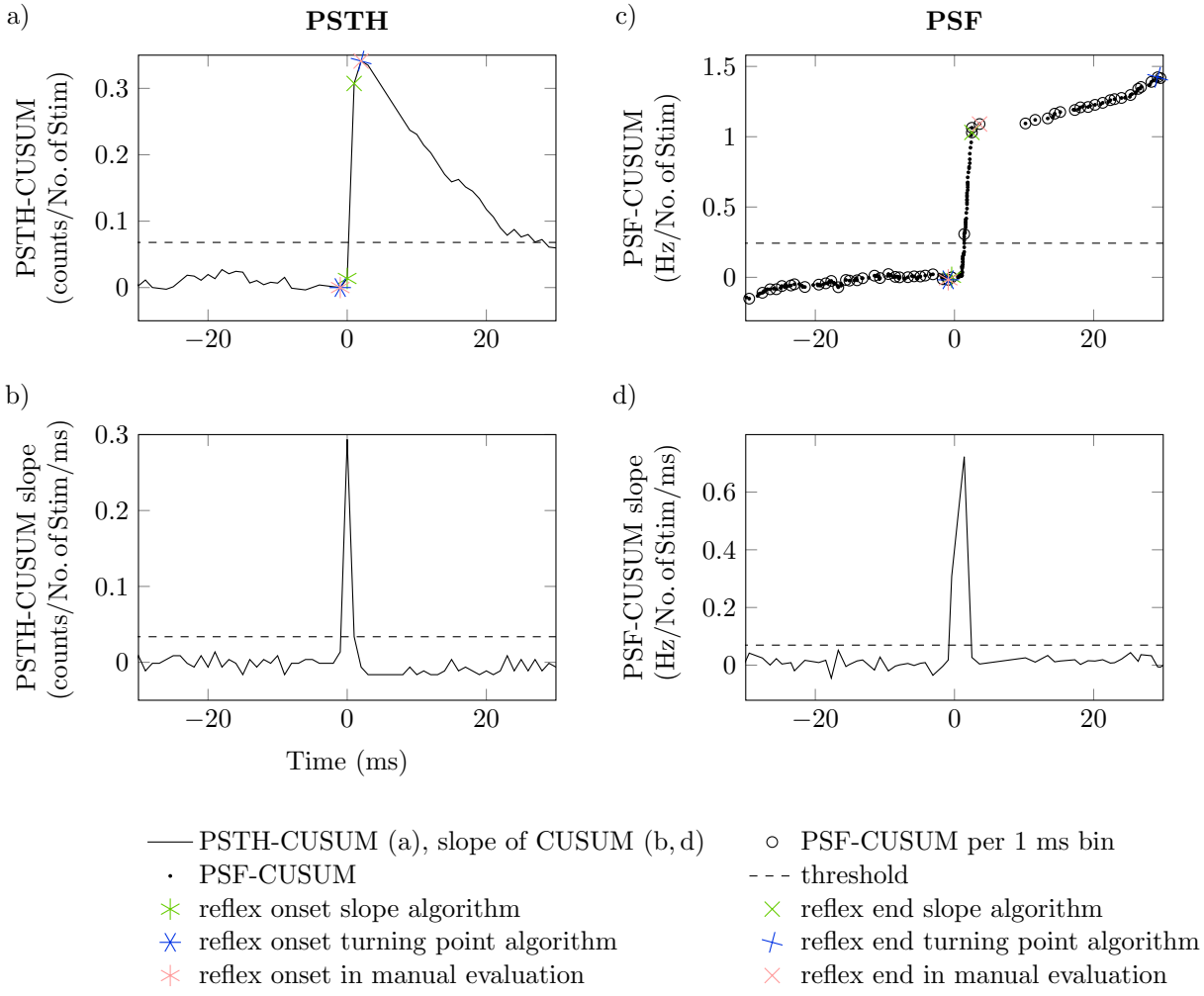

Figure 4.6: Comparison of the reflex onset and end determined with different evaluation methods. Shown are the PSTH-CUSUM (a) and its slope (b), as well as the PSF-CUSUM (c) and its slope (d). The reflex onset is marked with an asterisk (∗), and the reflex end is marked with a cross (×) for the slope algorithm (green), the turning point algorithm (blue) and the manual evaluation (pink). Note that the PSTH and the PSF examples stem from different motoneurons.

Section 5.1.

In total, 42 simulations were performed. The algorithm determined reflex amplitudes from PSTH-CUSUM for 9056 motoneurons. Only one motoneuron was removed after visual inspection, corresponding to 0.01 % of the motoneurons. The algorithm detected 8276 motoneurons with a significant reflex response in the PSF-CUSUM. From these, 40 motoneurons were discarded after visual inspection, corresponding to 0.48 % of the motoneurons.

The algorithm performed worst for simulations with a high background activity and a relatively low stimulus intensity. In one specific simulation, only 100 stimuli were applied (usually 200 stimuli were applied). In this simulation, we discarded one reflex response from the PSTH-CUSUM and ten out of 20 PSF-CUSUM reflex amplitudes. Across all other simulations, we never removed more than four reflex amplitudes from the PSF-CUSUM. When the noise input to the motoneurons was omitted in the simulations, all reflex amplitudes were approved.

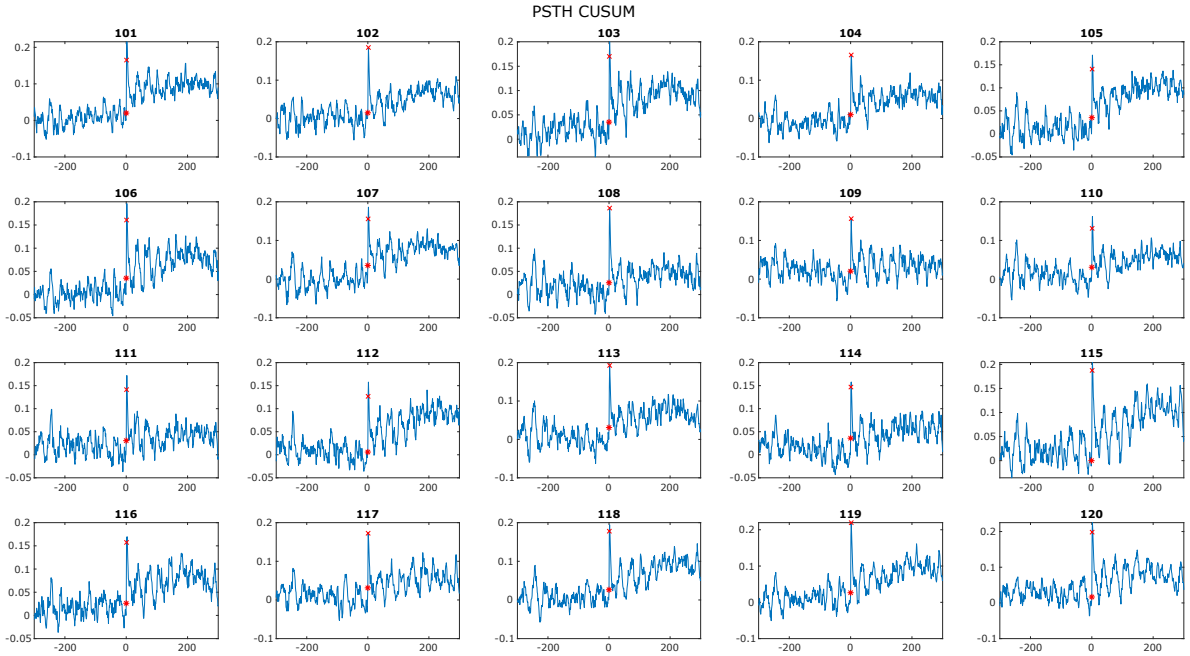

Figure 4.7: Example for the visual inspection of reflex amplitudes determined from the cumulative sum of the peristimulus timehistogram (PSTH-CUSUM). Shown are motoneurons 101 to 120 of a pool of 200. The red asterisk marks the reflex onset, and the red cross marks the reflex end. Peristimulus time in ms is shown on the x-axes and y-axes show PSTH CUSUM in counts/No. of Stim.

4.4 Discussion

The assessment of motoneuron reflex amplitudes *in vivo* relies on indirect methods based on recorded motor unit spike trains. The spike trains are commonly analysed using peristimulus analysis. We presented two modes of peristimulus analysis: the PSTH and the PSF. The limitations of these methods are discussed in Section 4.4.1.

Systematic investigations of reflex responses using computer simulations require an automated evaluation method. We presented and assessed two algorithms determining the reflex amplitude. The outcomes and implications for future studies are discussed in Section 4.4.2.

4.4.1 Limitations of peristimulus analysis

Several studies showed that secondary and later peaks and troughs in the PSTH can be caused by synchronisation of the neurons with respect to the stimulus (Awiszus et al., 1991; Türker and Powers, 1999, 2003; Yavuz et al., 2014). When an excitatory stimulus causes an action potential, the motoneuron will, from then on, discharge action potentials at multiples of the current interspike interval. Thus, secondary and later peaks in the PSTH can erroneously be interpreted as medium- or long-latency components of the reflex response. Something similar can happen after an inhibitory stimulus. By delaying the action potential, the inhibitory stimulus synchronises the motoneurons, which results in a peak in the PSTH. This peak might be misinterpreted as a period of excitation

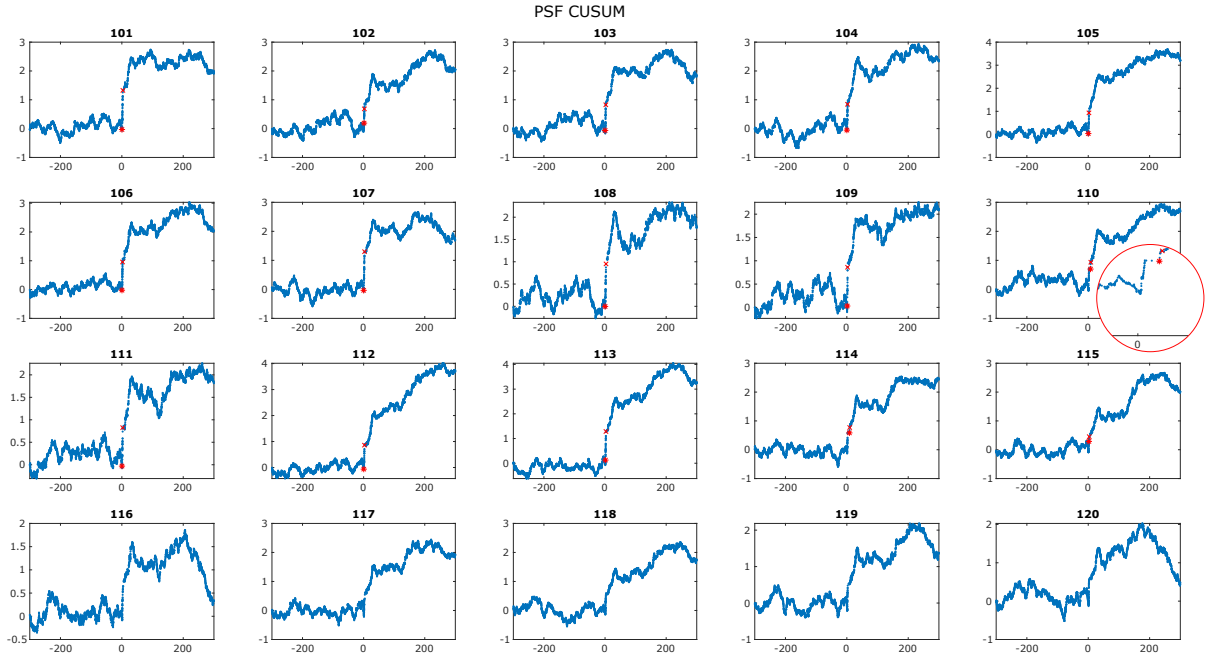

Figure 4.8: Example for the visual inspection of reflex amplitudes determined from the cumulative sum of the peristimulus frequencygram (PSF-CUSUM). Shown are motoneurons 101 to 120 of a pool of 200. The red asterisk marks the reflex onset, and the red cross marks the reflex end. The area with the marks is enlarged for motoneuron 110. Peristimulus time in ms is shown on the x-axes and y-axes show PSF CUSUM in Hz/No. of Stim. Missing red marks indicate that no significant reflex response was detected for motoneurons 116 to 120.

even though an inhibitory postsynaptic potential (IPSP) was applied (Moore et al., 1970; Türker and Powers, 1999). The same problem applies to using the CUSUM obtained from the PSTH (Türker and Powers, 2003). Consequently, the PSTH can only provide reliable information on the short-latency component of a reflex response.

After its introduction, it was proposed that the PSF method is free of the errors associated with probability-based methods as the PSTH (Türker and Cheng, 1994). Over time, it has been shown that the PSF is also affected by history-dependent events. Türker and Powers (1999) showed that the second spike after applying a PSP can still be influenced. In detail, depending on the timing of the PSP with respect to the last discharge, the second spike after an EPSP can be discharged with a lower frequency than the baseline activity. Accordingly, the second spike after an IPSP can show a history-dependent increase in firing rate. Türker and Powers (1999) suggested that these secondary effects can be explained by the summation of the conductance underlying the post-spike afterhyperpolarisation. In contrast to the synchronisation errors in the PSTH, this effect is real and does reflect actual motoneuron membrane characteristics. However, it has to be considered that this effect does not reflect further arriving PSPs.

Studies comparing the discussed methods suggest considering both the PSTH and the PSF and the CUSUM of both metrics (Türker and Powers, 1999, 2003). Nevertheless, recently, Türker (2022) challenged an article published a year earlier that claims to have discovered a new firing characteristic of motoneurons based on a secondary peak in the PSTH. However, they did not show the PSF, which could have provided further insight.

This example shows that there are still pitfalls and uncertainties in interpreting reflex experiments using peristimulus analysis.

4.4.2 The use of an automatic evaluation method

We proposed and compared two algorithms for determining the reflex onset and end from the PSTH- and the PSF-CUSUM. An experienced researcher in the field assessed the results. The turning point algorithm aims to mimic the manual evaluation. However, it often detects the reflex end too late in the PSF-CUSUM. The slope algorithm introduced a new criterion for the reflex onset and end by comparing the slope of the CUSUM to the values during the baseline. This method robustly detects the reflex responses in the PSTH- and the PSF-CUSUM. The slope algorithm is suitable for the PSTH and the PSF, and, in addition, the new slope-based criterion has a physiological meaning. These arguments lead to the selection of the slope algorithm to evaluate reflex responses from simulated motoneurons within this work.

The developed algorithm performs well for the examined monosynaptic stretch reflex simulation experiments. However, it might not be applicable to other types of simulations or experimental data. Further, consider that a method working in healthy individuals does not guarantee that it will work with pathological signals, which might have very different characteristics. Herein, we used stimuli that reflect a large compound EPSP, as we expect from a short stretch of the muscle or the electrical stimulation of the afferent nerve. These stimuli induce short reflex responses with a sharp rising phase and an abrupt end. These characteristics make these stimuli well-suited for the slope algorithm. However, we expect that the slope algorithm works less well with slower reflex responses, e. g., in response to a sinusoidal stretch.

This chapter additionally introduced a semi-automated validation procedure to avoid including unreasonable or faulty results in the evaluation. The process of visually inspecting 20 motoneurons at once and only confirming or removing motoneurons is much faster than determining each reflex amplitude manually. Therefore, the procedure is worth the extra effort. The visual inspection also confirmed that the algorithm robustly detects reflex amplitudes in the PSTH-CUSUM. A low number of stimuli and noise hamper the correct assignment of reflex responses in the PSF-CUSUM. However, the total number of manually removed motoneurons was low compared to the overall number of reflex responses. If the latency criterion, i. e., the considered reflex onset times, was tightened, the number of manually removed values could be further reduced. However, this requires knowledge about the expected delay of the reflex onset. These characteristics can well be estimated in the simulation but are subject to uncertainties in the experiment.

Manual evaluation is always subjective and depends on the experience of the examiner. Koutris et al. (2016) found that the inter-examiner results were fair-to-good to excellent for a CUSUM-based analysis of the EMG signal. Nevertheless, robust evaluation algorithms for reflex experiments have the potential to accelerate research and make it more objective. Emerging technologies like improved decomposition algorithms, high-density intramuscular EMG or magnetomyography, will likely increase the number of motor units that can be decomposed from *in-vivo* recordings (Klotz et al., 2023; Muceli et al., 2022). A large number of recorded motor units per subject in combination with an automated evaluation method allows the inclusion of more subjects per study, makes

studies from different research groups more comparable and can broaden the applicability as an experimental and clinical measure.

The algorithm presented in this section was tailored for the specific application using short stimuli and simulated data. However, similar problems exist in many areas, including medical applications. Therefore, methods that work for EMG should be tested for their applicability to peristimulus data. Further, methods from other fields, e. g., change point detection in heart or brain activity recordings, could be adapted for reflex studies (Aminikhanghahi and Cook, 2017).

5 Factors Influencing In-Vivo Estimates of Excitation Reflex Amplitudes in Motoneuron Pools

Spinal reflexes are a central component of motor control. Recording responses to artificially evoked reflexes is a common tool for studying motoneurons *in vivo*. Thereby, the size of the reflex response of a motoneuron is commonly quantified by the reflex amplitude (Chapter 4). In addition to the long-standing use of the reflex amplitude in basic research (e. g., Burke, 1999; Powers and Türker, 2010b; Yavuz et al., 2018), there are efforts to use the reflex amplitude in clinical settings (e. g., Cruccu and Deuschl, 2000; Nadler et al., 2004). This wide usage underscores the need to systematically study the relation between the biophysical mechanisms of reflex processing in the neuromuscular system and the size of *in-vivo* reflex amplitude estimates. Understanding *in-vivo* measures is essential for correct physiological interpretations and diagnoses.

The most commonly used methods to determine the motoneuron reflex amplitude are the peristimulus timehistogram (PSTH) and the peristimulus frequencygram (PSF). Both methods are based on delivering multiple reflex stimuli and on the statistical analysis of motoneuron activity with respect to the time of the reflex stimulus. The PSTH is based on counting spikes in time bins with respect to the stimulus time, and the PSF shows the instantaneous frequencies of the spikes (see Section 4.2 and Gerstein and Kiang, 1960; Türker and Cheng, 1994).

The size of the reflex response is commonly assumed to be correlated with the size of the synaptic input, i. e., the postsynaptic potential (PSP). For example, for single motoneurons, Türker and Powers (1999) found a linear relationship between excitatory postsynaptic potential (EPSP) size and reflex amplitude. Further studies showed how the PSP size could be determined from PSTH peaks; however, the relations varied between motoneurons, and the best method differed between applied conditions, e. g., the discharge frequency (for a review, see Powers and Türker, 2010a). In brain slice experiments, the time course or shape of the PSP was better reflected by the PSF than the PSTH (Türker and Powers, 1999, 2003).

All attempts to find a uniformly applicable "formula" for determining the magnitude of synaptic inputs from *in-vivo* recordings have not been successful to date. However, the efforts have successfully identified the factors contributing to PSP-evoked changes in motoneuron firing characteristics. Those include

- the magnitude and duration of the afterhyperpolarisation (AHP, Powers and Türker, 2010b);
- the time course of the firing threshold Matthews (2002), which varies within the interspike interval in a way that it follows the membrane potential trajectory of the afterhyperpolarisation (Calvin, 1974; Powers and Binder, 1996);
- random membrane potential fluctuations, i. e., noise (Herrmann and Gerstner, 2002; Matthews, 1999; Piotrkiewicz et al., 2009);

- persistent inward currents (PICs, Powers and Türker, 2010b);
- and the background discharge frequency (Herrmann and Gerstner, 2002; Jones and Bawa, 1997; Matthews, 1999).

In summary, current reflex analysis methods provide a relative estimate of PSP size under constant conditions and when considering a single motoneuron. Researchers found that the relationship between PSP size and reflex response is influenced by intrinsic motoneuron properties, such as e. g., AHP and threshold and also by external conditions determined by central and peripheral inputs (Herrmann and Gerstner, 2002; Matthews, 1999, 2002; Powers and Türker, 2010b). With current methods, these influences and their possible interactions can neither be quantified nor weighted. Because less attention has generally been paid to the PSF, we do not know whether the PSF and PSTH are equally affected by the abovementioned factors. In addition, it has been my personal experience at lectures and conferences that the reflex behaviour of motoneurons is not intuitive and even experienced researchers in this field have difficulties interpreting results.

Investigations of motoneuron reflex behaviour in human subjects suffer from two significant drawbacks: (i) it is difficult to impossible to control the conditions completely, and (ii) only a small number of motoneurons can be recorded per subject. One way around this is animal studies, where the postsynaptic potentials can be measured (e. g., Türker and Powers, 1999). However, animal experiments are costly and limited to relatively few neurons. Computer models offer advantages here. Not only can the conditions be controlled entirely, but models also allow the evaluation of internal variables inaccessible in experiments. Therefore, many of the factors mentioned above influencing the PSP amplitude were identified in simulation studies (e. g., Herrmann and Gerstner, 2002; Jones and Bawa, 1997; Matthews, 1999, 2002; Piotrkiewicz et al., 2009). However, these studies have looked at single motoneurons, and no conclusions can be drawn about how the reflex amplitude behaves across the motoneuron pool.

Therefore, this chapter aims to analyse how the reflex amplitude is distributed across a motoneuron pool and how it can be related to the EPSP size. We use a motoneuron pool model with 200 motoneurons as presented in Section 3.4 and simulate the monosynaptic stretch reflex, which is the most studied human muscle reflex (e. g., Yavuz et al., 2014). In the model, we investigate the influence of the following parameters on the reflex amplitude:

- EPSP size,
- size-related motoneuron properties,
- baseline discharge frequency
- and random membrane potential fluctuations, i. e., noise.

We compare the reflex amplitudes determined from the PSTH and the PSF to identify differences between the methods. The ultimate goal is to guide the development of reflex experiments that can provide distinct insights into neuromuscular physiology. This concerns, e. g., the number of stimuli or the force level to be used.

5.1 Simulation of reflex responses

We simulated excitatory reflex responses of a motoneuron pool. This section summarises the computational model, the simulation protocol and the numerical implementation.

5.1.1 Motoneuron pool model

A pool of 200 motoneurons was simulated. This number corresponds to a typical estimate of motor units in the human tibialis anterior muscle, which is often used for reflex experiments (Duchateau and Enoka, 2022).

Motoneurons were simulated using the model by Negro and Farina (2011), described in detail in Section 3.4. In short, each motoneuron is represented by a two-compartment (soma and dendrite) equivalent electric circuit model. The soma compartment contains three voltage-gated conductances (Na^+, slow and fast K^+) and a leakage conductance. The dendrite compartment contains a single leakage conductance. The parameters were exponentially distributed to obtain a motoneuron pool, as described in Section 3.4.2. Consequently, the pool contains many small, low-threshold and few large, high-threshold motoneurons.

5.1.2 Simulation protocol

The simulation mimics a reflex experiment eliciting the monosynaptic stretch reflex. Experimentally, the stretch reflex can be triggered by mechanically perturbing the muscle or by electrical stimulation of the afferent nerve (see Section 4.1). During sustained muscle contractions, the cumulative monosynaptic Ia afferent input mediates a short-latency reflex response of the motoneurons (Kandel et al., 2013).

Motoneurons receive multiple inputs from supraspinal and peripheral sources. The majority of the inputs is common to all motoneurons and mainly determines the force output (Negro et al., 2016b). Other synaptic inputs decorrelate the motoneurons (Maltenfort et al., 1998). Thus, the overall motoneuron input was composed of three parts: (i) a common drive that is similarly applied to all motoneurons, (ii) an independent drive individual to each motoneuron and (iii) the reflex stimulus that is again common to all motoneurons (Figure 5.1).

The common drive (i) was represented by a constant mean value mainly determining the discharge frequency and a zero-mean band-pass filtered Gaussian noise (15 Hz to 35 Hz, Conway et al., 1995; Halliday et al., 1998; Negro and Farina, 2011). The common drive mainly accounts for the constant force applied throughout the experiment. The independent input (ii) was modelled as zero-mean low-pass filtered Gaussian noise ($<$ 100 Hz, Negro and Farina, 2011). The filtering was performed with a first- and second-order Butterworth filter, respectively (Rao and Swamy, 2018). The standard deviation of the common noise was fixed to 20% of the mean drive, and the standard deviation of the independent input was scaled to account for 20% of the total noise (Negro et al., 2016b). This choice yielded values for the coefficient of variation (CoV) of the interspike interval (ISI) within the physiological range for all applied force levels (10% $<$ CoV ISI $<$ 30%, Matthews, 1996; Moritz et al., 2005). The coefficient of variation is defined as the ratio of the standard deviation to the mean.

The relation between the mean drive to a motoneuron pool and the total muscle force is generally unknown. We used the fraction of motoneurons from the pool, which shows sustained activity, as a force indicator. The force or contraction strength is commonly provided as a fraction of the maximum voluntary contraction (MVC). Following experimental data, we assume that 60 % of motoneurons are active at 20 % MVC and all motoneurons are recruited at 60 % MVC (largest motoneuron fires with 10 Hz, Moritz et al., 2005). As a result, all simulated motoneurons are active when applying a mean drive of 16.8 nA. By choosing the mean drives between 4 nA to 18 nA, we assume to cover a range from below 10 % MVC to not more than 70 % MVC.

The reflex stimulus (iii) represents the compound excitatory postsynaptic current (EPSC) resulting from the stimulation of Ia afferents. Monosynaptic stretch reflex EPSCs were reported to have relatively short rise times of approximately 1 ms (Hochman and McCrea, 1994; Lüscher et al., 1983). The reflex stimulus I_{stim} was modelled as

$$I_{\text{stim}} = I_0 * \frac{t}{1\,\text{ms}} * \exp\left(1 - \frac{t}{1\,\text{ms}}\right), \tag{5.1}$$

with a variable amplitude I_0, a fixed time constant of 1 ms and a duration of 40 ms. The stimulus amplitude I_0 varied from 4 nA to 10 nA. In each simulation, the stimulus was applied 200 times with normally distributed interstimulus intervals of 1000 ± 100 ms. All inputs were linearly summed and applied to the soma compartment of the motoneuron model, i. e., representing effective synaptic currents (Heckman and Binder, 1988, also see Section 3.5.1).

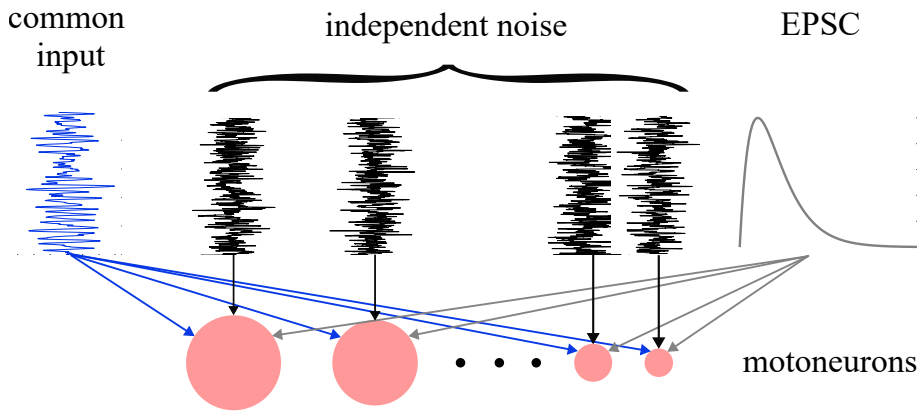

Figure 5.1: Schematic drawing of the inputs to the simulated motoneuron pool. Each motoneuron receives a common input and an excitatory postsynaptic current (EPSC), which are similar for all motoneurons. In addition, each motoneuron receives an individual independent noise input. Note that in the figure, the inputs are not scaled with respect to each other.

5.1.3 Numerical implementation

All simulations were performed with MATLAB R2021a (9.10.0.1602886). The motoneuron model is represented by a system of six ordinary differential equations, which was solved with MATLAB's ode23 (single-step, explicit Runge-Kutta solver, Shampine and Reichelt, 1997), an integration interval size of 0.1 ms and an absolute and relative error tolerance of 1×10^{-5}.

The simulation was parallelised to shorten the computation time. Therefore, the total number of stimulus cycles was divided by the number of cores and split accordingly. This splitting was possible since we assumed that the stimulus cycles are independent. The mean interstimulus interval of 1000 ms is long enough for the motoneurons to return to a steady state and no longer be influenced by the preceding stimulus. While the initial state of the motoneuron pool was similar on all cores, the perturbation times and the common and independent drive were differently initialised on each core. Usually, the simulation was run on five cores (40 stimuli per core), except for the simulation with 1000 stimuli, which was run on ten cores (100 stimuli per core).

5.2 Data analysis

The firing times of the simulated motoneurons were analysed using peristimulus analysis. More specifically, the PSTH and the PSF were calculated. In the PSTH, motoneuron discharges are counted within time bins and shown relative to the stimulus time. In the PSF, the instantaneous frequencies of the discharges are displayed with respect to the stimulus time. Further, cumulative sums (CUSUMs) of the PSTH and the PSF were calculated. Thereby, the differences between the values and the prestimulus mean value are cumulatively summed to visualise small but persistent trends in the data. In general, pre- and poststimulus times of 300 ms were considered and the time bin size was 1 ms. For further details on the methods, see Section 4.2.

We did not consider motoneurons with non-stationary firing patterns for the analysis. Following experimental studies, we assumed that motoneurons with a frequency of less than 7 Hz or a coefficient of variation of the baseline interspike interval greater than 35% fire too irregular and thus we excluded them from further analysis (e. g., Yavuz et al., 2018).

The reflex amplitudes were determined from the PSTH- and the PSF-CUSUM. Therefore, the automatic algorithm presented in Section 4.3 was used. In short, a significant reflex response is defined as a deflection in CUSUM that exceeds the largest prestimulus deflection. This definition also corresponds to the criterion most often used in experimental studies (e. g., Yavuz et al., 2014). The onset of the reflex response was determined by the time at which the steepness of the increase in CUSUM exceeds the steepest prestimulus slope. Similarly, the end of the reflex response was determined by the time at which the slope of the CUSUM returns to values below the steepest prestimulus slope. The reflex amplitude was calculated from the difference of the CUSUM values at reflex onset and end.

Reflex responses were only considered when the reflex onset occurred within a time window of $[-5\,\text{ms}, 15\,\text{ms}]$ around the stimulus time to reduce the number of erroneously assigned reflexes. Since the simulation did not consider conduction delays, earlier events were assumed to be unrelated to the stimulus, and later events were assumed to no longer reflect short-latency response. In addition, a manual check was performed. Thereby, reflex responses that mark later latency responses according to visual inspection were manually removed (see Section 4.3).

5.3 Results

First, we tested the predictive power of the simulation by comparing the reflex responses of the simulated motoneuron pool to recorded motor units. Then, the distribution of reflex amplitudes across the simulated motoneuron pool was analysed for PSTH and PSF. Further, we analysed and compared the influence of stimulus size, baseline discharge frequency, noise inputs and the number of applied stimuli on reflex amplitudes determined from PSTH- and PSF-CUSUM.

5.3.1 Comparison of simulated and experimental reflex responses

The PSTH and PSF for the simulated pool of 200 motoneurons were compared to experimentally recorded motor units from Yavuz et al. (2014) to test the validity of the computational model. In the experiment, a tap-like mechanical stimulus was used to elicit the stretch reflex, which is assumed to evoke a stimulus similar to what was applied in the simulation.

The PSTH and PSF for the simulated pool of 200 motoneurons and an exemplary recorded motor unit are shown in Figure 5.2. During the prestimulus time (time < 0 ms), both the simulated motoneurons as well as the recorded motor unit show a baseline activity that oscillates around a constant mean value. The mean baseline discharge frequency of the recorded motor units is 9.3 Hz, and the baseline discharge frequency of the simulated motoneurons ranges from 7.2 Hz to 16.5 Hz. In the simulated motoneurons, a peak in the PSTH as well as in the PSF can be observed at stimulus application time (time $=$ 0 ms). The delay of the peak in the experimental data is consistent with the conduction velocity of the nerves. The simulated motoneurons reach maximum frequencies of up to 29.9 Hz in the PSF. These values are comparable to the recorded motor unit, which shows a maximum frequency of 27 Hz. The peak sizes in the PSTH cannot be directly compared since they depend on the number of delivered stimuli, which differs between experiment and simulation.

The time courses of the PSTH- and PSF-CUSUM are well comparable between simulated and experimental data (Figure 5.3). Oscillations around zero in the prestimulus time indicate constant baseline activity. A steep increase after the application of the stimulus indicates increased discharge activity. In the PSTH-CUSUM, the peak is immediately followed by a decrease due to missing events during the silent period. The following up and down reflects motoneuron synchronisation. In the PSF-CUSUM, the values stay approximately constant after the peak, indicating discharge frequencies similar to the baseline activity. Note that experimentally recorded motor units often show a second peak, which marks the long-latency response (Kandel et al., 2013). As we did not model the respective pathways, we chose a motor unit for comparison that does not show the long-latency response.

Simulation and experimental CUSUM values can be quantitatively compared since the CUSUM is normalised to the number of stimuli. In the simulated motoneurons, the reflex amplitudes range from 0.22 counts/No. of Stim to 0.49 counts/No. of Stim in the PSTH-CUSUM and from 0.75 Hz/No. of Stim to 1.41 Hz/No. of Stim in the PSF-CUSUM, respectively. The exemplarily selected recorded motor unit shows a reflex amp-

litude of 0.4 counts/No. of Stim in the PSTH-CUSUM (mean for all recorded motor units: 0.241 ± 0.091 counts/No. of Stim) and 1.36 Hz/No. of Stim in the PSF-CUSUM (mean for all recorded motor units: 0.593 ± 0.555 counts/No. of Stim), respectively. In summary, the peak sizes in the PSTH-CUSUM and PSF-CUSUM are comparable for simulated and recorded motoneurons.

5.3.2 Distribution of reflex amplitudes in motoneuron pools

The distribution of reflex amplitudes across the pool of motoneurons was evaluated for two different drives (6 nA and 16 nA) and four stimulus sizes (4 nA, 6 nA, 8 nA and 10 nA). The drives resulted in baseline frequencies of approximately 7 Hz to 17 Hz for the low drive and 7 Hz to 40 Hz for the high drive. For the low drive, 148 motoneurons and for the high drive, 199 motoneurons were included in the analysis.

A higher stimulus size generally caused higher reflex amplitudes for all motoneurons (Figure 5.4). However, stimulus amplitudes that differ by only 2 nA produced overlapping reflex amplitudes. A heterogeneous picture emerges when looking at the distribution of reflex amplitudes across the motoneuron pool. In the low drive condition, the PSTH reflex amplitudes decrease slightly with increasing motoneuron discharge frequency. In contrast, the PSF reflex amplitudes are almost constant across the pool (Figure 5.4a, c). In the high drive condition, the PSTH reflex amplitudes are relatively constant for discharge frequencies below 30 Hz, increase for frequencies above 30 Hz and decrease again for the highest discharge frequencies (Figure 5.4b). The PSF reflex amplitudes monotonically increase with increasing discharge frequency (Figure 5.4d).

It is further noticeable that the algorithm detected more significant reflex responses in the PSTH. Especially for the high drive and low stimulus condition, considerably fewer motoneurons showed a significant reflex response in the PSF. The number of motoneurons with significant reflex amplitudes in the PSTH and PSF is analysed in more detail in Section 5.3.3.

5.3.3 Influence of the force level on reflex amplitudes

To investigate the relation between motoneuron reflex amplitude and applied drive in more detail, we tracked motoneurons across eight drive levels (mean drive 4 nA to 18 nA) for two stimulus sizes (amplitude 6 nA and 10 nA).

The current-frequency relations of the 200 simulated motoneurons are shown in Figure 5.5a. All motoneurons show increasing firing rates for increasing drives. With increasing drive, more motoneurons are successively and orderly recruited according to the size principle (Henneman et al., 1965a,b). The smallest motoneuron (MN 1) increases its mean baseline frequency from 10.2 Hz at 4 nA mean drive to 44.1 Hz at 18 nA mean drive. The largest motoneuron of the pool (MN 200) is recruited with 8.3 Hz at a mean drive level of 16 nA and discharges with 12.2 Hz at 18 nA drive. Thereby, the slope of the current-frequency relation is not constant, but the initial increase is steeper than the later part.

For all drives and both stimulus amplitudes, the number of motoneurons with significant reflex amplitudes in the PSTH was larger than or similar to those in the PSF (Table 5.1). A high drive and a low stimulus lead to the smallest number of motoneurons

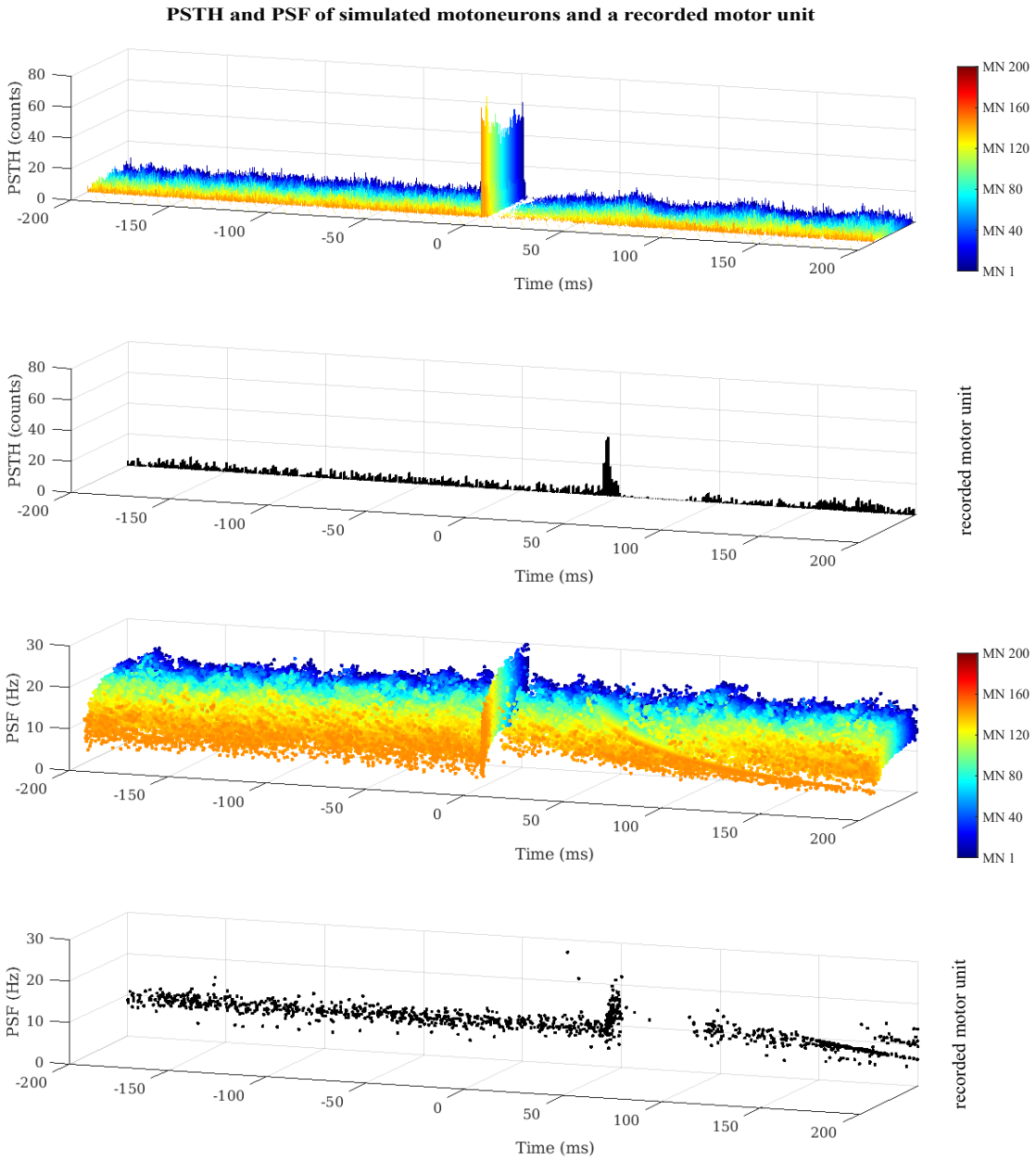

Figure 5.2: Peristimulus timehistogram (PSTH) and peristimulus frequencygram (PSF) for simulated motoneurons and an exemplary recorded motor unit in response to short excitatory stimuli (Yavuz et al., 2014). a) PSTH for a pool of 200 simulated motoneurons. The colour indicates the motoneuron (MN) index, whereby MN 1 corresponds to the smallest and MN 200 to the largest motoneuron of the pool. b) PSTH for a recorded motor unit. c) PSF for a pool of 200 simulated motoneurons. Colour coding as in (a). d) PSF for a recorded motor unit. In the simulation, 200 stimuli were delivered, and 321 stimuli were delivered in the experiment.

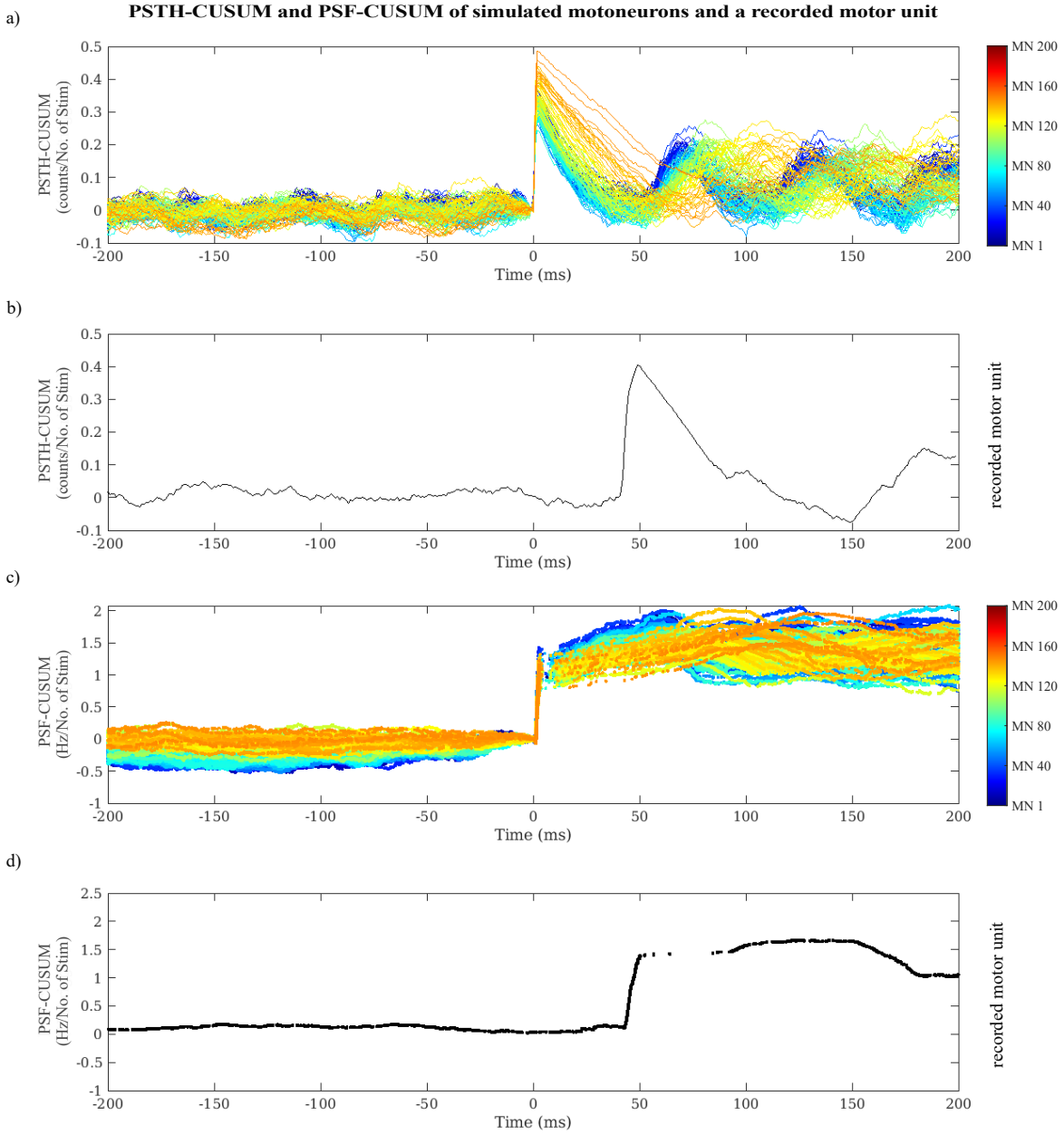

Figure 5.3: Cumulative sum (CUSUM) of peristimulus timehistogram (PSTH) and peristimulus frequencygram (PSF) for the simulated motoneurons and an exemplary recorded motor unit as shown in Figure 5.2. a) PSTH-CUSUM for a pool of 200 simulated motoneurons. The colour indicates the motoneuron (MN) index, whereby MN 1 corresponds to the smallest and MN 200 to the largest motoneuron of the pool. b) PSTH-CUSUM for a recorded motor unit. c) PSF-CUSUM for a pool of 200 simulated motoneurons. Colour coding as in (a). d) PSF-CUSUM for a recorded motor unit.

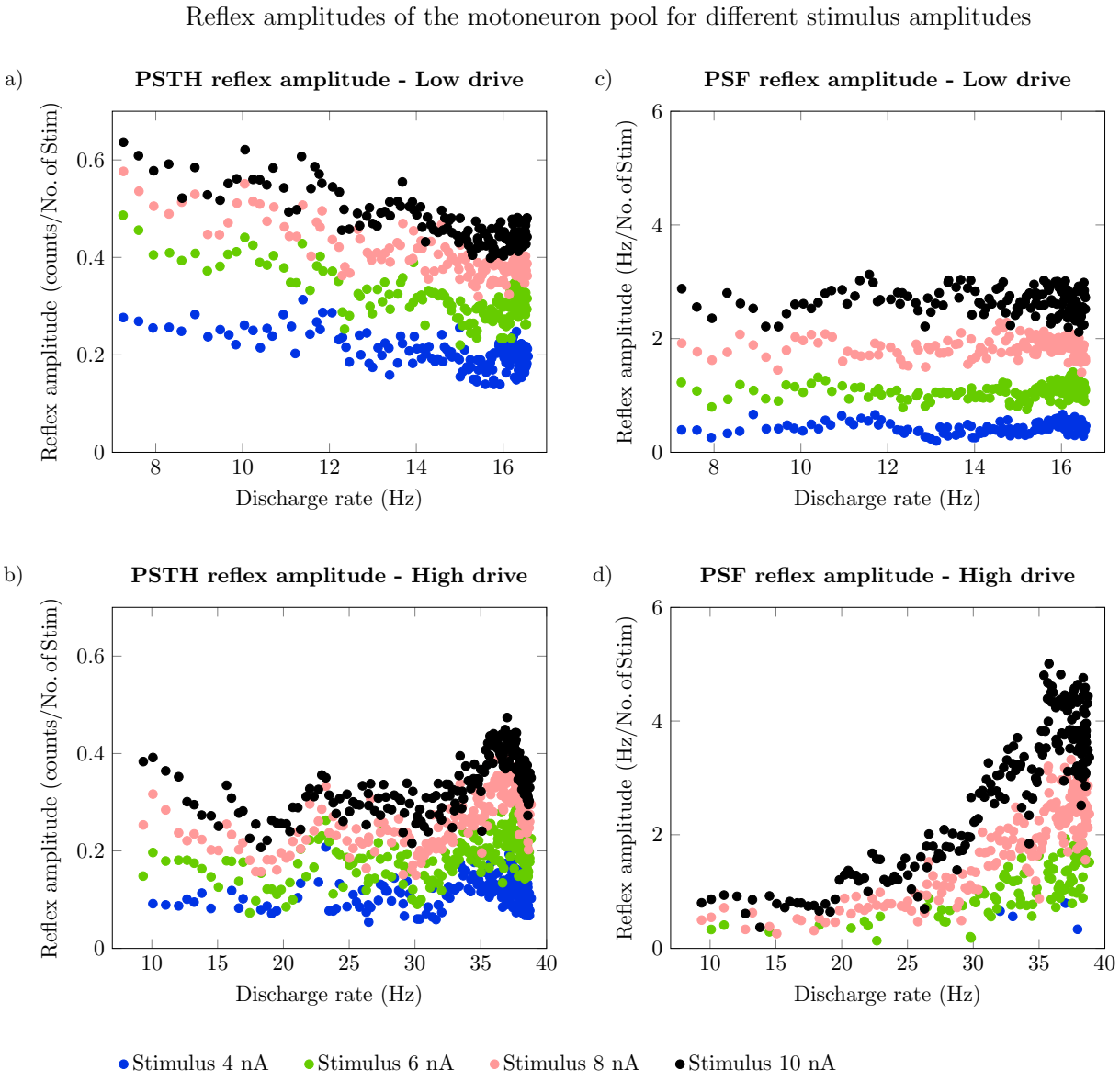

Figure 5.4: Reflex amplitudes of the motoneuron pool for different stimulus amplitudes. Reflex amplitudes were determined from the cumulative sum (CUSUM) of the peristimulus timehistogram (PSTH) and the peristimulus frequencygram (PSF) for a pool of 200 simulated motoneurons. Two drive levels (low 6 nA and high 16 nA) and four stimulus amplitudes (4 nA, 6 nA, 8 nA and 10 nA) were applied. In all simulations, 200 stimuli were delivered. a), b) Reflex amplitude determined from PSTH-CUSUM. c), d) reflex amplitude determined from PSF-CUSUM.

Table 5.1: Number of active motoneurons (MNs) and number of MNs with a significant reflex amplitude for two stimulus amplitudes. Reflex amplitudes were determined from the cumulative sum of the peristimulus timehistogram (PSTH) and the peristimulus frequencygram (PSF) and shown for PSTH/PSF. Simulation settings: two stimulus amplitudes (stim, 6 nA and 10 nA).

Drive (nA)	4	6	8	10	12	14	16	18
Active MNs	89	148	169	181	188	193	199	200
6 nA stim	89/89	148/148	168/168	179/174	188/151	193/146	199/91	197/40
10 nA stim	89/89	148/148	168/168	179/179	188/188	193/193	199/199	200/197

with significant reflex responses in the PSF.

As shown before, a higher stimulus leads to higher reflex amplitudes (Figure 5.5). The reflex amplitudes determined from the PSTH-CUSUM range from 0.07 counts/No. of Stim to 0.57 counts/No. of Stim for the smaller stimulus amplitude of 6 nA and range from 0.17 counts/No. of Stim to 0.7 counts/No. of Stim for the larger stimulus amplitude of 10 nA. Similarly, the reflex amplitudes determined from the PSF-CUSUM are with 0.11 Hz/No. of Stim to 2.02 Hz/No. of Stim smaller for the 6 nA stimulus than for the larger stimulus (0.35 Hz/No. of Stim to 6.68 Hz/No. of Stim).

The relation of reflex amplitude and drive differs between PSTH and PSF. In the PSTH, reflex amplitudes generally decrease with increasing drive and start to plateau for drives higher than 12 nA (Figure 5.5b, c). While the totality of values shows a clear trend for the pool of motoneurons, individual motoneurons (dots connected by lines) generally do not show monotonic behaviour.

The PSF reflex amplitudes of small motoneurons first decrease and then increase with increasing drive (Figure 5.5d, e). In contrast, the reflex amplitudes of larger motoneurons only decrease with increasing drive. The pool of motoneurons shows relatively similar reflex amplitudes for low drives, but the range of values increases with increasing drive. This behaviour is more pronounced for the higher stimulus amplitude. As observed for the reflex amplitudes in the PSTH, in the PSF, single motoneurons also do not show consistent trends across drive levels.

In Figure 5.6, the reflex amplitudes determined from the PSTH- and PSF-CUSUM were normalised by the baseline discharge frequency of the respective motoneuron. This normalisation yields qualitatively similar courses of the reflex amplitudes for both PSTH and PSF. That is, the normalised reflex amplitudes saturate for higher drives. Further, the range of values per drive level becomes narrower, especially for the PSF. Nevertheless, for the higher stimulus, the value range of reflex amplitudes determined from the PSF-CUSUM becomes wider again for higher drives (Figure 5.6d, mean drive 16 nA and 18 nA).

It is noticeable that the reflex amplitudes of motoneurons just after recruitment are consistently higher than those of the rest of the pool. Further, the distribution of reflex amplitudes across the pool of motoneurons is inconsistent across drive levels. For example, for the high stimulus and mean drives of 14 nA and 18 nA, the smaller motoneurons (blue) show the highest PSF reflex amplitudes (Figure 5.6d). In contrast, for the 16 nA drive, the motoneurons in green colour show the largest PSF reflex amplitudes. Similar heterogeneities can be found for the PSTH.

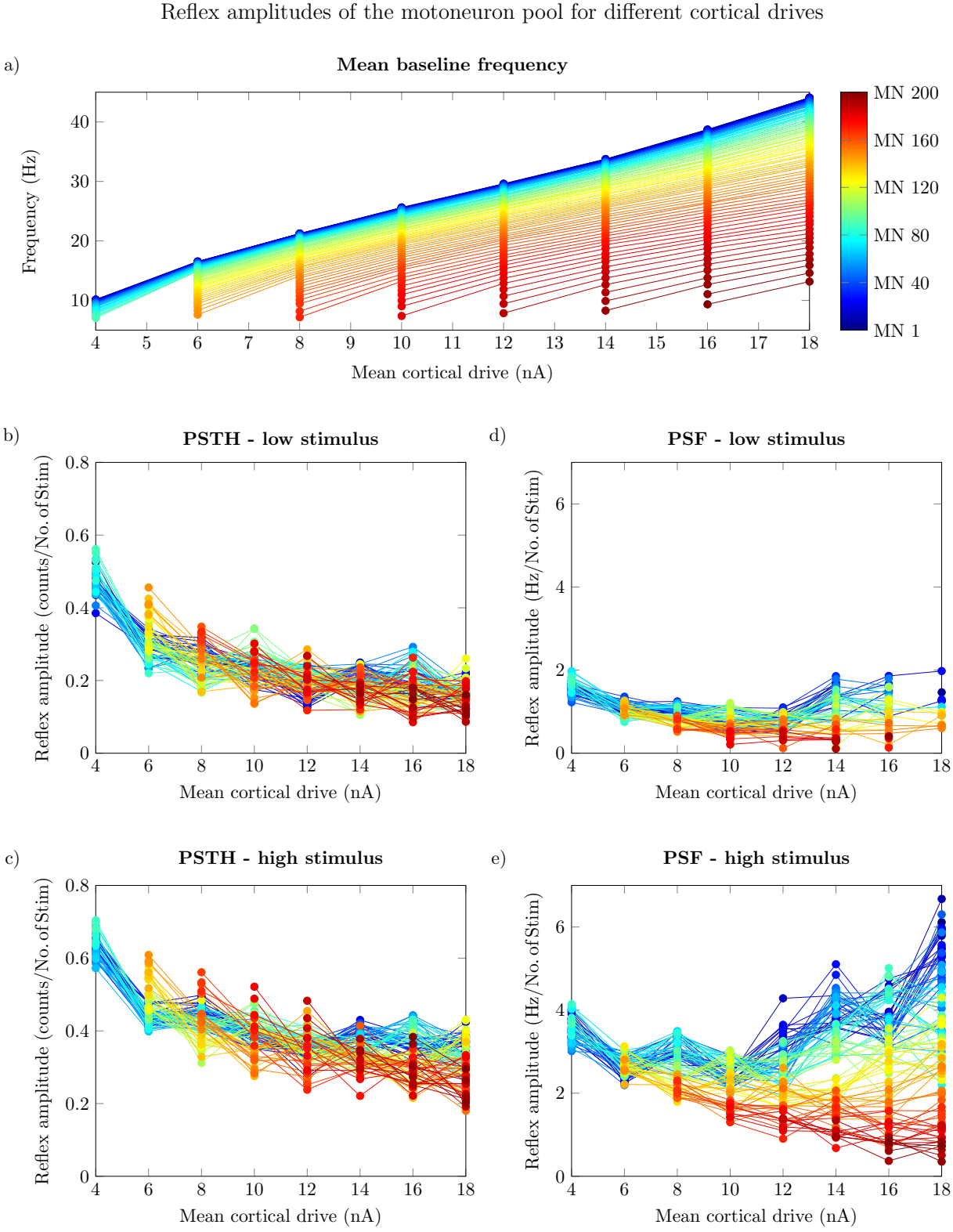

Figure 5.5: Reflex amplitudes of the motoneuron pool for different cortical drives and two sizes of stimulus amplitudes. a) Current-frequency relations for the pool of simulated motoneurons. b), c) Reflex amplitudes from peristimulus timehistogram (PSTH) for stimulus amplitudes of 6 nA and 10 nA. d), e) Reflex amplitudes from peristimulus frequencygram (PSF) for stimulus amplitudes of 6 nA and 10 nA. The colour indicates the motoneuron (MN) index, whereby MN 1 corresponds to the smallest and MN 200 to the largest motoneuron of the pool (every second MN is shown). In all simulations, 200 stimuli were delivered.

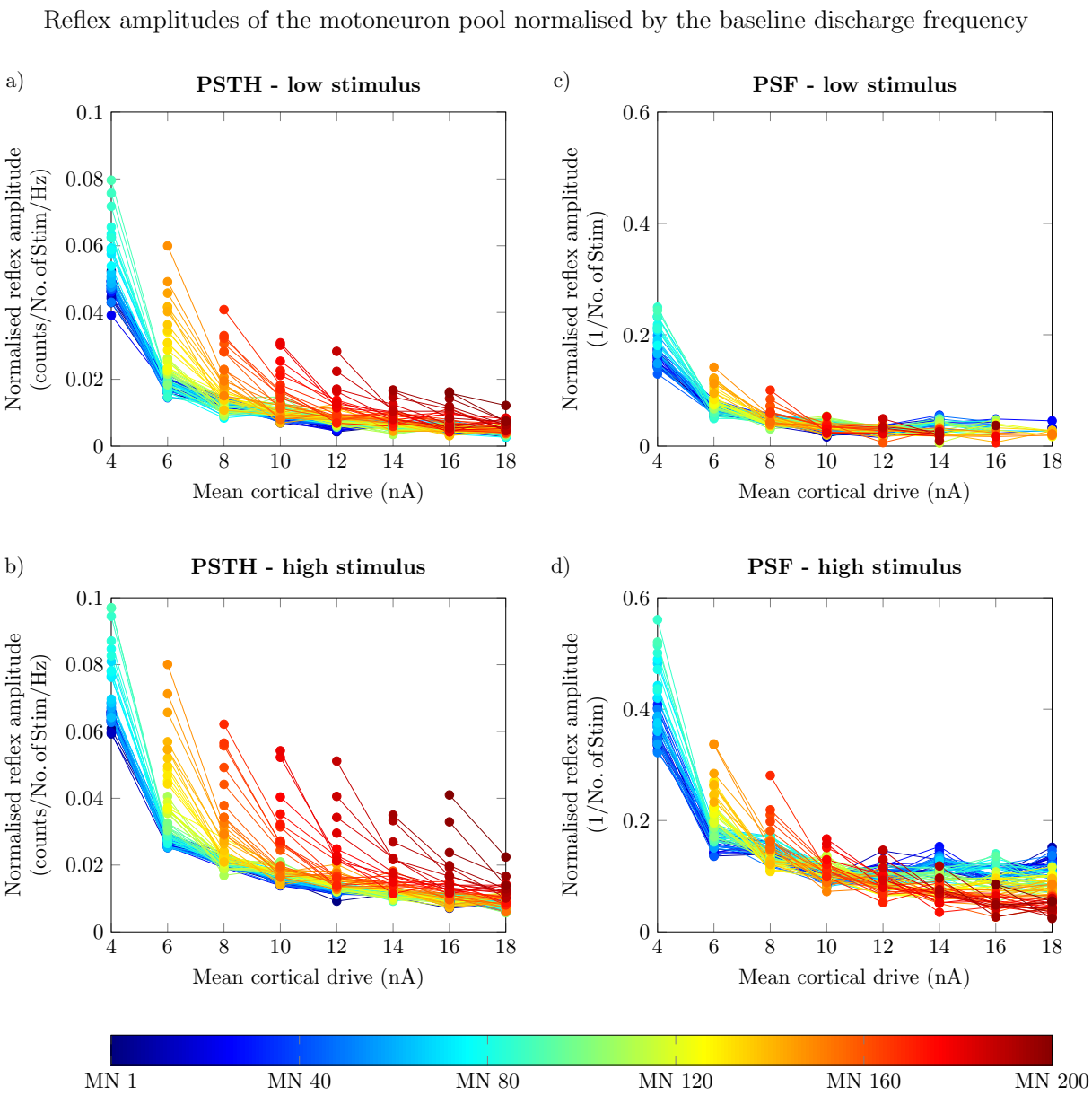

Figure 5.6: Reflex amplitudes of the motoneuron pool from Figure 5.5 normalised by the mean baseline discharge frequency. a), b) Normalised reflex amplitudes from peristimulus timehistogram (PSTH) for stimulus amplitudes of 6 nA and 10 nA. c), d) Normalised reflex amplitudes from peristimulus frequencygram (PSF) for stimulus amplitudes of 6 nA and 10 nA. The colour indicates the motoneuron (MN) index, whereby MN 1 corresponds to the smallest and MN 200 to the largest motoneuron of the pool (every second MN is shown).

Table 5.2: Number of active motoneurons (MNs) and number of MNs with a significant reflex amplitude in simulations without noise input. Reflex amplitudes determined from the cumulative sum of peristimulus timehistogram (PSTH) and peristimulus frequencygram (PSF) and shown for PSTH/PSF. Simulation settings: two stimulus amplitudes (stim, 6 nA and 10 nA), no noise inputs.

Drive (nA)	4	6	8	10	12	14	16	18
Active MNs	51	137	160	173	181	188	193	197
6 nA stim	51/51	137/137	160/160	173/173	181/181	188/188	193/193	197/197
10 nA stim	51/51	137/137	160/160	173/173	181/181	188/188	193/193	197/197

5.3.4 Influence of random membrane potential fluctuations on reflex amplitudes

In the physiological motoneuron, the membrane potential undergoes random fluctuations, which we consider by adding noise components to the input signal in the simulation. Here, we omit these noise components to estimate their effects on the reflex amplitude compared to the previous simulations. Figure 5.7 shows the reflex amplitudes for eight drive levels, no noise inputs and two stimulus amplitudes (6 nA and 10 nA). Except for removing the noise input, the conditions are similar to those in Figure 5.5.

Without the noise input, the baseline frequencies of the motoneuron pool are lower than with noise input (Figure 5.7a). The range of frequencies shown by the smallest motoneuron (MN 1) is 8.5 Hz to 42.8 Hz, and the largest recruited motoneuron is MN 197 of 200. The reflex amplitudes are overall higher than in the simulations with noise input. For the low stimulus amplitude, reflex amplitudes range from 0.12 counts/No. of Stim to 0.63 counts/No. of Stim for the PSTH and from 0.61 Hz/No. of Stim to 3.4 Hz/No. of Stim for the PSF, respectively. For the high stimulus amplitude, the reflex amplitudes range from 0.21 counts/No. of Stim to 0.74 counts/No. of Stim for the PSTH, and they range from 1.47 Hz/No. of Stim to 7.12 Hz/No. of Stim for the PSF. The trends as observed with noise, i. e., saturating reflex amplitudes for high drive levels in the PSTH and diverging reflex amplitudes for high drive levels in the PSF, are confirmed in the simulations without noise (Figure 5.7b-e).

When omitting the noise, less motoneurons are active and consequently, less motoneurons show a significant reflex amplitude (Table 5.2). In Table 5.2, it is noticeable that there are no differences between PSTH and PSF with respect to the number of motoneurons with a significant reflex amplitude.

5.3.5 Influence of the number of stimuli on reflex amplitudes

This section investigates the influence of the number of applied stimuli on the reflex amplitudes. We used a low and a high drive (6 nA and 16 nA), a stimulus amplitude of 6 nA and considered a minimum of 25 and up to 1000 stimuli for the evaluation.

In Figure 5.8, it can be observed that the variability of reflex amplitudes within the pool becomes smaller when more stimuli are considered. In the low drive condition, the

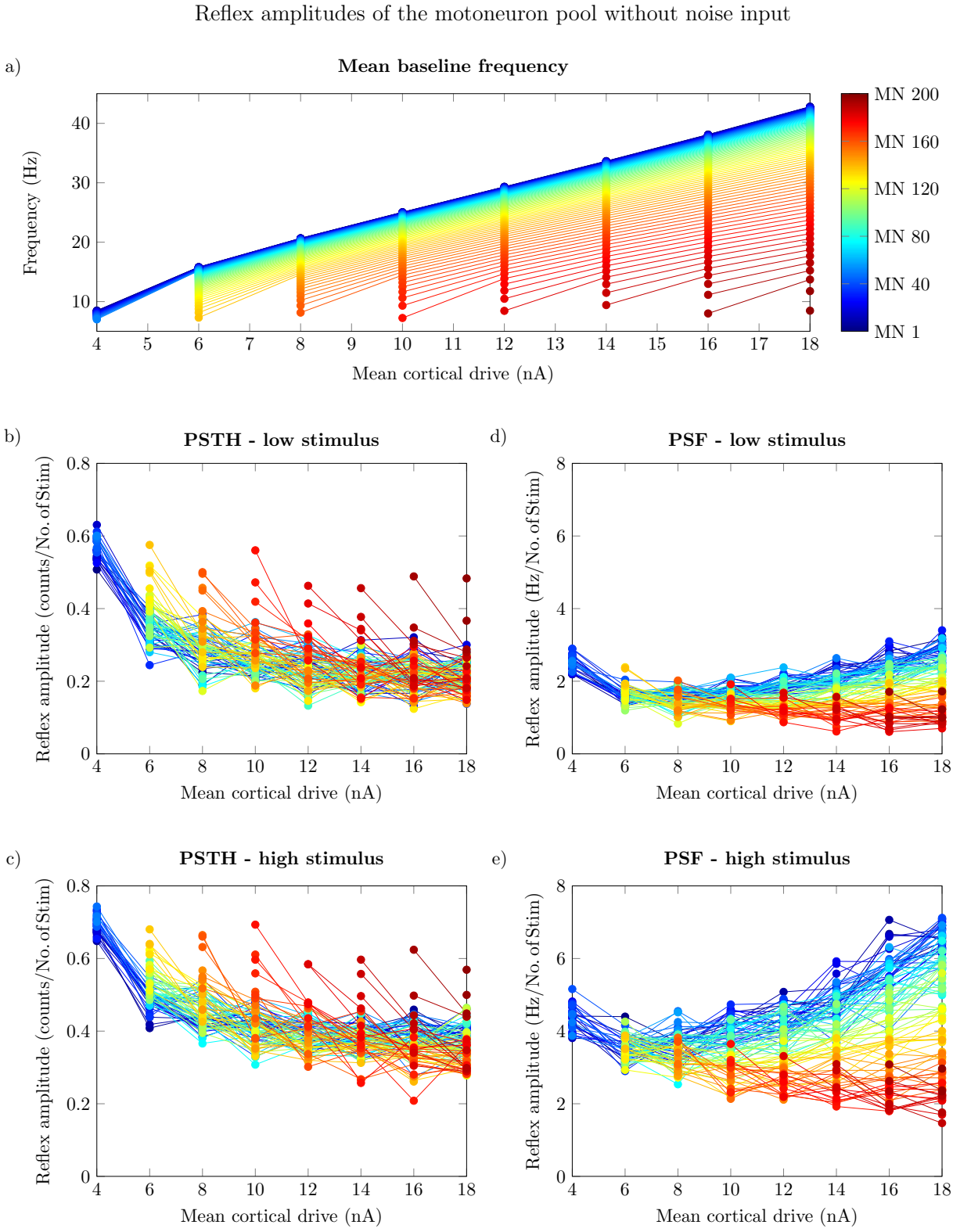

Figure 5.7: Reflex amplitudes of the motoneuron pool without noise input. a) Current frequency relations for the pool of simulated motoneurons. b), c) Reflex amplitudes from peristimulus timehistogram (PSTH) for stimulus amplitudes of 6 nA and 10 nA. d), e) Reflex amplitudes from peristimulus frequencygram (PSF) for stimulus amplitudes of 6 nA and 10 nA. The colour indicates the motoneuron (MN) index, whereby MN 1 corresponds to the smallest and MN 200 to the largest motoneuron of the pool (every second MN is shown). In all simulations, 200 stimuli were delivered. The noise components of the MN drive were removed.

Table 5.3: Mean reflex amplitude for the largest motoneurons of the pool and different numbers of stimuli (No. of Stim). Mean and standard deviation of the reflex amplitude of the motoneurons firing with 14 Hz to 17 Hz in the low drive condition and with 35 Hz to 39 Hz in the high drive condition, respectively. Simulation settings: Low and high drive (6 nA and 16 nA); stimulus amplitude 6 nA; 100, 200 and 1000 stimuli considered.

No. of Stim		100	200	1000
Low drive	PSTH reflex amplitude (counts/No. of Stim)	0.289 ± 0.039	0.289 ± 0.032	0.323 ± 0.014
	PSF reflex amplitude (Hz/No. of Stim)	1.062 ± 0.156	1.040 ± 0.125	1.221 ± 0.070
High drive	PSTH reflex amplitude (counts/No. of Stim)	0.235 ± 0.053	0.225 ± 0.040	0.224 ± 0.019
	PSF reflex amplitude (Hz/No. of Stim)	1.679 ± 0.321	1.860 ± 0.442	2.009 ± 0.190

reflex amplitudes are higher when more stimuli are applied. In Table 5.3, the mean reflex amplitudes for the motoneurons with a mean baseline frequency of 14 Hz to 17 Hz in the low drive and of 35 Hz to 39 Hz in the high drive condition are shown. For 1000 stimuli, the mean reflex amplitudes are highest and the standard deviations lowest for both drives and both metrics. Only the mean reflex amplitude determined from the PSTH with the high drive is relatively constant for all numbers of stimuli.

It is noticeable that there are differences in the number of motoneurons taken into account. For the lower drive, the number of applied stimuli only influences the number of motoneurons with a significant reflex amplitude when considering less than 50 stimuli (Table 5.4). For the higher drive, the number of motoneurons that show a significant reflex increases with the number of applied stimuli. For the PSTH, the maximum number is reached for 200 stimuli, and for PSF, it is reached for 600 stimuli. Interestingly, for 900 and 1000 applied stimuli, the number of motoneurons with a significant reflex amplitude in PSF reduces by one.

To investigate the reasons for this behaviour, the error boxes of the CUSUM, which are used as the threshold for a significant reflex, are shown in Figure 5.9. For both the PSTH- and the PSF-CUSUM, the error box size decreases when a higher number of stimuli is applied. Thereby, the difference between 100 and 200 applied stimuli is approximately as high as the difference between 200 and 1000 applied stimuli. The error box size plateaus for approximately 400 stimuli and more.

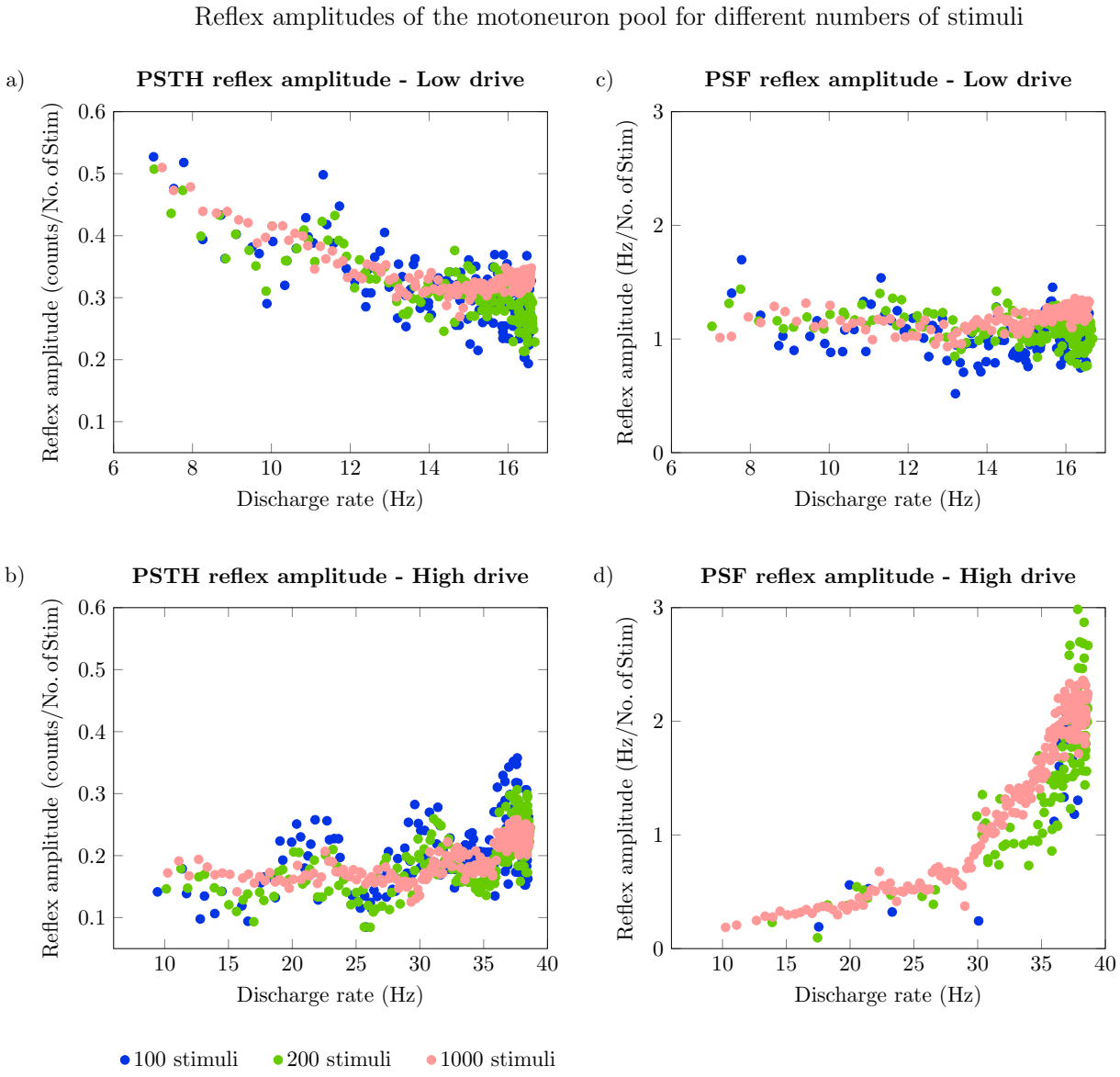

Figure 5.8: Reflex amplitudes of the motoneuron pool for different numbers of stimuli. Reflex amplitude determined from peristimulus timehistogram (PSTH, a, b) and peristimulus frequencygram (PSF, c, d) and for two drives (low 6 nA and high 16 nA) and different numbers of stimuli. Stimulus amplitude of 6 nA was constant.

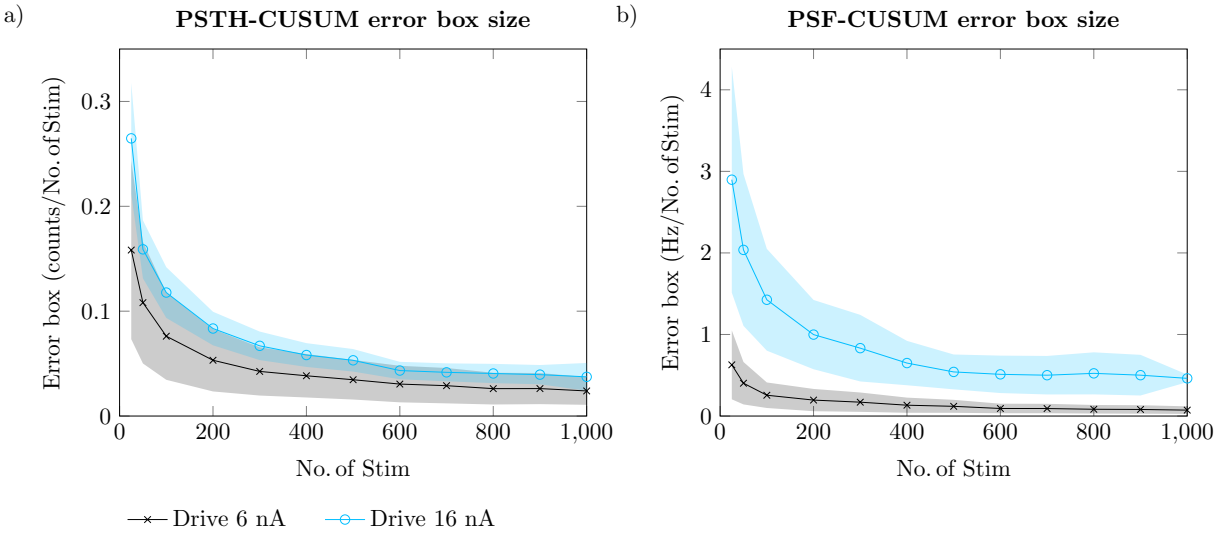

Figure 5.9: Error box size in CUSUM for different numbers of stimuli. Size of error box determined from PSTH-CUSUM (a) and PSF-CUSUM (b) for two drives (low 6 nA in black and high 16 nA in blue) and different number of stimuli. Shown are the mean (lines) and standard deviation (shaded areas) of the error boxes. Stimulus amplitude of 6 nA was constant. Error box size corresponds to the mean value over the motoneuron pool.

Table 5.4: Number of motoneurons (MNs) with a significant reflex amplitude for different numbers of stimuli (No. of Stim). Values are given for PSTH/PSF. Simulation settings: Low and high drive (6 nA and 16 nA), stimulus amplitude 6 nA, 25 to 1000 stimuli considered. In the low drive, 147 to 148 MNs and in the high drive, 198 to 199 MNs were included in the analysis (the number of active MNs differs due to small differences in the mean baseline frequency and coefficient of variation of the interspike interval due to inclusion of different numbers of data points).

No. of Stim	25	50	100	200	300	400
Low drive	124/49	147/140	148/147	148/148	147/147	147/147
High drive	120/1	174/8	194/20	198/114	198/158	198/176
No. of Stim	**500**	**600**	**700**	**800**	**900**	**1000**
Low drive	148/148	148/148	148/148	148/148	148/148	148/148
High drive	198/185	198/198	198/198	198/198	198/197	198/197

5.4 Discussion

In this work, for the first time, the reflex amplitudes determined from the PSTH- and PSF-CUSUM were analysed for different conditions and an entire pool of simulated motoneurons. This approach enables a detailed analysis of the factors influencing the reflex amplitude and provides valuable insights for collecting and interpreting experimental data.

Many factors that were previously shown to influence the relation between postsynaptic potential size and reflex amplitude were considered in the simulations. We employed different levels of baseline discharge frequency, noise and stimulus amplitude. We further used a motoneuron model whose channel dynamics reproduce physiological shapes of the AHP, which also influences the reflex response (Powers and Türker, 2010b; Zengel et al., 1985).

By comparing the peristimulus graphs (PSTH, PSF and CUSUM) of the simulated motoneurons to experimental recordings of monosynaptic short-latency reflexes, we showed the capability of the simulation to predict excitatory reflex responses. The qualitative time course of the reflex response, i. e., constant baseline activity followed by a peak, a silent period and the return to baseline activity, matches between simulation and experiment. In addition, both the baseline frequencies and reflex amplitudes are comparable between the simulated and recorded data. It should be noted that the validation applies only to short latency responses, i. e., the first reflex response following the stimulus. This study does not make any statement about later reflex responses.

5.4.1 Reflex amplitudes differ between PSTH and PSF

We compared the distribution of reflex amplitudes determined from two metrics (PSTH and PSF) across the entire pool of motoneurons and under different conditions. We identified a non-linear multi-variable influence of the motoneuron size and the applied conditions on the reflex amplitude. The non-linear integration process of motoneurons needs to be considered to explain this finding. Figure 5.10 shows the membrane potential trajectory when applying a stimulus with a variable delay relative to the previous discharge. The probability that a motoneuron will fire an action potential in response to a specific stimulus depends on the current value of the membrane potential at stimulus time. When the stimulus is delivered at the beginning of the interspike interval (Figure 5.10, pink) and if it is not sufficient to bring the motoneuron to the threshold, its effect will decay, and the interspike interval duration will not be affected by the stimulus. In contrast, when the stimulus is delivered at a time point where it brings the motoneuron to the threshold, it will immediately cause an action potential (Figure 5.10, blue) and shorten the current interspike interval compared to an undisturbed interval (Figure 5.10, black). Stimuli delivered between those extremes will shorten the interspike interval by a small amount (Figure 5.10, green). This behaviour was also explained and visualised by e. g., Türker and Powers (1999) and Powers and Türker (2010a).

In conclusion, the responsiveness of a motoneuron to a stimulus, and thus the reflex amplitude, depends on the fraction of the interspike interval during which the stimulus brings the motoneuron to the threshold. This time span depends on motoneuron-specific properties like the AHP shape and the spike threshold (Jones and Bawa, 1995; Powers and Türker, 2010a; Zengel et al., 1985) but also on the applied conditions, i. e., baseline

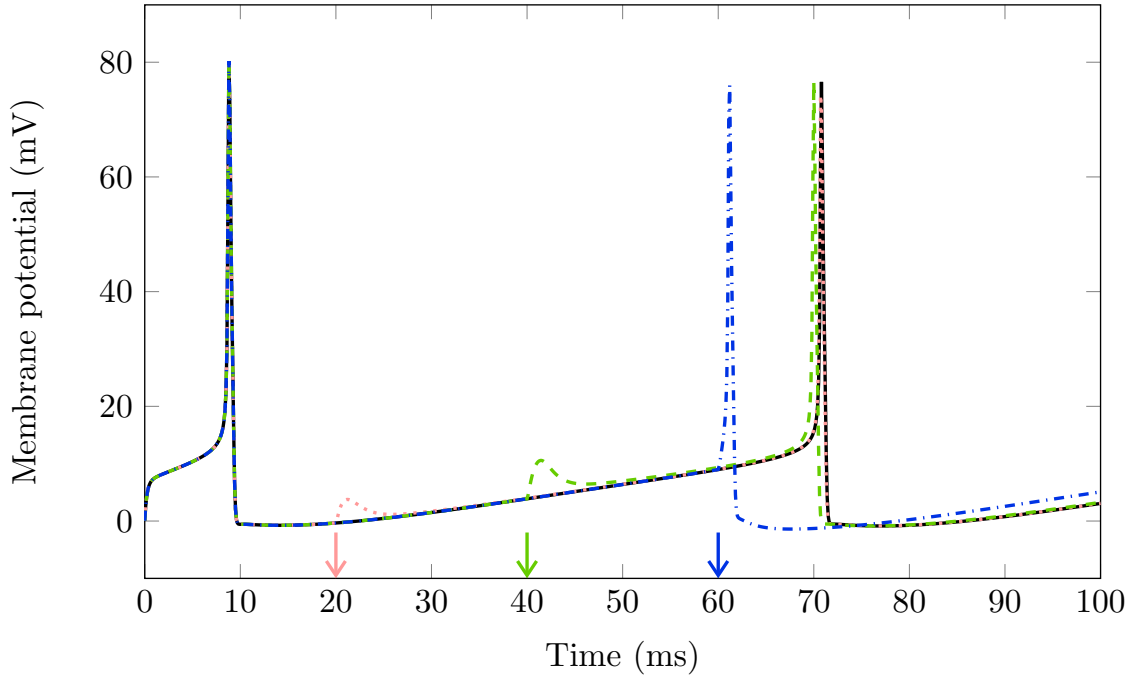

Figure 5.10: Membrane potential trajectories of one interspike interval with different stimulus times. The stimulus was applied at the time indicated by coloured arrows. The excitatory postsynaptic potential increases with membrane potential as the stimulus current amplitude was held constant. An undisturbed interspike interval is shown in black.

frequency determined by the mean drive, random fluctuations of the membrane potential determined by noise inputs and the size of the stimulus itself (Herrmann and Gerstner, 2002; Jones and Bawa, 1997; Matthews, 1999; Piotrkiewicz et al., 2009).

Whenever a stimulus is applied during the "excitable" fraction of the interspike interval, the action potential count in the PSTH is increased by one. Thereby, it does not matter how much the stimulus shortened the interspike interval. In contrast, the frequency values in the PSF are directly related to the shortening of the interspike interval in milliseconds. Thus, they depend on the random timing of the stimulus with respect to the last action potential. When the interspike interval is only slightly shortened, as expected in conditions with a large drive and small stimulus amplitudes, the reflex response is more difficult to detect in the PSF. Consequently, fewer motoneurons show a significant reflex amplitude under these conditions in the PSF than in the PSTH. This also explains why the variability among motoneurons of the pool is much higher in the PSF and increases with increasing baseline frequency.

Considering all performed simulations, more motoneurons showed a significant reflex response in the PSTH than in the PSF. This difference no longer existed when the noise was removed from the motoneuron drive. We conclude that the PSF is more sensitive to noise than the PSTH.

5.4.2 Characteristics of reflex amplitudes determined from the PSTH-CUSUM

In the simulated motoneuron pool, the reflex amplitudes determined from the PSTH-CUSUM increased with increasing stimulus amplitude. For a constant stimulus size, the reflex amplitudes of the motoneuron pool decreased with increasing drive and finally plateaued. In general, motoneurons operating closely above their recruitment threshold have the highest probability of responding to a stimulus. The higher the drive, the more motoneurons operate far above their recruitment threshold. Further, increasing drive affects the fraction of the interspike interval during which a specific motoneuron is excitable for a specific stimulus. Consequently, the distribution of reflex amplitudes across the motoneuron pool changes with increasing drive. We showed that noise components in the motoneuron drive generally reduce the reflex amplitude. This observation is in line with the dependency on the baseline firing rate. Noise inputs increase the baseline firing rate and, thus, lead to smaller reflex amplitudes.

Matthews (1999) and Herrmann and Gerstner (2002) both reported increased reflex amplitudes for higher stimulus amplitudes, as shown in this work. Piotrkiewicz et al. (2009) found an approximately linear relationship between EPSP size and reflex amplitude for high firing rates. Due to the high variability within the pool and the heterogeneity of the responses across the applied conditions, we did not attempt to find a linear relationship between reflex amplitude and stimulus size.

In their modelling studies, Matthews (1999) and Herrmann and Gerstner (2002) found that the peak of the PSTH-CUSUM first increases with increasing baseline frequency then decreases and finally plateaus. We could not observe an initial increase in reflex amplitude for low drives; however, Matthews (1999) considered firing frequencies as low as 2 Hz, which we assumed to be too irregular to consider for analysis. Our findings are further confirmed by a modelling study by Jones and Bawa (1997), which found decreasing reflex amplitudes for baseline discharge frequencies increasing from 5 Hz to 25 Hz. Experimental studies by Kudina (1980) and Jones and Bawa (1995) also found an inverse relationship between the PSTH peak size and the baseline discharge frequency. A reduction of the reflex amplitude by noise, as found in our modelling study, was also observed in the modelling studies of Matthews (1999) and Herrmann and Gerstner (2002).

5.4.3 Characteristics of reflex amplitudes determined from the PSF-CUSUM

The reflex amplitudes determined from the PSF-CUSUM showed a complex pattern in the simulation study. Considering the same simulated motoneuron and the same conditions, the reflex amplitude increased with stimulus size. However, the distribution of reflex amplitudes across the pool of motoneurons was not constant when increasing the drive, i. e., the baseline frequency of the pool. Roughly, the reflex amplitude in small motoneurons increased, and the reflex amplitude in large motoneurons decreased with increasing drive. When normalised by the baseline frequency, the reflex amplitudes for the entire pool were approximately inversely related to the drive; however, the distribution within the pool remained heterogeneous. As in the PSTH-CUSUM, noise components in the motoneuron drive generally reduced the reflex amplitude and the number of motoneurons

with a significant reflex response.

We used effective synaptic currents as reflex stimuli. Since the effective synaptic current is assumed to be directly related to the current-frequency relation, any increase in motoneuron frequency is supposed to represent the input current (Heckman and Binder, 1988). Türker and Powers (1999) indeed found linear relations between PSF peak size and stimulus amplitude. In the simulation, it was observed that the normalised PSF reflex amplitudes rapidly decrease with increasing discharge frequency after recruitment and plateau for further increases in frequency. The reflex amplitudes of the smallest motoneurons showed another increase for even higher frequencies. This behaviour shows a close similarity with the slope of the current-frequency relation, which rises steeply just after recruitment, takes a smaller and approximately constant slope for a large range of input currents and then increases steeply again (see Figure 5.6a). Together with the experimental findings, this suggests that the relation between reflex amplitude and input is indeed approximately linear for firing rates in the linear region of the current-frequency relation.

Türker and Powers (2005) claimed that "each data point in the PSF is an independent number and reflects the true value of the membrane excitability at that point in time". The simulation results put this statement into perspective. A data point with an increased frequency in the PSF often only indicates that the stimulus was large enough to bring the motoneuron to the threshold. Further, since the PSF was shown to be very sensitive to noise inputs and the random timing of the stimulus, there is a large variability in reflex amplitudes. As suggested by Türker and Powers (2003), summarising multiple motor units in the PSF reduces the variability and may overcome this problem to a certain extent.

In summary, absolute PSF values and the reflex amplitude distribution across the motoneuron pool depend on the motoneurons' baseline frequencies, the slope of their current-frequency relations and the random timing of the stimulus. As proposed by e. g., Türker and Powers (1999) and Powers and Türker (2010a), a model of the membrane potential trajectory is necessary to estimate the size of the EPSP from the PSF.

5.4.4 Implications for experimental studies

The PSTH and the PSF are established methods, but since their development, the community discusses their reliability and predictive power. This study showed which factors shape the reflex amplitude and how the influence of these factors changes across the motoneuron pool and the applied conditions. From this, we derived implications for the design of experimental studies.

During the primary range of firing, the motoneuron's average membrane potential trajectory is assumed to reach a constant distance to the threshold toward the end of the interspike interval so that spikes are triggered by random fluctuations in synaptic noise rather than by a linear rise to threshold (Kudina, 1999). This corresponds to the range of relatively low baseline frequencies, where we found considerably higher reflex amplitudes than when larger drives were applied. This observation suggests using high baseline frequencies, i. e., discard motoneurons e. g., up to 5 Hz above their recruitment frequency. Alternatively, a symmetrical interspike interval histogram could be used as an indicator for regular firing behaviour as e. g., suggested by Powers and Türker (2010a). However,

note that as soon as some motoneurons reach the secondary firing range, the slope of their current-frequency relation changes rapidly and considerably (Kernell, 1965). This results in another increase in reflex amplitudes as seen e. g., for small motoneurons at the highest drives considered in this work. Suitable ranges of firing frequencies for human motoneurons should be defined.

Due to the large variability in reflex amplitude, even among motoneurons with very similar properties, a single motoneuron's reflex amplitude is not representative. This can be overcome by summarising motoneurons with similar frequencies. Consequently, recording many motoneurons with relatively high frequencies is beneficial for the predictive power of the determined reflex amplitudes. Türker and Powers (2003) showed that more stimuli and a higher baseline frequency improve the match between PSF and PSP shape. We confirmed that a high number of reflex stimuli is especially relevant for the PSF. In contrast, the PSTH is more robust against small numbers of applied stimuli. While in experimental studies, 100 applied stimuli are often considered sufficient (e. g., Yavuz et al., 2014), the simulation results suggest applying at least 200 but preferably 400 stimuli to reach the plateau size of the error box. Thereby, the number of motor units with a significant PSF reflex amplitude is expected to increase considerably. We also showed that applying more than 400 stimuli does not considerably improve the result.

The requirements, i. e., delivering a high amount of stimuli and recording many motor units at discharge frequencies considerably above their recruitment threshold, are in a field of tension. Motoneurons generally increase their discharge frequency with increasing force. This behaviour would suggest performing reflex experiments at high forces. However, maintaining a high force level and delivering many stimuli exclude each other. Further, fatigue must be considered at high force levels, which adds another contributor to reflex amplitude. Using motor unit tracking across several experimental trials might enable delivering a larger number of stimuli and at higher forces than previously possible (Martinez-Valdes et al., 2017). However, the number of motor units that can be tracked across all trials tends to decrease with the number of trials (Martinez-Valdes et al., 2017).

If single motor units are not representative and moderate to high forces are desired, classical intramuscular EMG is not recommended to investigate the reflex strength. Intramuscular EMG allows recording only one or two motor units simultaneously and is challenging to decompose at high forces, such that it is often used at 10 % MVC or below (Merletti and Farina, 2009; Yavuz et al., 2015). High-density surface EMG (HDsEMG) provides a better alternative. Yavuz et al. (2015) showed that HDsEMG can be used to record reflex responses at forces as high as 50 % MVC. Currently, decomposition algorithms tend to deliver fewer motor units at higher forces. High-density intramuscular EMG electrodes provide another alternative since they allow recording several tens of motor units with a single electrode (Muceli et al., 2022). However, to the author's knowledge, they have not yet been used in reflex recordings.

In summary, it is suggested to select recording techniques that allow the performance of reflex experiments at moderately high forces and that are, at the same time, suited for long recording periods to apply as many stimuli as possible. In any case, it is recommended to discard motor units close above their recruitment threshold. The uncertainty of the results can be reduced by summarising similar motor units. Understanding the characteristic properties of the PSTH and PSF is crucial to selecting the appropriate analysis method and for interpreting the results. As suggested by Türker and Powers (2003) we

strongly support that one should always use PSTH in combination with PSF to avoid misinterpretations due to motoneuron synchronisation.

Lastly, this study pointed out that comparing reflex amplitudes obtained from different experiments is challenging. Reflex amplitudes are very sensitive to the combination of motoneuron properties and applied conditions, which are usually not completely known. Thus, multi-variable analysis or model-based approaches are needed.

5.4.5 Is the reflex amplitude an appropriate tool to determine the distribution of afferent inputs to the motoneuron pool?

This work and several previous studies showed that the reflex amplitude is correlated with the stimulus strength or EPSP size (e. g., Matthews, 1999; Türker and Powers, 1999). This finding led researchers to assume that a motoneuron showing a higher reflex amplitude than another motoneuron from the same pool received a stronger stimulus. If this assumption is correct, it would provide a means to study the distribution of afferent inputs to the motoneuron pool.

Previous research paints a heterogeneous picture of the distribution of Ia monosynaptic afferent inputs to the motoneuron pool. For example, Binboğa and Türker (2012) found that the H-reflex amplitude is higher in larger motor units of the human soleus muscle, while Awiszus and Feistner (1993) found the opposite with a similar experimental setup. The former hypothesis is, e. g., supported by Heckman and Binder (1988), while the latter is backed by, e. g., Mazzocchio et al. (1995); Semmler and Türker (1994).

The simulations performed in this work suggest that the assumptions underlying those studies do not hold. The reflex size only relates to the input size when considering the same motoneuron under constant conditions. We found that motoneuron size and the baseline firing frequency modulate the size of the reflex amplitude. For example, in Figure 5.4, we showed that the reflex amplitudes differ considerably across the motoneuron pool, even though a uniformly distributed stimulus was applied. The distribution across the pool also changes with the applied motoneuron drive. Moreover, due to the large variability of reflex amplitudes among similar neurons, a single motoneuron's reflex response is not representative.

It must further be considered that the effective synaptic current, i. e., that eventually determines action potential generation, only provides an estimate of the actual input current (Heckman and Binder, 1988). Several processes might modulate the input signal, e. g., active dendrite conductances (e. g., Binder et al., 2020), recurrent Renshaw inhibition (Windhorst, 1990) or presynaptic inhibition (e. g., Stein, 1995), about which statements can hardly be made *in vivo*. It is also questionable how statements on the distribution across the motoneuron pool can be made when recording motoneurons at low forces when larger motor units are not recruited or fire with extremely low and irregular discharge frequencies.

In conclusion, this study suggests that reflex responses of a motor unit population and at different forces should be considered to determine input distributions. The distribution of reflex responses across the pool must be interpreted considering the influence of motoneuron size and baseline firing rates. Comparing the distribution to model predictions can provide guidance. Since the reflex amplitudes determined from the PSTH-CUSUM

were shown to be less sensitive to the baseline firing rate, they might be better suited for statements about the EPSP size.

5.4.6 Implications for neuromuscular modelling

Experimental data on reflex amplitudes is subject to many uncertainties. Nevertheless, reflex measurements are one of the few methods available to study the behaviour of motoneurons *in vivo* and in isolation. Therefore, computational models of the neuromuscular system require data obtained from reflex experiments for model parametrisation and validation. Knowing the limitations of the methods will help in using the data.

The gain of the afferent input to the motoneuron pool is an important parameter when including reflex pathways and sensory feedback loops in a model of the neuromuscular system. When the gain shall be determined with the help of experimental data, a mean value of the reflex amplitude from the PSTH-CUSUM provides a good estimate. Chapter 7 presents an example use case. Reflex amplitudes determined from the PSF-CUSUM are more sensitive to individual motoneurons' properties and discharge frequencies and, thus, are less suggested to fit model results. However, the PSF is suited to study the distinction between inhibitory and excitatory reflexes, as, e. g., in Chapter 6.

As discussed in the previous section, conflicting findings exist on the distribution of afferent inputs to the motoneuron pool. In consequence, many modelling studies distributed Ia feedback uniformly (e. g., Elias et al., 2014; Lin and Crago, 2002a), while others used stronger Ia feedback for larger motoneurons (e. g., Dideriksen et al., 2015). This study has raised doubts about the approaches used to determine the distribution. For the lack of better knowledge, we recommend distributing feedback uniformly or using optimisation procedures to define the feedback gains for a particular motor task.

Another potential area of application for motoneuron models is the augmentation of data. Therefore, the parameters of a motor neuron model are first optimised to predict *in-vivo* behaviour (Caillet et al., 2022a; Ornelas-Kobayashi et al., 2023). Then, this model can be used to increase the amount of data for further evaluation.

5.4.7 Limitations

The limitations of the motoneuron model were extensively discussed in Section 3.4.4. Here, we briefly describe the limitations relevant to this work.

Reducing the branched dendritic structure to a single compartment in the motoneuron model simplifies the physiological structure of a motoneuron. Dendrites themselves contain ion channels, which were not considered in this model. These channels influence the shape of an incoming signal on its way to the soma. Especially, PICs can considerably modulate the motoneuron's input-output function (Binder et al., 2020). However, due to their slow time dynamics, we expect no major changes in PIC activity during short stimuli (Binder et al., 2020). In addition, we assumed the motoneuron inputs to represent effective synaptic currents that finally reach the soma. Only this current is relevant for recruitment and rate coding (Heckman and Binder, 1988). Thus, this study only makes statements about inputs finally reaching the soma. Any modulation by the motoneuron properties is not considered.

The motoneuron model does not consider threshold variations within an interspike

interval (Calvin, 1974; Powers and Binder, 1996). The spike threshold was shown to vary within the interspike interval in a way that it follows the membrane potential trajectory of the AHP (Calvin, 1974; Powers and Binder, 1996). That is, the threshold is lower at the beginning of the interspike interval and then increases. In the employed model, the spike threshold is highest just after the action potential, then decreases and finally plateaus. Thus, we might overestimate the efficacy of stimuli delivered late in the interspike interval. The effect of the spike threshold on reflex amplitudes could be investigated by adapting a spike-response model, as e. g., proposed by Herrmann and Gerstner (2002), to consider different threshold time courses.

Previous studies showed that the amount of common drive delivered to a motoneuron pool increases with force level and fatigue (Castronovo et al., 2015). As the motoneuron model does not show frequency saturation of small motoneurons at high forces (Monster and Chan, 1977), we limited the drive levels to avoid reaching unphysiological ranges of the current-frequency relation. Further, we fixed the amount of noise and independent drive with respect to the mean drive.

We can only make a limited statement about which contraction forces our applied drives correspond to. In accordance with Moritz et al. (2005), we assumed that 60 % MVC is reached when the largest motoneuron in the pool fires with 10 Hz. This was the case for the chosen noise inputs with a mean drive of 16.8 nA. Thus, we assume that we covered approximately a range of below 10 % to not more than 70 % MVC (see Section 5.1.2).

We did not consider nerve conduction delays since we did not model a specific muscle or pathway. The conduction delay does not affect the reflex amplitude. If reflex latencies should be considered, appropriate delays can be easily implemented from the known conduction velocities of afferent and efferent nerves and the estimated conduction distances from the muscle to the location of the respective motoneuron pool in the spinal cord.

In this study, the reflex amplitude was exclusively determined from the PSTH- and PSF-CUSUM time courses. There are other approaches to determine reflex strength that might also be applicable as, e. g., a moving average on the PSF (e. g., Piotrkiewicz et al., 2009).

5.4.8 Summary and outlook

We used a computational model of a motoneuron pool to investigate the factors influencing the reflex amplitudes determined from the PSTH- and PSF-CUSUM. We found a highly non-linear multi-variable influence of internal motoneuron properties and external conditions on reflex amplitudes. The reflex amplitudes determined from the PSTH-CUSUM are mainly determined by the "excitable portion" of the interspike interval, which depends on internal motoneuron properties as well as the applied conditions. Reflex amplitudes determined from the PSTH-CUSUM are suited for quantitative comparisons between experiments and for estimating the EPSP size when the conditions are known. Reflex amplitudes determined from PSF-CUSUM are sensitive to the motoneuron's current-frequency relation, which is determined by the motoneuron's properties and the baseline frequency. Further, the random timing of the stimulus with respect to the last discharge and the number of applied stimuli massively influence the reflex amplitudes determined from the PSF-CUSUM. Reflex amplitudes determined from the PSF-CUSUM are suited to determine the sign of a reflex response and to determine differences between motoneuron

types.

Reflex amplitudes from single motoneurons were found to be generally not representative due to the large variability within the motoneuron pool. Instead, it is suggested to summarise motoneurons with similar baseline discharge frequencies.

This study aimed to fill a gap in the knowledge of the reflex behaviour of single motoneurons. There is a large dark field because of the small number of motor units that can be recorded or decomposed with current experimental techniques. Emerging techniques that can capture motor units from deeper regions of the muscle can increase the number of motor units that can be analysed. For example, high-density intramuscular EMG electrodes are already available and enable simultaneous recording of a relatively large number of motor units with good signal quality (Muceli et al., 2022). Moreover, new non-invasive techniques like improved electrode grids for surface EMG, magnetomyography (MMG) or ultrafast ultrasound are currently being developed and have the potential to provide more complete motoneuron pool data and validate the predictions made by this study (Caillet et al., 2023; Ghahremani Arekhloo et al., 2023; Klotz et al., 2023; Rohlén et al., 2020). Reflex experiments will benefit from improvements in recording and decomposition technologies.

Re-examining reflex responses using new technologies provides an opportunity to investigate sex differences and fill a gap in current knowledge. It has been reported that females may have different motor unit behaviour and use different neuromuscular control strategies than males (Lulic-Kuryllo and Inglis, 2022).

This study only investigated excitatory reflex responses. Extending this study to inhibitory stimuli is expected to provide valuable insights for interpreting, e. g., experiments on reciprocal inhibition. Further input distributions can be applied in the simulation to better judge the reflex amplitude as a tool to determine the distribution of afferent inputs to the motoneuron pool, as discussed in Section 5.4.5. Comparing the reflex amplitudes determined from the PSTH- and PSF-CUSUM to other techniques, e. g., a moving average on the PSF (e. g., Piotrkiewicz et al., 2009), the maximum PSF or the rise time and duration of reflex responses would be a further valuable extension of this study.

The insights gained from this simulation study can not only be applied to muscle reflexes but, e. g., also to pain reflexes (e. g., Rossi et al., 2003). With an appropriate model of the underlying mechanism, computer simulations can also help to identify pathological reflex patterns. A better quantitative understanding of reflex amplitudes has the potential to assess, e. g., spasticity. Up-to-date measures that can distinguish different levels of severity of spasticity are still missing (Aloraini et al., 2015; Biering-Sørensen et al., 2006). In light of this study, considering reflex amplitudes of the entire motoneuron pool is a promising approach to clinically monitoring disease progression or treatment outcomes.

Especially for clinical applications, keeping the examination time to a minimum is desirable. The number of required stimuli during the procedure can be reduced by merging spike trains of two or more similar motor units to create the PSTH and PSF. The similarity of motor units can be determined based on their recruitment threshold and firing rate (Gogeascoechea et al., 2023). Another alternative is augmenting the data. Based on a relatively short recording period, motoneuron models are parametrised to reproduce the recorded firing behaviour and used to predict the reflex responses (e. g., Caillet et al., 2022a; Ornelas-Kobayashi et al., 2023).

6 The Role of h-Currents in Motoneuron Postinhibitory Excitation

This chapter was largely published in Schmid et al. (2024).

Sherrington, one of the pioneers of reflex studies, noted in his 1909 studies that "reflex inhibition of the vastocrureus and other extensor muscles in decerebrate rigidity is followed regularly, under certain circumstances, on withdrawal of the inhibitory stimulus, by a rebound contraction" (Sherrington, 1909). Interestingly, the "rebound contraction" persisted after de-afferentation (Sherrington, 1909). Later, the same phenomenon of motor unit postinhibitory excitation was reported in several studies (e. g., Aoki and Yamamura, 1980; Kozhina, 1983; Özyurt et al., 2019; Türker and Powers, 1999; Uysal et al., 2019). The proposed mechanisms include reflex pathways activated by muscle spindles and intrinsic neuron characteristics originating from the behaviour of specific ion channels. However, none of these studies has systematically investigated the phenomenon's origin.

Similar to Sherrington's findings, we observed a consistent rebound-like excitation following electrically evoked reciprocal inhibition in human tibialis anterior motor units (Figure 6.1c, Yavuz et al., 2018). Reciprocal inhibition is a component of the stretch reflex pathway, which is disynaptically elicited by muscle spindles of an antagonistic muscle (Figure 6.1a, Crone et al., 1987; Kudina, 1980). Here, reciprocal inhibition was superimposed on sustained isometric contractions of the tibialis anterior muscle by electrical stimulation of the tibial nerve.

Increased excitability elicited by a purely inhibitory stimulus is a well-known phenomenon in different cells of the mammalian neural system, and various ion channels were found to cause or facilitate this behaviour *in vitro* (e. g., Aizenman and Linden, 1999; Bertrand and Cazalets, 1998; Dodla et al., 2006; Ito and Oshima, 1965; Kandel and Spencer, 1961). Therefore, it is surprising that intrinsic motoneuron mechanisms are rarely considered to explain the postinhibitory increase in activity of motor units *in vivo*. Instead, excitatory synaptic inputs based on reflex pathways were lately considered (e. g., Aoki and Yamamura, 1980; Kozhina, 1983; Özyurt et al., 2019; Uysal et al., 2019).

Ito and Oshima (1965) first described membrane potential overshoots caused by hyperpolarisation-activated inward currents in cat spinal motoneurons. Takahashi (1990) found that this current, which is commonly named h-current or I_h, is mediated by sodium and potassium ions. The corresponding channel family was identified as hyperpolarisation-activated cyclic nucleotide-gated non-selective cation channels (HCN channels), which are expressed throughout the soma and dendrites of spinal motoneurons (Milligan et al., 2006). Here, we refer to this group of channels as h-channels and the corresponding currents as h-currents.

Based on the large body of evidence for intrinsic postinhibitory excitation mechanisms from *in-vitro* studies, we hypothesise that intrinsic motoneuron mechanisms, specifically h-currents, also contribute to the postinhibitory excitation in motor units observed *in vivo* (Figure 6.1b). In this chapter, we analyse the incidence and amplitude of postinhibitory

excitation in human motor units following electrically elicited reciprocal inhibition of the tibialis anterior muscle. Then, we use a computational motoneuron model to reproduce the experimental results and understand the role of h-currents in postinhibitory excitation. To this end, we employ a compartmental electric circuit model, which is based on previous works by Cisi and Kohn (2008), Negro and Farina (2011) and Powers et al. (2012). We analyse and compare the discharge behaviour of both *in-silico* and *in-vivo* motoneurons using the peristimulus frequencygram (PSF, Türker and Cheng, 1994).

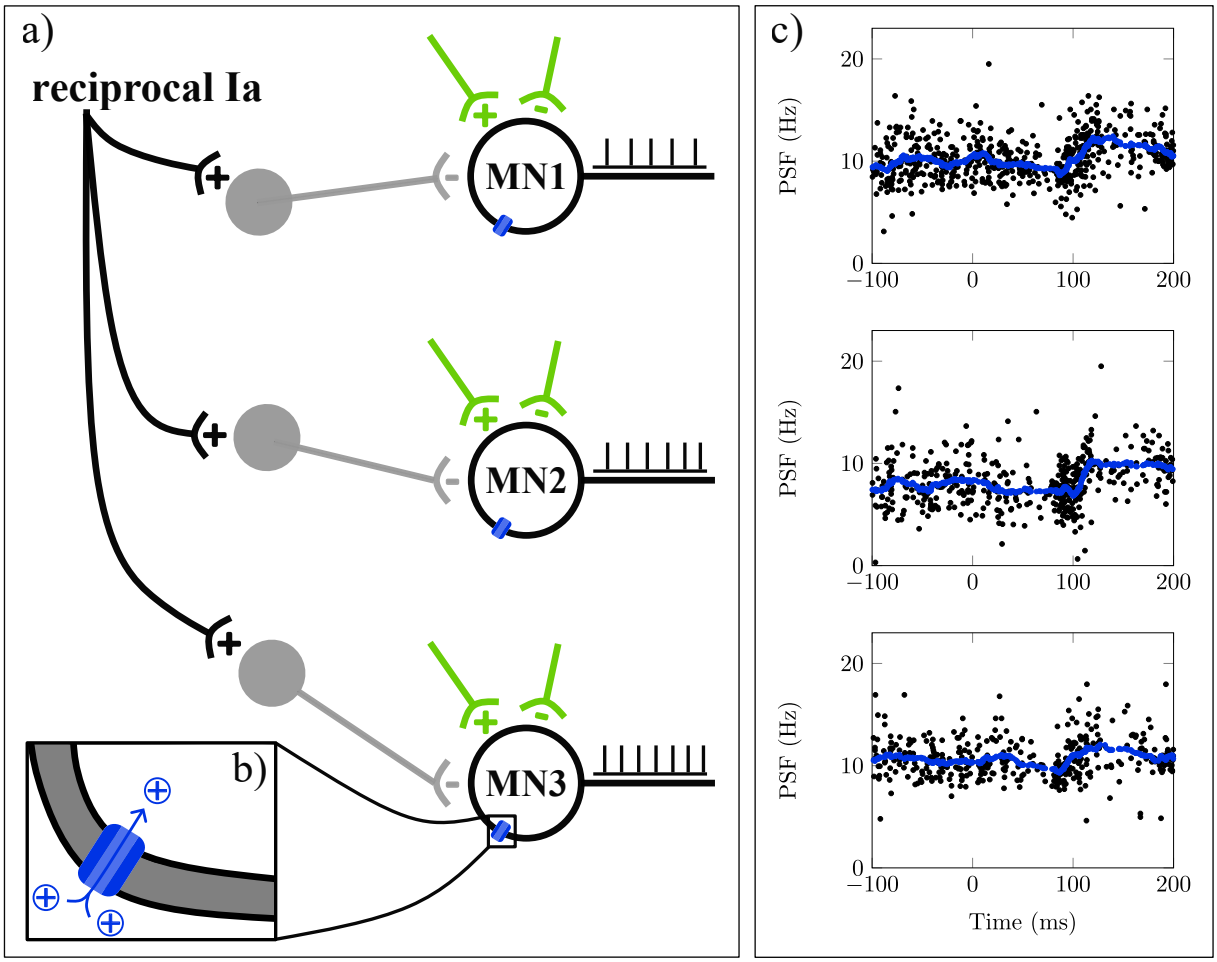

Figure 6.1: Postinhibitory excitation in human motor units. a) Motoneurons (MNs) receive multiple, typically unknown synaptic inputs (green). Particularly, reciprocal inhibition is mediated by interneurons (grey). In humans, recording motor unit spike trains (black) allows for studying the function of motoneurons. b) The integration of synaptic inputs in motoneurons is determined by ion channels (blue). c) Peristimulus frequencygram (PSF) of three exemplary tibialis anterior motor units in response to reciprocal inhibition, elicited by electrical stimulation of the tibial nerve during sustained isometric contractions. The moving average is shown in blue, data from Yavuz et al. (2018). It is unclear if the observed postinhibitory excitation is caused by neural pathways or intrinsic motoneuron properties. [from Schmid et al. (2024) under CC BY 4.0]

6.1 Summary of the experimental protocol

Motor unit reciprocal inhibition data from a previous study (Yavuz et al., 2018) were used to investigate the incidence rate and strength of postinhibitory excitation activity *in vivo*. The data were acquired with the approval of the local ethical committee of the University Medical Center, Georg-August–University of Göttingen (approval date: 1/10/12). The high-density surface electromyogram (HDsEMG) was recorded (sampling rate: 10 240 Hz) from tibialis anterior muscles during steady isometric contraction at 10 % and 20 % of the maximum voluntary contraction (MVC). Stimulating the tibial nerve through monopolar stimulation electrodes elicited reciprocal inhibition on the tibialis anterior muscle. The metal pin anode and cathode electrodes were placed on the skin of the popliteal fossa to stimulate the nerve. The activity of individual motor units was identified by decomposing HDsEMG data using a blind source separation technique (Holobar and Zazula, 2007; Negro et al., 2016a). Further details about the experimental protocol and analysis can be found in Yavuz et al. (2018).

6.2 Computational modelling

For this study, a motoneuron model was developed based on the electric circuit model described in Section 3.4. Modifications to the model performed for this study are described in Section 6.2.1. The model parametrisation is described in Section 6.2.2, and the performed simulations are presented in Section 6.2.3.

6.2.1 The compartmental neuron model

A single motoneuron was simulated using an electric circuit model based on the motoneuron model proposed in Negro and Farina (2011). A detailed description of this model can be found in Section 3.4. In short, the *in-silico* motoneuron consists of two compartments, i. e., the soma and a lumped dendrite. The soma compartment includes voltage-gated conductances that describe sodium and slow and fast potassium channels. Further, both compartments include an additional leakage conductance. For the present investigation, we added a voltage-gated h-channel conductance in the soma and the dendrite compartment (Figure 6.2d). Further, external currents cannot only be applied to the soma but also to the dendrite compartment. Accordingly, the membrane potential in each compartment can be described by the following differential equations:

$$C^{\mathrm{d}}\frac{\mathrm{d}V_{\mathrm{m}}^{\mathrm{d}}(t)}{\mathrm{d}t} = -I_{\mathrm{L}}^{\mathrm{d}} - I_{\mathrm{C}}^{\mathrm{d}} - I_{\mathrm{H}}^{\mathrm{d}} + I_{\mathrm{inj}}^{\mathrm{d}}\,, \tag{6.1}$$

$$C^{\mathrm{s}}\frac{\mathrm{d}V_{\mathrm{m}}^{\mathrm{s}}(t)}{\mathrm{d}t} = -I_{\mathrm{L}}^{\mathrm{s}} - I_{\mathrm{C}}^{\mathrm{s}} - I_{\mathrm{Na}} - I_{\mathrm{Kf}} - I_{\mathrm{Ks}} - I_{\mathrm{H}}^{\mathrm{s}} + I_{\mathrm{inj}}^{\mathrm{s}}\,. \tag{6.2}$$

Therein, $V_{\mathrm{m}}(t)$ is the membrane voltage at time t, and C is the membrane capacitance. The superscripts 's' and 'd' denote the soma and the dendrite compartment, respectively. The currents I_{Na}, I_{Kf} and I_{Ks} describe the flow of ions through sodium and fast and slow potassium channels, respectively. Further, I_{C} describes the coupling current between the two compartments whereby $I_{\mathrm{C}}^{\mathrm{d}} = -I_{\mathrm{C}}^{\mathrm{s}}$, I_{L} is a leakage current and I_{inj} denotes currents injected into the compartments, e. g., by an external electrode. Currents are modelled

and parametrised as described in Negro and Farina (2011). H-channels were found to be expressed widely across motoneurons. Consequently, they are placed in both soma and dendrite compartments (Milligan et al., 2006). The mathematical description of the h-current and its parameters are provided in Equations (6.3) to (6.5).

The h-current, I_{H}, is described by Powers et al. (2012):

$$I_{\mathrm{H}} = \bar{g}_{\mathrm{H}}\, s\, (V_{\mathrm{m}} - E_{\mathrm{H}})\ , \tag{6.3}$$

$$\frac{\mathrm{d}s}{\mathrm{d}t} = \frac{s_\infty - s}{\tau_{\mathrm{H}}}\ , \tag{6.4}$$

$$s_\infty = \frac{1}{1 + \exp\left(\frac{V - V_{\mathrm{half}}}{V_{\mathrm{slope}}}\right)}\ . \tag{6.5}$$

Thereby, E_{H} denotes the reversal potential of the h-conductance and $\bar{g}_{\mathrm{H}}$ the maximum conductance, which is obtained by multiplying the maximum specific h-conductance $\overline{G}_{\mathrm{H}}$ with the area of the soma compartment. The transient behaviour of the gating variable s is determined by the voltage-independent time constant τ_{H}, the half-maximum activation potential V_{half} and a slope factor V_{slope}. Note that Equations (6.3) to (6.5) refer to both compartments, i. e., V_{m} corresponds to $V_{\mathrm{m}}^{\mathrm{s}}$ and s to s^{s} for the soma compartment and to $V_{\mathrm{m}}^{\mathrm{d}}$ and s^{d} for the dendrite compartment.

6.2.2 Model parametrisation

Following a study by Duchateau and Enoka (2022), we assumed that for the tibialis anterior muscle and contraction strengths of less than 20 % MVC, all recruited and consequently all recorded motor units are of slow type. Model parameters for different motor unit types have been published by Cisi and Kohn (2008) (see their Table 2). We chose the input resistance and the size parameters (diameter and length) of both the soma and the dendrite compartment according to the mean values for slow-type motoneurons (Table A.4). The size-independent electrophysiological parameters were also adopted from Cisi and Kohn (2008) (Table 3.2).

Since the h-channel was not considered by either Cisi and Kohn (2008) or Negro and Farina (2011), we used the implementation by Powers et al. (2012) as a guide. Powers et al. (2012) used experimental recordings by Larkman and Kelly (1992) for the parametrisation of the channel and we adopted the time constant as well as the slope factor, i. e., $\tau_{\mathrm{H}} = 50\,\mathrm{ms}$ and $V_{\mathrm{slope}} = 8\,\mathrm{mV}$. In contrast to Powers et al. (2012), we assumed that persistent inward currents play a minor role in our study (Pearcey et al., 2020). Thus, we adapted the reversal potential $E_{\mathrm{H}} = 20\,\mathrm{mV}$ and half-maximum activation potential $V_{\mathrm{half}} = -20\,\mathrm{mV}$ with respect to the original implementation. The selected values agree with experimental data (Bayliss et al., 1994; Larkman and Kelly, 1992). Note that all potentials are given relative to the resting potential.

The above parameters determine the temporal dynamics of the h-current. The maximum conductance $\bar{g}_{\mathrm{H}}$, which can also be interpreted as the density of h-channels in the membrane, determines the maximum amount of h-current that can flow across the membrane. Experimental current-clamp studies from Bertrand and Cazalets (1998) and Kiehn et al. (2000) were used to parametrise $\bar{g}_{\mathrm{H}}$. Therefore, the simulated membrane potential trajectory in response to injection of hyperpolarising current steps was compared to *in-vitro* results. The simulated neuron shows the characteristic undershoot and overshoot

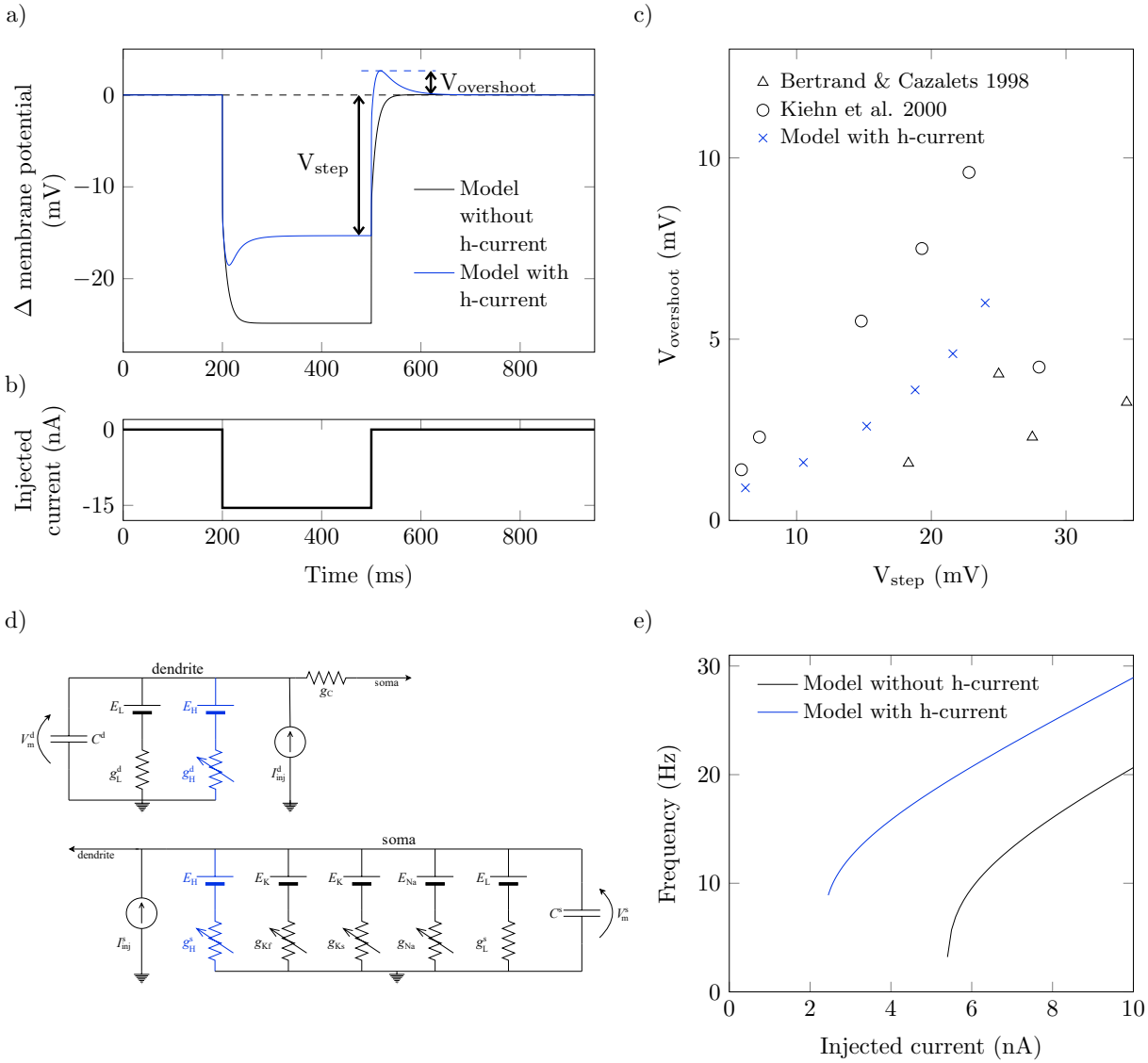

Figure 6.2: Characteristic behaviour of the computational motoneuron model. a) Membrane potential time course of the simulated motoneurons without (black) and with h-current (blue) in response to injection of the current step shown in (b). Membrane potential is given relative to the resting potential. c) Steady-state membrane potential (V_{step}) vs. overshoot membrane potential ($V_{\text{overshoot}}$) of the simulated neuron (x) compared to data obtained from Kiehn et al. (2000) (o) and Bertrand and Cazalets (1998) (△). d) Equivalent electric circuit of the motoneuron model. Blue colour highlights components added compared to the previous version of the model (Negro and Farina, 2011). e) Current-frequency relation for the model without (black) and with (blue) h-currents. [from Schmid et al. (2024) under CC BY 4.0]

at the beginning and end of the applied current step (Figure 6.2a, b), which is typically attributed to h-currents (e. g., Bayliss et al., 1994; Bertrand and Cazalets, 1998; Ito and Oshima, 1965; Larkman and Kelly, 1992).

For a quantitative comparison, the steady-state membrane potential just before the release of the current step, V_{step}, was compared to the maximum size of the membrane potential overshoot after the release of the current step, $V_{\text{overshoot}}$ (Figure 6.2a-c). The current step was applied for 300 ms to reach a steady membrane potential. With a max-

imum specific conductance of $\overline{G}_{\mathrm{H}} = 2\,\mathrm{mS\,cm^{-2}}$ the simulated neuron showed overshoot potentials of 0.84 mV to 6 mV in response to current injections that hyperpolarise the membrane potential by 6 mV to 24 mV. This is well within the range of values reported in Bertrand and Cazalets (1998) and Kiehn et al. (2000), i. e., overshoot potentials of 0.96 mV to 9.6 mV for potential steps of 5.9 mV to 34.5 mV (Figure 6.2c). Note that adding the h-current does not lead to subthreshold oscillations and thus preserves the integrator nature of the motoneuron model (Fig 6.2a).

Adding the h-current increases the neuron's resting potential due to an additional inflow of current, which was also reported by Powers et al. (2012). Consequently, the h-current model has a decreased rheobase, but the gain of the current-frequency relation is hardly affected (Figure 6.2e). We ensure comparability between the models by considering the simulated neurons at the same working point, defined by the frequency.

In order to assess the reliability of the results with regard to uncertainties in the parametrisation, exemplary simulations with varied parameters for the time constant τ_{H}, maximum conductance $\overline{G}_{\mathrm{H}}$, half-maximum activation potential V_{half} and reversal potential E_{H} of the h-channel were carried out. Further, variations in motoneuron size and the influence of artificial persistent inward currents (PICs) were exemplarily tested.

6.2.3 Simulation of reciprocal inhibition

The applied simulation protocol aims to mimic the experimental procedure described in Section 6.1. Repeated injections of inhibitory current pulses causing an inhibitory postsynaptic potential (IPSP) imitate the stimulus delivered in the reflex experiment. The stimuli were applied 200 times with a random interstimulus interval of 1000 ± 100 ms. All simulations were performed with MATLAB R2021a (9.10.0.2015706). The motoneuron model is represented by a system of eight ordinary differential equations, which was solved with MATLAB's ode23 solver (single-step, explicit Runge-Kutta solver, Shampine and Reichelt, 1997) and an absolute and relative error tolerance of 1×10^{-5}.

Injected currents drive the activity of the motoneuron model. The input is composed of up to three components to replicate the experimental protocol: (i) inhibitory current pulses simulating reciprocal inhibition, (ii) a constant current representing the mean cortical drive to the neuron and determining the contraction strength, (iii) additive noise representing all afferent and efferent inputs to the motoneuron that are not explicitly modelled.

Reciprocal inhibition (i) was simulated by injecting a current kernel representing the compound inhibitory postsynaptic current (IPSC). The postsynaptic current I_{PSC} is described by

$$I_{\mathrm{PSC}} = -I_0 \frac{t}{\tau_{\mathrm{PSC}}} \exp\left(1 - \frac{t}{\tau_{\mathrm{PSC}}}\right), \tag{6.6}$$

with t representing the time since the beginning of the current injection. The time constant $\tau_{\mathrm{PSC}} = 4$ ms was fixed (Curtis and Eccles, 1959), while the amplitude I_0 ranged from 2.5 to 15 nA to cover a large range of IPSP strengths. The IPSC was applied for 20 ms, as this, for the chosen amplitudes, achieved the minimum firing rate at a time comparable to the experiment. The current-induced IPSPs usually last longer than 20 ms (Fig 6.4a, b).

The constant input into the neuron (ii) was chosen to obtain different baseline firing rates of approximately 10, 14, and 18 Hz. The noise component (iii) was composed of

two parts, a zero-mean, band-pass filtered (15 Hz to 35 Hz) and a zero-mean low-pass filtered (< 100 Hz) white noise (Conway et al., 1995; Halliday et al., 1998). The filtering was performed with a first- and second-order Butterworth filter, respectively (Rao and Swamy, 2018). The standard deviation of the noise input was scaled relative to the mean drive such that the band-pass filtered component accounts for 80 % of the total standard deviation (Negro et al., 2016b). To investigate the effect of noisy inputs in the investigated reflex scenario, we applied different noise levels by scaling the total standard deviation of the summed noise input to 0 %, 12.5 %, and 25 % of the constant input current (ii).

The input components (i) to (iii) were linearly summed and applied to the soma compartment, assuming they represent effective synaptic currents (Heckman and Binder, 1988; Negro and Farina, 2011). To account for the delay caused by the nerve conduction velocity, a constant delay of 50 ms between the IPSC application and the membrane potential output was introduced.

6.3 Data analysis

Motoneuron activity is described through discrete discharge times, i. e., a binary spike train. For the *in-vivo* experiment, spike trains were reconstructed by the decomposition of the recorded HDsEMG (for details, see Holobar and Zazula, 2007; Negro et al., 2016a; Yavuz et al., 2018). In the simulation, the spike trains were directly obtained from the trajectory of the soma membrane potential.

The firing behaviour of motoneurons before and after stimulation was analysed using the peristimulus frequencygram (PSF) method (Figure 6.3a). The PSF shows the instantaneous discharge rates of motoneurons relative to the stimulus time (see Section 4.2.2 and Türker and Cheng, 1994). Significant perturbations in discharge rate compared to baseline activity after the stimulus are likely related to the stimulating event. With increasing delay between the stimulus and the event, the probability that changes in discharge rate may reflect other processes increases (Powers and Türker, 2010a; Türker and Powers, 2003; Yavuz et al., 2014). The characteristics of the PSF response are assumed to depend on the sign and the magnitude of a (reflex-induced) postsynaptic potential (Powers and Türker, 2010a). As shown in Chapter 5, the PSF is influenced by many factors, which cannot all be controlled in the experimental setup. Thus, we refrain from a quantitative comparison with experimental data.

The strength of reciprocal inhibition and the consecutive excitation was determined by computing the cumulative sum of the PSF (PSF-CUSUM, see Figure 6.3b, Section 4.2.3 and Türker et al., 1996). The PSF-CUSUM allows the measurement of subtle but consistent changes in the instantaneous discharge frequency. It was obtained by cumulatively summing the difference between the average baseline frequency ($-300\,\text{ms} \leq \text{time} < 0\,\text{ms}$) and the instantaneous frequency value of each discharge.

The largest absolute deflection of the PSF-CUSUM from zero during the baseline was determined as the significance threshold (error box) for reflex responses (Figure 6.3b, dashed lines). Troughs and peaks exceeding the error box represent significant inhibition and excitation responses. The response amplitude (inhibition or excitation) was defined as the difference between two turning points in the PSF-CUSUM (Figure 6.3b, arrows). The turning points correspond to the start and end points of the monotonous slope of a significant reflex response and were determined manually (Section 4.2.3). We are aware

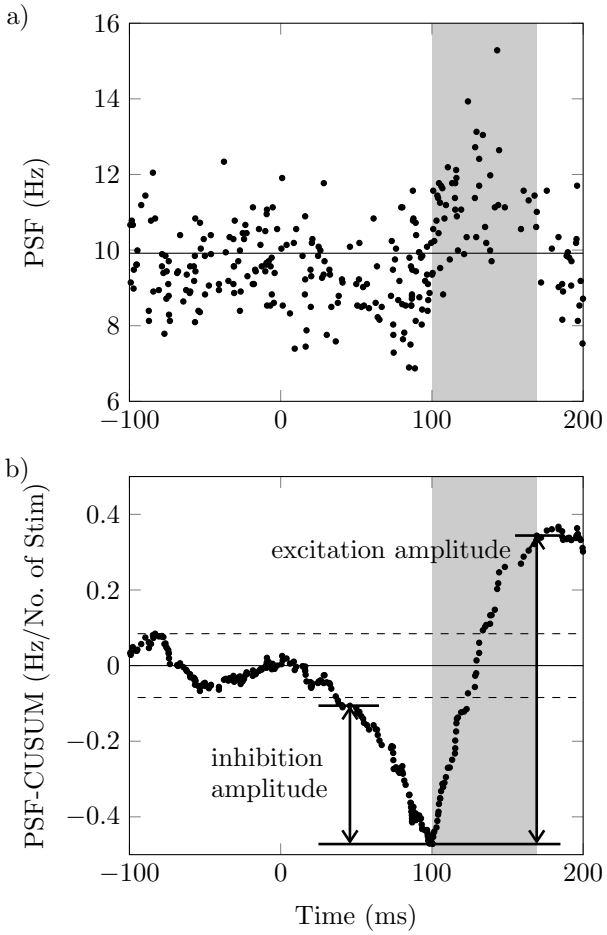

Figure 6.3: Peristimulus analysis for an exemplary selected tibialis anterior motor unit. a) Peristimulus frequencygram (PSF). b) Cumulative sum of PSF (PSF-CUSUM). The electrical stimulus to the tibial nerve was applied at time zero. Solid horizontal lines show prestimulus mean values, and dashed lines mark the significance threshold for reflex responses. Arrows show the distance between manually determined turning points in PSF-CUSUM, i. e., inhibition and excitation amplitude. The period of postinhibitory excitation is highlighted with a grey colour. Data from Yavuz et al. (2018). [modified from Schmid et al. (2024) under CC BY 4.0]

that the duration of the inhibition is relevant. We did not consider the duration since we always used the same IPSC duration. The PSF-CUSUM was normalised by the number of delivered stimuli to compare amplitudes across subjects and trials with different numbers of stimuli. Consequently, the PSF-CUSUM is shown in units of Hz/No. of Stim. It is worth noting that each deflection from zero directly relates to a change in the motoneuron's activity in simulations when the membrane noise is not added.

Recorded motor units were included in the analysis when at least 90 stimuli could be delivered. For simulated neurons, 200 stimuli were applied.

6.3.1 Statistical analysis

Experimentally recorded motor units were grouped according to their response behaviour in the first poststimulus interval. The mean baseline discharge rates and the coefficient of variation of the baseline interspike intervals (CoV ISI) were compared between groups.

The coefficient of variation is defined as the ratio of the standard deviation to the mean.

The simulation results indicated that motor units respond to the inhibitory stimulus with excitation in the first poststimulus interval in a stimulus-time dependent manner (Section 6.4.3). Thus, two groups of motor units were built: motor units with excitation in the first poststimulus ISI and those without excitation in the first poststimulus ISI. A motor unit was considered to show excitation when it responded to at least 10 % of delivered stimuli with a discharge at least one standard deviation higher than the baseline discharge rate. Mean baseline discharge rates and the coefficient of variation of the interspike interval were obtained from the PSF for all motor units. Motor units with a CoV ISI > 35 % were excluded from the statistical analyses (cf. Yavuz et al., 2018). A visual analysis based on a quantile-quantile plot and a histogram, as well as a Shapiro-Wilk test, were used to determine if the data was normally distributed (BenSaïda, 2023). Since the mean baseline discharge rates were normally distributed, they were compared between the groups using a two-sample t-test (MATLAB Version R2021a 9.10.0.2015706). The CoV ISI was compared using a Wilcoxon rank sum test (also Mann-Whitney U test) since the data was not normally distributed (Gibbons and Chakraborti, 2011). In all tests, the significance level was $p < 0.05$.

6.4 Results

First, we will describe the postinhibitory excitation pattern observed in human motor units. Then, we will analyse the conditions under which we observed postinhibitory excitation in the simulated motoneuron. In the simulated motoneuron, we will determine the hallmarks of h-current-mediated postinhibitory excitation. The insights will be used to analyse the experimental data for evidence of h-current activity.

6.4.1 Postinhibitory excitation in human motor units

We examined the incidence and amplitude of postinhibitory excitation in 159 tibialis anterior motor units identified during the reciprocal inhibition experiment, i. e., electrical stimulation of the tibial nerve during sustained isometric contractions. Therefore, we analysed the peristimulus frequencygram (PSF), which shows the instantaneous discharge rates of motor units relative to the stimulus time (Türker and Cheng, 1994). The amplitude of inhibition and excitation responses was determined from the cumulative sum of the PSF (PSF-CUSUM) as described in Section 6.3. PSF and PSF-CUSUM of an exemplary motor unit are shown in Figure 6.3. In the prestimulus period, the PSF-CUSUM is characterised by oscillations around zero (Figure 6.3b). A persistent drop in PSF-CUSUM following the stimulus, which was applied at time zero, indicates the inhibitory response. Notably, the time delay between the electric stimulus and the onset of the inhibition is consistent with the axonal action potential conduction velocity. A subsequent sustained increase in PSF-CUSUM indicates postinhibitory excitation.

In total, 159 motoneurons of 9 subjects were examined. All examined motor units had a significant inhibition response, and the mean inhibition amplitude was 0.67 ± 0.47 Hz/No. of Stim. 89 motor units showed significant postinhibitory excitation, and the mean amplitude of the postinhibitory excitation was 1.80 ± 2.08 Hz/No. of Stim. The mean baseline discharge rate of the analysed motor units was 10.12 ± 1.66 Hz.

6.4.2 Postinhibitory excitation in simulated motoneurons

The results for one exemplary reciprocal inhibition simulation are summarised in Figure 6.4. Thereby, we directly compared the behaviour of the motoneuron model with the h-current present (Figure 6.4a) and the h-current knock-out model (Figure 6.4b). Before applying the inhibitory postsynaptic current (IPSC), both simulated neurons show a stationary baseline activity, i.e., stable mean discharge rate and interspike interval variability. Both motoneurons show an inhibitory response, consisting of a silent period followed by a period of reduced discharge rates, which is apparent by a decrease in the PSF-CUSUM (Figure 6.4c, d). Although the same IPSC was applied to both computational neurons, the inhibition amplitude is larger in the neuron without h-current (1.11 Hz/No. of Stim vs. 0.34 Hz/No. of Stim). After the inhibition, only the neuron with h-current shows a significant excitation response (amplitude 0.33 Hz/No. of Stim).

To investigate the role of different factors in postinhibitory excitation, we simulated reciprocal inhibition of the motoneuron with the h-current under various conditions, i. e., varying the amplitude of the IPSC, the mean drive and the input noise level. Modifying the mean drive and noise level yielded baseline frequencies between 9.99 Hz and 18.52 Hz and a coefficient of variation of the interspike interval ranging from 0 % to 12 % respectively (Table 6.1). Notably, increasing the noise also yields a higher baseline discharge rate. This finding can be explained by the fact that higher random oscillations of the membrane potential are more likely to exceed the depolarisation threshold and, therefore, trigger action potentials at higher firing rates.

For all conditions, the simulated motoneuron showed an inhibition response with inhibition amplitudes ranging from 0.26 Hz/No. of Stim to 1.67 Hz/No. of Stim. However, an excitation response was not always observable. The simulated motoneuron showed postinhibitory excitation amplitudes between 0 Hz/No. of Stim, i. e., no significant excitation response, and 0.64 Hz/No. of Stim. Figure 6.5 summarises the results from all simulations. It can be observed that the excitation amplitude increases with the size of the IPSC. When fixing both the mean drive and the noise level, the relationship between IPSC size and the excitation amplitude can be approximated with a linear regression model, especially for no/low noise and low/medium drive ($98\% < R^2 \leq 99.9\%$, Table 6.1). For a fixed IPSC size, the excitation amplitude was higher for a lower drive, i. e., lower baseline firing rates. Generally, the amplitude of the postinhibitory excitation decreased with increasing noise and disappeared under high noise and medium to high drive conditions.

In summary, postinhibitory excitation could only be observed in simulated neurons with h-currents. Systematically varying the model parameters revealed that the postinhibitory excitation amplitude correlates with the IPSC size. However, the excitation amplitude is modulated by the mean drive and the noise level. Increasing the baseline firing rate or noise decreases the excitation amplitude, even to a degree where excitation is no longer observed, at low noise and high drive or high noise and medium to high drives.

6.4.3 Postinhibitory excitation is stimulus-time dependent

We used the *in-silico* model to mechanistically link the observed postinhibitory excitation responses and the biophysical behaviour of motoneurons. This approach was possible because the simulation allows us to observe all internal system parameters, e. g., the membrane potential trajectory, and relate them to each other. The effect of h-currents

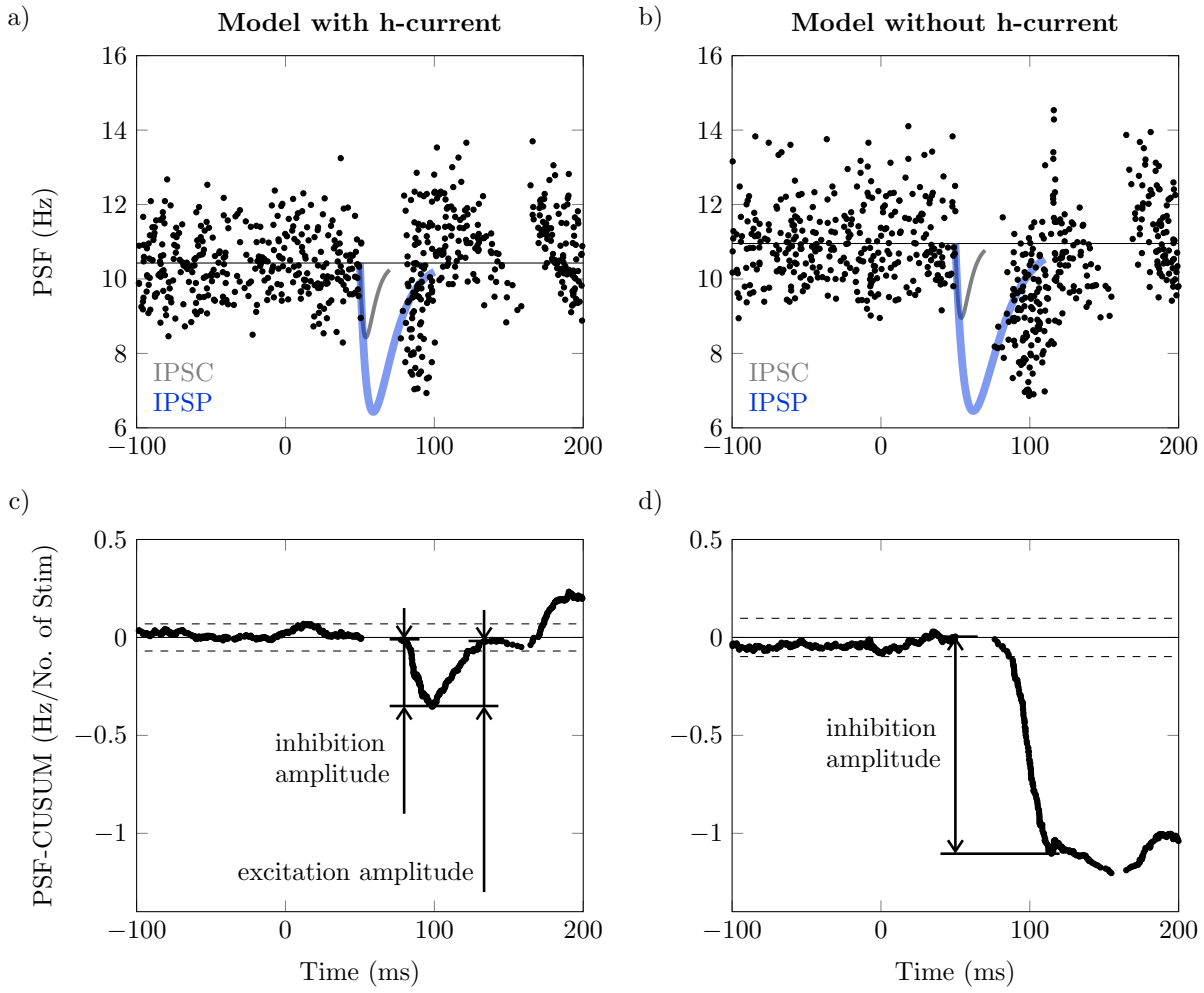

Figure 6.4: Peristimulus analysis for simulated motoneurons. a) Peristimulus frequencygram (PSF) for a simulated neuron with h-current. b) PSF for a simulated neuron without h-current. In (a) and (b), the injected inhibitory postsynaptic current (IPSC) and the schematic trajectory of the induced inhibitory postsynaptic potential (IPSP) are depicted in gray and blue color, respectively. The actual time course of the membrane potential depends on the membrane potential value and the size of other inputs at IPSC application time. c) PSF cumulative sum (PSF-CUSUM) for a simulated neuron with h-current. d) PSF-CUSUM for a simulated neuron without h-current. The time course of the inhibitory postsynaptic current is shown in grey colour (amplitude −10 nA). Solid horizontal lines show prestimulus mean values, and dashed lines mark the significance threshold for reflex responses. Arrows show the distance between two manually determined turning points in PSF-CUSUM, i. e., inhibition and excitation amplitude. [modified from Schmid et al. (2024) under CC BY 4.0]

was isolated by comparing the trajectories of the membrane potential of computational motoneurons with and without h-channel. Here, we considered an exemplary simulation with a low drive and an IPSC amplitude of −10 nA and a duration of 20 ms. To focus on the effect of the h-current, we also omitted noise inputs in these simulations.

The simulations revealed that when applying an inhibitory current pulse, the instantaneous discharge rate of the simulated motoneurons always depends on the time delay between the stimulus-induced inhibitory postsynaptic potential (IPSP) and the previous

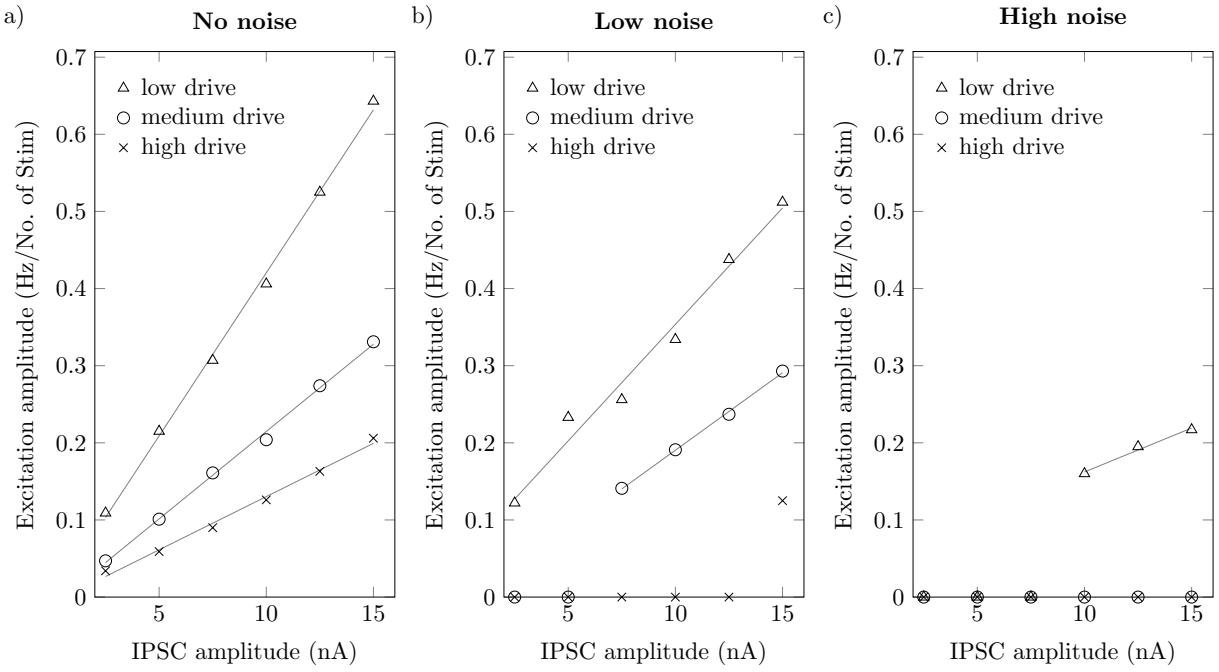

Figure 6.5: Postinhibitory excitation in different simulation settings. Excitation amplitudes in relation to inhibitory postsynaptic current (IPSC) amplitude and for three different baseline discharge rates (low (△), medium (o), and high (x) drive) and with three different amounts of noise (standard deviation 0 % (a), 12.5 % (b) and 25 % (c) of mean drive). Grey lines show linear regressions. [from Schmid et al. (2024) under CC BY 4.0]

Table 6.1: Results of the linear regression analysis. Mean frequency and coefficient of variation of the interspike interval (CoV ISI) of the baseline activity as well as slope and coefficient of determination (R^2) values of the linear regression for nine different combinations of mean drive and noise input are given. Linear regression was performed using the least-squares method, provided that more than one data point was available (otherwise marked with n.a.).

Noise	Drive	Baseline frequency (Hz)	CoV ISI (%)	Slope (Hz/No. of Stim/nA)	R^2
No	Low	9.994	0.048	0.042	0.998
	Medium	13.995	0.069	0.023	0.997
	High	17.994	0.079	0.013	0.993
Low	Low	10.431	8.718	0.03	0.981
	Medium	14.153	6.395	0.02	0.999
	High	18.026	5.98	n.a.	n.a.
High	Low	11.255	12.123	0.011	0.983
	Medium	14.602	10.166	n.a.	n.a.
	High	18.53	10.108	n.a.	n.a.

motoneuron discharge t_{stim} (Figure 6.6). Particularly, the model with h-current showed two opposing responses (Figure 6.6a, b). For large t_{stim} values (Figure 6.6a, green trace), the next action potential was delayed compared to an unperturbed reference simulation (Figure 6.6a, black trace), i. e., the neuron was inhibited. In contrast, for a shorter t_{stim} (Figure 6.6a, blue trace), the interspike interval was shortened compared to the undisturbed reference simulation, i. e., the neuron was excited. Thereby, the amount of postinhibitory excitation depends on the exact timing of the IPSP with respect to the previous spike. The insert in Figure 6.6a shows that the IPSP induced a positive inward ionic current flux that continued even after the end of the IPSP. Thus, the additional depolarisation (blue line above the unperturbed black line) is caused by the h-current. Excitation in response to inhibitory stimuli was observed only in simulations with h-current. In the model without h-current, the IPSP consistently inhibited the neuron. Thereby, later IPSPs that prolonged the interspike interval (large t_{stim}) caused a stronger inhibition than earlier IPSPs (Figure 6.6c, d).

This characteristic time-dependent behaviour of the computational motoneuron with h-current can also be visualised in the PSF and PSF-CUSUM plots. Therefore, the spike trains shown in the PSF plots were clustered into two groups. In detail, we separated spike trains where the instantaneous discharge frequency of the first poststimulus spike was significantly (by more than one standard deviation) higher or lower than the baseline discharge rate. Figure 6.7 shows the same data as previously reported in Figure 6.3 and Figure 6.4. However, spike trains where the first postinhibitory spike shows significant excitation are visualised in blue (excitation cluster). Spike trains where the first postinhibitory spike shows significant inhibition are shown in green (inhibition cluster). The results of an exemplary simulated motoneuron with h-current are shown in Figure 6.7b, e and clearly show distinct excitation and inhibition clusters. This behaviour is also evident from the PSF-CUSUMs of the clustered spike trains (Figure 6.7h). The initial decrease in overall PSF-CUSUM (black) is caused by the inhibition cluster (green). As expected, the timing of the prestimulus spikes indicates that the IPSP was delivered late in the motoneuron's afterhyperpolarisation period (large t_{stim}, cf. Figure 6.6). The initial inhibition is followed by the excitation response (blue) that ultimately predominates the overall PSF-CUSUM. The longer latency of the spikes associated with the excitation cluster, as well as the pattern of the prestimulus spikes, are in agreement with our finding that excitation is observed when the IPSP is delivered early in the afterhyperpolarisation period of the motoneuron (small t_{stim}). In conclusion, it is possible to find evidence for h-current activity using PSF analysis.

Hence, we investigated experimentally recorded motor units that showed significant postinhibitory excitation with the described cluster-based PSF analysis. In total, 45 of 89 motor units with significant postinhibitory excitation showed frequencies significantly higher than the baseline frequency in the first poststimulus interval (to at least 10 % of delivered stimuli). The results for an exemplary chosen experimentally recorded motor unit are shown in Figure 6.7a, d, g. Indeed, one can observe the same characteristic behaviour as for the simulated motoneuron with h-current, i. e., distinct inhibition and excitation clusters, whereby the inhibition precedes the excitation.

The mean baseline discharge rate significantly differed between motor units with and without significant postinhibitory excitation in the first poststimulus interval ($p < 0.01$). The mean discharge rate of the motor units with excitation in the first poststimulus ISI was

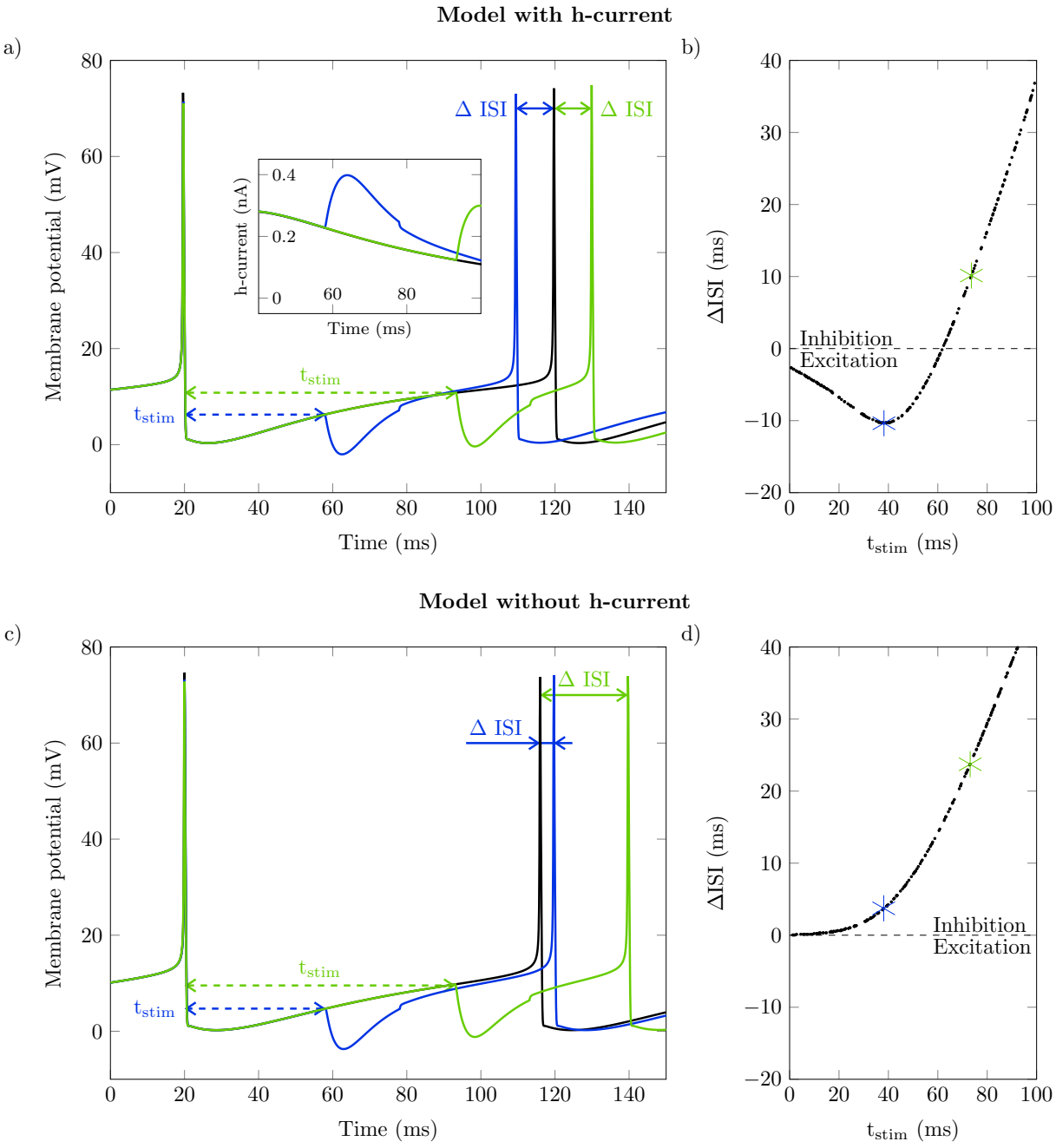

Figure 6.6: Analysis of history-dependent interspike interval duration in simulated motoneurons. Top row: model with h-current, bottom row: model without h-current. Baseline frequency 10 Hz, no noise, inhibitory postsynaptic current (IPSC) amplitude −10 nA. a), c) Membrane potential trajectory without stimulus (black, undisturbed interval) and with stimulus applied at two exemplary time points (blue, green). Dashed arrows mark IPSC application time with respect to the last discharge (t_{stim}), and solid arrows mark the change of the interspike interval with respect to the undisturbed interval (Δ ISI). Insert in (a) shows h-current for the shown interspike intervals between 40 ms and 100 ms. Here, a positive sign indicates current flux into the cell. b), d) Change of interspike interval duration (Δ ISI) over time of IPSC application with respect to the last discharge (t_{stim}). Intervals shown in (a) and (c) are marked with asterisks. Dashed lines separate prolonged interspike intervals (inhibition) from shortened interspike intervals (excitation). [from Schmid et al. (2024) under CC BY 4.0]

with 9.54 ± 1.38 Hz significantly lower than in the motor units that showed no excitation in the first poststimulus interval (10.48 ± 1.69 Hz, Figure 6.8a). In contrast, the CoV ISI between the two groups was not significantly different ($p = 0.21$). The CoV ISI of the motor units with excitation in the first poststimulus ISI was 0.17 ± 0.06 and that of the other units 0.18 ± 0.05 (Figure 6.8b). Note that some motor units showed excitatory discharges in the second poststimulus interval. However, those motor units were not the focus of this work.

The analysis was also performed for the simulated neuron without h-current for completeness. As expected, for the motoneuron without h-current, the number of samples in the excitation cluster is very low and does not cause a relevant excitation response (Figure 6.7c, f, i).

6.4.4 Influence of other model parameters on postinhibitory excitation

The model parameters were varied for exemplary simulation scenarios to assess the robustness of the identified behaviour. All simulations were performed with a stimulus amplitude of 10 nA, and the drive was chosen to result in a baseline firing rate of 10 Hz. First, the parametrisation of the h-channel was varied. Thereby, one parameter each was increased and decreased compared to the default parametrisation. Figure 6.9 shows the stimulus-time dependent shortening/lengthening of the first poststimulus ISI for the default parametrisation (black) and the applied parameter variations.

From all parameter variations applied, changing the time constant showed the most prominent effect (Figure 6.9a) on the interval duration. The fraction and magnitude of shortened ISIs (excitation) considerably increased when applying a reduced time constant. In contrast, a longer time constant slightly reduced the fraction of shortened ISIs. However, note that in the simulation with the prolonged time constant ($\tau_H = 100$ ms) and for very late stimuli, the effect of h-channel mediated current inflow lasted so long that the second poststimulus interval was shortened. Variations in maximum specific conductance and half-maximum activation potential resulted in comparable outcomes (Figure 6.9b, c). With a higher maximum conductance and a more depolarised half-maximum activation potential, the fraction of shortened ISIs increased compared to the default values. Almost no change in ISI length was detectable for stimuli applied shortly after the last action potential. Reducing the reversal potential of the h-channel to more hyperpolarised values increased the fraction of shortened intervals. This effect was more pronounced for stimuli applied shortly after the last action potential.

Second, the motoneuron size properties were varied. A FR-type motoneuron was simulated using the parameters from Cisi and Kohn (2008) (see Table A.4). Since, according to Manuel et al. (2007), larger motoneurons express the resonant behaviour more, the maximum specific h-conductance was doubled in one case and maintained in the other. In Figure 6.10a, it can be seen that none of the modifications had a major influence on the model behaviour.

Third, the influence of PICs on the rebound behaviour was investigated. Following Manuel et al. (2007) we introduced a fast PIC with a time constant of 1 ms and a slow PIC with a time constant of 100 ms. The fast PIC shifted the entire curve to the left, such that the most pronounced shortening of the ISI occurs for smaller t_{stim} values (Figure 6.10b).

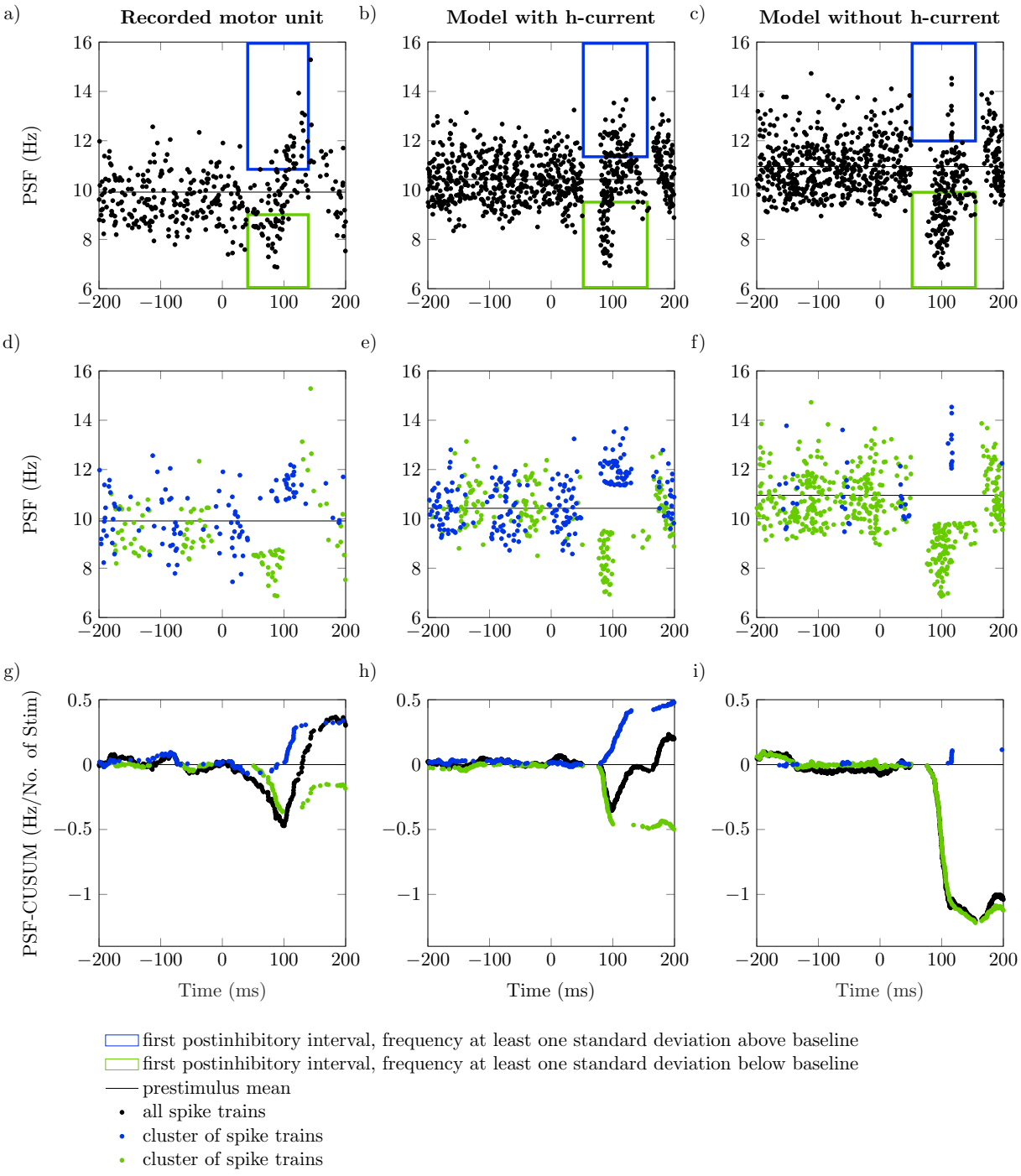

Figure 6.7: Cluster-based analysis of peristimulus frequencygram (PSF). PSF and PSF cumulative sum (PSF-CUSUM) for one experimentally recorded motor unit and a simulated motoneuron with and without h-current (data from Figure 6.3 and Figure 6.4). The blue boxes in panels (a - c) cluster the first postinhibitory spikes that fire at least one standard deviation above the mean baseline frequency (black line). Accordingly, the green boxes cluster all first postinhibitory spikes that fire at least one standard deviation below the mean baseline frequency. d) - f): Clusters of spike trains from which the first poststimulus spikes appear in the blue or green box, respectively. g) - i): PSF-CUSUM of all spike trains (black) and clusters of spike trains (blue, green). [modified from Schmid et al. (2024) under CC BY 4.0]

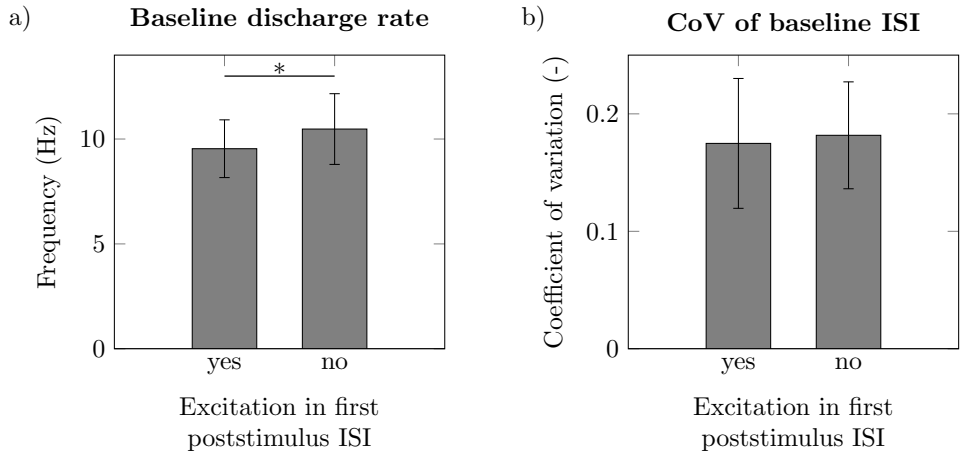

Figure 6.8: Mean baseline discharge rate (a) and mean coefficient of variation (CoV) of the baseline interspike intervals (ISI) (b) of experimentally recorded motor units with and without significant excitation responses in the first poststimulus ISI. The asterisk indicates that mean values are significantly different between groups ($p < 0.01$). Error bars mark standard deviations.

The slow PIC reduced the amount of excitation for all stimulation times.

In summary, reducing the time constant of the h-channel resulted in the most pronounced change in the stimulus-time-dependent interval duration. None of the parameter variations resulted in a change of the qualitative pattern of a stimulus-time-dependent distinction between lengthened and shortened ISIs. Therefore, it can be concluded that h-channels lead, within the tested parameter combinations, to stimulus time-dependent excitation in response to inhibitory stimuli.

6.5 Discussion

We identified an excitatory response that frequently follows a strong reciprocal inhibition in motor units of the human tibialis anterior muscle. For the first time in motor units recorded *in vivo*, we investigated if an intrinsic motoneuron property can cause this phenomenon. Particularly, we hypothesised that a hyperpolarisation-activated inward current (h-current) may be one of the factors that contribute to this excitatory response pattern. Using a computational motoneuron model, we showed that the h-current could lead to an excitation response after an inhibitory stimulus when 1) the IPSP is applied at an appropriate time window in the neuron's integration phase, 2) the IPSP has a sufficiently large amplitude and 3) other inputs to the neuron are small. Further, it was shown that evidence for hyperpolarisation-activated inward current mediated postinhibitory excitation can be tested *in vivo* using cluster-based PSF analysis. The integrated evaluation of both *in-vivo* and *in-silico* data presented within this chapter show that h-currents could be a mechanism that facilitates postinhibitory excitation in motoneurons. These findings challenge an established paradigm that postinhibitory excitation in motoneurons is dominantly caused by reflex pathways and underlines that intrinsic motoneuron properties must be considered when interpreting *in-vivo* reflex experiments.

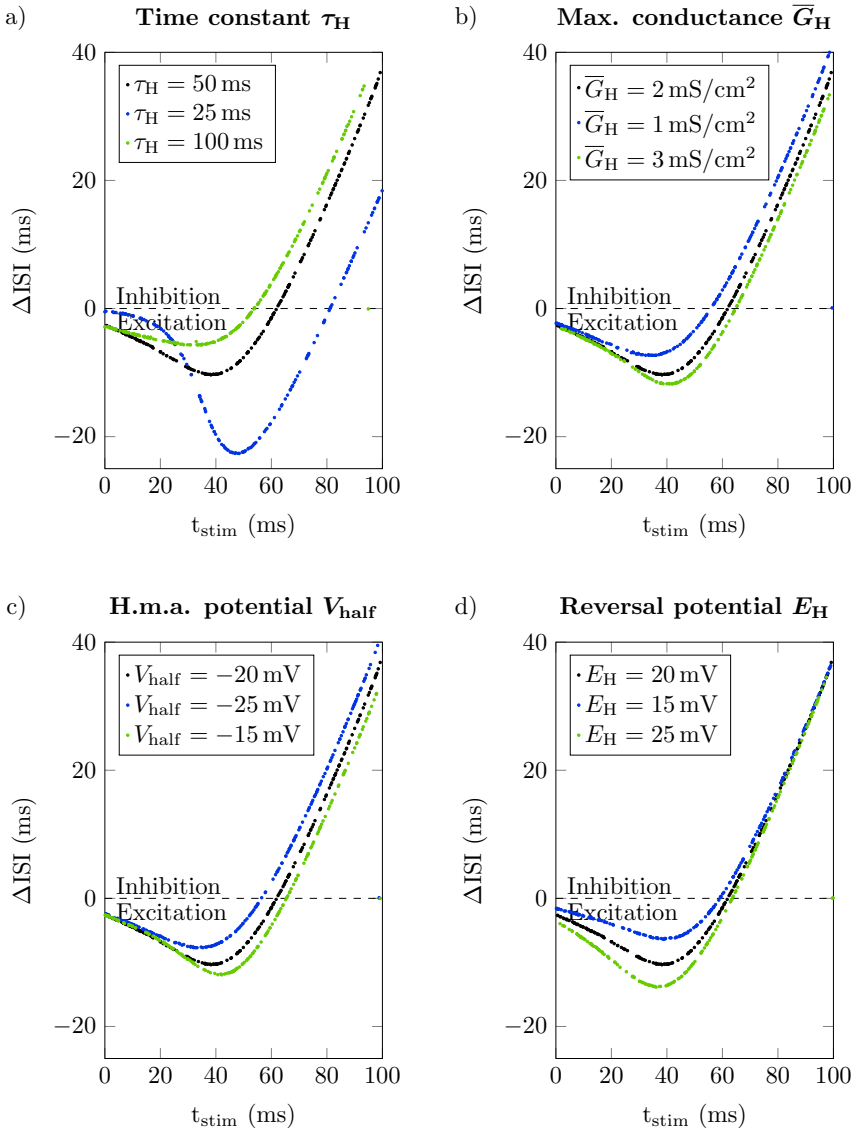

Figure 6.9: Stimulus-time-dependent duration of interspike intervals (ISIs) for different parametrisations of the h-channel. Change of interspike interval duration (Δ ISI) over time of stimulus application with respect to the last discharge (t_{stim}) for chosen default parametristaion of the h-channel (black) and parameter variations for the time constant τ_H (a), the maximum specific conductance $\overline{G}_H$ (b), the half-maximum activation (H.m.a.) potential V_{half} (c) and the reversal potential of the h-channel E_H (d). Lengthened intervals indicate excitation, while shortened intervals indicate inhibition of the respective motoneuron. [modified from Schmid et al. (2024) under CC BY 4.0]

6.5.1 Insights on mechanisms of postinhibitory excitation

A detailed analysis of the *in-silico* experiments showed that h-currents cause a non-linear, history-dependent input-output relation for short inhibitory stimuli. Excitation or inhibition depends on the delay between the applied IPSP and the previous motoneuron discharge. H-currents are activated at hyperpolarised membrane potentials (e. g., Larkman and Kelly, 1992). Counterintuitively, an IPSP can increase the net current influx into the cell. If the IPSP is applied when the motoneuron is close to its depolarisation

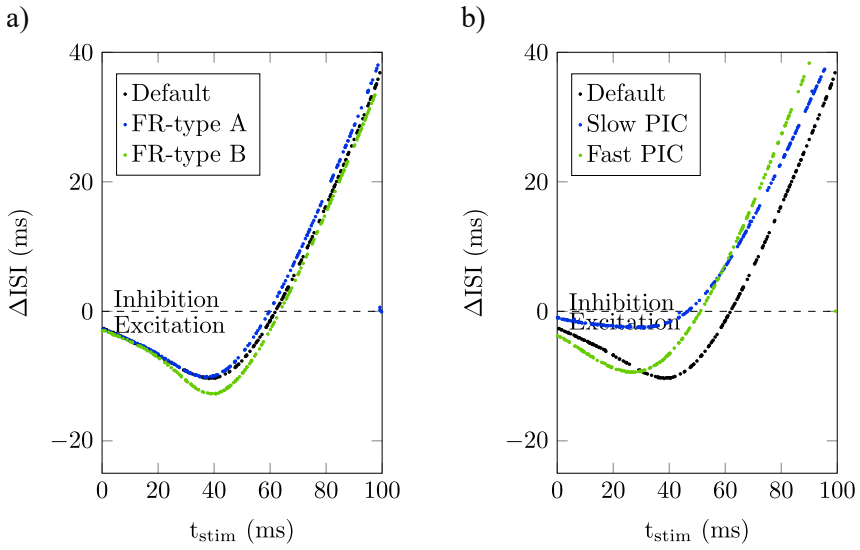

Figure 6.10: Stimulus-time-dependent duration of interspike intervals (ISIs) for different parametrisations of the motoneuron model. Change of interspike interval duration (Δ ISI) over time of stimulus (IPSP) application with respect to the last discharge (t_{stim}). Default parameters are shown in black. a) Variation of the motoneuron size. FR-type motoneurons correspond to motoneurons with size-dependent parameters according to the mean values for FR-type neurons in Cisi and Kohn (2008). Version A and B employ a maximum specific h-channel conductance of $\overline{G}_{H,A} = 2\,\mathrm{mS\,cm^{-2}}$ and $\overline{G}_{H,B} = 4\,\mathrm{mS\,cm^{-2}}$, respectively. b) Influence of persistent inward currents (PICs) injected into the dendrite compartment of the motoneuron model. PIC dynamics according to Manuel et al. (2007). Maximum specific PIC-conductance $\overline{G}_{PIC} = 0.1\,\mathrm{mS\,cm^{-2}}$. Slow PIC: time constant $\tau_{PIC} = 100\,\mathrm{ms}$, reversal potential $E_{PIC} = 140\,\mathrm{mV}$. Fast PIC: $\tau_{PIC} = 1\,\mathrm{ms}$, $E_{PIC} = 120\,\mathrm{mV}$. Baseline frequency 10 Hz, no noise, inhibitory postsynaptic current amplitude $-10\,\mathrm{nA}$. [from Schmid et al. (2024) under CC BY 4.0]

threshold, the instantaneous effect of the IPSP is dominant. Hence, one will observe inhibition. However, if the motoneuron is inhibited earlier in the integration phase, the IPSP-induced additional h-current influx ultimately dominates the IPSP and causes excitation.

Through a cluster-based PSF analysis, the opposing motoneuron responses can be visualised for both *in-silico* and *in-vivo* data. Thereby, spike trains are grouped according to the relative instantaneous discharge rate of the first poststimulus discharge. It was shown that a considerable fraction of the experimentally recorded motor units showed characteristic clusters of both excitation and inhibition. The same patterns were observed for the simulated motoneurons with h-currents. Hence, these findings suggest h-current activity in human motor units.

The model predicted that the excitation response negatively correlates with a motoneuron's firing rate and can even become undetectable at high noise levels. This prediction is in line with our *in-vivo* results. Only those experimentally recorded motor units with comparably low firing rates showed a significant postinhibitory excitation in the first poststimulus interval. In this work, the 'high noise' condition was characterised by a coefficient of variation of the interspike interval ranging from 10 % to 12 %. This range is at the lower end of what was reported for humans (e. g., Matthews, 1996; Moritz et al., 2005). This further explains our finding that the excitation response was not

observable in all investigated motor units. Long inhibitory stimuli in combination with high discharge rates might have also prevented Türker and Powers (1999) from observing excitation in the first poststimulus interval when they used a comparable cluster-based PSF analysis to investigate the effect of large inhibitory postsynaptic potentials in rat hypoglossal motoneurons.

Notably, other factors may modulate h-current mediated postinhibitory excitation. For example, persistent inward currents (PICs) can modulate h-current activity (Manuel et al., 2007). Adding a fast and a slow PIC to the motoneuron model, we could still observe history-dependent excitation (Figure 6.10b). However, Even though PICs were shown to play a minor role during Ia reciprocal inhibition (Pearcey et al., 2020), their role in postinhibitory excitation should be investigated in future studies.

Postinhibitory excitation of motoneurons is a well-known phenomenon that was repeatedly observed both in living humans and for *in-vitro* preparations (e. g., Özyurt et al., 2019; Türker and Powers, 1999; Uysal et al., 2019). However, no consensus regarding the biophysical origin of this phenomenon has yet been firmly established. Previously proposed mechanisms include intrinsic motoneuron properties like summation effects of the ionic channel conductances that are active during the afterhyperpolarisation (Türker and Powers, 1999) or neuronal pathways, e. g., Ia and II stretch reflexes (Özyurt et al., 2019; Uysal et al., 2019). In the presented simulations, we did not consider other neuronal pathways that potentially contribute to the postinhibitory excitation. Notably, the results shown in this work only consider the first poststimulus discharge. On this time scale, the involvement of a neural pathway is unlikely. Nevertheless, we cannot exclude that the electrical stimulation of the nerve excites additional pathways, which cause an excitatory postsynaptic potential with a short delay and reinforce the postinhibitory excitation. Regarding other internal mechanisms, we could observe a mild effect of afterhyperpolarisation summation in the simulations, leading to increased discharge rates of the second poststimulus spike. Further, additional simulations with a longer time constant for the h-channel showed that, under certain circumstances, the h-current could last long enough to slightly increase the frequency of the second poststimulus discharge of the neuron. Due to the uncertainty of the parameters, we refrain from a quantitative comparison with the experimental data. Nevertheless, the notably higher excitation amplitudes in the experimentally recorded motor units indicate that h-currents are not the only mechanism playing a role in the postinhibitory excitation phenomenon.

We conclude that h-currents can facilitate postinhibitory excitation observed at the first poststimulus discharge (e. g., Özyurt et al., 2019; Yavuz et al., 2018). However, other factors must be considered to fully uncover the complex behaviour of motoneurons in response to an IPSP. For example, postinhibitory excitation of the second poststimulus discharge (e. g., Türker and Powers, 1999; Uysal et al., 2019) cannot be fully explained by h-currents.

6.5.2 Limitations

In this study, we used a computer model to assist the interpretation of empirical observations from reflex experiments in living humans. However, measuring all model parameters needed to directly replicate the corresponding *in-vivo* experiment is currently not feasible. Thus, the presented simulations are a simplification of the underlying physiology.

The utilised model reduces the structure of the dendritic tree into a single model compartment and does not explicitly describe all channels found in human motoneurons. Nevertheless, previous studies showed that a two-compartment model with a limited number of conductances can replicate realistic motoneuron firing patterns (Cisi and Kohn, 2008; Negro and Farina, 2011). Adding h-channels yields the simplest model to address the posed research question sufficiently. The h-channel modulates the rheobase of the simulated motoneuron. To compare the model with h-currents and the knock-out model, we adjusted the input current such that both models operate at comparable points of their current-frequency relation. This guarantees that differences are exclusively attributed to h-currents. Specifically, the membrane potential and the ion channel gating variables deviate from each other by less than 10 % on average for identically long interspike intervals. The parametrisation of the h-channel can reproduce the magnitude of membrane potential overshoots in response to hyperpolarising currents steps as observed *in vitro* (Bertrand and Cazalets, 1998; Kiehn et al., 2000). The resulting overall conductivity deviates from *in-vitro* measurements (e. g., Kjaerulff and Kiehn, 2001; Larkman and Kelly, 1992). However, the other conductivities in the model were also chosen to reproduce macroscopic cell behaviour, and thus, they cannot be directly interpreted as channel densities. To compensate for the temperature difference between the *in-vitro* experiment and *in-vivo* conditions, we followed a time-dynamics correction proposed by Powers et al. (2012). Although it is impossible to validate the utilised implementation directly, additional simulations showed that varying the h-channel parameters or motoneuron size does not affect the general behaviour of the model (Figure 6.9, Figure 6.10a).

Reciprocal inhibition indirectly stimulates the motoneurons through the afferent nerve. The magnitude of the inhibitory input to the motoneuron caused by interneurons is unknown. To compare the simulations and experimental data, we chose the amplitude of the injected current such that the inhibition amplitudes and latencies determined from the PSF-CUSUM are in the same range as for the experimental study. In this way, we assume that the injected current produces an IPSP comparable to the *in-vivo* conditions. Nevertheless, a quantitative comparison of the postinhibitory excitation amplitudes of *in-silico* and *in-vivo* motoneurons is beyond the scope of this study, also due to the uncertainties associated with the PSF (see Chapter 5). Contrary to the recommendations from Section 5.4.4, we included motor units with only 90 delivered stimuli for the analysis. Therefore, only the averaged reflex amplitudes across all motor units were considered.

Further, instead of explicitly modelling synapses, the input signals represent effective synaptic currents, i. e., currents that eventually reach the soma. This simplification is reasonable since only these currents affect the generation of action potentials (Heckman and Binder, 1988). Still, injecting the inhibitory stimuli into the soma bypasses h-channels located on the dendrite to a certain extent and, hence, underestimates the effect of h-channels. Synapses for reciprocal inhibition are located close to the soma (Burke et al., 1971; Stuart and Redman, 1990), and thus, the thereby introduced error is assumed to be small.

Postinhibitory excitation is a phenomenon that was repeatedly shown *in vitro* in different species and cell types and attributed to different mechanisms, e.g., h-channels, (calcium-activated) potassium conductances, low threshold sodium conductances, delayed recovery of the sodium inactivation gate (anode break excitation), T-type calcium channels, or N-methyl-D-aspartate (NMDA) receptors (Aizenman and Linden, 1999; Angstadt

et al., 2005; Bertrand and Cazalets, 1998; Dodla et al., 2006; Hodgkin and Huxley, 1952d; Kiehn et al., 2000; Rajaram et al., 2019). One particular strength of computer models is the possibility of studying the influence of an isolated phenomenon. The family of h-channels is a likely candidate as its gating variable shows steep slopes for hyperpolarised membrane potentials, and its time constant allows it to react at the timescale of one interspike interval (Bayliss et al., 1994; Larkman and Kelly, 1992; Powers et al., 2012). Note that anode break excitation can be excluded in our model since the sodium inactivation gate is almost entirely open at resting potential. We cannot rule out the possibility that one or several of these channel mechanisms may also contribute to the postinhibitory excitation in motor units. Nevertheless, it highlights that internal motoneuron properties must be considered to investigate postinhibitory excitation in human motor units.

6.5.3 Functional significance and future directions

We showed that h-current mediated postinhibitory excitation is most pronounced when a motoneuron operates close to its recruitment threshold and for strong inhibitory stimuli. This is an interesting finding regarding the functional significance of h-currents. We speculate that h-currents temporally increase the excitability of a motoneuron and potentially protect a motor unit from derecruitment. In previous studies, h-currents were shown to increase the excitability of human motor axons after hyperpolarisation and to play a role in specific diseases associated with hyperexcitability, e. g., neuropathic pain and restless legs syndrome (Chaplan et al., 2003; Czesnik et al., 2019; Tomlinson et al., 2010). Our results indicate that h-currents can act as an ultra-fast and short-term adaptation mechanism in the motor control system that fine-tunes spinal excitability.

Coupling the motoneuron model with a skeletal muscle model could provide further insights into the functional role of postinhibitory excitation and its influence on, e. g., force steadiness and force variability (e. g., Röhrle et al., 2019). Future modelling studies should further address the possible causes of postinhibitory excitation, each in isolation but in comparison. Nevertheless, the most promising way to quantify the contribution of h-currents to postinhibitory excitation is *in-vitro* studies, also due to the uncertainty of the channel parameters in the model. This study pointed out that choosing evaluation and analysis methods that account for activation history is crucial.

6.5.4 Summary and conclusion

We investigated how hyperpolarisation-activated inward currents (h-currents) can contribute to postinhibitory excitation in human motor units. Using a computational model, we showed that h-currents can shorten interspike intervals in response to strong inhibitory stimuli and, thus, facilitate postinhibitory excitation. This effect is history-dependent and most pronounced in conditions with low firing rates and low noise, i. e., few other inputs. Furthermore, this study showed that intrinsic motoneuron properties must be considered for interpreting reflex responses. The presented PSF cluster method reveals history-dependent effects. Excitation in the first poststimulus interval after reciprocal inhibition was found in a significant portion of the analysed human motor units. According to the simulation results, we speculate that the h-current serves as a modulatory mechanism that increases the excitability of motoneurons.

7 Interfaces for a Monosynaptic Stretch Reflex Model

The monosynaptic connection of muscle spindle primary afferents and α-motoneurons is a distinctive feature of neuromuscular control. Muscle spindles are specialised sensory organs that sense muscle stretch and stretch velocity. When a muscle is stretched, the muscle spindles' afferent signal yields an excitation of the muscles' α-motoneurons and, consequently, of the muscle itself (Kandel et al., 2013). For further details on the stretch reflex, see Section 2.4.2.

The monosynaptic stretch reflex is the only monosynaptic pathway between a sensory organ and α-motoneurons, representing a central element of motor control (Kandel et al., 2013). Further, it is the neuromuscular reflex that is best measurable *in vivo*. This makes the monosynaptic stretch reflex a central component of any computational model of the neuromuscular system that aims to address neuromuscular control strategies.

Combining a model of a motoneuron pool and a muscle spindle model to build a model of the monosynaptic stretch reflex poses some challenges. First, the output variables of muscle spindle models generally do not match the input variables of motoneuron models. In detail, muscle spindle models usually create a frequency as output and motoneuron models take current or voltage as input. Second, the strength of the connection, the so-called gain, has to be determined.

There is no standard procedure for defining spindle-neuron interfaces or determining the gains. In the literature, physiologically meaningless gain factors, as well as different spike-based interface approaches, are used (e. g., Dideriksen et al., 2015; Li et al., 2015; Schouten et al., 2008; Schuurmans et al., 2009; Zhang et al., 2009). The gains are either arbitrarily defined, physiologically informed or fitted to obtain some desired force output (e. g., Dideriksen et al., 2015; Elias and Kohn, 2013; Lin and Crago, 2002a; Raphael et al., 2010; Zhang et al., 2009).

In this chapter, we want to connect the muscle spindle model by Mileusnic et al. (2006) with the motoneuron pool model described in Section 3.4. Thereby, the frequency output of the muscle spindle model needs to be converted into a current value for the motoneuron pool model. We use experimentally determined reflex amplitudes to determine the gain, using the knowledge gained in Chapter 5.

In this chapter, we aim to

(i) compare two approaches for the interface between a spindle model and a motoneuron pool model, namely a conversion factor and a spike-based approach;

(ii) determine the respective gains of both interface approaches based on experimental recordings of the monosynaptic stretch reflex from Yavuz et al. (2014);

(iii) show that the proposed model qualitatively predicts motoneuron responses to different applied stretch patterns (tap, ramp-and-hold, sinusoidal) for both interface types.

The utilised models and the interface approaches are presented in Section 7.1. The data analysis techniques are summarised in Section 7.2. Section 7.3 presents suitable gains

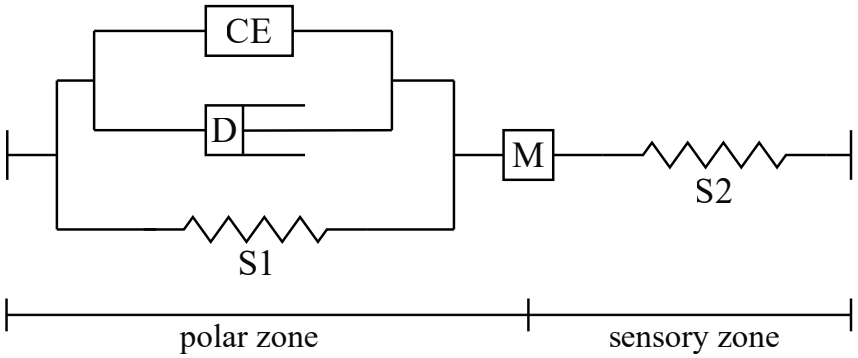

Figure 7.1: Schematic representation of an intrafusal fibre in the muscle spindle model of Mileusnic et al. (2006). CE: contractile element, D: damping element, M: mass, S1: spring in the polar zone, S2: spring in the sensory zone.

for the interfaces and compares the simulation outcomes to experimental data. Finally, implications for future modelling approaches are discussed in Section 7.4.

7.1 Computational modelling of the stretch reflex

The monosynaptic reflex model comprises a motoneuron pool and a muscle spindle model. Those are briefly described in Section 7.1.1 and Section 7.1.2. Two approaches for the interface between the two sub-models are presented in Section 7.1.3 (spike-based interface) and Section 7.1.4 (conversion factor interface).

7.1.1 Muscle spindle model

Muscle spindle primary activity was simulated using the model developed by Mileusnic et al. (2006). The model computes the afferent nerve's firing frequency based on the intrafusal fibres' mechanical behaviour, the muscle fascicle length and the discharge frequencies of the static and dynamic γ-motoneurons, which adjust the spindle sensitivity.

Inspired by the biological structure of the intrafusal fibres, the intrafusal fibre model consists of a sensory and a polar zone (Figure 7.1). The polar zone is modelled as a spring parallel to a contractile element and a damping element. A single spring represents the sensory zone. The polar zone's contractile force and damping coefficient are scaled by γ-motoneuron activity. When a stretch applies to the intrafusal fibre, the mechanical stress in the components determines the length of the polar and the sensory zones. The stretch in the sensory zone is multiplied by a scaling factor, transforming it into a frequency and obtaining the contribution of the intrafusal fibre to the primary afferent firing. All intrafusal fibre types, i. e., bag1, bag2 and chain fibres, are modelled based on the components shown in Figure 7.1. The parameters account for the different properties of the intrafusal fibre types. Obtaining the firing frequency of the primary afferent is a two-step process. First, the frequency contributions of the bag2 and chain fibres are summed and compared to the bag1 frequency contribution. Then, the larger frequency contribution is summed with a fraction of the smaller. This process accounts for the occlusion effect observed in experimental studies (Banks, 1994; Schäfer, 1974).

Where possible, Mileusnic et al. (2006) estimated the model parameters directly from

experimental measurements. The remaining parameters were optimised using cat soleus muscle spindle afferent recordings and validated using cat gastrocnemius medialis muscle spindle afferent recordings. Herein, we adopted all equations and parameters from Mileusnic et al. (2006) and refer to their publication for further details.

7.1.2 Motoneuron pool model

The same motoneuron pool model previously used in Chapter 5 was used here. Motoneurons were simulated using the model developed by Negro and Farina (2011), which is presented in detail in Section 3.4. In brief, each motoneuron is characterised by a two-compartment electric circuit model, representing a soma and a dendrite. The soma compartment includes three voltage-gated conductances (Na^+, slow $K^+$and fast K^+) along with a leakage conductance. The dendrite compartment contains a single leakage conductance.

The parameters were distributed exponentially across the motoneurons to establish a motoneuron pool, as elaborated in Section 3.4.2. Consequently, this pool consists of many small, low-threshold motoneurons and only a few large, high-threshold motoneurons. A total of 200 motoneurons was simulated, corresponding to a typical motor unit count in the human tibialis anterior muscle (Duchateau and Enoka, 2022). This muscle is frequently employed in reflex experiments (e. g., Yavuz et al., 2014, 2018).

7.1.3 Spike-based interface

Considering the muscle spindle model of Mileusnic et al. (2006) and the α-motoneuron pool model of Negro and Farina (2011), a frequency signal has to be converted into an electrical current, which is injected into the α-motoneurons. Inspired by the physiological principle of cell-to-cell communication via action potentials, we use a spike train as the interface variable. In other words, the time-continuous frequency signal is converted into a discrete spike train that contains the time points of the muscle spindle afferent action potentials. Then, the spike train is converted into a train of current kernels, which serves as input for the motoneurons.

We assumed a pool of 50 muscle spindles, all receiving the same stretch input. In human muscles, we would expect more spindles; however, since the motoneuron pool is fitted to cat data, we selected a number typical for cat hindlimb muscles (Banks, 2006). Noise was imposed on the afferent frequency of each muscle spindle to account for variations within the spindle pool. In detail, the resulting coefficient of variation (CoV) of the spindle interspike intervals, which is defined as the ratio of the standard deviation to the mean, matches experimental data, i. e., 8 % in the absence of fusimotor drive (Burke et al., 1979). Therefore, an initial randomisation factor was defined for every spindle from a normal distribution with a mean one and a standard deviation of 0.08.

Transforming the continuous frequency into a spike train is visualised in Figure 7.2. In each time step and for every spindle, the duration of the current interspike interval is computed and multiplied by the respective randomisation factor. Then, the time since the last spike t_{lastAP} is compared to the current interspike interval duration for every spindle. If the difference between the current time and t_{lastAP} is smaller than the current interval duration, no spike is generated (Figure 7.2a). If the difference between the current time

and t_{lastAP} equals or exceeds the current interval duration, a spike is generated and written to the spindle spike train (Figure 7.2b). Now, t_{lastAP} is updated by the current time and a new randomisation factor is drawn (Figure 7.2c). Finally, the spike is delayed by the afferent conduction time (see Section 7.1.5). Note that at the beginning of the simulation, t_{lastAP} is initialised to a (theoretical) time point in the past based on the interspike interval duration calculated from the spindle frequency at the initial length.

Each spike resulting from the spindle activity induces a postsynaptic current (PSC) kernel in the motoneurons. We model the PSC kernel in the shape of an exponential decay with a time constant of 0.5 ms, a duration of 10 ms and variable gain I_0 (Finkel and Redman, 1983). The current kernel for one spindle i, PSC_i, yields

$$PSC_i = I_0 \exp\left(\frac{t}{0.5\,\mathrm{ms}}\right), \quad i \in [1, 50] \; . \tag{7.1}$$

The postsynaptic current is obtained by convolving the spike train with Equation (7.1). Since muscle spindles send their feedback to most motoneurons from a pool, the PSCs from all 50 spindles are linearly summed (Lucas et al., 1984; Mendell and Henneman, 1971; Powers and Binder, 2000). As the weighting of muscle spindle feedback across α-motoneuron pools is still under debate (see e. g., Section 5.4.5 and Awiszus and Feistner, 1993; Binboğa and Türker, 2012; Heckman and Binder, 1988; Mazzocchio et al., 1995; Semmler and Türker, 1994), we assume a uniform weighting, i. e., each muscle spindle is similarly connected to every α-motoneuron. Consequently, the gain I_0 is a uniform parameter. This choice is discussed in Section 7.4.2.

7.1.4 Conversion factor interface

The second approach for the interface between the muscle spindle and the motoneuron model employs a simple conversion factor. The continuous spindle feedback value f_{spindle} in units of Hz is multiplied by a physiologically meaningless factor y, making it suitable as the motoneuron input. The factor y must be chosen of a magnitude so that the resulting value is in the range of nA. The postsynaptic current PSC yields

$$PSC = y\, f_{\mathrm{spindle}} \; . \tag{7.2}$$

The respective conduction time delays the resulting postsynaptic current value according to Section 7.1.5. Note that the conversion factor y represents both the gain and the size of the spindle pool. That means that considering a single representative muscle spindle is sufficient.

7.1.5 Simulation of the stretch reflex

The stretch reflex experiments by Yavuz et al. (2014), to which we compare the simulation results, were performed at not more than 20 % of the maximum voluntary contraction (MVC) force. We simulated low-force muscle contraction by stimulating the entire α-motoneuron pool with a common input. It consists of a constant input of 5.1 nA and a band-pass filtered Gaussian noise component (amplitude 0.00 ± 1.02 nA, 15 Hz to 35 Hz, Negro and Farina, 2011). Further, each α-motoneuron receives an individual input signal to account for the stochastic behaviour of the membrane dynamics and individual synaptic

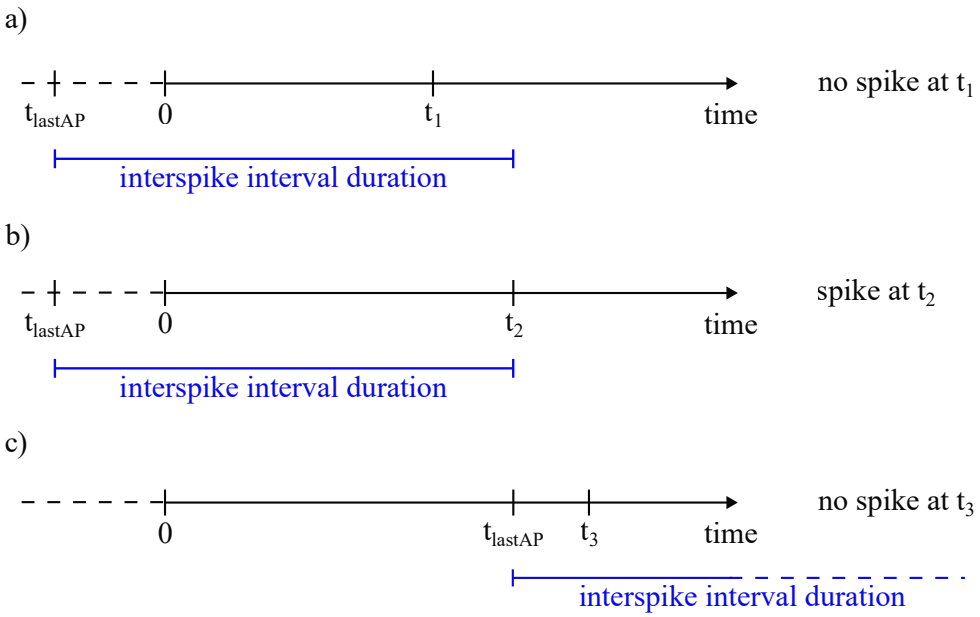

Figure 7.2: Visualisation of the frequency to spike train conversion. a) The time difference between the current time t_1 and the time of the last action potential t_{lastAP} is smaller than the current interspike interval duration (blue). Thus, no spike is produced at t_1. Note that t_{lastAP} is initialised to correspond to a time prior to the start of the simulation. b) The time difference between t_2 and t_{lastAP} equals the current interspike interval duration. Thus, a spike is produced at t_2. c) t_{lastAP} was updated to correspond to t_2. The time difference between t_3 and t_{lastAP} is smaller than the current interspike interval duration. Thus, no spike is produced at t_3.

connections (amplitude 0.000 ± 0.255 nA, low-pass filtered Gaussian noise < 100 Hz, Negro and Farina, 2011). The filtering was performed with a first- and second-order Butterworth filter, respectively (Rao and Swamy, 2018).

The stretch stimuli applied to the muscle spindle model mimic the mechanical perturbations applied to the ankle joint in the experimental recordings by Yavuz et al. (2014). Three perturbations were applied: a tap-like, a ramp-and-hold and a sinusoidal stretch. The stretch amplitude, velocity and duration used in the experimental study and the corresponding values for the simulation are displayed in Table 7.1. We omitted the fusimotor drive since its activity patterns in humans are still unknown (Macefield and Knellwolf, 2018). Further, due to the low conduction velocity of γ-axons of less than $45\,\mathrm{m\,s^{-1}}$, we expect no significant changes in the fusimotor drive during reflex responses (Kandel et al., 2013; Macefield and Knellwolf, 2018).

The mechanical stimuli were applied 200 times per simulation experiment and with an inter-stimulus interval of 1000 ± 100 ms. The total motoneuron input corresponds to the sum of the common and individual input signals representing muscle contraction and the postsynaptic current emerging from the presented interfaces.

The afferent pathways between muscle spindles and motoneurons and the efferent pathways between motoneurons and the neuromuscular junctions delay the transmission of action potentials. We assumed a one-way anatomical length of the pathways of 1.2 m and normally distributed afferent conduction velocities of $105 \pm 10\,\mathrm{m\,s^{-1}}$ for the afferent pathways (Heckman and Binder, 1988; Hunt, 1954). This yields conduction times of 11 ± 1 ms. The conduction velocities of the efferent pathways between the α-motoneuron pool and

Table 7.1: Mechanical perturbation parameters for the muscle spindle model. Parameters from the experimental study by Yavuz et al. (2014) are provided for comparison. The velocity of the sinusoidal perturbation is not constant but emerges from the derivative of the sinus function.

Stretch type	Experiment			Simulation		
	Amplitude	Velocity	Duration	Amplitude*	Velocity**	Duration
Tap	1°	100 ° s^{-1}	0 ms	0.3 mm	60 mm s^{-1}	10 ms
Ramp-and-hold	4°	200 ° s^{-1}	400 ms	1.2 mm	60 mm s^{-1}	420 ms
Sinusoidal	1°	n.a.	100 ms	0.3 mm	n.a.	100 ms

*In the muscle spindle model by Mileusnic et al. (2006), the fibre stretch was calculated relative to the optimal fibre length. We assumed an optimal fibre length of 45 mm, a fibre length range of 37 mm to 60 mm for ankle joint angles between −30° and 45° and a linear relation between fibre length and joint angle (Maganaris, 2001). Consequently, a joint rotation of 1° corresponds to a fibre stretch of 0.3 mm.

**The velocity input for the spindle model was calculated by MATLAB's gradient function. Even though the spindle model takes acceleration as an input, we set the acceleration to zero. The sharp transitions in the modelled perturbation lead to acceleration peaks, which produce unphysiologically high firing rates.

the neuromuscular junctions, i. e., where the spike trains are registered for evaluation, are exponentially distributed and range from 70 m s^{-1} to 100 m s^{-1} (Heckman and Binder, 1988; Zengel et al., 1985). Accordingly, the efferent conduction delays were exponentially distributed across the α-motoneuron pool from 12 ms to 17 ms.

7.1.6 Numerical implementation

All simulations were performed with MATLAB R2021a (9.10.0.1602886). The motoneuron model is represented by a system of six ordinary differential equations, which was solved with MATLAB's ode23 (single-step, explicit Runge-Kutta solver, Shampine and Reichelt, 1997), an integration interval size of 0.1 ms and an absolute and relative error tolerance of 1×10^{-5}. The muscle spindle model requires solving a system of differential algebraic equations. We chose an integration interval size of 1 ms and MATLAB's ode15s solver (variable-step, variable-order solver, Shampine and Reichelt, 1997) with an absolute and relative error tolerance of 1×10^{-5}.

The motoneuron and the muscle spindle model were not solved with a common time step size but successively. The solving scheme is depicted in Figure 7.3. First, the spindle feedback is calculated for one time step and added to the motoneuron drive. Then, the motoneuron pool behaviour is computed for the same time span but in smaller time steps.

The simulation was parallelised to reduce computation time, dividing the total number of stimulus cycles by the number of cores. The mean inter-stimulus interval of 1000 ms provided sufficient time for motoneurons to return to a steady state. Thus, we assumed that cycles are independent of each other. The initial state of the motoneuron pool was consistent across all cores. The perturbation times, the common drive, and the independent drive were initialised differently on each core. The simulation was executed on five cores, each handling 40 stimuli.

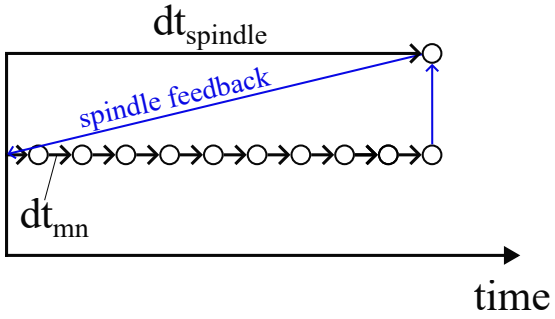

Figure 7.3: Time stepping scheme of the stretch reflex simulation. After every iteration of the muscle spindle model with time step $dt_{spindle}$, the spindle feedback is forwarded to the motoneuron model. Then, ten iterations of the motoneuron model are performed with time step dt_{mn}.

7.2 Data analysis

We compared the simulation results to experimental stretch reflex data from short-latency responses in human tibialis anterior muscles (Yavuz et al., 2014). Therefore, we applied peristimulus analysis to simulated motoneuron spike trains. In detail, we calculated the peristimulus frequencygram (PSF), i. e., showing the instantaneous discharge frequencies with respect to the timing of the stimulus, and the peristimulus timehistogram (PSTH), i. e., depicting the number of discharges per time bin with respect to the timing of the stimulus. We considered a prestimulus time of 400 ms, a poststimulus time of 250 ms and a bin width of 1 ms. The reflex strength was quantified by the reflex amplitude, which was determined from the cumulative sum (CUSUM) of the peristimulus graphs. For further details on peristimulus analysis, see Section 4.2. The algorithms described in Section 4.3 were employed to determine the reflex amplitudes. The slope algorithm was used for tap-like stretch stimuli, while the turning point algorithm was used for the ramp-and-hold simulations (due to better performance in this setting). The responses to the sinusoidal stretch were only qualitatively evaluated since this stretch pattern causes a so-called long lasting excitation instead of a short-latency response Yavuz et al. (2014).

Based on the results of Chapter 5, we concluded that the reflex amplitudes obtained from the PSTH are more suitable for conclusions on the size of the motoneuron input than the reflex amplitudes determined from the PSF. Thus, we used the PSTH reflex amplitudes to determine the gains. Nevertheless, the PSF and PSF-CUSUM were qualitatively compared to experimental data. We further showed that the reflex amplitude of a single motoneuron is not representative of the pool. Since the applied activation of the motoneuron pool is small, i. e., yielding less than 20 % MVC, all active motoneurons were assumed to have relatively similar properties and can be summarised. Thus, we considered the mean reflex amplitude from the entire pool. Motoneurons with irregular firing patterns, i. e., with a CoV of their interspike interval (ISI) of more than 35 % or a baseline discharge frequency of less than 12 Hz, were excluded from the analysis.

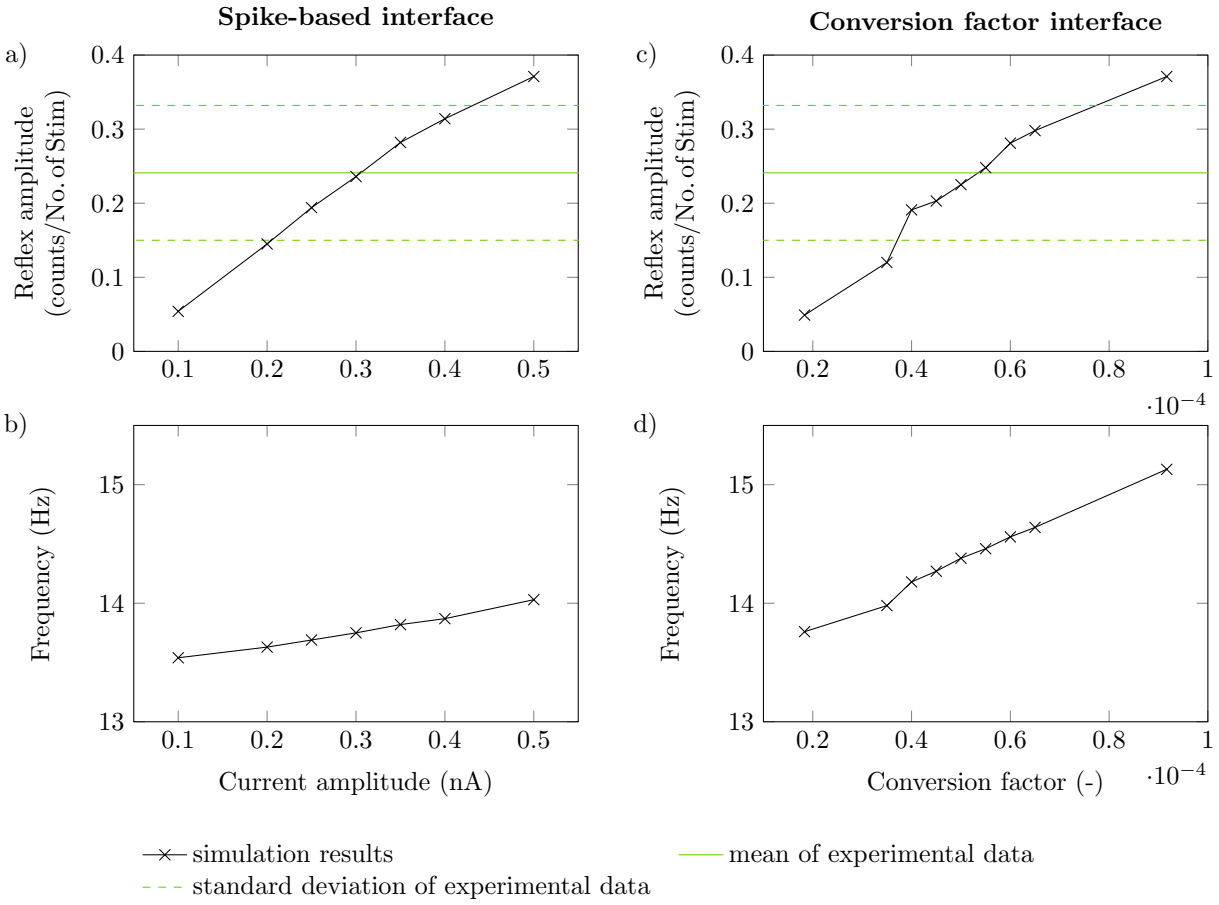

Figure 7.4: Mean peristimulus timehistogram (PSTH) reflex amplitudes of the motoneuron pool with two interface versions and different gains. a) Mean PSTH reflex amplitude from simulations with the spike-based interface. b) Mean baseline discharge frequency from simulations with the spike-based interface. c) Mean PSTH reflex amplitude from simulations with the conversion factor interface. d) Mean baseline discharge frequency from simulations with the conversion factor interface.

7.3 Results

First, we compared the simulated reflex amplitudes obtained from the PSTH and for a tap-like mechanical stimulus with experimental data to determine the gain amplitudes for both interface approaches. Then, with the determined gains, the PSTH and the PSF obtained with both interfaces were compared to experimental data for the tap-like, ramp-and-hold and sinusoidal stimulus.

7.3.1 Determination of the interface gains

The mean reflex amplitudes in the PSTH-CUSUM and the mean baseline discharge frequencies were investigated for different gain values and both interface approaches. From each simulation experiment, approximately 100 motoneurons were included in the analysis, varying with the chosen gain.

The mean reflex amplitudes and baseline discharge frequencies obtained with the two interface approaches are depicted in Figure 7.4. The spike-based interface leads to stronger

reflex responses for a similar baseline frequency than the conversion factor interface. The applied range of gain values produces similar reflex amplitudes with both interfaces. However, the baseline frequencies increase more with the conversion factor interface, indicating that the spike-based interface contributes less to the baseline frequency and more to the reflex response.

The mean amplitude of the short-latency response in the experimental data was 0.241 ± 0.091 counts/No. of Stim (Yavuz et al., 2014). For the spike-based interface, a PSC amplitude of 0.3 nA gave the best agreement with the experimental data (reflex amplitude 0.236 counts/No. of Stim, baseline frequency 13.75 Hz, CoV ISI 11.6 %). For the conversion factor interface, a gain factor of 5.5×10^{-5} gave the best agreement (reflex amplitude 0.248 counts/No. of Stim, baseline frequency 14.46 Hz, CoV ISI 10.8 %). Notably, for a relatively large range of gain values, the reflex amplitudes of the simulated motoneurons are within one standard deviation of the experimental data (approximately ± 30 to 40 % gain from the best match).

The results shown in the following sections were all obtained with the best matching gain value, i. e., 0.3 nA for the spike-based interface and 5.5×10^{-5} for the conversion factor interface.

7.3.2 Comparison with experimental data: tap stimulus

The tap-like stretch pattern, the resulting muscle spindle frequency and the postsynaptic current for both interfaces are shown in Figure 7.5a, d, g. Between stimuli, a baseline stretch of one is applied, which yields a baseline spindle frequency of approximately 11 Hz. A sharp peak characterises the tap-like perturbation, also reflected in the spindle frequency. The maximum spindle frequency reached for the tap perturbation was 81.9 Hz.

The PSTH and its CUSUM for an exemplary recorded motor unit and a motoneuron from simulations with both interfaces are shown in Figure 7.6a-d. Both simulations produce very similar results. The peaks in the PSTH and the PSTH-CUSUM are almost the same size. The latency of the response is shorter with the spike-based interface. Due to the different numbers of applied stimuli, absolute PSTH values cannot be compared to experimental data. However, the size of the peaks in the normalised PSTH-CUSUM is comparable in the experiment and the simulation. In both the experiment and simulation, the PSTH peak is followed by a silent period, corresponding to a CUSUM decline.

For the same motoneurons, the PSF and PSF-CUSUM are shown in Figure 7.6e-h. The baseline discharge frequency is higher in the simulated data. However, the qualitative pattern is similar, i. e., the frequency increases after the stimulus and a delay, followed by a silent period and the return to the baseline. As in the PSTH, the peak appears with a shorter latency using the spike-based interface. The peak in the PSF-CUSUM is considerably higher with the conversion factor interface than with the spike-based interface, but both peaks are higher than in the experimental data. After reaching the peak, the CUSUM stays elevated in both simulation and experiment.

In summary, the experiment and the simulations show qualitatively similar patterns in the PSTH and the PSF. Matching peak sizes of the PSTH were expected since the PSTH reflex amplitude was used to determine the gains. With the chosen settings, the simulation overestimates the PSF peak size.

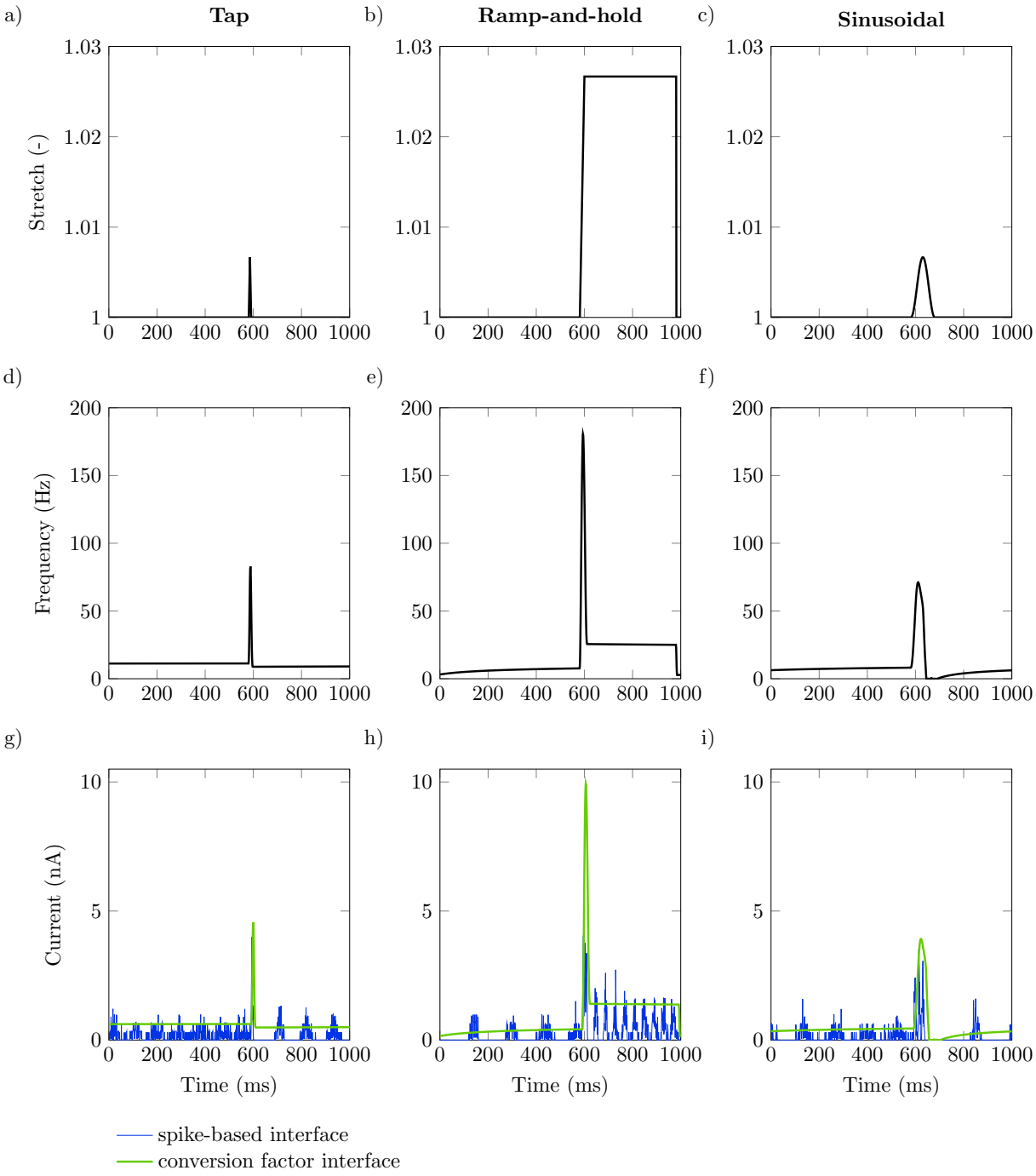

Figure 7.5: Fibre stretch, Ia afferent feedback and postsynaptic current for three perturbation types. a) - c) Fibre stretch applied during tap, ramp-and-hold and sinusoidal perturbations. d) - f) Muscle spindle Ia afferent frequency for the respective perturbation types. g) - i) Postsynaptic current with the spike-based interface (blue) and the conversion factor interface (green) for the respective perturbation types.

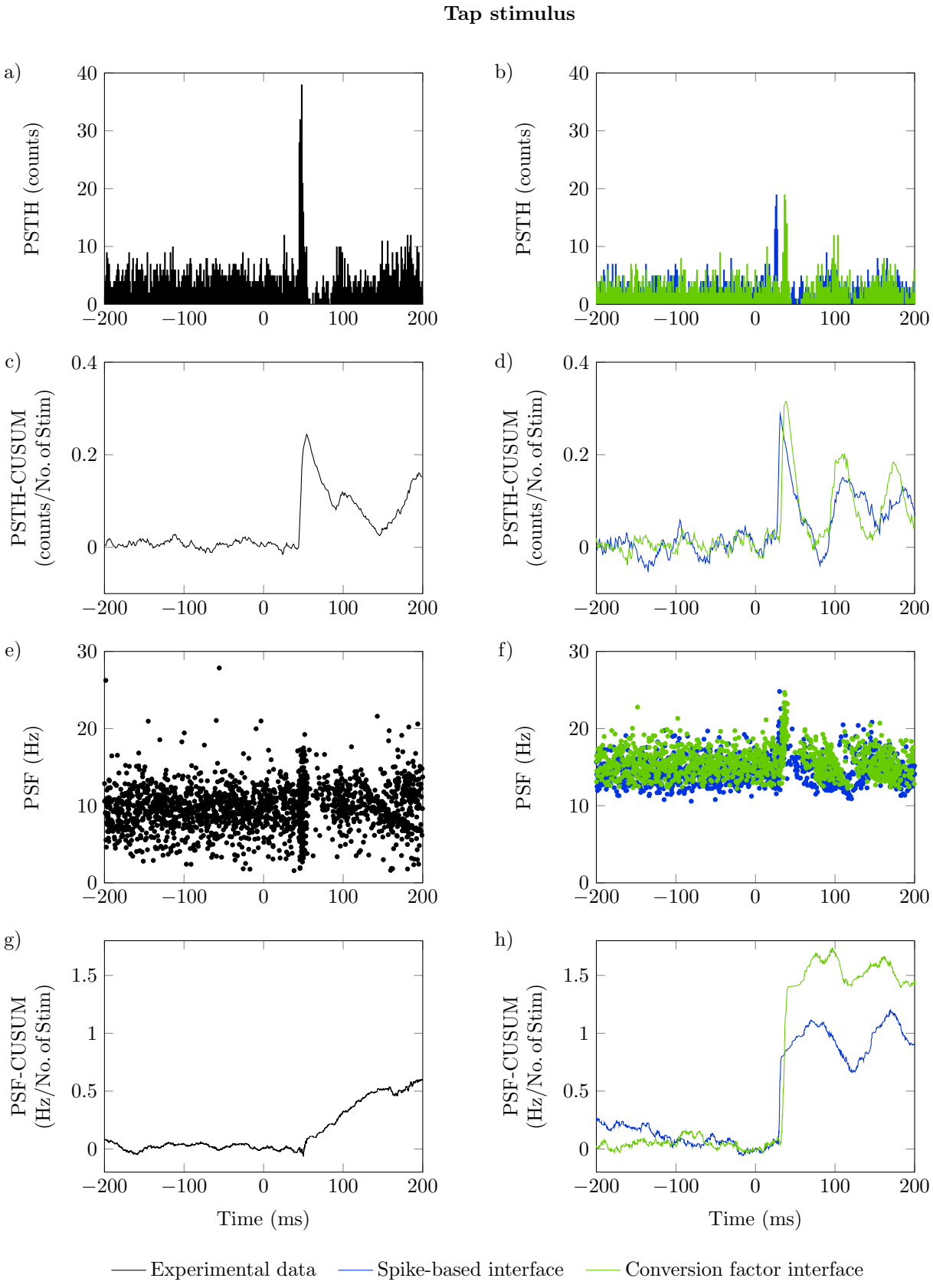

Figure 7.6: Peristimulus analysis for a tap-like stimulus. Peristimulus timehistogram (PSTH) of an exemplary recorded motor unit (a) and a simulated motoneuron with spike-based and conversion factor interface (b). PSTH-CUSUM of the same recorded motor unit (c) and simulated motoneuron (d). Peristimulus frequencygram (PSF) of the same recorded motor unit (e) and simulated motoneuron (f). PSF-CUSUM of the same recorded motor unit (g) and simulated motoneuron (h). Experimental data by Yavuz et al. (2014).

7.3.3 Comparison with experimental data: ramp-and-hold stimulus

When the ramp-and-hold type of stimulus was applied, the spindle frequency increased rapidly to a maximum of 179.6 Hz during the ramp phase (Figure 7.5e). During the hold phase, the spindle frequency plateaued at 25.5 Hz and declined to baseline values after the release of the stimulus. Spindle frequencies reached up to 7.6 Hz during the baseline period.

In the recorded human motor units, the mean reflex amplitude of the short-latency response to a ramp-and-hold stimulus was 0.358 ± 0.163 counts/No. of Stim (Yavuz et al., 2014). In the simulation with the spike-based interface, the mean reflex amplitude was with 0.301 counts/No. of Stim slightly smaller than in the experiment. In contrast, the mean reflex amplitude with the conversion factor interface was with 0.423 counts/No. of Stim slightly higher than in the experiment. Note that the reflex amplitudes from the simulated motoneurons were obtained using the turning point algorithm (see Section 4.3).

The PSTH for an exemplary recorded motor unit and a simulated motoneuron is shown in Figure 7.7a-d. All graphs show a pronounced poststimulus peak followed by a silent period. After that, smaller peaks indicate synchronisation, which is more pronounced in the simulation. With the conversion factor interface, the short-latency peak is higher and broader than with the spike-based interface. This difference is also reflected in the CUSUM.

The PSF and PSF-CUSUM for the ramp-and-hold perturbation are shown in Figure 7.7e-h. As with the tap-like stimulus, the baseline frequency is higher in the simulations. Both simulated and recorded motoneurons show a pronounced peak followed by a silent period. Then, discharge frequencies gradually return to baseline, which is more distinct in the recorded motor unit. Further silent periods occur, especially in the simulation, indicating motoneuron synchronisation. The maximum firing frequencies with the conversion factor interface are considerably higher and reach values similar to those of the recorded motor unit. Several successive saddle points characterise the PSF-CUSUM curves. Thereby, the value of the first saddle point of the spike-based interface is comparable to the first saddle point of the experiment. The first saddle point of the conversion factor interface is much higher and reaches values comparable to the second saddle point of the recorded motor unit.

7.3.4 Comparison with experimental data: sinusoidal stimulus

When a sinusoidal stretch was applied to the muscle spindle model, the frequency increased to a maximum of 71.2 Hz, then decreased and, after an undershoot, gradually returned to baseline values of approximately 8.1 Hz (Figure 7.5f). Thereby, both the ascent and the descent are less steep than with the tap or ramp stimulus. This lack of steepness is also why one cannot determine a short-latency response. Therefore, we only qualitatively compare the outcomes to experimental data.

Figure 7.8a-d shows the PSTH and PSTH-CUSUM for an exemplary recorded motor unit and simulated motoneuron. With a delay after the stimulus, the PSTH increases, which is better visible in the CUSUM graph. The PSTH and the CUSUM time courses are comparable for the simulations and the experimental recording. The conversion factor interface gives a higher reflex response when comparing the interfaces.

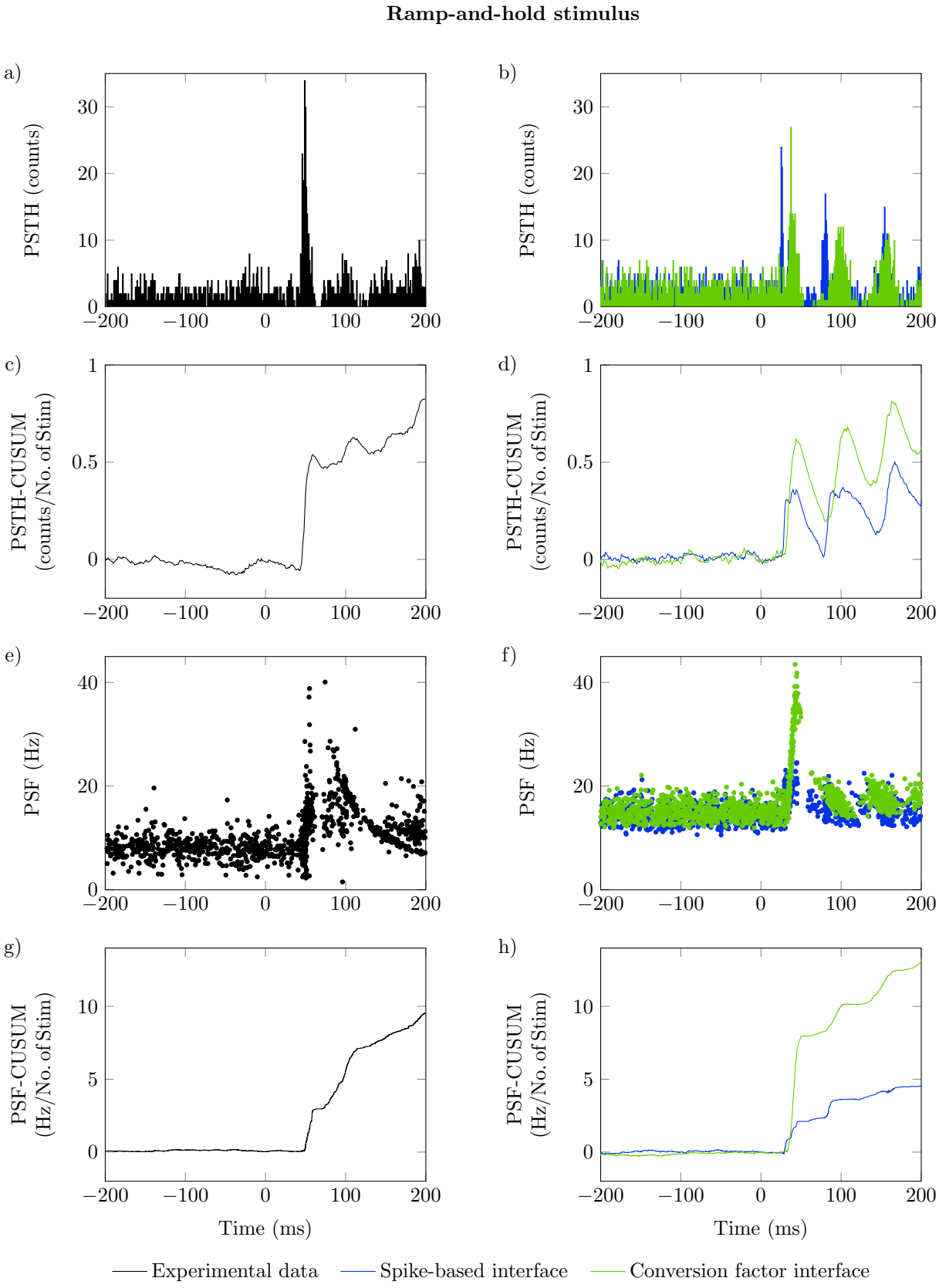

Figure 7.7: Peristimulus analysis for a ramp-and-hold stimulus. Peristimulus timehistogram (PSTH) of an exemplary recorded motor unit (a) and a simulated motoneuron with spike-based and conversion factor interface (b). PSTH-CUSUM of the same recorded motor unit (c) and simulated motoneuron (d). Peristimulus frequencygram (PSF) of the same recorded motor unit (e) and imulated motoneuron (f). PSF-CUSUM of the same recorded motor unit (g) and simulated motoneuron (h). Experimental data by Yavuz et al. (2014).

The PSF and PSF-CUSUM also agree qualitatively between simulations and experimental recordings (Figure 7.8e-h). Here, the conversion factor interface also produces a higher reflex response.

7.4 Discussion

This chapter investigated different options for designing the coupling between the muscle spindle model by Mileusnic et al. (2006) and the motoneuron pool model by Negro and Farina (2011). Although the muscle spindle model of Mileusnic et al. (2006) is computationally demanding, requiring the solution of a system of differential algebraic equations, its comprehensiveness makes it the model of choice. By using the relative stretch of the muscle fibres rather than the absolute length as input, the Mileusnic model can be applied to different muscles. In addition, it reproduces experimental data very well over a wide range of stretch scenarios by accounting for rate saturation and non-linear occlusion. For a more elaborate discussion of the individual models, please refer to the original publications (Mileusnic et al., 2006; Negro and Farina, 2011).

We compared two different interface approaches to couple the models. One approach was based on a conversion factor, and the other mimicked the physiological process of spike train generation. We were able to show that both approaches, with appropriate gains, can well predict the short-latency response of the monosynaptic stretch reflex in response to a tap-like perturbation. With the gains determined from the tap experiment, reflex responses to ramp-and-hold and sinusoidal stretches could be predicted qualitatively but not quantitatively.

7.4.1 Comparison of interface approaches and gain determination

Using both interface approaches, we could reproduce the experimentally determined reflex amplitudes in response to a tap-like stimulus. However, for the same amplitude, the baseline frequency and the CoV of the interspike interval were higher with the spike-based interface. This discrepancy can be attributed to the additional noise generated by the randomised spikes. In both interface configurations, an increased gain leads to higher reflex amplitudes and baseline frequencies. Nevertheless, this relationship was not linear, which can be attributed to the non-linear current-frequency relation of motoneurons (see Section 3.4.3). The reflex latency was shorter with the spike-based interface as increasing the spindle frequency triggers a spike quickly, whereas the effect gradually accumulates with the conversion factor.

Regarding the gain determination, we chose the stretch reflex amplitude as the target parameter in this work. In Chapter 5, we showed that a single motoneuron's reflex amplitude is not representative of the pool. Thus, we considered the mean reflex amplitude of all simulated motoneurons and recorded motor units. We only used the reflex amplitude determined from the PSTH since it was shown to be less influenced by random factors than the reflex amplitude determined from the PSF. Excluding motoneurons with baseline frequencies below 12 Hz, we followed another suggestion from Chapter 5, i. e., to exclude motoneurons that fire just above their recruitment threshold. We did not exclude motor units from the experimental recordings (see Section 7.4.2 for discussion).

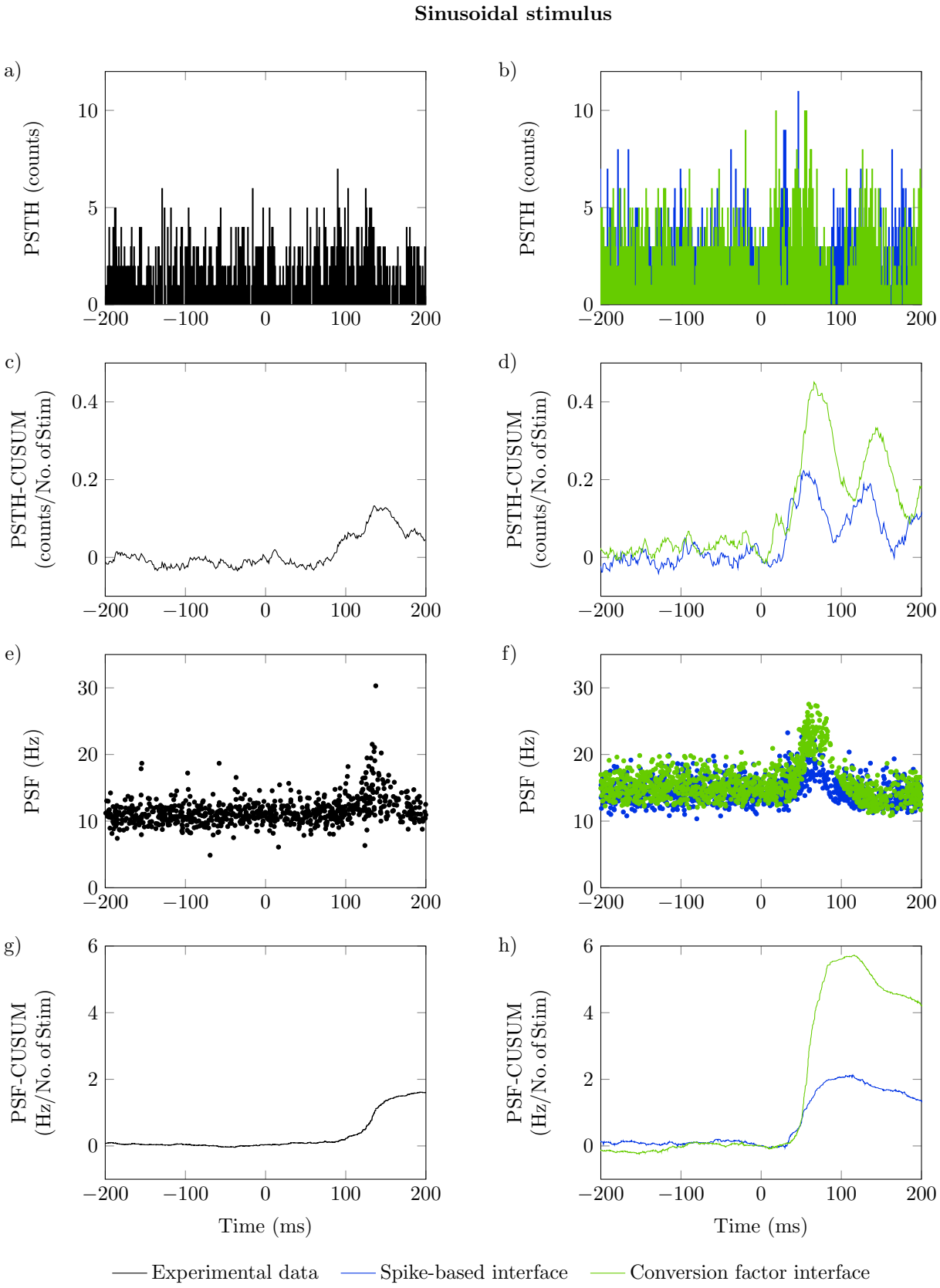

Figure 7.8: Peristimulus analysis for a sinusoidal stimulus. Peristimulus timehistogram (PSTH) of an exemplary recorded motor unit (a) and a simulated motoneuron with spike-based and conversion factor interface (b). PSTH-CUSUM of the same recorded motor unit (c) and simulated motoneuron (d). Peristimulus frequencygram (PSF) of the same recorded motor unit (e) and simulated motoneuron (f). PSF-CUSUM of the same recorded motor unit (g) and simulated motoneuron (h). Experimental data by Yavuz et al. (2014).

The spike-based interface approach aims to mimic the physiological process of neuronal communication via action potentials. We chose the number of spindles according to a typical value for cat hindlimb muscles (Banks, 2006). We obtained the best fit with the experimental stretch reflex amplitudes using a gain of 0.3 nA. The amplitude of postsynaptic currents evoked by single Ia afferent impulses was found to range between 0.5 nA to 2 nA (Finkel and Redman, 1983), which is slightly higher but of the same magnitude as our value. Missing sources of inhibitory input might be a reason for this discrepancy (see Section 7.4.2). The gain of the conversion factor interface does not have a physiological equivalent.

When we applied a ramp-and-hold stimulus, the gains determined from the tap-like stimulus scenario could not reproduce the experimentally determined reflex amplitudes. The conversion factor interface overestimated the reflex amplitude, while the spike-based interface underestimated the experimental results. As shown in Chapter 5, the reflex amplitude depends on the timing of the postsynaptic current with respect to the last action potential of the motoneuron. This uncertainty factor disappears when using a continuous input since the interspike interval is shortened more reliably, resulting in a larger reflex amplitude. This explanation is supported by the simulations with a sinusoidal stretch, where the conversion interface also yielded higher reflex responses than the spike-based interface.

The results of this study suggest that it is crucial to choose gains specific to the interface approach and movement scenario. Beyond that, experimental studies found reflex gains to be task-specific. For example, Johannsson et al. (2017) found differences in H-reflex amplitude between subjects when standing upstairs and downstairs. Pinar et al. (2010) showed that H-reflex amplitude varies with the task and the availability of visual control. These findings support our conclusion that reflex gains parametrised for one type of movement are not generally transferable to other movements.

In the literature, the gains were usually chosen to reproduce global target parameters like muscle force or joint position (e. g., Elias et al., 2014; Lin and Crago, 2002a; Raphael et al., 2010; Schouten et al., 2008). Thereby, interface approaches similar to the conversion factor interface are more common (e. g., Li et al., 2015; Raphael et al., 2010; Schouten et al., 2008; Zhang et al., 2009), but the spike-based interface was also used before (e. g., Dideriksen et al., 2015; Elias et al., 2014; Schuurmans et al., 2009). However, none of the studies compared different approaches or explored their transferability to other scenarios. Here, both interfaces enable the qualitative prediction of a motoneuron pool's monosynaptic stretch reflex response. As seen in Figure 7.5 the continuous interface can be interpreted as a smoothed or averaged version of the spike-based interface.

The major advantage of the conversion factor interface is its easy implementation. This makes it especially suitable for large-scale simulations with many components. Thus, it is employed in the neuromuscular system model proposed in Homs-Pons et al. (2024). The spike-based approach is suitable for investigating processes related to action potential generation. For example, in the simulation, it could be observed that a strong stimulus synchronises spindles. Possible implications of this effect on motor control can only be investigated with an interface approach that considers the activity of individual spindles.

The core of the spike-based interface is transforming the continuous frequency value into a discrete spike train. Often, a Poisson process is used for this (e. g., Schuurmans et al., 2009; Vannucci et al., 2017). However, normal Poisson processes do not account

for neuronal refractoriness. Since they favour shorter interspike intervals, they cannot be used to describe realistic muscle spindle interspike interval distributions (Burke et al., 1979; Gerstner et al., 2014; Nordh et al., 1983). Thus, a renewal process is preferable. Thereby, spikes are generated with a stochastic intensity that depends on the time since the last spike (Ross, 2014). Note that the approach described in Section 7.1.3 yields similar results as a renewal process. Interestingly, efforts are currently being made to develop a completely biophysically based spindle model that directly generates spike train (Housley et al., 2024). If this model proves advantageous, the spike-based interface can be used for coupling it to a motoneuron model.

In conclusion, selecting the interface and the relevant data for parametrisation relies on several factors. Some aspects to consider, though certainly not an exhaustive list, include the model's inherent characteristics, the adaptability and computational complexity of the framework in which the model is deployed, and the specific research question.

7.4.2 Limitations

Limitations to discuss here address the muscle spindle model, the motoneuron model and the interface. Regarding the stretch input for the muscle spindle model, we used a simple linear relation to relate the joint angle perturbation and the muscle fibre stretch (Table 7.1). This simplification neglects the tendon's mechanical and lever arm properties. Moreover, we omitted the acceleration input since the sudden changes in stretch velocity led to unphysiologically high acceleration and spindle frequency values. Most spindle models do not consider acceleration, and its use is at least questionable. Using the Mileusnic spindle model, Vannucci et al. (2017) found that in realistic motion scenarios, the acceleration input only affected the spindle frequency by about 1 %. We also omitted the fusimotor drive. It is uncertain what it looks like, and due to the low conduction velocity of the γ-axons, we assume that it only contributes to the steady-state behaviour of the spindle and does not change during stimulus application (Kandel et al., 2013; Macefield and Knellwolf, 2018). For a detailed discussion of the muscle spindle model and its comparison with experimental recordings, see Mileusnic et al. (2006).

We distributed the muscle spindle feedback uniformly to the motoneuron pool. There are conflicting findings concerning the distribution of Ia afferent activity on motoneurons. For example, Binboğa and Türker (2012) found that the H-reflex amplitude is higher in larger motor units of the human soleus muscle, while Awiszus and Feistner (1993) found the opposite with a similar experimental setup. In consequence, many modelling studies distribute Ia feedback uniformly (e. g., Elias et al., 2014; Lin and Crago, 2002a). In contrast, Dideriksen et al. (2015) used stronger Ia feedback in larger neurons. It was already discussed in Section 5.4.5 that reflex experiments have limited predictive power with respect to the distribution of afferent inputs into the motoneuron pool. Therefore, a uniform distribution is as good as any other distribution until more reliable data is available.

The motoneuron baseline frequency was higher in the simulations than in the experiment. The motoneuron model was parametrised with cat data, and the discharge frequencies of cat motoneurons are generally higher than those of human motoneurons (Manuel et al., 2019). The gain of the current-frequency relation, an important determinant of the reflex amplitude, is assumed to be lower in humans than in cats (Manuel et al., 2019).

Since the muscle spindle frequencies also differ between humans and cats, a quantitative comparison of reflex amplitudes is fraught with many uncertainties that cannot be easily resolved. Further, the criterion for excluding motoneurons with a low baseline discharge frequency was more stringent for the simulated motoneurons than for the recorded motor units. This decision is justifiable for a conceptual study such as this. However, if actual questions are addressed, the data for parametrisation should be selected carefully.

Reflex pathways are subject to modulation, e. g., by recurrent inhibition of motoneurons and presynaptic inhibition of Ia afferents (Baldissera et al., 2011). Further, persistent inward currents can amplify sensory inputs, changing the reflex gain (Binder et al., 2020). These effects were not considered in the model. Moreover, motoneurons also show medium- and long-latency responses to stretch reflexes (Kandel et al., 2013). The respective pathways are still under debate and were not considered in this model (e. g., Grey et al., 2001; Schuurmans et al., 2009). While these pathways play no role in the short-latency response, they contribute to the later parts of the reflex responses, especially during ramp-and-hold and sinusoidal perturbations. In the simulation, the synchronisation of motoneurons was stronger than in the experimental recordings. This finding can likely be attributed to a lack of further synaptic inputs that would have a desynchronising effect. Other limitations of the motoneuron model are discussed in Section 3.4.4.

In the physiological system, the monosynaptic reflex pathway is a closed loop. That is, the response of motoneurons to the sensory signal affects the muscle's contraction force and, therefore, its length. This length change, in turn, affects the sensory signal. However, due to the conduction delays, this would not affect the short-latency response.

7.4.3 Future directions

A computational model of the stretch reflex offers a variety of possibilities to investigate physiological and pathological aspects of stretch reflexes, e. g., their role in ageing and spasticity (e. g., Aloraini et al., 2015; Biering-Sørensen et al., 2006; Nadler et al., 2002). The results of this chapter represent a starting point for integrating the stretch reflex into a model of the neuromuscular system.

Closing the loop, i. e., including a model for muscle contraction, will enable us to relate motoneuron reflex behaviour with more global output parameters like muscle force. In addition, muscle models can estimate the fibre stretch as input for the muscle spindle model. Chaud et al. (2012) and Dideriksen et al. (2015), for example, employed simplified one-dimensional Hill-type muscle models to close the stretch reflex loop. These models can only provide an averaged estimate of muscle stretch. In contrast, three-dimensional (continuum-mechanical) muscle models can estimate the spatial distribution of fibre stretch throughout the muscle (e.g., Blemker et al., 2005; Heidlauf and Röhrle, 2014; Johansson et al., 2000; Röhrle et al., 2008). However, incorporating a three-dimensional muscle model within a neuromuscular system framework massively increases the computational costs. Thus, specialised frameworks built for high-performance computers are required (Homs-Pons et al., 2024; Maier, 2021).

Both presented interface approaches can be used to include other sensory pathways. Considering an antagonistic muscle enables us to consider the reciprocal inhibition pathway, which is also triggered by muscle spindles. Further, Golgi-tendon organs can be added to incorporate the Ib reflex pathways. Models for Golgi-tendon organs exist in the

literature (e. g., Crago, 2018; Song et al., 2008). The challenge is to find suitable data for the parametrisation. The reciprocal inhibition pathway can be assessed experimentally (Yavuz et al., 2018). In contrast, Ib reflex data is sparse and isolating the pathway is difficult since the respective spinal interneurons are not exclusively used by Ib afferents (Jankowska et al., 1981; Rogasch et al., 2011). Aiming to reproduce global output parameters such as muscle force or joint position can ensure reasonable parametrisation.

8 Conclusion and Outlook

"*Essentially, all models are wrong, but some are useful.*"

George Edward Pelham Box[1]

8.1 Summary and key findings

This PhD thesis aimed to investigate human α-motoneuron discharge properties during stretch reflexes using an *in silico* approach. Human physiology is inherently hierarchical and acts across multiple length and time scales. Therefore, this work aimed not to model the physiological system in all its complexity but rather to represent partial aspects of reality well enough to make valuable statements and predictions. Recording reflex responses of single motoneurons *in vivo* requires delivering the reflex stimulus several hundred times. Consequently, a motoneuron model with a reasonable computational cost is required to conduct the relevant *in-silico* experiments. We chose a two-compartment Hodgkin-Huxley type model to simulate the α-motoneuron pool. The model considers a soma and a dendrite compartment and predicts the time course of the membrane potential in response to input currents by considering the behaviour of significant ion channels. Therefore, the chosen model balances computational simplicity and physiological correctness. We simulated motoneuron reflex responses in both the monosynaptic and reciprocal inhibition pathways of the stretch reflex.

The motoneuron reflex responses were analysed using the peristimulus timehistogram (PSTH) and the peristimulus frequencygram (PSF). The strength of the reflex response, i. e., the reflex amplitude, was determined from the cumulative sums (CUSUMs) of both metrics. This work evaluated more than 10 000 motoneuron reflex responses. This amount made manual evaluation of reflex amplitudes, the gold standard method, unfeasible. Therefore, we developed an algorithm that automates the evaluation of reflex amplitudes. To assess the validity of interpretations drawn from the peristimulus analysis, we investigated how the PSTH and PSF reflex responses are influenced by the motoneuron size and the experimental conditions. Therefore, we simulated excitatory reflexes in the motoneuron pool under numerous conditions.

In addition to the motoneuron behaviour in excitatory reflexes, we also investigated the reciprocal inhibition reflex. In experimental studies, an excitation of unknown origin was occasionally observed following the inhibition response. We hypothesised that hyperpolarisation-activated inward currents (h-currents) contribute to this postinhibitory excitation. We added the respective ion channel to the motoneuron model and investigated its role in postinhibitory excitation. As the PSF and not the PSTH can distinguish changes in motoneuron discharge frequency from synchronisation, only the PSF was used in this study. A novel evaluation method, which is based on separating spike trains in the PSF, was introduced to visualise history-dependent effects on the reflex response.

The above investigations could be performed without explicitly modelling the sens-

[1] George Edward Pelham Box (18 October 1919 – 28 March 2013) was a British mathematician/statistician.

ory organs delivering the signals causing reflex responses. More sophisticated *in-silico* investigations of the neuromuscular system may require considering the overall system, including sensory organs and muscles. Therefore, in the last chapter of this work, the foundation was laid for including the stretch reflex in a model of the neuromuscular system. Two approaches to designing the interface to a muscle spindle model were presented and compared.

The simulations and analyses in this work provide novel insights into the mechanisms of motoneuron behaviour during stretch reflexes and the methods for recording them *in vivo*. The key findings of this thesis are listed and summarised below:

- Regarding the detection of significant reflex responses, the steepness of the reflex response, determined by the CUSUM of the PSTH or the PSF, is a suitable indicator for the onset and end of the reflex response when using a short and strong excitatory stimulus. This indicator can be used to determine the reflex amplitude using an algorithm instead of a manual evaluation.

- Using the computational model, we showed that motoneuron properties and experimental conditions influence *in-vivo* estimates of motoneuron reflex responses, determined from the CUSUMs of the PSTH and the PSF, in a highly non-linear way. We concluded that reflex amplitudes determined from the PSTH-CUSUM are better suited to investigate motoneuron inputs. Reflex amplitudes determined from the PSF-CUSUM are suited to determine the sign of a reflex response and to investigate the excitability of motoneurons based on their size.

- We derived advice for the design of experimental studies investigating motoneuron reflex responses. Since reflex amplitudes from single motoneurons were generally not representative of the pool, we suggest summarising motoneurons with similar baseline discharge frequencies. Further, motoneurons acting shortly above their recruitment threshold show very non-linear behaviour with respect to reflex stimuli, and they should be excluded from the analysis.

- Hyperpolarisation-activated inward currents can contribute to postinhibitory excitation in human motor units. Using the computational model, we showed that h-currents can shorten interspike intervals in response to strong inhibitory stimuli and facilitate postinhibitory excitation. This effect is stimulus-time dependent and most pronounced in conditions with low firing rates and low noise, i. e., when few other inputs into the motoneuron are present.

- We used findings from the simulation study to analyse the reflex responses of recorded human motor units. Excitation in the first poststimulus interval after reciprocal inhibition was found in a significant portion of the motor units. We conclude that h-currents serve as a modulatory system that can increase motoneuron excitability.

- Integration of the stretch reflex into a neuromuscular system model requires coupling of the motoneuron model with a spindle model. An interface approach based on spike trains and an approach based on a conversion factor is suitable when appropriate data is used for the parametrisation. However, identifying suitable data for parametrisation poses a significant challenge, especially regarding pathways that are less accessible than the monosynaptic stretch reflex.

In summary, motoneuron internal properties and experimental conditions contribute to the reflex behaviour of α-motoneurons. Common reflex evaluation methods are prone to history-dependent effects. This was shown for both the excitatory monosynaptic stretch reflex simulated in Chapter 5 and the reciprocal inhibition reflex studied in Chapter 6. We conclude that detailed analyses using the PSTH and PSF and taking spike train history into account are advisable. Further, computational models can help identify the determinants of good study design and choose appropriate analysis methods.

8.2 Outlook

In the sense of the quote of George Edward Pelham Box, the models employed in this work helped to identify potential discrepancies between what we think we know and what may be true. The simulation results challenge our current knowledge and provide an idea of what we might have overlooked. We need to transfer the findings to experimental studies to capitalise on this. These will either confirm the findings from the simulations or generate new hypotheses, which, in turn, will provide an impetus for further *in-silico* studies. The knowledge gained must be translated into clinical applications for patients to benefit from the research. We therefore conclude with perspectives for modelling approaches, experimental studies and clinical applications.

8.2.1 Perspectives for neuromuscular system modelling

The simulations carried out within this work laid the foundation for further *in-silico* investigations, as already discussed in the relevant chapters. In short, the study on factors influencing *in-vivo* estimates of excitation reflex amplitudes in motoneuron pools (Chapter 5) can be extended to analyse inhibitory reflex responses. It is also essential to evaluate how well other estimates of reflex strength, e. g., the reflex duration or metrics that are not based on the peristimulus CUSUM, can represent the input signal.

In Chapter 6 of this work, we showed that postinhibitory excitation in motoneurons may be facilitated by several factors, from which we investigated the contribution of h-currents in detail. Future studies should also explore the role of other structures, including additional ion channels and sensory pathways.

System models allow for investigating behaviours emerging from the interrelations of its components. Simple reflex models can be extended to models considering more aspects of the neuromuscular system, e. g., muscle spindles or Golgi-tendon organs and their respective pathways or muscle and joint mechanics. Models for these components are available from the literature. When coupling two or more models, new interface variables emerge that need to be parametrised. In Chapter 7, this challenge was exemplarily addressed for coupling the motoneuron pool and a muscle spindle model.

The findings on model coupling and parametrisation can be transferred to Golgi-tendon organ models. Golgi-tendon organs are sensitive to muscle force and inhibit homonymous muscles (Anderson, 1974; Jami, 1992). There exist models for single Golgi-tendon organs, but the summed activity of all Golgi-tendon organs was shown to sufficiently represent muscle force (Prochazka and Gorassini, 1998a; Reinking et al., 1975). Accordingly, ensemble models representing all Golgi-tendon organs of a muscle were primarily developed (e. g., Crago, 2018; Lin and Crago, 2002a; Mileusnic and Loeb, 2009). The interface

approaches presented in Chapter 7 can be applied for the coupling with a motoneuron pool model. Golgi-tendon organs activate di- or polysynaptic pathways (Jami, 1992). When using the spike-based approach, interneurons can explicitly be modelled, as e. g., in Cisi and Kohn (2008); Dideriksen et al. (2015). Alternatively, the conversion factor interface can represent the interneuronal pathway and thereby simplify the integration of Golgi-tendon organ models.

Skeletal muscle mechanics can be described by one- and three-dimensional, i. e., continuum mechanical, models. Both modelling approaches can predict active and passive muscle behaviour and, thus, provide input signals for sensory organ models (e. g., Blemker et al., 2005; Heidlauf and Röhrle, 2014; Röhrle et al., 2008; Schmitt et al., 2019). While one-dimensional models provide a single averaged estimate for fibre stretch and muscle force, three-dimensional models provide spatial distributions of stretch and stress. An approach for using these values as inputs to sensory organ models is described in Haggie, Schmid et al. (2023). In short, locations need to be assigned to the sensory organs. Then, the required input variables, e. g., , stretch, stretch rate or tension, can be obtained from the respective locations. While Golgi-tendon organs are located at the musculotendinous junctions (Schoultz and Swett, 1972), muscle spindles are spread across the muscle (Kokkorogiannis, 2004). Estimates of total muscle force for ensemble Golgi-tendon organ models can also be obtained from three-dimensional models by summarising local stresses across a defined area representing the musculotendinous junction.

Considering a system with more than one muscle, e. g., agonist and antagonist, increases the number of neuronal pathways to be considered. Muscles are not only mechanically coupled via joints, but they also exchange neural feedback (Kandel et al., 2013). In addition to receiving sensory inputs from numerous sources, spinal motoneurons also bridge the gap between the motor cortex area of the brain and the muscles (Lemon, 2008). Consequently, α-motoneurons are a central component when studying the effect of cortical processes on muscle activity, and reflex pathways are a relevant element in a model of the corticomusular pathway, as e. g., proposed by Haggie, Schmid et al. (2023).

The different combinations of components in a model describing (parts of) the neuromuscular system have in common that the data required for the interface parametrisation can usually not be directly recorded *in vivo* and suitable targets for the model parametrisation have to be defined. Therefore, coupling sub-models within the neuromuscular system remains a challenge.

Implementation of neuromuscular system models brings further challenges. Holistic models of the neuromuscular system usually contain components that are mathematically described by different classes of equations, e. g., algebraic, ordinary or partial differential equations, and act on different lengths and time scales. Simulating, e. g., reflex experiments, requires simulating the system's behaviour for several minutes. Efficient implementation of multi-scale and/or multi-component models requires parallelisation of algorithms and access to high-performance computers (Bradley et al., 2018; Maier et al., 2019). There exist many specialised software tools for the individual components, e. g., neurons or muscles (for an overview, see e. g., Haggie, Schmid et al., 2023). There are also approaches to provide platforms that enable the integration of various components of the neuromuscular system, but they are complex to use (e. g., Maier, 2021).

In addition to high-performance computing, another approach addressing the complexity of the simulations is model order reduction methods or surrogate models (e. g., Homs-

Pons et al., 2024; Mordhorst et al., 2017). Surrogate models can be the answer to the challenge of real-time simulations. Real-time computing is, e. g., required when using model predictions to control prostheses or exoskeletons (e. g., Eilenberg et al., 2010; Lotti et al., 2020).

Models of the neuromuscular system can be applied to numerous fields of research. In the remainder of this section, selected visions are presented in more detail. Concerning the stretch reflex, a major unknown is the contribution of the fusimotor drive to the muscle spindle and reflex activity. The fusimotor activity cannot be recorded *in vivo*. Consequently, there is an ongoing debate on the role of fusimotor drive in natural movements (Dimitriou, 2022). Computational models might help to clarify the role(s) of fusimotor drive, e. g., its potential contribution to the task-dependent modulation of reflexes (Dimitriou, 2022). Another unresolved question is how exactly muscle spindles encode information and contribute to coordinated movements and how their spatial position within the muscle influences this process (Day et al., 2017; Knellwolf et al., 2019; Kokkorogiannis, 2004). Addressing this question requires a three-dimensional muscle model to obtain the spatially heterogeneous distribution of muscle fibre stretch (e. g., Blemker et al., 2005; Heidlauf and Röhrle, 2014; Röhrle et al., 2008).

In addition to questions of basic physiology, many questions concerning pathological conditions are still open. Invasive changes, such as an amputation, severely disrupt the finely tuned neuromuscular system. Conventional amputation techniques destroy the mechanical link between agonist and antagonist muscles in the residual limb (Greitemann et al., 2016; Ovadia and Askari, 2015). In consequence, the sensory feedback pathways are also impaired. A new procedure, the so-called agonist-antagonist myoneural interface (AMI) aims to maintain the natural mechanical and sensory coupling between two residual muscles after limb amputation (Herr and Carty, 2021). The AMI approach reconnects the residual muscles by an (artificial) tendon (Herr and Carty, 2021). Preliminary studies indicate that the procedure indeed preserves the sensory feedback (Sreenivasa et al., 2015). However, many aspects still need to be clarified. For example, it is unknown how the tension in the connecting tendon, i. e., determining the muscles' pre-stretch, influences the interaction of the muscles in an AMI construct. In Homs-Pons et al. (2024), a modelling approach is presented to address this problem. These simulations and experiments can contribute to a better understanding of the procedure and improve surgery outcomes.

The developers of the AMI also envision that the AMI improves the control of prostheses (Herr et al., 2021). Until today, despite all technical advancements, prosthesis acceptance is unsatisfactorily low, mainly due to lack of comfort and function (Smail et al., 2021). Restoring sensory perception could revolutionise the field; however, the technology is still in its infancy (Cimolato et al., 2023; Farina et al., 2023; Kim et al., 2023). Neuromuscular system models can generate estimations of sensory stimulation paradigms surpassing vibrotactile feedback, which is presently employed (Witteveen et al., 2015).

Computational models can be used not only to address particular research questions but also to generate virtual subject populations, which can enrich or augment data that is difficult to obtain experimentally. Also, simulations can be used for teaching/learning fundamental mechanisms in physiology.

8.2.2 Perspectives for experimental studies

This work shows how simulation and experimental studies can complement each other. When addressing the reciprocal inhibition experiment in Chapter 6, the research question emerged from an unexplained phenomenon observed in experimental studies. The performed simulations offer a potential explanation that now requires confirmation through experiments. *In-vitro* studies are the most promising approach in this case.

When addressing the monosynaptic stretch reflex in Chapter 5, we used a simulation of a motoneuron pool to emphasise the pitfalls in interpreting experimental data. From this, we derived recommendations on how to improve experimental study designs to perform meaningful experiments. The future of *in-vivo* reflex experiments should be driven by increasing the number of recordable motor units and the range of forces at which reflex experiments are performed. Both can be achieved by applying recently developed or emerging technologies, e. g., improved electrode grids for the surface electromyogram (EMG), high-density intramuscular EMG, motor unit tracking, magnetomyography or ultrafast ultrasound (Caillet et al., 2023; Ghahremani Arekhloo et al., 2023; Klotz et al., 2023; Martinez-Valdes et al., 2017; Muceli et al., 2022; Rohlén et al., 2020). Re-examining reflex responses also offers the opportunity to address unknown or poorly understood aspects of reflex activity, such as differences between the sexes or pathological changes. Further, the conclusions drawn in Chapter 5 can be used to re-evaluate and re-interpret already collected data.

If more motor units can be recorded *in vivo*, the time-intensive manual evaluation of the data becomes a hurdle. Algorithms are required to determine the onset and end of reflex responses automatically and reliably. The approach applied in this work, i. e., using the slope of the PSTH- and PSF-CUSUM, showed promising results when applied to short excitatory stimuli. The suitability of this approach to evaluate experimental data needs to be investigated. In a preliminary study, it showed agreement with the manual evaluation for tap-like and ramp-and-hold mechanical stimuli. However, the performance using sinusoidal mechanical and electrical stimuli was unsatisfactory[2] (Grupp, 2023). Here, further investigations, including more datasets, are required. Therefore, the potential of signal processing techniques used in other fields working with similar signals should be investigated. This field of research can benefit considerably from interdisciplinary cooperation.

8.2.3 Perspectives for clinical applications

The use of computational modelling and simulations in clinical practice has two facets. One is the transfer of knowledge gained from simulations into clinical applications, and the other is the integration of simulations into clinical processes.

Investigating motor unit reflex responses using peristimulus analysis can provide detailed insights into pathological changes in motoneuron behaviour. So far, these methods are part of basic research in physiology but not of the clinical routine. Using reflex amplitude estimates as a diagnostic tool must be fast and easy for clinical routine. Based on this work, three aspects seem especially crucial. First, the provided approach for the automatic and fast determination of reflex amplitudes must be generalised for different reflex types. Second, the number of required stimuli and, consequently, the examination

[2]This was shown in a Bachelor thesis by Teresa Grupp.

time must be reduced for reflex experiments. This can be achieved by merging spike trains of similar motor units or augmenting data using motoneuron models (e. g., Caillet et al., 2022a; Ornelas-Kobayashi et al., 2023). Third, large-scale multi-component computer simulations must be used to increase further the understanding of reflex pathways and their contribution to physiological and pathological motor control.

A survey amongst clinicians conducted in 2020 and 2021 demonstrated the potential of computational modelling and simulations for future clinical use. Although the study is not representative, and there is probably a bias towards clinicians who have been in contact with the field of simulations, there are some promising findings. The two most frequently mentioned areas of application for simulations were planning of interventions and teaching/training (Lesage et al., 2023). Patient-specific simulations of the neuromuscular system are made more difficult by the poor accessibility of the neuronal structures. Nevertheless, computational models, e. g., of reflex pathways or the AMI, can be used for teaching and training. From a simulation engineering point of view, it is encouraging that most clinicians surveyed see a future role for modelling and simulation experts in clinical premises (Lesage et al., 2023). If the two fields work together more closely, there is a substantial potential mutual benefit, similar to what is already practised today between simulation engineers and experimentalists.

A Motoneuron Model Parameters

This appendix summarises the motoneuron model parameters used in this work.

Motoneuron pool model

Tables A.1 and A.2 show the motoneuron pool model parameters used in Chapters 4, 5 and 7.

Table A.1: Constant parameters of the motoneuron pool. Parameters are adopted from Cisi and Kohn (2008) if not indicated otherwise. This table corresponds to Table 3.2 in the manuscript.

Parameter	Symbol	Value
Membrane specific capacitance ($\mu F\,cm^{-2}$)	C_m	1*
Cytoplasm resistivity ($k\Omega\,cm$)	R_i	0.07**
Na^+ equilibrium potential (mV)	E_{Na}	120
K^+ equilibrium potential (mV)	E_K	−10
Leakage equilibrium potential (mV)	E_L	0
Maximum specific Na^+ conductance ($mS\,cm^{-2}$)	$\overline{G}_{Na}$	30
Maximum specific fast K^+ conductance ($mS\,cm^{-2}$)	$\overline{G}_{Kf}$	4
Maximum specific slow K^+ conductance ($mS\,cm^{-2}$)	$\overline{G}_{Ks}$	16

*Burke et al. (1994); Cole (1972); Fleshman et al. (1988) **Barrett and Crill (1974); Burke et al. (1994)

Table A.2: Parameters that vary across the motoneuron (MN) pool. Values are given for the smallest and the largest MN of the pool. Parameters are adopted from Cisi and Kohn (2008). This table corresponds to Table 3.3 in the manuscript.

Parameter	Symbol	Value	
		Smallest MN	Largest MN
Soma diameter (cm)	d^s	77.5×10^{-4}	113×10^{-4}
Soma length (cm)	l^s	77.5×10^{-4}	113×10^{-4}
Soma specific resistance ($k\Omega\,cm^{-2}$)	R_m^s	1.15	0.65
Dendrite diameter (cm)	d^d	41.5×10^{-4}	92.5×10^{-4}
Dendrite length (cm)	l^d	0.55	1.06
Dendrite specific resistance ($k\Omega\,cm^{-2}$)	R_m^d	14.4	6.05

Motoneuron model with h-channel

Tables A.3 and A.4 show the parameters for the motoneuron model with h-channel used in Chapter 6.

Table A.3: Constant parameters of the motoneuron model with h-channel. Parameters are adopted from Cisi and Kohn (2008) if not indicated otherwise.

Parameter	Symbol	Value
Membrane specific capacitance ($\mu F\,cm^{-2}$)	C_m	1*
Cytoplasm resistivity ($k\Omega\,cm$)	R_i	0.07**
Na^+ equilibrium potential (mV)	E_{Na}	120
K^+ equilibrium potential (mV)	E_K	−10
Leakage equilibrium potential (mV)	E_L	0
H-current Equilibrium potential (mV)	E_H	20‡
Maximum specific Na^+ conductance ($mS\,cm^{-2}$)	$\overline{G}_{Na}$	30
Maximum specific fast K^+ conductance ($mS\,cm^{-2}$)	$\overline{G}_{Kf}$	4
Maximum specific slow K^+ conductance ($mS\,cm^{-2}$)	$\overline{G}_{Ks}$	16
Maximum specific h-conductance ($mS\,cm^{-2}$)	$\overline{G}_H$	2‡‡

*Burke et al. (1994); Cole (1972); Fleshman et al. (1988) **Barrett and Crill (1974); Burke et al. (1994)

‡Bayliss et al. (1994); Larkman and Kelly (1992) ‡‡Bertrand and Cazalets (1998); Kiehn et al. (2000)

Table A.4: Parameters for the motoneuron model with h-current. Parameters correspond to the mean values of S-type and FR-type motoneurons in Cisi and Kohn (2008).

Parameter	Symbol	S-type	FR-type
Soma diameter (cm)	d^s	80×10^{-4}	85×10^{-4}
Soma length (cm)	l^s	80×10^{-4}	85×10^{-4}
Soma specific resistance ($k\Omega\,cm^{-2}$)	R_m^s	1.1	1
Dendrite diameter (cm)	d^d	52×10^{-4}	73×10^{-4}
Dendrite length (cm)	l^d	0.615	0.745
Dendrite specific resistance ($k\Omega\,cm^{-2}$)	R_m^d	12.55	8.825

Bibliography

Aidley, D. J. (1998). *The physiology of excitable cells*. Cambridge University Press, 3rd edition.

Aizenman, C. D. and Linden, D. J. (1999). Regulation of the rebound depolarization and spontaneous firing patterns of deep nuclear neurons in slices of rat cerebellum. *Journal of Neurophysiology*, 82(4):1697–1709.

Aloraini, S. M., Gäverth, J., Yeung, E., and MacKay-Lyons, M. (2015). Assessment of spasticity after stroke using clinical measures: a systematic review. *Disability and Rehabilitation*, 37(25):2313–2323.

Altan, N. E. (2022). *Data-driven modelling of neuromechanical adaptation in skeletal muscles in response to isometric exercise*. Phd thesis, University of Stuttgart.

Aminikhanghahi, S. and Cook, D. J. (2017). A survey of methods for time series change point detection. *Knowledge and Information Systems*, 51(2):339–367.

Anderson, J. H. (1974). Dynamic characteristics of Golgi tendon organs. *Brain Research*, 67(3):531–537.

Angstadt, J. D., Grassmann, J. L., Theriault, K. M., and Levasseur, S. M. (2005). Mechanisms of postinhibitory rebound and its modulation by serotonin in excitatory swim motor neurons of the medicinal leech. *Journal of Comparative Physiology A*, 191:715–732.

Aoki, M. and Yamamura, T. (1980). Postinhibitory rebound facilitation of the extension reflex in the high spinal cat. *The Japanese Journal of Physiology*, 30(3):465–471.

Awiszus, F. and Feistner, H. (1993). The relationship between estimates of Ia-EPSP amplitude and conduction velocity in human soleus motoneurons. *Experimental Brain Research*, 95:365–370.

Awiszus, F., Feistner, H., and Schäfer, S. S. (1991). On a method to detect long-latency excitations and inhibitions of single hand muscle motoneurons in man. *Experimental Brain Research*, 86:440–446.

Baldissera, F., Hultborn, H., and Illert, M. (2011). *Integration in Spinal Neuronal Systems*, pages 509–595. John Wiley & Sons, Ltd.

Banks, R. W. (1994). The motor innervation of mammalian muscle spindles. *Progress in Neurobiology*, 43(4):323–362.

Banks, R. W. (2006). An allometric analysis of the number of muscle spindles in mammalian skeletal muscles. *Journal of Anatomy*, 208(6):753–768.

Barrett, J. N. and Crill, W. E. (1974). Specific membrane properties of cat motoneurones. *The Journal of Physiology*, 239(2):301–324.

Bayliss, D. A., Viana, F., Bellingham, M. C., and Berger, A. J. (1994). Characteristics and postnatal development of a hyperpolarization-activated inward current in rat hypoglossal motoneurons in vitro. *Journal of Neurophysiology*, 71(1):119–128.

BenSaïda, A. (2023). Ahmed bensaïda (2023). shapiro-wilk and shapiro-francia normality tests. (https://www.mathworks.com/matlabcentral/fileexchange/13964-shapiro-wilk-and-shapiro-francia-normality-tests). MATLAB Central File Exchange. Retrieved May 15, 2023.

Bertrand, S. and Cazalets, J.-R. (1998). Postinhibitory rebound during locomotor-like activity in neonatal rat motoneurons in vitro. *Journal of Neurophysiology*, 79(1):342–351.

Bessou, P., Laporte, Y., and Pagès, B. (1968). A method of analysing the responses of spindle primary endings to fusimotor stimulation. *The Journal of Physiology*, 196(1):37–45.

Biering-Sørensen, F., Nielsen, J. B., and Klinge, K. (2006). Spasticity-assessment: a review. *Spinal Cord*, 44(12):708–722.

Binboğa, E. and Türker, K. S. (2012). Compound group I excitatory input is differentially distributed to human soleus motoneurons. *Clinical Neurophysiology*, 123(11):2192–2199.

Binder, M. D., Powers, R. K., and Heckman, C. J. (2020). Nonlinear input-output functions of motoneurons. *Physiology*, 35(1):31–39.

Blemker, S. S., Pinsky, P. M., and Delp, S. L. (2005). A 3D model of muscle reveals the causes of nonuniform strains in the biceps brachii. *Journal of Biomechanics*, 38(4):657–665.

Blum, K. P., Campbell, K. S., Horslen, B. C., Nardelli, P., Housley, S. N., Cope, T. C., and Ting, L. H. (2020). Diverse and complex muscle spindle afferent firing properties emerge from multiscale muscle mechanics. *Elife*, 9:e55177.

Booth, V., Rinzel, J., and Kiehn, O. (1997). Compartmental model of vertebrate motoneurons for Ca2+-dependent spiking and plateau potentials under pharmacological treatment. *Journal of Neurophysiology*, 78(6):3371–3385.

Boyd, I. A. and Kalu, K. U. (1979). Scaling factor relating conduction velocity and diameter for myelinated afferent nerve fibres in the cat hind limb. *The Journal of Physiology*, 289(1):277–297.

Bradley, C. P., Emamy, N., Ertl, T., Göddeke, D., Hessenthaler, A., Klotz, T., Krämer, A., Krone, M., Maier, B., Mehl, M., et al. (2018). Enabling detailed, biophysics-based skeletal muscle models on hpc systems. *Frontiers in Physiology*, 9.

Brinkworth, R. S. A. and Türker, K. S. (2003). A method for quantifying reflex responses from intra-muscular and surface electromyogram. *Journal of Neuroscience Methods*, 122(2):179–193.

Burke, D., Skuse, N. F., and Stuart, D. G. (1979). The regularity of muscle spindle discharge in man. *The Journal of Physiology*, 291(1):277–290.

Burke, R. (2022). *Spinal Motoneurons*, pages 1437–1473. Springer International Publishing, Cham.

Burke, R. E. (1999). The use of state-dependent modulation of spinal reflexes as a tool to investigate the organization of spinal interneurons. *Experimental Brain Research*, 128:263–277.

Burke, R. E., Fedina, L., and Lundberg, A. (1971). Spatial synaptic distribution of recurrent and group Ia inhibitory systems in cat spinal motoneurones. *The Journal of Physiology*, 214(2):305–326.

Burke, R. E., Fyffe, R. E., and Moschovakis, A. K. (1994). Electrotonic architecture of cat gamma motoneurons. *Journal of Neurophysiology*, 72(5):2302–2316.

Burke, R. E., Levine, D. N., Tsairis, P., and Zajac, F. E. (1973). Physiological types and histochemical profiles in motor units of the cat gastrocnemius. *The Journal of Physiology*, 234(3):723–748.

Burke, R. E., Strick, P. L., Kanda, K., Kim, C., and Walmsley, B. (1977). Anatomy of medial gastrocnemius and soleus motor nuclei in cat spinal cord. *Journal of Neurophysiology*, 40(3):667–680.

Burkitt, A. N. (2006). A review of the integrate-and-fire neuron model: I. Homogeneous synaptic input. *Biological Cybernetics*, 95:1–19.

Bursztyn, L., Eytan, O., Jaffa, A. J., and Elad, D. (2007). Mathematical model of excitation-contraction in a uterine smooth muscle cell. *American Journal of Physiology-Cell Physiology*, 292(5):C1816–C1829.

Caillet, A. H., Avrillon, S., Kundu, A., Yu, T., Phillips, A. T. M., Modenese, L., and Farina, D. (2023). Larger and denser: An optimal design for surface grids of EMG electrodes to identify greater and more representative samples of motor units. *eNeuro*, 10(9).

Caillet, A. H., Phillips, A. T. M., Farina, D., and Modenese, L. (2022a). Estimation of the firing behaviour of a complete motoneuron pool by combining electromyography signal decomposition and realistic motoneuron modelling. *PLOS Computational Biology*, 18(9):e1010556.

Caillet, A. H., Phillips, A. T. M., Farina, D., and Modenese, L. (2022b). Mathematical relationships between spinal motoneuron properties. *Elife*, 11:e76489.

Calvin, W. H. (1974). Three modes of repetitive firing and the role of threshold time course between spikes. *Brain Research*, 69(2):341–346.

Castronovo, A. M., Negro, F., Conforto, S., and Farina, D. (2015). The proportion of common synaptic input to motor neurons increases with an increase in net excitatory input. *Journal of Applied Physiology*, 119(11):1337–1346.

Chaplan, S. R., Guo, H.-Q., Lee, D. H., Luo, L., Liu, C., Kuei, C., Velumian, A. A., Butler, M. P., Brown, S. M., and Dubin, A. E. (2003). Neuronal hyperpolarization-activated pacemaker channels drive neuropathic pain. *Journal of Neuroscience*, 23(4):1169–1178.

Chapra, S. C. and Canale, R. P. (2010). *Numerical methods for engineers*. Mcgraw-hill, 6th edition.

Chaud, V. M., Elias, L. A., Watanabe, R. N., and Kohn, A. F. (2012). A simulation study of the effects of activation-dependent muscle stiffness on proprioceptive feedback and short-latency reflex. In *2012 4th IEEE RAS & EMBS International Conference on Biomedical Robotics and Biomechatronics (BioRob)*, pages 133–138.

Chen, X. Y., Chen, L., and Wolpaw, J. R. (2003). Conditioned H-reflex increase persists after transection of the main corticospinal tract in rats. *Journal of Neurophysiology*, 90(5):3572–3578.

Cimolato, A., Ciotti, F., Kljajić, J., Valle, G., and Raspopovic, S. (2023). Symbiotic electroneural and musculoskeletal framework to encode proprioception via neurostimulation: ProprioStim. *Iscience*, 26(3):106248.

Cisi, R. R. L. and Kohn, A. F. (2008). Simulation system of spinal cord motor nuclei and associated nerves and muscles, in a web-based architecture. *Journal of Computational Neuroscience*, 25(3):520–542.

Cole, K. S. (1972). *Membranes, ions and impulses: a chapter of classical biophysics*, volume 1. Univ of California Press.

Conway, B. A., Halliday, D. M., Farmer, S. F., Shahani, U., Maas, P., Weir, A., and Rosenberg, J. R. (1995). Synchronization between motor cortex and spinal motoneuronal pool during the performance of a maintained motor task in man. *The Journal of Physiology*, 489(3):917–924.

Crago, P. E. (2018). Neuromodulation by combined sensory and motor stimulation in the peripheral nerve: tendon organ afferent activity. *Journal of Neural Engineering*, 16(1):016015.

Crone, C., Hultborn, H., Jespersen, B., and Nielsen, J. (1987). Reciprocal Ia inhibition between ankle flexors and extensors in man. *The Journal of Physiology*, 389(1):163–185.

Cruccu, G. and Deuschl, G. (2000). The clinical use of brainstem reflexes and hand-muscle reflexes. *Clinical Neurophysiology*, 111(3):371–387.

Cullheim, S., Fleshman, J. W., Glenn, L. L., and Burke, R. E. (1987). Membrane area and dendritic structure in type-identified triceps surae alpha motoneurons. *Journal of Comparative Neurology*, 255(1):68–81.

Curtis, D. R. and Eccles, J. C. (1959). The time courses of excitatory and inhibitory synaptic actions. *The Journal of Physiology*, 145(3):529–546.

Czesnik, D., Howells, J., Bartl, M., Veiz, E., Ketzler, R., Kemmet, O., Walters, A. S., Trenkwalder, C., Burke, D., and Paulus, W. (2019). Ih contributes to increased motoneuron excitability in restless legs syndrome. *The Journal of Physiology*, 597(2):599–609.

Day, J., Bent, L. R., Birznieks, I., Macefield, V. G., and Cresswell, A. G. (2017). Muscle spindles in human tibialis anterior encode muscle fascicle length changes. *Journal of Neurophysiology*, 117(4):1489–1498.

De Luca, C. J. and Hostage, E. C. (2010). Relationship between firing rate and recruitment threshold of motoneurons in voluntary isometric contractions. *Journal of Neurophysiology*, 104(2):1034–1046.

Del Vecchio, A., Holobar, A., Falla, D., Felici, F., Enoka, R. M., and Farina, D. (2020). Tutorial: Analysis of motor unit discharge characteristics from high-density surface EMG signals. *Journal of Electromyography and Kinesiology*, 53:102426.

Destexhe, A. (1997). Conductance-based integrate-and-fire models. *Neural Computation*, 9(3):503–514.

Destexhe, A. and Huguenard, J. (2000). *Which formalism to use for modeling voltage-dependent conductances*. CRC Press Boca Raton, FL.

Dideriksen, J. L., Negro, F., and Farina, D. (2015). The optimal neural strategy for a stable motor task requires a compromise between level of muscle cocontraction and synaptic gain of afferent feedback. *Journal of Neurophysiology*, 114(3):1895–1911.

Dimitriou, M. (2022). Human muscle spindles are wired to function as controllable signal-processing devices. *Elife*, 11:e78091.

Dodla, R., Svirskis, G., and Rinzel, J. (2006). Well-timed, brief inhibition can promote spiking: Postinhibitory facilitation. *Journal of Neurophysiology*, 95(4):2664–2677.

Duchateau, J. and Enoka, R. M. (2022). Distribution of motor unit properties across human muscles. *Journal of Applied Physiology*, 132(1):1–13.

Eccles, J. C. (1948). Conduction and synaptic transmission in the nervous system. *Annual Review of Physiology*, 10(1):93–116.

Eilenberg, M. F., Geyer, H., and Herr, H. (2010). Control of a powered ankle–foot prosthesis based on a neuromuscular model. *IEEE Transactions on Neural Systems and Rehabilitation Engineering*, 18(2):164–173.

Elias, L. A. and Kohn, A. F. (2013). Individual and collective properties of computationally efficient motoneuron models of types S and F with active dendrites. *Neurocomputing*, 99:521–533.

Elias, L. A., Watanabe, R. N., and Kohn, A. F. (2014). Spinal mechanisms may provide a combination of intermittent and continuous control of human posture: predictions from a biologically based neuromusculoskeletal model. *PLoS Computational Biology*, 10(11):e1003944.

Ellaway, P. H. (1978). Cumulative sum technique and its application to the analysis of peristimulus time histograms. *Electroencephalography and Clinical Neurophysiology*, 45(2):302–304.

Ellaway, P. H., Taylor, A., and Durbaba, R. (2015). Muscle spindle and fusimotor activity in locomotion. *Journal of Anatomy*, 227(2):157–166.

Enoka, R. M. (2008). *Neuromechanics of Human Movement*. Human Kinetics.

Enoka, R. M. and Fuglevand, A. J. (2001). Motor unit physiology: some unresolved issues. *Muscle & Nerve: Official Journal of the American Association of Electrodiagnostic Medicine*, 24(1):4–17.

Farina, D. and Holobar, A. (2016). Characterization of human motor units from surface EMG decomposition. *Proceedings of the IEEE*, 104(2):353–373.

Farina, D., Vujaklija, I., Brånemark, R., Bull, A. M. J., Dietl, H., Graimann, B., Hargrove, L. J., Hoffmann, K.-P., Huang, H., Ingvarsson, T., et al. (2023). Toward higher-performance bionic limbs for wider clinical use. *Nature Biomedical Engineering*, 7(4):473–485.

Finkel, A. S. and Redman, S. J. (1983). The synaptic current evoked in cat spinal motoneurones by impulses in single group 1a axons. *The Journal of Physiology*, 342(1):615–632.

Fleshman, J. W., Segev, I., and Burke, R. B. (1988). Electrotonic architecture of type-identified alpha-motoneurons in the cat spinal cord. *Journal of Neurophysiology*, 60(1):60–85.

Fuglevand, A. J., Winter, D. A., and Patla, A. E. (1993). Models of recruitment and rate coding organization in motor-unit pools. *Journal of Neurophysiology*, 70(6):2470–2488.

Fyffe, R. E. W. (2001). *Spinal motoneurons: synaptic inputs and receptor organization*. CRC Press Boca Raton, FL.

Gandevia, S. C., Macefield, G., Burke, D., and McKenzie, D. K. (1990). Voluntary activation of human motor axons in the absence of muscle afferent feedback: the control of the deafferented hand. *Brain*, 113(5):1563–1581.

Gerstein, G. L. and Kiang, N. Y.-S. (1960). An approach to the quantitative analysis of electrophysiological data from single neurons. *Biophysical Journal*, 1(1):15–28.

Gerstner, W., Kistler, W. M., Naud, R., and Paninski, L. (2014). *Neuronal dynamics: From single neurons to networks and models of cognition*. Cambridge University Press.

Ghahremani Arekhloo, N., Parvizi, H., Zuo, S., Wang, H., Nazarpour, K., Marquetand, J., and Heidari, H. (2023). Alignment of magnetic sensing and clinical magnetomyography. *Frontiers in Neuroscience*, 17.

Gibbons, J. D. and Chakraborti, S. (2011). Nonparametric statistical inference. In *International encyclopedia of statistical science*, pages 977–979. Springer.

Gogeascoechea, A., Ornelas-Kobayashi, R., Yavuz, U. S., and Sartori, M. (2023). Characterization of motor unit firing and twitch properties for decoding musculoskeletal force in the human ankle joint in vivo. *IEEE Transactions on Neural Systems and Rehabilitation Engineering*, 31:4040–4050.

Granit, R., Kernell, D., and Lamarre, Y. (1966). Synaptic stimulation superimposed on motoneurones firing in the 'secondary range' to injected current. *The Journal of Physiology*, 187(2):401–415.

Greitemann, B., Brückner, L., Schäfer, M., and Baumgartner, R. (2016). Amputation und prothesenversorgung. *Zeitschrift für Orthopädie und Unfallchirurgie*.

Grey, M. J., Ladouceur, M., Andersen, J. B., Nielsen, J. B., and Sinkjær, T. (2001). Group II muscle afferents probably contribute to the medium latency soleus stretch reflex during walking in humans. *The Journal of Physiology*, 534:925–933.

Grill, S. E. and Hallett, M. (1995). Velocity sensitivity of human muscle spindle afferents and slowly adapting type II cutaneous mechanoreceptors. *The Journal of Physiology*, 489(2):593–602.

Grupp, T. (2023). Vergleich zwischen manueller und automatisierter Bestimmung von Reflexamplituden. Bachelor thesis, University of Stuttgart.

Gustafsson, B. and Pinter, M. J. (1984). An investigation of threshold properties among cat spinal alpha-motoneurones. *The Journal of Physiology*, 357(1):453–483.

Haggie, L., Schmid, L., Röhrle, O., Besier, T., McMorland, A., and Saini, H. (2023). Linking cortex and contraction - integrating models along the corticomuscular pathway. *Frontiers in Physiology*, 14.

Halliday, D. M., Conway, B. A., Farmer, S. F., and Rosenberg, J. R. (1998). Using electroencephalography to study functional coupling between cortical activity and electromyograms during voluntary contractions in humans. *Neuroscience Letters*, 241(1):5–8.

Hamill, O. P., Marty, A., Neher, E., Sakmann, B., and Sigworth, F. J. (1981). Improved patch-clamp techniques for high-resolution current recording from cells and cell-free membrane patches. *Pflügers Archiv*, 391:85–100.

Heckman, C. J. and Binder, M. D. (1988). Analysis of effective synaptic currents generated by homonymous ia afferent fibers in motoneurons of the cat. *Journal of Neurophysiology*, 60(6):1946–1966.

Heckman, C. J. and Binder, M. D. (1991). Computer simulation of the steady-state input-output function of the cat medial gastrocnemius motoneuron pool. *Journal of Neurophysiology*, 65(4):952–967.

Heckman, C. J. and Enoka, R. M. (2012). *Motor Unit*, pages 2629–2682. John Wiley & Sons, Ltd.

Heckman, C. J., Gorassini, M. A., and Bennett, D. J. (2005). Persistent inward currents in motoneuron dendrites: implications for motor output. *Muscle & Nerve: Official Journal of the American Association of Electrodiagnostic Medicine*, 31(2):135–156.

Heidlauf, T. and Röhrle, O. (2014). A multiscale chemo-electro-mechanical skeletal muscle model to analyze muscle contraction and force generation for different muscle fiber arrangements. *Frontiers in Physiology*, 5.

Henneman, E., Somjen, G., and Carpenter, D. O. (1965a). Excitability and inhibitibility of motoneurons of different sizes. *Journal of Neurophysiology*, 28(3):599–620.

Henneman, E., Somjen, G., and Carpenter, D. O. (1965b). Functional significance of cell size in spinal motoneurons. *Journal of Neurophysiology*, 28(3):560–580.

Herr, H. and Carty, M. J. (2021). The agonist-antagonist myoneural interface. *Techniques in Orthopaedics*, 36:337–344.

Herr, H. M., Clites, T. R., Srinivasan, S., Talbot, S. G., Dumanian, G. A., Cederna, P. S., and Carty, M. J. (2021). Reinventing extremity amputation in the era of functional limb restoration. *Annals of Surgery*, 273(2):269–279.

Herrmann, A. and Gerstner, W. (2002). Noise and the PSTH response to current transients: II. Integrate-and-fire model with slow recovery and application to motoneuron data. *Journal of Computational Neuroscience*, 12:83–95.

Hiebert, G. W. and Pearson, K. G. (1999). Contribution of sensory feedback to the generation of extensor activity during walking in the decerebrate cat. *Journal of Neurophysiology*, 81(2):758–770.

Hille, B. (2001). *Ion channels of excitable membranes*. Sinauer Associates, 3rd edition.

Hochman, S. and McCrea, D. A. (1994). Effects of chronic spinalization on ankle extensor motoneurons. I. Composite monosynaptic Ia EPSPs in four motoneuron pools. *Journal of Neurophysiology*, 71(4):1452–1467.

Hodgkin, A. L. and Huxley, A. F. (1952a). The components of membrane conductance in the giant axon of Loligo. *The Journal of Physiology*, 116(4):473–496.

Hodgkin, A. L. and Huxley, A. F. (1952b). Currents carried by sodium and potassium ions through the membrane of the giant axon of Loligo. *The Journal of Physiology*, 116(4):449–472.

Hodgkin, A. L. and Huxley, A. F. (1952c). The dual effect of membrane potential on sodium conductance in the giant axon of Loligo. *The Journal of Physiology*, 116(4):497–506.

Hodgkin, A. L. and Huxley, A. F. (1952d). A quantitative description of membrane current and its application to conduction and excitation in nerve. *The Journal of Physiology*, 117:500–544.

Hodgkin, A. L., Huxley, A. F., and Katz, B. (1952). Measurement of current-voltage relations in the membrane of the giant axon of Loligo. *The Journal of Physiology*, 116(4):424–448.

Holobar, A. and Zazula, D. (2007). Multichannel blind source separation using convolution kernel compensation. *IEEE Transactions on Signal Processing*, 55(9):4487–4496.

Homs-Pons, C., Lautenschlager, R., Schmid, L., Ernst, J., Göddeke, D., Röhrle, O., and Schulte, M. (2024). Coupled simulations and parameter inversion for neural system and electrophysiological muscle models. *GAMM-Mitteilungen*, e202370009.

Housley, S. N., Powers, R. K., Nardelli, P., Lee, S., Blum, K., Bewick, G. S., Banks, R. W., and Cope, T. C. (2024). Biophysical model of muscle spindle encoding. *Experimental Physiology*, 109(1):55–65.

Hulliger, M., Nordh, E., and Vallbo, A. B. (1985). Discharge in muscle spindle afferents related to direction of slow precision movements in man. *The Journal of Physiology*, 362(1):437–453.

Hunt, C. C. (1954). Relation of function to diameter in afferent fibers of muscle nerves. *The Journal of General Physiology*, 38(1):117–131.

Ito, M. and Oshima, T. (1965). Electrical behaviour of the motoneurone membrane during intracellularly applied current steps. *The Journal of Physiology*, 180(3):607–635.

Jami, L. (1992). Golgi tendon organs in mammalian skeletal muscle: functional properties and central actions. *Physiological Reviews*, 72(3):623–666.

Jankowska, E., Johannisson, T., and Lipski, J. (1981). Common interneurones in reflex pathways from group 1a and 1b afferents of ankle extensors in the cat. *The Journal of Physiology*, 310(1):381–402.

Jensen, D. B., Stecina, K., Wienecke, J., Hedegaard, A., Sukiasyan, N., Hultborn, H. R., and Meehan, C. F. (2018). The subprimary range of firing is present in both cat and mouse spinal motoneurons and its relationship to force development is similar for the two species. *Journal of Neuroscience*, 38(45):9741–9753.

Johannsson, J., Duchateau, J., and Baudry, S. (2017). Spinal and corticospinal pathways are differently modulated when standing at the bottom and the top of a three-step staircase in young and older adults. *European Journal of Applied Physiology*, 117:1165–1174.

Johansson, T., Meier, P., and Blickhan, R. (2000). A Finite-Element Model for the mechanical analysis of skeletal muscles. *Journal of Theoretical Biology*, 206(1):131–149.

Johnston, D. and Wu, S. M.-S. (1995). *Foundations of cellular neurophysiology*. MIT press.

Jones, K. E. and Bawa, P. (1995). Responses of human motoneurons to la inputs: effects of background firing rate. *Canadian Journal of Physiology and Pharmacology*, 73(9):1224–1234.

Jones, K. E. and Bawa, P. (1997). Computer simulation of the responses of human motoneurons to composite 1A EPSPS: effects of background firing rate. *Journal of Neurophysiology*, 77(1):405–420.

Kakuda, N. (2000). Response of human muscle spindle afferents to sinusoidal stretching with a wide range of amplitudes. *The Journal of Physiology*, 527(2):397–404.

Kandel, E. R., Schwartz, J. H., Jessell, T. M., Siegelbaum, S., Hudspeth, A. J., Mack, S., et al. (2013). *Principles of neural science*. McGraw-Hill New York, 5th edition.

Kandel, E. R. and Spencer, W. A. (1961). Electrophysiology of hippocampal neurons: II. after-potentials and repetitive firing. *Journal of Neurophysiology*, 24(3):243–259.

Kapardi, M., Pithapuram, M. V., Rangayyan, Y. M., Iyengar, R. S., Singh, A. K., Sripada, S., and Raghavan, M. (2022). In-silico neuro musculoskeletal model reproduces the movement types obtained by spinal micro stimulation. *Computer Methods and Programs in Biomedicine*, 220:106804.

Keenan, K. G., Farina, D., Merletti, R., and Enoka, R. M. (2006). Amplitude cancellation reduces the size of motor unit potentials averaged from the surface EMG. *Journal of Applied Physiology*, 100(6):1928–1937.

Kernell, D. (1965). High-frequency repetitive firing of cat lumbosacral motoneurones stimulated by long-lasting injected currents. *Acta Physiologica Scandinavica*, 65(1-2):74–86.

Kernell, D. (2006). *The motoneurone and its muscle fibres*. Oxford University Press.

Kiehn, O., Kjaerulff, O., Tresch, M. C., and Harris-Warrick, R. M. (2000). Contributions of intrinsic motor neuron properties to the production of rhythmic motor output in the mammalian spinal cord. *Brain Research Bulletin*, 53(5):649–659.

Kim, D., Triolo, R., and Charkhkar, H. (2023). Plantar somatosensory restoration enhances gait, speed perception, and motor adaptation. *Science Robotics*, 8(83):eadf8997.

Kjaerulff, O. and Kiehn, O. (2001). 5-HT modulation of multiple inward rectifiers in motoneurons in intact preparations of the neonatal rat spinal cord. *Journal of Neurophysiology*, 85(2):580–593.

Klotz, T., Lehmann, L., Negro, F., and Röhrle, O. (2023). High-density magnetomyography is superior to high-density surface electromyography for motor unit decomposition: a simulation study. *Journal of Neural Engineering*.

Knellwolf, T. P., Burton, A. R., Hammam, E., and Macefield, V. G. (2019). Firing properties of muscle spindles supplying the intrinsic foot muscles of humans in unloaded and freestanding conditions. *Journal of Neurophysiology*, 121(1):74–84.

Kokkorogiannis, T. (2004). Somatic and intramuscular distribution of muscle spindles and their relation to muscular angiotypes. *Journal of Theoretical Biology*, 229(2):263–280.

Koutris, M., Türker, K. S., van der Weijden, J. J., van Selms, M. K., and Lobbezoo, F. (2016). Two different analyzing methods for inhibitory reflexes: Do they yield comparable outcomes? *Journal of Neuroscience Methods*, 274:49–52.

Kozhina, G. V. (1983). The role of reflex mechanisms in postinhibitory rebound studied by analysis of human single motor unit activity. *Neurophysiology*, 15(1):67–75.

Kudina, L. P. (1980). Reflex effects of muscle afferents on antagonist studied on single firing motor units in man. *Electroencephalography and Clinical Neurophysiology*, 50(3-4):214–221.

Kudina, L. P. (1999). Analysis of firing behaviour of human motoneurones within 'subprimary range'. *Journal of Physiology-Paris*, 93(1-2):115–123.

Kudina, L. P. and Alexeeva, N. L. (1992). After-potentials and control of repetitive firing in human motoneurones. *Electroencephalography and Clinical Neurophysiology/Evoked Potentials Section*, 85(5):345–353.

Lapicque, L. (1907). Recherches quantitatives sur l'excitation electrique des nerfs traitee comme une polarization. *Journal de physiologie et de pathologie générale*, 9:620–635.

Larkman, P. M. and Kelly, J. S. (1992). Ionic mechanisms mediating 5-hydroxytryptamine-and noradrenaline-evoked depolarization of adult rat facial motoneurones. *The Journal of Physiology*, 456(1):473–490.

Lavigne, G., Frysinger, R., and Lund, J. P. (1983). Human factors in the measurement of the masseteric silent period. *Journal of Dental Research*, 62(9):985–988.

Lemon, R. N. (2008). Descending pathways in motor control. *Annual Review of Neuroscience*, 31:195–218.

Lesage, R., Van Oudheusden, M., Schievano, S., Van Hoyweghen, I., Geris, L., and Capelli, C. (2023). Mapping the use of computational modelling and simulation in clinics: A survey. *Frontiers in Medical Technology*, 5.

Li, S., Zhuang, C., Hao, M., He, X., Marquez, J. C., Niu, C. M., and Lan, N. (2015). Coordinated alpha and gamma control of muscles and spindles in movement and posture. *Frontiers in Computational Neuroscience*, 9.

Liddell, E. G. T. and Sherrington, C. S. (1925). Recruitment and some other features of reflex inhibition. *Proceedings of the Royal Society of London. Series B, Containing Papers of a Biological Character*, 97(686):488–518.

Lin, C.-C. K. and Crago, P. E. (2002a). Neural and mechanical contributions to the stretch reflex: a model synthesis. *Annals of Biomedical Engineering*, 30:54–67.

Lin, C.-C. K. and Crago, P. E. (2002b). Structural model of the muscle spindle. *Annals of Biomedical Engineering*, 30(1):68–83.

Lotti, N., Xiloyannis, M., Durandau, G., Galofaro, E., Sanguineti, V., Masia, L., and Sartori, M. (2020). Adaptive model-based myoelectric control for a soft wearable arm exosuit: A new generation of wearable robot control. *IEEE Robotics & Automation Magazine*, 27(1):43–53.

Lucas, S. M., Cope, T. C., and Binder, M. D. (1984). Analysis of individual Ia-afferent EPSPs in a homonymous motoneuron pool with respect to muscle topography. *Journal of Neurophysiology*, 51(1):64–74.

Lulic-Kuryllo, T. and Inglis, J. G. (2022). Sex differences in motor unit behaviour: A review. *Journal of Electromyography and Kinesiology*, 66:102689.

Lüscher, H. R., Ruenzel, P., and Henneman, E. (1983). Composite EPSPs in motoneurons of different sizes before and during PTP: implications for transmission failure and its relief in Ia projections. *Journal of Neurophysiology*, 49(1):269–289.

Macefield, V. G. and Knellwolf, T. P. (2018). Functional properties of human muscle spindles. *Journal of Neurophysiology*, 120(2):452–467.

Maganaris, C. N. (2001). Force-length characteristics of in vivo human skeletal muscle. *Acta Physiologica Scandinavica*, 172(4):279–285.

Maier, B. (2021). *Scalable Biohysical Simulations of the Neuromuscular System*. PhD thesis, University of Stuttgart.

Maier, B., Emamy, N., Krämer, A., and Mehl, M. (2019). Highly parallel multi-physics simulation of muscular activation and EMG. In *COUPLED VIII: proceedings of the VIII International Conference on Computational Methods for Coupled Problems in Science and Engineering*, pages 610–621. CIMNE.

Maltenfort, M. G. and Burke, R. E. (2003). Spindle model responsive to mixed fusimotor inputs and testable predictions of β feedback effects. *Journal of Neurophysiology*, 89(5):2797–2809.

Maltenfort, M. G., Heckman, C. J., and Rymer, W. Z. (1998). Decorrelating actions of renshaw interneurons on the firing of spinal motoneurons within a motor nucleus: a simulation study. *Journal of Neurophysiology*, 80(1):309–323.

Manuel, M., Chardon, M., Tysseling, V., and Heckman, C. J. (2019). Scaling of motor output, from mouse to humans. *Physiology*, 34(1):5–13.

Manuel, M., Meunier, C., Donnet, M., and Zytnicki, D. (2007). Resonant or not, two amplification modes of proprioceptive inputs by persistent inward currents in spinal motoneurons. *Journal of Neuroscience*, 27(47):12977–12988.

Marshall, N. J., Glaser, J. I., Trautmann, E. M., Amematsro, E. A., Perkins, S. M., Shadlen, M. N., Abbott, L. F., Cunningham, J. P., and Churchland, M. M. (2022). Flexible neural control of motor units. *Nature Neuroscience*, 25(11):1492–1504.

Martinez-Valdes, E., Negro, F., Laine, C. M., Falla, D., Mayer, F., and Farina, D. (2017). Tracking motor units longitudinally across experimental sessions with high-density surface electromyography. *The Journal of Physiology*, 595(5):1479–1496.

Matthews, P. B. C. (1962). The differentiation of two types of fusimotor fibre by their effects on the dynamic response of muscle spindle primary endings. *Quarterly Journal of Experimental Physiology and Cognate Medical Sciences: Translation and Integration*, 47(4):324–333.

Matthews, P. B. C. (1996). Relationship of firing intervals of human motor units to the trajectory of post-spike after-hyperpolarization and synaptic noise. *The Journal of Physiology*, 492(2):597–628.

Matthews, P. B. C. (1999). The effect of firing on the excitability of a model motoneurone and its implications for cortical stimulation. *The Journal of Physiology*, 518(3):867–882.

Matthews, P. B. C. (2002). Measurement of excitability of tonically firing neurones tested in a variable-threshold model motoneurone. *The Journal of Physiology*, 544(1):315–332.

Mazzocchio, R., Rothwell, J. C., and Rossi, A. (1995). Distribution of Ia effects onto human hand muscle motoneurones as revealed using an H reflex technique. *The Journal of Physiology*, 489(1):263–273.

Mendell, L. M. and Henneman, E. (1971). Terminals of single Ia fibers: location, density, and distribution within a pool of 300 homonymous motoneurons. *Journal of Neurophysiology*, 34(1):171–187.

Merletti, R. and Farina, D. (2009). Analysis of intramuscular electromyogram signals. *Philosophical Transactions of the Royal Society A: Mathematical, Physical and Engineering Sciences*, 367(1887):357–368.

Merletti, R. and Farina, D. (2016). *Surface electromyography: physiology, engineering, and applications*. John Wiley & Sons.

Mileusnic, M. P., Brown, I. E., Lan, N., and Loeb, G. E. (2006). Mathematical models of proprioceptors. I. Control and transduction in the muscle spindle. *Journal of Neurophysiology*, 96(4):1772–1788.

Mileusnic, M. P. and Loeb, G. E. (2009). Force estimation from ensembles of Golgi tendon organs. *Journal of Neural Engineering*, 6(3):036001.

Milligan, C. J., Edwards, I. J., and Deuchars, J. (2006). HCN1 ion channel immunoreactivity in spinal cord and medulla oblongata. *Brain Research*, 1081(1):79–91.

Monster, A. W. and Chan, H. (1977). Isometric force production by motor units of extensor digitorum communis muscle in man. *Journal of Neurophysiology*, 40(6):1432–1443.

Moore, G. P., Segundo, J. P., Perkel, D. H., and Levitan, H. (1970). Statistical signs of synaptic interaction in neurons. *Biophysical Journal*, 10(9):876–900.

Moraud, E. M., Capogrosso, M., Formento, E., Wenger, N., DiGiovanna, J., Courtine, G., and Micera, S. (2016). Mechanisms underlying the neuromodulation of spinal circuits for correcting gait and balance deficits after spinal cord injury. *Neuron*, 89(4):814–828.

Mordhorst, M., Strecker, T., Wirtz, D., Heidlauf, T., and Röhrle, O. (2017). POD-DEIM reduction of computational EMG models. *Journal of Computational Science*, 19:86–96.

Moritz, C. T., Barry, B. K., Pascoe, M. A., and Enoka, R. M. (2005). Discharge rate variability influences the variation in force fluctuations across the working range of a hand muscle. *Journal of Neurophysiology*, 93(5):2449–2459.

Muceli, S., Poppendieck, W., Holobar, A., Gandevia, S., Liebetanz, D., and Farina, D. (2022). Blind identification of the spinal cord output in humans with high-density electrode arrays implanted in muscles. *Science Advances*, 8(46):eabo5040.

Nadler, M. A., Harrison, L. M., and Stephens, J. A. (2002). Changes in cutaneomuscular reflex responses in relation to normal ageing in man. *Experimental Brain Research*, 146:48–53.

Nadler, M. A., Harrison, L. M., and Stephens, J. A. (2004). Cutaneomuscular reflexes following stroke: a 2-year longitudinal study. *Journal of the Neurological Sciences*, 217(2):195–203.

Negro, F. and Farina, D. (2011). Decorrelation of cortical inputs and motoneuron output. *Journal of Neurophysiology*, 106(5):2688–2697.

Negro, F., Muceli, S., Castronovo, A. M., Holobar, A., and Farina, D. (2016a). Multi-channel intramuscular and surface EMG decomposition by convolutive blind source separation. *Journal of Neural Engineering*, 13(2):026027.

Negro, F., Yavuz, U. Ş., and Farina, D. (2016b). The human motor neuron pools receive a dominant slow-varying common synaptic input. *The Journal of Physiology*, 594(19):5491–5505.

Nelson, M. E. (2005). *Electrophysiological models*, pages 285–301. Wiley.

Nordh, E., Hilliger, M., and Vallbo, Å. B. (1983). The variability of inter-spike intervals of human spindle afferents in relaxed muscles. *Brain Research*, 271(1):89–99.

O'Donovan, M. J. and Falgairolle, M. (2022). *Vertebrate Motoneurons*, volume 28. Springer Nature.

Ornelas-Kobayashi, R., Gogeascoechea, A., and Sartori, M. (2023). Person-specific biophysical modeling of alpha-motoneuron pools driven by in vivo decoded neural synaptic input. *IEEE Transactions on Neural Systems and Rehabilitation Engineering*, 31:1532–1541.

Ovadia, S. A. and Askari, M. (2015). Upper extremity amputations and prosthetics. In *Seminars in Plastic Surgery*, volume 29, pages 055–061. Thieme Medical Publishers.

Ovalle, W. K. and Smith, R. S. (1972). Histochemical identification of three types of intrafusal muscle fibers in the cat and monkey based on the myosin ATPase reaction. *Canadian Journal of Physiology and Pharmacology*, 50(3):195–202.

Özyurt, M. G., Piotrkiewicz, M., Topkara, B., Weisskircher, H.-W., and Türker, K. S. (2019). Motor units as tools to evaluate profile of human Renshaw inhibition. *The Journal of Physiology*, 597(8):2185–2199.

Pearcey, G. E. P., Khurram, O. U., Beauchamp, J. A., and Heckman, C. J. (2020). Exploring the effects of Ia reciprocal inhibition on neuromodulatory commands in the human lower limb. *The FASEB Journal*, 34:1–1.

Pierrot-Deseilligny, E. and Burke, D. (2005). *The circuitry of the human spinal cord: its role in motor control and movement disorders*. Cambridge university press.

Pierrot-Deseilligny, E. and Mazevet, D. (2000). The monosynaptic reflex: a tool to investigate motor control in humans. interest and limits. *Neurophysiologie Clinique/Clinical Neurophysiology*, 30(2):67–80.

Pinar, S., Kitano, K., and Koceja, D. M. (2010). Role of vision and task complexity on soleus H-reflex gain. *Journal of Electromyography and Kinesiology*, 20(2):354–358.

Piotrkiewicz, M., Kudina, L., and Jakubiec, M. (2009). Computer simulation study of the relationship between the profile of excitatory postsynaptic potential and stimulus-correlated motoneuron firing. *Biological Cybernetics*, 100:215–230.

Pithapuram, M. V. and Raghavan, M. (2022). Automatic rule-based generation of spinal cord connectome model for a neuro-musculoskeletal limb in-silico. *IOP SciNotes*, 3(1):014001.

Potvin, J. R. and Fuglevand, A. J. (2017). A motor unit-based model of muscle fatigue. *PLoS Computational Biology*, 13(6):e1005581.

Powers, R. K. and Binder, M. D. (1985). Distribution of oligosynaptic group I input to the cat medial gastrocnemius motoneuron pool. *Journal of Neurophysiology*, 53(2):497–517.

Powers, R. K. and Binder, M. D. (1996). Experimental evaluation of input-output models of motoneuron discharge. *Journal of Neurophysiology*, 75(1):367–379.

Powers, R. K. and Binder, M. D. (2000). Summation of effective synaptic currents and firing rate modulation in cat spinal motoneurons. *Journal of Neurophysiology*, 83(1):483–500.

Powers, R. K. and Binder, M. D. (2007). Input-output functions of mammalian motoneurons. *Reviews of Physiology, Biochemistry and Pharmacology*, pages 137–263.

Powers, R. K., ElBasiouny, S. M., Rymer, W. Z., and Heckman, C. J. (2012). Contribution of intrinsic properties and synaptic inputs to motoneuron discharge patterns: a simulation study. *Journal of Neurophysiology*, 107(3):808–823.

Powers, R. K., Robinson, F. R., Konodi, M. A., and Binder, M. D. (1992). Effective synaptic current can be estimated from measurements of neuronal discharge. *Journal of Neurophysiology*, 68(3):964–968.

Powers, R. K., Sawczuk, A., Musick, J. R., and Binder, M. D. (1999). Multiple mechanisms of spike-frequency adaptation in motoneurones. *Journal of Physiology-Paris*, 93(1-2):101–114.

Powers, R. K. and Türker, K. (2010a). Estimates of EPSP amplitude based on changes in motoneuron discharge rate and probability. *Experimental Brain Research*, 206(4):427–440.

Powers, R. K. and Türker, K. S. (2010b). Deciphering the contribution of intrinsic and synaptic currents to the effects of transient synaptic inputs on human motor unit discharge. *Clinical Neurophysiology*, 121(10):1643–1654.

Prochazka, A. and Gorassini, M. (1998a). Ensemble firing of muscle afferents recorded during normal locomotion in cats. *The Journal of Physiology*, 507(1):293–304.

Prochazka, A. and Gorassini, M. (1998b). Models of ensemble firing of muscle spindle afferents recorded during normal locomotion in cats. *The Journal of Physiology*, 507(1):277–291.

Rajaram, E., Kaltenbach, C., Fischl, M. J., Mrowka, L., Alexandrova, O., Grothe, B., Hennig, M. H., and Kopp-Scheinpflug, C. (2019). Slow NMDA-mediated excitation accelerates offset-response latencies generated via a post-inhibitory rebound mechanism. *eNeuro*, 6(3).

Rall, W. (1962a). Electrophysiology of a dendritic neuron model. *Biophysical Journal*, 2(2, Part 2):145.

Rall, W. (1962b). Theory of physiological properties of dendrites. *Annals of the New York Academy of Sciences*, 96(4):1071–1092.

Rall, W., Burke, R. E., Holmes, W. R., Jack, J. J., Redman, S. J., and Segev, I. (1992). Matching dendritic neuron models to experimental data. *Physiological Reviews*, 72(suppl_4):S159–S186.

Rao, K. D. and Swamy, M. N. S. (2018). *Digital signal processing: Theory and practice*. Springer.

Raphael, G., Tsianos, G. A., and Loeb, G. E. (2010). Spinal-like regulator facilitates control of a two-degree-of-freedom wrist. *Journal of Neuroscience*, 30(28):9431–9444.

Reinking, R. M., Stephens, J. A., and Stuart, D. G. (1975). The tendon organs of cat medial gastrocnemius: significance of motor unit type and size for the activation of Ib afferents. *The Journal of Physiology*, 250(3):491–512.

Rogasch, N. C., Burne, J. A., Binboğa, E., and Türker, K. S. (2011). Synaptic potentials contributing to reflex inhibition in gastrocnemius following tendon electrical stimulation. *Clinical Neurophysiology*, 122(6):1190–1196.

Rohlén, R., Stålberg, E., and Grönlund, C. (2020). Identification of single motor units in skeletal muscle under low force isometric voluntary contractions using ultrafast ultrasound. *Scientific Reports*, 10(1):22382.

Röhrle, O., Davidson, J. B., and Pullan, A. J. (2008). Bridging scales: A three-dimensional electromechanical Finite Element Model of skeletal muscle. *SIAM Journal on Scientific Computing*, 30(6):2882–2904.

Röhrle, O., Yavuz, U. Ş., Klotz, T., Negro, F., and Heidlauf, T. (2019). Multiscale modeling of the neuromuscular system: Coupling neurophysiology and skeletal muscle mechanics. *WIREs Systems Biology and Medicine*, 11(6):e1457.

Ross, S. M. (2014). *Introduction to probability models*. Academic press.

Rossi, P., Pierelli, F., Parisi, L., Perrotta, A., Bartolo, M., Amabile, G., and Serrao, M. (2003). Effect of painful heterotopic stimulation on the cutaneous silent period in the upper limbs. *Clinical Neurophysiology*, 114(1):1–6.

Schäfer, S. S. (1974). The discharge frequencies of primary muscle spindle endings during simultaneous stimulation of two fusimotor filaments. *Pflügers Archiv*, 350(4):359–372.

Schmid, L., Klotz, T., Röhrle, O., Powers, R. K., Negro, F., and Yavuz, U. Ş. (2024). Postinhibitory excitation in motoneurons can be facilitated by hyperpolarization-activated inward currents: A simulation study. *PLOS Computational Biology*, 20(1):1–22.

Schmid, L., Klotz, T., and Yavuz, U. Ş. (2022). Spindle model responsive to mixed fusimotor inputs: an updated version of the Maltenfort and Burke (2003) model. *Physiome*.

Schmitt, S., Günther, M., and Häufle, D. F. B. (2019). The dynamics of the skeletal muscle: A systems biophysics perspective on muscle modeling with the focus on Hill-type muscle models. *GAMM-Mitteilungen*, 42(3):e201900013.

Schoultz, T. W. and Swett, J. E. (1972). The fine structure of the Golgi tendon organ. *Journal of Neurocytology*, 1(1):1–25.

Schouten, A. C., Mugge, W., and van der Helm, F. C. T. (2008). NMClab, a model to assess the contributions of muscle visco-elasticity and afferent feedback to joint dynamics. *Journal of Biomechanics*, 41(8):1659–1667.

Schuurmans, J., de Vlugt, E., Schouten, A. C., Meskers, C. G. M., de Groot, J. H., and van der Helm, F. C. T. (2009). The monosynaptic Ia afferent pathway can largely explain the stretch duration effect of the long latency M2 response. *Experimental Brain Research*, 193(4):491–500.

Schwindt, P. C. and Calvin, W. H. (1973). Equivalence of synaptic and injected current in determining the membrane potential trajectory during motoneuron rhythmic firing. *Brain Research*, 59:389–394.

Scott, J. G. and Mendell, L. M. (1976). Individual EPSPs produced by single triceps surae Ia afferent fibers in homonymous and heteronymous motoneurons. *Journal of Neurophysiology*, 39(4):679–692.

Semmler, J. G. and Türker, K. S. (1994). Compound group I excitatory input is differentially distributed to motoneurones of the human tibialis anterior. *Neuroscience Letters*, 178(2):206–210.

Shampine, L. F. and Reichelt, M. W. (1997). The matlab ode suite. *SIAM journal on scientific computing*, 18(1):1–22.

Sherrington, C. S. (1906). *The integrative action of the nervous system*. New York, C Scribner and Sons.

Sherrington, C. S. (1909). On plastic tonus and proprioceptive reflexes. *Quarterly Journal of Experimental Physiology*, 2(2):109–156.

Smail, L. C., Neal, C., Wilkins, C., and Packham, T. L. (2021). Comfort and function remain key factors in upper limb prosthetic abandonment: findings of a scoping review. *Disability and Rehabilitation: Assistive Technology*, 16(8):821–830.

Song, D., Lan, N., Loeb, G. E., and Gordon, J. (2008). Model-based sensorimotor integration for multi-joint control: development of a virtual arm model. *Annals of Biomedical Engineering*, 36:1033–1048.

Sreenivasa, M., Ayusawa, K., and Nakamura, Y. (2015). Modeling and identification of a realistic spiking neural network and musculoskeletal model of the human arm, and an application to the stretch reflex. *IEEE Transactions on Neural Systems and Rehabilitation Engineering*, 24(5):591–602.

Staude, G. and Wolf, W. (1999). Objective motor response onset detection in surface myoelectric signals. *Medical Engineering & Physics*, 21(6-7):449–467.

Stauffer, E. K., Watt, D. G., Taylor, A., Reinking, R. M., and Stuart, D. G. (1976). Analysis of muscle receptor connections by spike-triggered averaging. 2. Spindle group II afferents. *Journal of Neurophysiology*, 39(6):1393–1402.

Stein, R. B. (1995). Presynaptic inhibition in humans. *Progress in Neurobiology*, 47(6):533–544.

Stienen, A. H. A., Schouten, A. C., Schuurmans, J., and Van Der Helm, F. C. T. (2007). Analysis of reflex modulation with a biologically realistic neural network. *Journal of Computational Neuroscience*, 23:333–348.

Stuart, G. J. and Redman, S. J. (1990). Voltage dependence of Ia reciprocal inhibitory currents in cat spinal motoneurones. *The Journal of Physiology*, 420(1):111–125.

Takahashi, T. (1990). Inward rectification in neonatal rat spinal motoneurones. *The Journal of Physiology*, 423(1):47–62.

Taylor, A. M. and Enoka, R. M. (2004). Quantification of the factors that influence discharge correlation in model motor neurons. *Journal of Neurophysiology*, 91(2):796–814.

Tomlinson, S., Burke, D., Hanna, M., Koltzenburg, M., and Bostock, H. (2010). In vivo assessment of HCN channel current (Ih) in human motor axons. *Muscle & Nerve: Official Journal of the American Association of Electrodiagnostic Medicine*, 41(2):247–256.

Traub, R. D., Wong, R. K., Miles, R., and Michelson, H. (1991). A model of a CA3 hippocampal pyramidal neuron incorporating voltage-clamp data on intrinsic conductances. *Journal of Neurophysiology*, 66(2):635–650.

Türker, K. S. (2022). An opinion on the 'delayed spikes' in human motoneurons. *Experimental Brain Research*, 240(1):1–3.

Türker, K. S. and Cheng, H. B. (1994). Motor-unit firing frequency can be used for the estimation of synaptic potentials in human motoneurones. *Journal of Neuroscience Methods*, 53(2):225–234.

Türker, K. S. and Powers, R. K. (1999). Effects of large excitatory and inhibitory inputs on motoneuron discharge rate and probability. *Journal of Neurophysiology*, 82(2):829–840.

Türker, K. S. and Powers, R. K. (2003). Estimation of postsynaptic potentials in rat hypoglossal motoneurones: insights for human work. *The Journal of Physiology*, 551(2):419–431.

Türker, K. S. and Powers, R. K. (2005). Black box revisited: a technique for estimating postsynaptic potentials in neurons. *Trends in Neurosciences*, 28(7):379–386.

Türker, K. S., Schmied, A., and Cheng, H. B. (1996). Correlated changes in the firing rate of human motor units during voluntary contraction. *Experimental Brain Research*, 111(3):455–464.

Türker, K. S., Yang, J., and Brodin, P. (1997). Conditions for excitatory or inhibitory masseteric reflexes elicited by tooth pressure in man. *Archives of Oral Biology*, 42(2):121–128.

Uysal, H., Özyurt, M. G., Göztepe, M. B., and Türker, K. S. (2019). Medium latency excitatory reflex of soleus re-examined. *Experimental Brain Research*, 237(7):1717–1725.

Vaisman, L., Zariffa, J., and Popovic, M. R. (2010). Application of singular spectrum-based change-point analysis to EMG-onset detection. *Journal of Electromyography and Kinesiology*, 20(4):750–760.

Vannucci, L., Falotico, E., and Laschi, C. (2017). Proprioceptive feedback through a neuromorphic muscle spindle model. *Frontiers in Neuroscience*, 11.

Watt, D. G., Stauffer, E. K., Taylor, A., Reinking, R. M., and Stuart, D. G. (1976). Analysis of muscle receptor connections by spike-triggered averaging. 1. spindle primary and tendon organ afferents. *Journal of Neurophysiology*, 39(6):1375–1392.

Windhorst, U. (1990). Activation of Renshaw cells. *Progress in Neurobiology*, 35(2):135–179.

Witteveen, H. J. B., Rietman, H. S., and Veltink, P. H. (2015). Vibrotactile grasping force and hand aperture feedback for myoelectric forearm prosthesis users. *Prosthetics and Orthotics International*, 39(3):204–212.

Yavuz, Ş. U., Mrachacz-Kersting, N., Sebik, O., Berna Ünver, M., Farina, D., and Türker, K. S. (2014). Human stretch reflex pathways reexamined. *Journal of Neurophysiology*, 111(3):602–612.

Yavuz, U. Ş., Negro, F., Diedrichs, R., and Farina, D. (2018). Reciprocal inhibition between motor neurons of the tibialis anterior and triceps surae in humans. *Journal of Neurophysiology*, 119(5):1699–1706.

Yavuz, U. Ş., Negro, F., Sebik, O., Holobar, A., Frömmel, C., Türker, K. S., and Farina, D. (2015). Estimating reflex responses in large populations of motor units by decomposition of the high-density surface electromyogram. *The Journal of Physiology*, 593(19):4305–4318.

York, G., Osborne, H., Sriya, P., Astill, S., de Kamps, M., and Chakrabarty, S. (2022). The effect of limb position on a static knee extension task can be explained with a simple spinal cord circuit model. *Journal of Neurophysiology*, 127(1):173–187.

Zengel, J. E., Reid, S. A., Sypert, G. W., and Munson, J. B. (1985). Membrane electrical properties and prediction of motor-unit type of medial gastrocnemius motoneurons in the cat. *Journal of Neurophysiology*, 53(5):1323–1344.

Zhang, D., Poignet, P., Bo, A. P. L., and Ang, W. T. (2009). Exploring peripheral mechanism of tremor on neuromusculoskeletal model: A general simulation study. *IEEE Transactions on Biomedical Engineering*, 56(10):2359–2369.